How can we make a diverse range of aromatic sulfates to explore sulfatase-substrate relationships?

A thesis

submitted in partial fulfilment

of the requirements for the degree

of

Master of Science (Research) in Chemistry

at

The University of Waikato

by

Peiyao Wang

THE UNIVERSITY OF
WAIKATO
Te Whare Wānanga o Waikato

2026

Abstract

Antibody–drug conjugates (ADCs) are an emerging class of targeted therapeutics that combine the high specificity of monoclonal antibodies (mAbs) with the potent cytotoxicity of small-molecule drugs. A critical component of ADC design is the linker between mAbs and payload, as its chemical stability and cleavage behaviour directly determine therapeutic efficacy, selectivity, and safety. While peptide-based cleavable linkers dominate current clinical ADC platforms, their susceptibility to premature cleavage and instability in certain biological contexts has motivated the exploration of alternative enzymatically cleavable linkers.

Arylsulfatase-cleavable linkers have recently attracted increasing interest as a promising alternative due to their excellent efficiency and reported stability in both human and mouse plasma. The cleavage of sulfate is catalysed by lysosomal sulfatases. Sulfatases were expressed in some tumour environments, which further support the selectivity of ADCs. However, systematic study for the characterization of structure and the analysis of properties is still insufficient, which limited the development of sulfatase-cleavable linker in certain degree.

In this study, a diverse library of substituted aryl sulfates was synthesised to probe sulfatase–substrate interactions and to establish a robust analytical framework for their characterisation. The synthetic strategy enabled the preparation of aryl sulfates bearing a range of electron-donating and electron-withdrawing substituents at different positions on the aromatic ring, allowing systematic evaluation of electronic and structural effects. The resulting compounds were fully characterised using nuclear magnetic resonance (NMR), high-performance liquid chromatography (HPLC), mass spectrometry (MS), and UV–visible (UV–Vis) spectroscopy.

Acknowledgements

I would like to express my sincere gratitude to my academic supervisor, Dr. Benjamin Dickson, for his guidance, patience, and continuous support throughout this research project. His insightful feedback and encouragement were invaluable during the experimental work, data interpretation, and the writing of this thesis. I am especially grateful for the intellectual independence he encouraged, which greatly contributed to my development as a researcher.

I would also like to thank Dr. Tameryn Stringer for her guidance and support in the laboratory, and for generously sharing her expertise during my experimental work.

My sincere thanks also go to Emma Dickson for her helpful suggestions on my thesis. I am also grateful for her kindness and the delicious desserts she shared, which brought comfort during stressful moments of researching. I would like to thank the University of Waikato chemistry staff for their assistance throughout this work. In particular, I thank Karla Watson and Dr. Megan Grainger for their help with HPLC operation and troubleshooting, Annie Barker for assistance with UV-Vis spectroscopy and laboratory training, Jenny Stockdill for support with laboratory equipment and consumables, and Dr. Simeon Atiga for his guidance with NMR spectroscopy. I am thankful to my senior colleagues, Jiaming Liu and Madushani Dissanayaka, for their generosity in sharing experience, offering advice, and providing encouragement throughout my research. Their support and companionship contributed to a collaborative and positive research environment. Finally, I would like to thank my family, Yang Genlian, Wang Zhaoming, and Wang Hui, for their love and support, and my cats, Maoye and Linlin, for the comfort they brought me along the way.

Table of Contents

Abstract i
Acknowledgements ii
Table of Contents iii
List of Figures v
List of Tables vii
List of Acronyms and Abbreviations ix
1. Introduction 1
1.1 Cancer and chemotherapy 1
1.2 Antibody-drug conjugates (ADCs) 3
1.2.1 Introduction of ADCs 3
1.2.2 The first-generation ADCs 5
1.2.3 The second-generation ADCs 6
1.2.4 The third-generation ADCs 9
1.3 Representative ADC therapeutics 11
1.4 Linker chemistry 17
1.4.1 Non-cleavable linkers 18
1.4.2 Cleavable linkers 20
1.4.3 Enzyme cleavable linkers 23
1.4.3.1 Peptidase cleavable linkers 24
1.4.3.2 β-Glucuronide cleavable linkers 27
1.4.4 Sulfatase cleavable linker 32
1.5 Sulfatases 35
1.5.1 The sulfatase family 35
1.5.3 The function and related diseases 39
1.6 Sulfate synthesis 43
1.6.1 Direct methods (converting phenols to sulfates) 43
1.6.2 Indirect methods (via protecting group approaches) 47
1.7 This work 57
2. Result and Discussion 59
2.1 Evaluation of Synthetic Outcomes 59
2.1.1 Preparation of Chlorosulfate **28** and Imidazolium **33** 59
2.1.2 Synthesis and Characterisation of Aryl Sulfates Prepared with **33** 61
2.1.2.1 Synthesis of Fluorine-substituted Sulfate **35a**-**35c** 62
2.1.2.2 Synthesis of Boc-protected Amino-substituted Sulfate **35d**-**35f** 68
2.1.2.3 Synthesis of cyano-substituted sulfate **35g** 76
2.1.2.4 Synthesis of Methyl Ester-substituted Sulfates **35h**-**35j** 77
2.2.1.5 Synthesis of Aldehyde-Substituted Sulfate Diesters **35k-35m** 83
2.1.3 Preparation of Amino-substituted Sulfate Diesters **35n**-**35p** 87
2.1.4 Preparation of Aryl Sulfate Diester **35q**-**35s** Bearing an Ethyl Carbamate Substituent 89

2.1.5 Synthesis and Characterization of Deprotected Aryl Sulfates **36** 96
2.2 Investigation of analytical techniques to support enzymatic hydrolysis monitoring 112
2.2.1 Characteristics of Ultraviolet–Visible Absorption Spectroscopy 113
2.2.2 Analysis of High-Performance Liquid Chromatography (HPLC) 117
2.3 Future Work 121
3. Experimental 124
3.1 General Experimental 124
3.2 Synthetic Compounds 125
3.2.1 General Procedure for sulfation reactions 125
3.2.2 Synthetic compounds 126
References: 148

List of Figures

Figure 1. The chemical structure of Methotrexate (**1**) and Doxorubicin (**2**).....5
Figure 2. The chemical structure of Gemtuzumab ozogamicin (**3**). 6
Figure 3. The chemical structure of Brentuximab vedotin (**4**) and Ado-trastuzumab emtansine (**5**).....8
Figure 4. The chemical structure of MEDI4276 (**7**), vadastuximab talirine (**8**), IMGN779 (**9**). 10
Figure 5. Schematic illustration of the proposed mechanism of action of **3**. (A) The hP67.6 antibody component of **3** specifically binds to the CD33 antigen on the surface of AML cells. (B) The **3**-CD33 complex is internalized into the cell via vesicle-mediated endocytosis. (C) The calicheamicin derivative is released through linker hydrolysis, migrates intracellularly, and binds to DNA. (D) Calicheamicin induces DNA double-strand breaks. (E) DNA double-strand breaks ultimately lead to cell death.....12
Figure 6. Schematic representation of the mechanism of 6. (A) The G544 antibody specifically binds to the CD22 antigen on the surface of ALL cells. (B) The ADC-CD22 complex is internalized by the cell. (C) Within the lysosome, the acid-sensitive N-acetylbutyric acid linker is cleaved, releasing the payload N-acetyl-γ-calicheamicin. (D) Calicheamicin intercalates into DNA, inducing double-strand breaks and ultimately triggering apoptosis. (E) Drug efflux of calicheamicin. 15
Figure 7. Mechanism of action of **10**. (A) The IgG1 antibody binds to the CD79b antigen on the surface of B cells. (B) The ADC-CD79b complex is internalized into the cell. (C) Within the lysosome, the complex is proteolytically cleaved, releasing MMAE. (D) MMAE is released from the lysosome. (E) MMAE binds to microtubules in the cytoplasm, causing G2/M phase arrest and ultimately inducing apoptosis of DLBCL cells. 16
Figure 8. The chemical structure of Trastuzumab deruxtecan (**12**). 17
Figure 9. Drug release of non-cleavable ADCs. 18
Figure 10. The chemical structure of Tmab-SMCC-DM1 (**15**) and Tmab-SPP-DM1 (**16**).....19
Figure 11. The hydrolysis of **3** (A) and **6** (B). 21
Figure 12. Mechanism of action of sacituzumab govitecan-hziy (**13**).....22
Figure 14. Hydrolysis of the β-glucuronide cleavable linker.....29
Figure 15. The chemical structure of cysteine-linker-MMAE/MMAF (**17**) and cysteine-linker-DPO (**18**).....30
Figure 16. The chemical structure of camptothecin (**19**), 7-butyl-10-amino-CPT (**20**) and 7-butyl-9-amino-10,11-methylenedioxy-CPT (**21**).....31
Figure 17. Design of linker-AMC model compounds by the Bargh's team. The linker-payloads were envisaged to be attached to mAb via an ortho-amide bond (A) or a benzyl-alkyl bond (B). 33
Figure 18. Hydrolysis reaction of sulfatases.....35

Figure 19. Formylglycine-generating enzyme (FGE) catalyses the post-translational oxidation of a conserved cysteine residue within the sulfatase active-site motif to formylglycine. 37
Figure 21. Order of reactivity for sulfate monoester protecting groups. 54
Figure 22. Yields of sulfate diester formation via imidazolium **33**. 62
Figure 23. Yields of sulfate diester deprotection. 97
Figure 24. The UV-Vis spectrum of phenol.[193] 113
Figure 25. The UV-Vis results of 4-aminophenol, 4-fluorophenol, 4-N-Boc aminophenol, 4-cyanophenol, and 4-COOCH3 phenol. 115
Figure 26. The UV-Vis results of sulfates and their responding phenols. 117
Figure 27. The HPLC results of sulfate and their corresponding phenols. 119

List of Tables

Table 1. Representative ADC therapeutics and their characteristics. 11

List of Scheme

Scheme 1. Overview of sulfated peptide synthesis. 44
Scheme 2. Synthesis of tetrabutylammonium 2-chlorophenyl sulfate (**24**). 45
Scheme 3. Preparation of sulphated substrates using Chlorosulfonic acid (**25**). 46
Scheme 4. The introduction of an SO_3 group via phenyl chlorosulfate (**26**). 48
Scheme 5. Introduction of SO_3 group via isobutyl sulfonate (**27**). 50
Scheme 6. Protection of SO_3 group via TFE group. 51
Scheme 7. Introduction of SO_3 group via 2,2,2-trichloroethyl chlorosulfate (**28**). 53
Scheme 8. Synthesis of Protected Sulfate Monoesters via three protecting groups respectively. 55
Scheme 9. Introduction of SO_3 group via sulfuryl imidazolium salt. 57
Scheme 10. The synthesis of 2,2,2-trichloroethyl chlorosulfate (**28**). 59
Scheme 11. The synthesis of 2,3-dimethyl-1-((2,2,2-trichloroethoxy)sulfonyl)-1H-imidazol-3-ium (**33**).[184] 60
Scheme 12. The synthesis of **35a**. 63
Scheme 13. The synthesis of **35b** and **35c**. 65
Scheme 14. The Boc protection of 4-aminophenol.[187] 69
Scheme 15. The synthesis of **35d**. 70
Scheme 16. The synthesis of **35e** and **35f**. 72
Scheme 17. The synthesis of **35g**. 76
Scheme 18. The synthesis of **34c**.[188] 78
Scheme 19. The synthesis of **35h**. 79
Scheme 20. The synthesis of **35i**. 81
Scheme 21. The synthesis of **35k**. 83
Scheme 22. The synthesis of **35l** and **35m**. 85
Scheme 23. The deprotection of the pre-synthesized Boc-protected sulfate **35d**. 87
Scheme 24. The synthesis of **35o** and **35p**. 89
Scheme 25. The synthesis of **35q**. 90
Scheme 26. The synthesis of **35r** and **35s.** 91
Scheme 27. The synthesis of **34d** and **35s-1**. 92
Scheme 28. The synthesis of **36d**. 101
Scheme 29. The synthesis of **36g**. 104
Scheme 30. The synthesis of **36h**. 105
Scheme 31. The synthesis of **36j**. 108

Scheme 32. The synthesis of **36m**. 110

List of Acronyms and Abbreviations

$[M+H]^+$	Molecular ion plus proton
$[M-H]^-$	Molecular ion subtract proton
$[M+Na]^+$	Molecular ion plus sodium
°C	Degrees Celsius
^{1}H-NMR	Proton nuclear magnetic resonance
^{13}C-APT	Carbon attached proton test
ADC	Antibody–Drug Conjugate
AcOH	Acetic Acid
DAR	Drug–Antibody Ratio
DMF	N,N-Dimethylformamide
DMSO	Dimethyl Sulfoxide
DNA-PK	DNA-Dependent Protein Kinase
EtOAc	Ethyl Acetate
ESI	Electrospray Ionisation
HPLC	High-Performance Liquid Chromatography
H_2SO_4	Sulfuric Acid
HMBC	Heteronuclear Multiple Bond Correlation
HSQC	Heteronuclear Single Quantum Coherence
LC	Liquid Chromatography
LC–MS	Liquid Chromatography–Mass Spectrometry
MS	Mass Spectrometry
MeOH	Methanol
$NaHCO_3$	Sodium Bicarbonate
NH_4OAc	Ammonium Acetate
NH_4HCO_3	Ammonium Bicarbonate
Na_2SO_4	Sodium Sulfate

NMR	Nuclear Magnetic Resonance
RP-HPLC	Reversed-Phase High-Performance Liquid Chromatography
UV-Vis	Ultraviolet–Visible Spectroscopy
1D	One dimensional
2D	Two dimensional
Boc	*tert*-Butoxycarbonyl
Boc_2O	Di-*tert-butyl* dicarbonate
DCM	Dichloromethane
dd	Doublet of doublets
ddd	Doublet of doublets of doublets
DMF	Dimethylformamide
DNA	Deoxyribonucleic acid
Et_3N	Triethylamine
IC_{50}	Half-maximal inhibitory concentration
M	Molar
M_w	Molecular weight
TCE	2,2,2-Trichloroethyl
TCECS	2,2,2-Trichloroethyl Chlorosulfate
TFA	Trifluoroacetic Acid
THF	Tetrahydrofuran
TLC	Thin-Layer Chromatography

1. Introduction

1.1 Cancer and chemotherapy

As the second leading cause of death worldwide, the number of cancer patients is increasing every year, and treatment still faces huge challenges.[1] Cancer is not a single disease but a collective term encompassing more than 200 pathological types, making it extremely difficult to cure.[2] Currently, primary tumours are typically treated with a combination of therapies, commonly including surgery, localized radiotherapy, and chemotherapy.[3] Surgical resection, one of the most traditional and important treatment methods, is especially suitable for localized solid tumours.[4] However, surgery inevitably causes trauma, which may affect patients' quality of life, and there is a risk that it may promote tumour recurrence or metastasis after the operation. Localized radiotherapy offers the advantage of being non-invasive and primarily targets localized tumour lesions.[5] Nevertheless, its efficacy against distant metastases or systemic tumours is limited. At the same time, there is a risk of damaging the adjacent healthy tissues, which may lead to acute or chronic adverse effects. Chemotherapeutic agents act throughout the human body via the bloodstream, capable of killing primary tumours and small metastatic lesions, making them particularly suitable for advanced or metastatic cancers.[6] However, these agents also have significant toxicity towards rapidly dividing healthy cells, easily causing serious side effects such as myelosuppression, nausea and hair loss, and may contribute to drug resistance, thereby reducing the quality of life.[7,8] Therefore, to achieve breakthroughs in cancer treatment, it is not only necessary to develop therapeutic strategies that can effectively kill cancer cells and to rationally combine and apply chemotherapy drugs in a proper sequence, but also to minimize the damage to normal cells as much as possible, thereby reducing the side effects.

The emergence of monoclonal antibodies (mAbs) represents a landmark breakthrough

in the development of anticancer drugs. On the surface of cancer cells, there is a class of molecules with high specificity (antigens), which are usually overexpressed or mutated.[1] Monoclonal antibodies derived from B lymphocytes can specifically recognize and bind to the target antigens, and induce cancer cell death through various mechanisms, such as blocking tumour cell signal transduction pathways or mediating antibody-dependent cytotoxicity.[9] The first two mAb drug approved for clinical use, trastuzumab and lapatinib, both targeted HER2-positive breast cancer.[10,11] Trastuzumab blocks the dimerization of HER2 by binding to its extracellular domain, causing cell-cycle arrest at G1 phase. This inhibits the activity of signalling pathways and hinders the proliferation of cancer cells.[12] Lapatinib, in contrast, works by inhibiting the activity of HER2-associated tyrosine kinases, thereby restricting the growth and division of cancer cells.[13] However, the efficacy of most "naked" mAbs is limited. For example, trastuzumab is only effective for patients with HER2 overexpression, while patients with negative HER2 status or low HER2 expression do not benefit from this treatment. This implies that approximately 70-80% of breast cancer patients cannot benefit from it.[14]

To enhance the therapeutic effect of mAbs, they were conjugated with small-molecule cytotoxins, resulting in the development of antibody-drug conjugates (ADCs). Nearly a century ago, Paul Ehrlich proposed the "magic bullet" concept, envisioning a chemical entity that could actively seek and eliminate pathogenic factors.[15] It was not until ADC drugs such as Mylotarg® and Besponsa® were approved by FDA and launched on the market that this idea was validated and gained widespread attention. In recent years, ADC technology has been rapidly developed, giving rise to numerous candidate drugs for different types of tumours. As more ADCs enter clinical trials, the number of anti-cancer drugs based on ADC technology will continue increasing, and they are expected to become key drugs in the new generation of anti-cancer treatments.

1.2 Antibody-drug conjugates (ADCs)

1.2.1 Introduction of ADCs

To minimize the damage of conventional chemotherapy to healthy cells, an increasing number of researchers have shifted their focus toward targeted therapy. Targeted therapy aims to selectively intervene in molecular targets and signalling pathways that are critical for the proliferation and survival of cancer cells.[16] These targets are often overexpressed within tumour cells or on their surfaces. Therefore, targeted therapy holds promise for developing drugs that can selectively kill cancer cells while having relatively low toxicity to the host, thereby significantly improving the therapeutic index.[17] Among the various strategies, antibody-drug conjugates (ADCs) have emerged as a major aspect of research.

ADCs consist of three components: the mAb, the linker, and the cytotoxic payload.[18] Monoclonal antibodies are monovalent and specifically recognize a single epitope.[19] Moreover, they are all produced from a single B-cell clone. In 1975, researchers first generated mAbs in mice using hybridoma technology.[20] The core of this technology lies in fusing B lymphocytes with specific immune functions to immortalized myeloma cells, thereby producing hybridoma cells that can continuously secrete specific antibodies and have unlimited proliferation capability. ADCs exploit mAbs to recognize antigens that are overexpressed on tumour cell surfaces, enabling the selective delivery of drugs. For instance, HER2 (human epidermal growth factor receptor 2) is amplified or overexpressed in approximately 15-30% of breast cancers, making it an ideal candidate for targeted therapy.[21]

The payload is a small-molecule drug responsible for directly killing tumour cells.[18] Once the antibody binds to a specific cell surface receptor, the ADC-antibody complex will enter the tumour cell via endocytosis and release the payload, thereby inducing the

death of the target cell. The payload is a key factor determining the activity and overall performance of an ADC. For use in ADCs, payloads need to meet some requirements, including extremely high cytotoxic activity, appropriate chemical modification sites, retention of biological activity after conjugation, good water solubility, sufficient stability in aqueous formulations and physiological conditions, and a clear and predictable mechanism of action.[22] Additionally, the ideal payload should be easy to synthesize and can be obtained through cost-effective processes. Since most cytotoxins have strong hydrophobicity, they are prone to inducing antibody aggregation. These issues should be mitigated to ensure the long-term stability of ADCs. The risk of rapid clearance and potential immunogenicity should also be reduced during the payload design process.[23]

One of the greatest challenges in achieving effective conjugation between the payload and the mAb lies in the selection of an appropriate linker. The linker is a bridge between the cytotoxin and the mAb, and it is a critical component of ADC. If the drug is released prematurely in blood circulation, it will cause significant systemic toxicity and reduce the therapeutic index. Consequently, the linker must remain stable in the bloodstream.[24] Linkers are critical not only for efficient drug delivery but also for modulating ADC toxicity. The choice of linker usually depends on the properties of the target cell and the payload, and is also based on the process of endocytosis and degradation of the ADC-antibody complex.[25] ADC linkers can be categorized as “cleavable” and “non-cleavable”. Non-cleavable linkers lack an intrinsic chemical trigger, so the antibody is degraded via proteolysis to release the payload, typically still containing a linker residue, after the ADC is internalized into the lysosome.[26] In contrast, the cleavable linker is designed to release the unmodified payload under specific intracellular conditions, enabling efficient tumour elimination.[27]

1.2.2 The first-generation ADCs

In first-generation ADCs, anticancer drugs were primarily conjugated to murine mAbs via non-cleavable linkers. Typical examples include KS1/4-methotrexate and BR96-doxorubicin: the former uses an amide bond to connect the murine mAb KS1/4 with Methotrexate (**1**), and was designed for the treatment of non-small cell lung cancer; while the latter employs an acid-sensitive hydrazone to connect the chimeric mAb BR96 with Doxorubicin (**2**), and was designed for the therapy of metastatic breast cancer.[28] However, both *in vitro* and in vivo studies demonstrated that the antitumour efficacy of these first-generation ADCs was only moderate and often lower than that of the free drugs.[24] Their limited therapeutic performance was mainly attributed to insufficient drug potency, low expression of target antigens, inefficient ADC internalization and tumour localization, suboptimal linker stability, and immune responses against murine or chimeric antibodies.

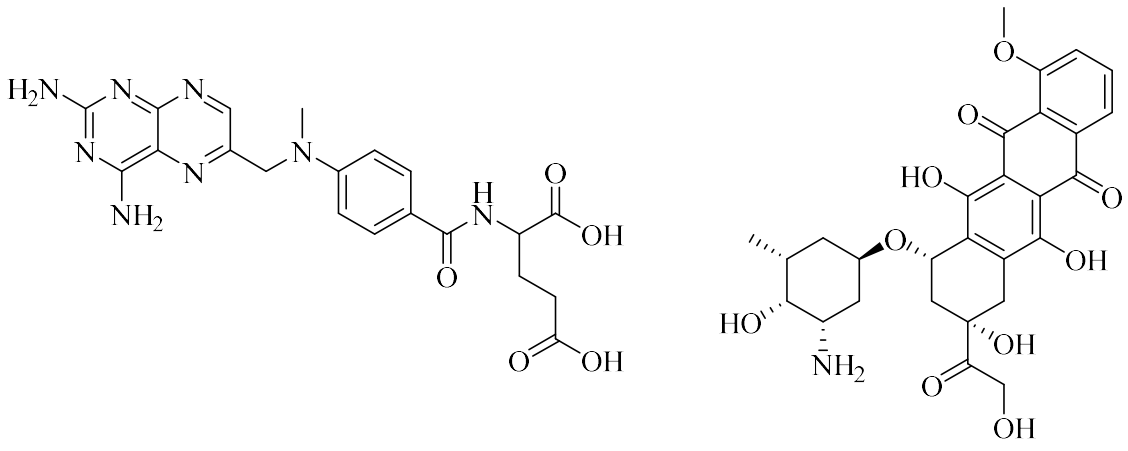

Methotrexate (**1**) Doxorubicin (**2**)

Figure 1. The chemical structure of Methotrexate (**1**) and Doxorubicin (**2**).

To address these issues, Wyeth and Celltech improved the first-generation ADCs by developing Gemtuzumab ozogamicin (**3**, Mylotarg®, Pfizer).[29] Gemtuzumab ozogamicin (**3**) became an effective therapy for acute myeloid leukemia (AML) by targeting CD33.[30] To enhance efficacy, a highly potent calicheamicin derivative was

employed as the payload, and a humanized antibody was introduced to reduce immunogenicity. Although clinical trials demonstrated favourable antitumour activity, subsequent data raised concerns regarding safety and adverse effects, leading Pfizer to voluntarily withdraw the drug approximately ten years after its initial approval.[31]

First-generation ADCs, represented by KS1/4-methotrexate and BR96-doxorubicin, have multiple limitations, including inadequate linker stability (resulting in non-specific drug release), insufficient number of drug molecules delivered intracellularly, low tumour localization efficiency of mAbs in patients, the immune responses and generation of human anti-mouse antibodies (HAMAS) elicited by murine or chimeric mAbs.[32] These shortcomings promoted the transition toward the second-generation ADCs.[33]

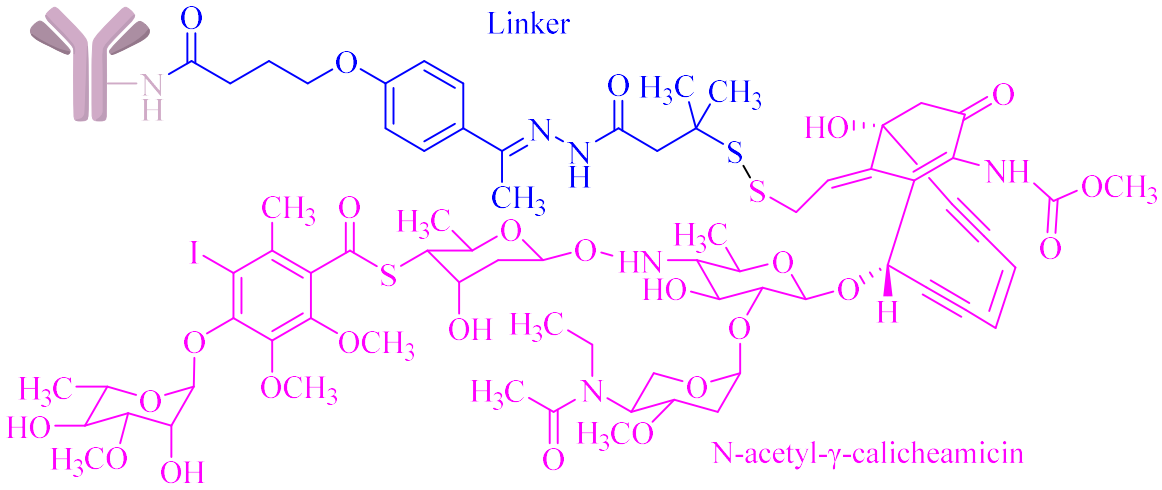

Gemtuzumab ozogamicin (**3**)

Figure 2. The chemical structure of Gemtuzumab ozogamicin (**3**).

1.2.3 The second-generation ADCs

The lessons learned from first-generation ADCs have driven the development of second-generation ADCs. These next-generation ADCs have optimized mAb technology, achieving higher selectivity for tumour cells while significantly reducing

off-target effects on healthy cells.[18] Second-generation ADCs no longer rely on murine or chimeric antibodies but predominantly employ humanized mAbs, typically of the humanized IgG mAbs.[34] First, in the humanized mAbs, all regions except the complementarity-determining regions (CDRs) are of human origin, thereby significantly reducing immunogenicity and lowering the risk of inducing anti-drug antibody (ADA) responses.[35] Second, the humanized mAbs retain the human Fc regions, which bind to the neonatal Fc receptors, enabling intracellular recycling and preventing lysosomal degradation.[36] Together, the non-human CDRs and the human Fc regions contribute to prolonged serum half-life of humanized mAbs, thereby supporting predictable pharmacokinetics and the repeated dosing of ADCs. Although humanized IgG4 was initially favoured for early second-generation ADCs, humanized IgG1 has become the predominant scaffold in later second-generation ADCs. Humanized IgG1 exhibit greater structural stability and tuneable Fc-mediated immune effector functions, which not only improve the homogeneity of ADCs but also enhance in vivo stability.

At the same time, researchers have developed highly potent small-molecule payloads with 100-1,000-fold increased activity, including auristatin and maytansinoid derivatives, providing strong support for ADC efficacy.[37,38] Moreover, compared with calicheamicin derivatives, auristatin and maytansinoid derivatives exhibit lower hydrophobicity, thereby reducing the risk of ADC aggregation.[39] Conjugation strategies have also been optimized. To achieve a controlled and well-defined drug-to-antibody ratio (DAR), cysteine residues are selected as conjugation sites, and drugs are attached via reduction of interchain disulfide bonds exposed on the antibody surface, thereby enhancing the precision of DAR.[40]

These advances are exemplified by three FDA-approved drugs — brentuximab vedotin (**4**), ado-trastuzumab emtansine (**5**), and inotuzumab ozogamicin (**6**) (further discussed in Section 1.3) — which exhibit robust clinical efficacy and chemistry, manufacturing and controls (CMC) characteristics.[41–43] Nevertheless, despite improving these

characteristics, second-generation ADCs still have certain limitations. First, auristatin and maytansinoid derivatives are extremely potent cytotoxic agents, such that even trace amounts of free payload are sufficient to induce cell death.[39] Consequently, minimal off-target payload release can readily lead to local concentrations reaching lethal thresholds, rendering auristatin- and maytansinoid-based ADCs intrinsically associated with a low therapeutic index and a narrow therapeutic window. Second, most ADC targets are not strictly tumour-specific antigens but are also expressed at low levels in normal tissues, inevitably making off-tumour toxicity in vivo.[44] Third, increased DAR significantly enhances the hydrophobicity of ADCs and promotes ADC aggregation, which accelerates clearance and shortens serum half-life.[45] In addition, cysteine-based conjugation represents a controlled yet non-site-specific strategy, inevitably resulting in heterogeneous populations comprising both unconjugated mAbs and ADCs.[46] Under conditions of limited antigen availability, these species compete for antigen binding, thereby further reducing effective payload delivery. Accordingly, continued optimization of payload selection, antibody scaffolds, conjugation strategies, and linker design remains a central focus in the ongoing development of ADCs.

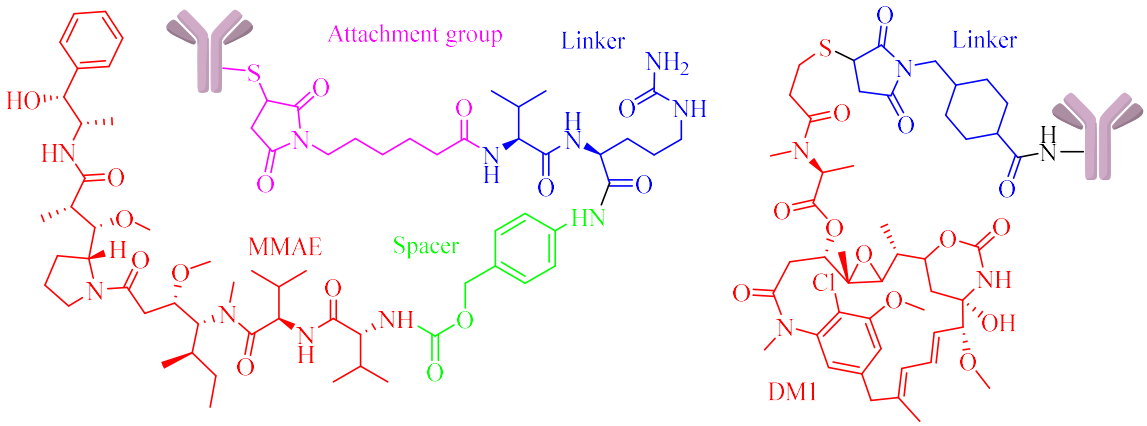

Brentuximab vedotin (**4**)

Ado-trastuzumab emtansine (**5**)

Figure 3. The chemical structure of Brentuximab vedotin (**4**) and Ado-trastuzumab emtansine (**5**).

1.2.4 The third-generation ADCs

Over the past decade, the experience gained from the development of the first- and second-generation ADCs has been applied to the design of the third-generation ADCs. Compared with the first two generations of ADCs, third-generation ADCs exhibit markedly improved therapeutic indices and CMC characteristics. The key technology that enables the successful development of third-generation ADCs is site-specific conjugation. First, site-specific conjugation of small-molecule payloads to engineered mAbs enables precise and homogeneous DARs. This strategy virtually eliminates unconjugated antibodies (DAR = 0), resulting in a highly uniform ADC population. A homogeneous DAR simplifies structural characterization and enhances the feasibility of process scale-up and batch-to-batch consistency, thereby conferring more industrially robust CMC characteristics. Second, site-specific conjugation minimizes the exposure of hydrophobic patches, significantly reducing ADC aggregation and further lowering the risk of nonspecific clearance.

In addition, highly stable linkers — such as maleimidocaproyl linkers, valine-citrulline dipeptide linkers, and cleavable disulfide linkers — have been widely adopted in the third-generation ADCs, leading to improved tumour delivery efficiency and reduced systemic toxicity at eq.alent dosing levels. Moreover, substantial advances have been achieved in payload design. Second-generation ADCs predominantly employ auristatin or maytansinoid derivatives, which induce tumour cell apoptosis by inhibiting microtubule polymerization and therefore require actively dividing cells, rendering them less effective against low-proliferative tumours. In contrast, third-generation ADCs utilize pyrrolobenzodiazepine (PBD) or indolinobenzodiazepine (iBD) moieties, which selectively bind to the DNA minor groove and form covalent adducts or crosslinks with guanine (G), thereby inducing highly persistent and poorly repairable DNA damage that ultimately triggers apoptosis in a cell-cycle-independent manner. Additionally, microtubule inhibition-mediated cytotoxicity is partially reversible upon

drug withdrawal, whereas DNA crosslinking induced by PBD or iBD moieties causes an irreversible and lethal form of cellular damage.

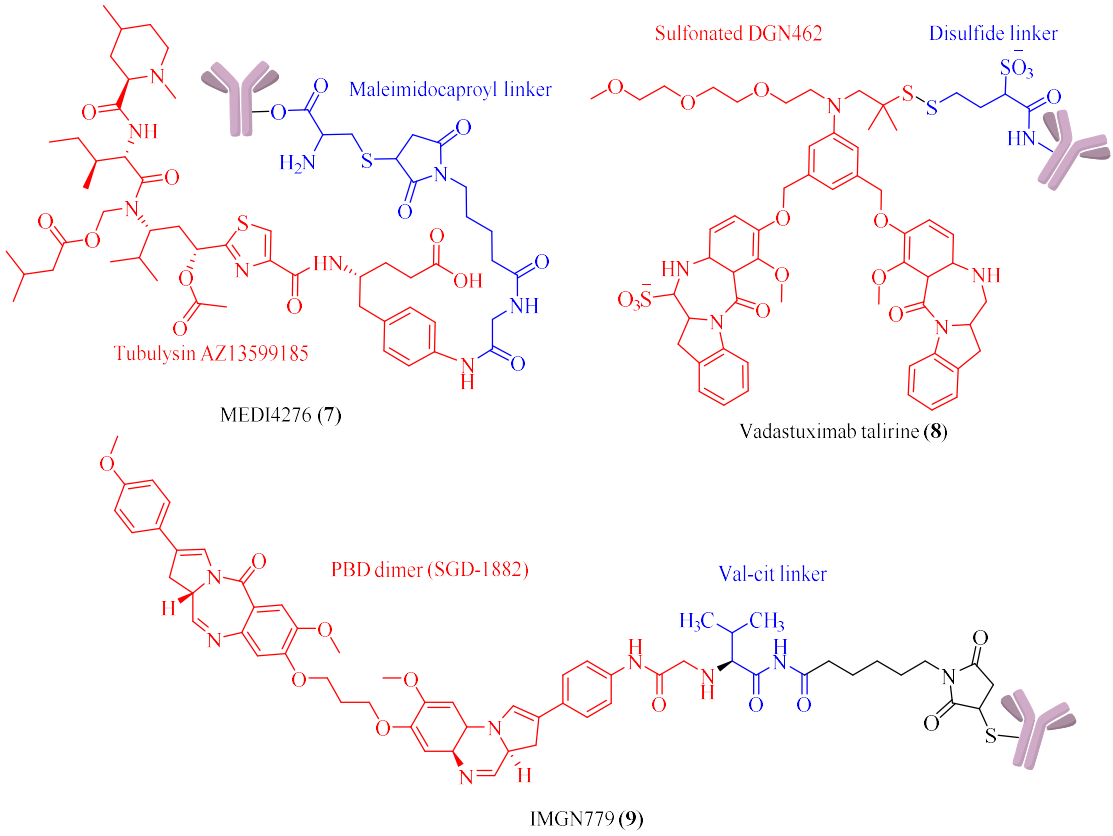

Figure 4. The chemical structure of MEDI4276 (**7**), vadastuximab talirine (**8**), IMGN779 (**9**).

Through systematic optimization of mAbs, linkers, and conjugation chemistry, the third-generation ADCs have a markedly improved therapeutic index.[18] Site-specific conjugation is recognized as a key technology for the successful development of third-generation ADCs, ensuring high homogeneity and precise control of the drug-to-antibody ratio (DAR).[46] The third-generation ADCs were formed by site-specific conjugation of small-molecule drugs with engineered monoclonal antibodies, resulting in a uniform DAR of 2 or 4. There is less need to worry about systemic toxicity, and the presence of unconjugated antibodies can be avoided. These ADCs exhibit higher stability and superior pharmacokinetic properties. Their payloads can be released effectively and stably, which contributes to the stronger efficacy of the third-generation

ADCs and enables them to be employed to antigens with low expression levels.

These advances are well exemplified by three representative ADCs that have entered clinical trial, they are MEDI4276 (**7**), vadastuximab talirine (**8**), and IMGN779 (**9**).[47–49] MEDI4276 (**7**) is directed toward solid tumour indications such as breast cancer and gastric cancer, whereas vadastuximab talirine (**8**) and IMGN779 (**9**) are both designed on the treatment of acute myeloid leukemia (AML).

1.3 Representative ADC therapeutics

Table 1. Representative ADC therapeutics and their characteristics.

Trade Name	Generic Name	Indication	Target	mAb	Payload	Linker	Year of Approval
Gemtuzumab ozogamicin (**3**)	MYLOTARG	AML	CD33	hP67.6	Calicheamicin	Hydrazone linker	2010/2017
Inotuzumab ozogamicin (**6**)	BESPONSA	ALL	CD22	G544	Calicheamicin	Acetyl butyrate linker	2017
Brentuximab vedotin (**4**)	ADCETRIS	HL and ALCL	CD30	cAC10	MMAE	Val-Cit linker	2011
Ado-trastuzumab emtansine (**5**)	KADCYLA	mBC	HER2	Trastuzumab	DM1	Thioether linker MCC	2013
Polatuzumab vedotin (**10**)	POLIVY	DLBCL	CD79b	IgG1	MMAE	Val-Cit linker	2019
Enfortumab vedotin (**11**)	PADCEV	UC	Nectin-4	IgG1	MMAE	Val-Cit linker	2019
Trastuzumab deruxtecan (**12**)	ENHERTU	BC and NSCLC	HER2	Trastuzumab	DXd	Tetrapeptide linker	2019

In 2000, **3** was approved by the U.S. Food and Drug Administration (FDA) as one of the first ADCs for the treatment of acute myeloid leukaemia (AML).[50] **3** was developed by Pfizer, and comprises three components: (1) hP67.6, a recombinant humanized IgG4 mAb; (2) the highly potent cytotoxic payload calicheamicin; and (3) a hydrolysable hydrazone linker.[29] The mAb hP67.6 specifically recognizes the CD33 antigen on the surface of leukaemia cells, and forms a complex that is subsequently internalized by the cell. Calicheamicin is then released intracellularly via hydrolysis and binds to DNA,

thus causing double-strand breaks and inducing cell death. Initially, researchers from Seattle Genetics and Wyeth-Ayerst Research validated the specificity and cytotoxicity of **3** against $CD33^+$ leukaemia cells in *in vitro* and murine xenograft models.[51] In a Phase I clinical trial involving patients with relapsed or refractory $CD33^+$ AML, **3** demonstrated good tolerability. Based on the positive outcomes from Phase I and II trials, the drug received early approval.[52]

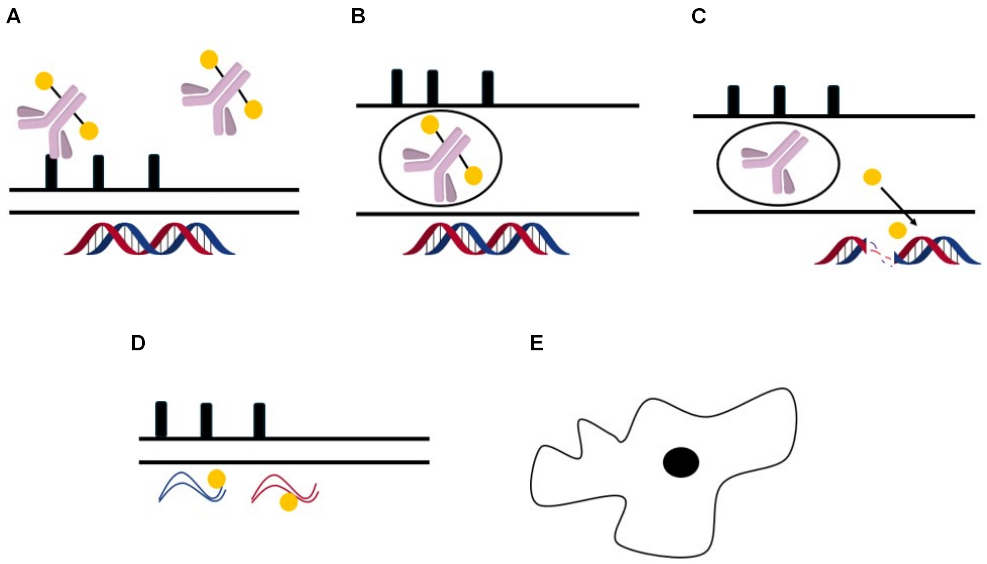

Figure 5. Schematic illustration of the proposed mechanism of action of **3**. (A) The hP67.6 antibody component of **3** specifically binds to the CD33 antigen on the surface of AML cells. (B) The **3**-CD33 complex is internalized into the cell via vesicle-mediated endocytosis. (C) The calicheamicin derivative is released through linker hydrolysis, migrates intracellularly, and binds to DNA. (D) Calicheamicin induces DNA double-strand breaks. (E) DNA double-strand breaks ultimately lead to cell death.

However, **3** gradually revealed serious safety concerns during post-marketing use and confirmatory clinical trials. Owing to the extremely potent DNA-damaging activity of its cytotoxic payload, calicheamicin, and the high sensitivity of hepatic sinusoidal endothelial cells and Kupffer cells to DNA damage, even minimal levels of the off-tumour delivery are sufficient to induce significant hepatotoxicity.[53] When **3** was internalized by $CD33^+$ cells within the hepatic sinusoids, the calicheamicin-mediated sinusoidal injury could be induced. Further studies by Giles' team demonstrated that **3**

may induce veno-occlusive disease (VOD) even in patients who had not undergone hematopoietic stem cell transplantation.[54] In addition, in the confirmatory phase III randomized clinical trial SWOG S0106, **3** was added to standard "3+7" (daunorubicin + cytarabine) induction chemotherapy followed by post-consolidation therapy.[55] The results showed that the inclusion of **3** during induction or post-consolidation treatment failed to improve complete remission (CR) rates, relapse-free survival (RFS), or overall survival (OS), but instead was associated with an increased rate of treatment-related mortality. These findings directly prompted the FDA to re-evaluate the conditions of its accelerated approval. Following extensive discussions with the FDA, Pfizer ultimately decided to withdraw the marketing application for **3** on October 15, 2010.[56]

On September 1, 2017, the U.S. Food and Drug Administration (FDA) approved **3** for the treatment of newly diagnosed CD33-positive acute myeloid leukaemia (AML) in adults, as well as for the treatment of relapsed or refractory CD33-positive AML in adults and paediatric patients aged 2 years and older.[56] Based on the results of the ALFA-0701 trial, **3** was further approved for use in combination with daunorubicin and cytarabine in adults with newly diagnosed AML, or as monotherapy in certain adult and paediatric patients.[57] In the ALFA-0701 trial, **3** was added to standard "3+7" (daunorubicin + cytarabine) induction chemotherapy.[58] The results demonstrated that the addition of **3** significantly prolonged event-free survival (EFS), but did not result in a significant increase in the complete remission (CR) rate. In other words, **3** did not exert its clinical benefit by increasing the proportion of patients achieving remission, but rather by extending the duration of remission in responding patients and delaying disease relapse. In addition, the study showed that combination therapy with **3** significantly reduced the risk of relapse and improved 5-year overall survival. However, when **3** was administered in combination with daunorubicin and cytarabine, adverse events such as haemorrhage and infection were observed.

In addition to the aforementioned side effects, **3** has several other limitations. The

hydrazone linker exhibits poor stability, resulting in approximately 50% of the small-molecule payload being released into circulation within 48 hours.[59] Ozogamicin is a semi-synthetic derivative of calicheamicin (*N*-acetyl-γ-calicheamicin dimethylhydrazine dichloride), and is a DNA-binding cytotoxic antibiotic of the enediyne class.[60] Calicheamicin is highly hydrophobic, easily resulting in ADC aggregation, decreased ADC stability, increased clearance within the human body, and shorten lifetime of ADC.

Inotuzumab ozogamicin (**6**) is another representative first-generation ADC. It was approved by FDA in 2017 for adults with relapsed or refractory $CD22^+$ precursor B-cell acute lymphoblastic leukemia (ALL). In 2024, the approval of **6** was extended to children aged one year and older.[61] **6** consists of three components: (1) G544, a humanized IgG4 anti-CD22 mAb; (2) *N*-acetyl-γ-calicheamicin; and (3) an acid-labile acetyl butyrate linker.[62] CD22 is expressed on the surface of leukemic progenitor cells in over 90% of ALL patients, while it is absent on hematopoietic stem cells and non-target tissues, which is conducive to selective targeting.[63] After internalization of ADC, the acetyl butyrate linker is hydrolysed, and then *N*-acetyl-γ-calicheamicin dimethylhydrazine is released.[43] Its mechanism of action is the same as that of **6**, but compared with the hydrazone linker, the acetyl butyrate linker provides greater stability in blood circulation and is cleaved controllably in the acidic intracellular environment.

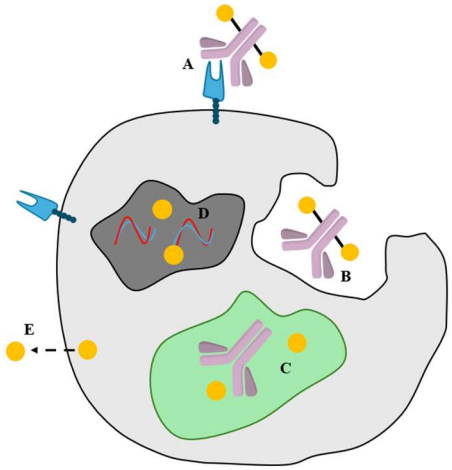

Figure 6. Schematic representation of the mechanism of 6. (A) The G544 antibody specifically binds to the CD22 antigen on the surface of ALL cells. (B) The ADC-CD22 complex is internalized by the cell. (C) Within the lysosome, the acid-sensitive N-acetylbutyric acid linker is cleaved, releasing the payload N-acetyl-γ-calicheamicin. (D) Calicheamicin intercalates into DNA, inducing double-strand breaks and ultimately triggering apoptosis. (E) Drug efflux of calicheamicin.

Nevertheless, **3** and **6** still have several limitations: (1) some mAbs of them are derived from mice and may trigger immunogenic response; (2) acid-sensitive linkers may be cleaved in non-target acidic environments, resulting in premature cytotoxin release; (3) the hydrophobic payloads may induce ADC aggregation, affecting half-life and clearance; and (4) the thiol-based conjugation produces heterogeneous DARs, notably impacting efficacy and pharmacokinetics/pharmacodynamics (PK/PD), and also reduces the therapeutic index.[43,64]

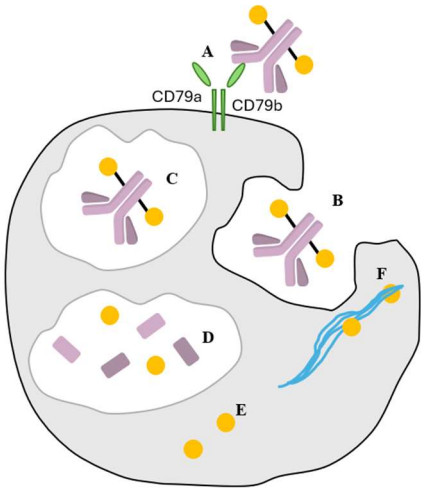

Figure 7. Mechanism of action of **10**. (A) The IgG1 antibody binds to the CD79b antigen on the surface of B cells. (B) The ADC-CD79b complex is internalized into the cell. (C) Within the lysosome, the complex is proteolytically cleaved, releasing MMAE. (D) MMAE is released from the lysosome. (E) MMAE binds to microtubules in the cytoplasm, causing G2/M phase arrest and ultimately inducing apoptosis of DLBCL cells.

Representative examples of second-generation ADCs include brentuximab vedotin (**4**), ado-trastuzumab emtansine (**5**), and polatuzumab vedotin (**10**).[41,42,65] Brentuximab vedotin (**4**) consists of the anti-CD30 IgG1 mAb cAC10, the microtubule-disrupting agent monomethyl auristatin E (MMAE), and a stable valine-citrulline dipeptide linker. **4** was approved by FDA in 2011 for the treatment of Hodgkin lymphoma (HL) and anaplastic large cell lymphoma (ALCL).[66] **5** is composed of a humanized anti-HER2 IgG1 mAb, the microtubule inhibitor DM1, and a stable thioether linker MCC. Trastuzumab emtansine was approved by FDA in 2013 for the treatment of HER2-positive metastatic breast cancer (mBC).[67] **10** targets CD79b and uses a valine-citrulline dipeptide linker to connect MMAE. In 2019, the approval of **10** was granted by FDA for the treatment of diffuse large B-cell lymphoma (DLBCL).[68]

Representative examples of third-generation ADCs include enfortumab vedotin (**11**) and trastuzumab deruxtecan (**12**).[69,70] **11** was approved by FDA in 2019 for the treatment of adults with locally advanced or metastatic urothelial carcinoma.[71] It consists of a humanized IgG1 mAb, a valine-citrulline linker, and MMAE.[72] **12** was

approved by FDA in 2019 for HER2-positive unresectable or metastatic solid tumours in adults previously treated with HER2-targeted therapies.[73] It is composed of a humanized anti-HER2 IgG1 mAb, the topoisomerase I inhibitor DXd, and an enzyme-cleavable tetrapeptide linker. It is reported that the tetrapeptide linker is more stable in blood circulation, consequently reducing the risk of off-target cytotoxicity.[74]

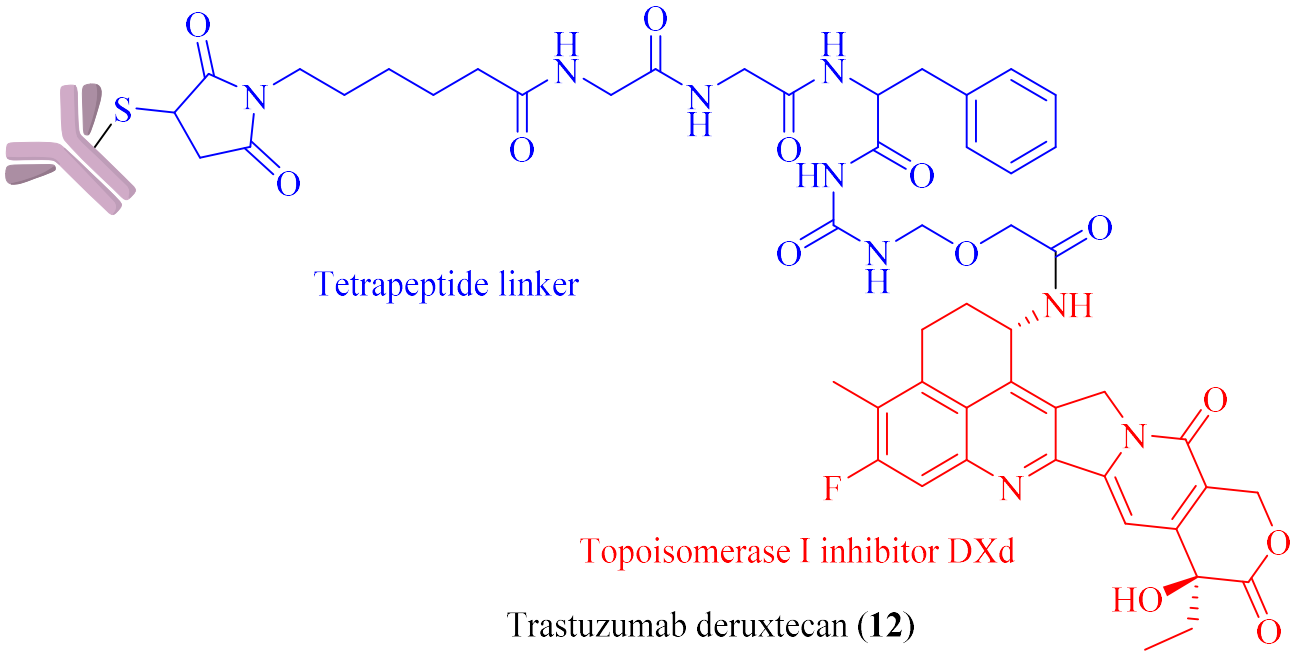

Trastuzumab deruxtecan (**12**)

Figure 8. The chemical structure of Trastuzumab deruxtecan (**12**).

1.4 Linker chemistry

In the framework of an ADC, the linker acts as a bridge that connects the mAb and payload. Hence, linker technology is an important factor in ADC research and has been improved quickly in recent years. Generally, linkers can be divided into non-cleavable linkers and cleavable linkers, both of which feature an antibody-attachment and a payload-attachment.[75] An ideal linker should have stability in the circulatory system but be released efficiently in the target cells. Moreover, satisfactory linkers should have appropriate physicochemical properties, which do not induce the aggregation of ADCs and affect PK/PD and stability of ADCs.

1.4.1 Non-cleavable linkers

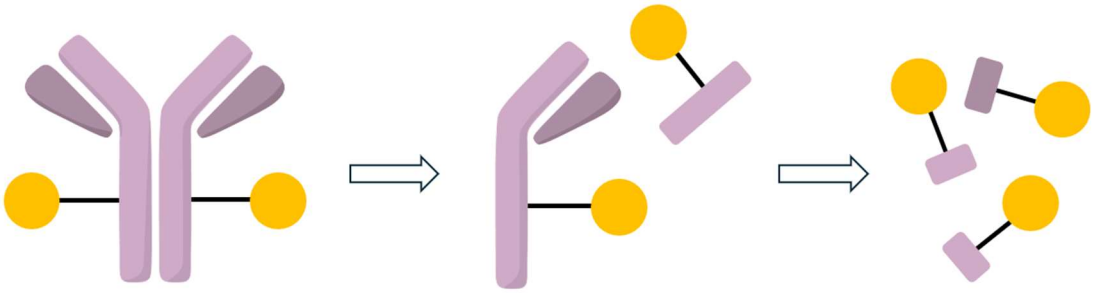

Figure 9. Drug release of non-cleavable ADCs.

Non-cleavable linkers cannot be cleaved to release cytotoxins, so ADCs using non-cleavable linkers require complete metabolism of mAbs to their constituent amino acids to release payloads, and the payload maintains an element of the linker in its final structure.[37] **5** is an example that utilizes the non-cleavable thioether linker to connect trastuzumab and DM1. In the early stages of developing trastuzumab emtansine, both the non-cleavable SMCC (*N*-succinimidyl 4-(*N*-maleimidomethyl)cyclohexane-1-carboxylate) linker and the disulfide SPP (*N*-succinimidyl 4-(2-pyridyldithio)pentanoate) linker were highly competitive.[76] To select the final linker of trastuzumab-DM1, Phillips and colleagues evaluated the tolerability of trastuzumab-SPP-DM1 and trastuzumab-SMCC-DM1 in Sprague-Dawley rats. Compared with the SPP-linked conjugate, the ADC incorporating the SMCC linker exhibited at least a two-fold improvement in tolerability in this single-dose acute toxicity study. Thus, conjugates utilizing SMCC linkers double the therapeutic index to mice as conjugates utilizing SPP linkers, making SMCC the preferred linker for **5**.

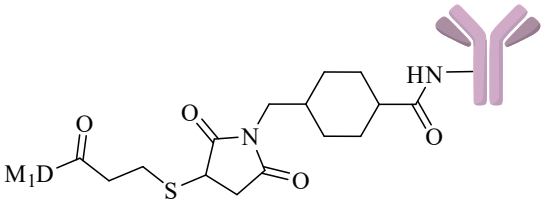

Tmab-SMCC-DM1 (**15**)

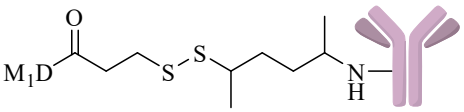

Tmab-SPP-DM1 (**16**)

Figure 10. The chemical structure of Tmab-SMCC-DM1 (**15**) and Tmab-SPP-DM1 (**16**).

Pharmacokinetic (PK) data showed that **5** was cleared faster than free trastuzumab.[77] To investigate the effect of the thiol-maleimide linkage on off-target degradation, Ponte and colleagues designed an all-carbon skeleton linker to replace SMCC in the conjugates.[78] They used an EGFR-targeting ADC (J2898A-SMCC-DM1) and compared it to a control ADC (J2898A-$(CH_2)_3$-DM). It was found that the former had a slightly faster clearance rate than the latter. As a result, there may be some payload loss in SMCC-DM1, which may be caused by a thiol-maleimide-dependent mechanism. Furthermore, the result of *ex vivo* experiments showed that thiol-maleimide exchange can indeed occur and lead to the release of thiol-containing maytansinoid DM1.

There are no cleavage sites in the structure of non-cleavable linkers, and thus they will not break due to chemical conditions such as proteases, hydrolases, or pH changes.[27] Therefore, compared with cleavable linkers, they exhibit higher stability in blood circulation. Moreover, the active form of the released payload typically remains conjugated to an amino acid residue, making it charged and relatively bulky. These charged, highly hydrophilic molecules are not easily recognized or transported by multidrug-resistant (MDR) transporters.[79] As a result, they can maintain higher and more sustained effective concentrations within tumour cells, thereby partially mitigating MDR-mediated drug resistance.

However, the charged amino acid residues decrease the cell permeability of the payload after the mAbs are metabolized. Consequently, the payload cannot be transferred to nearby cells, preventing non-cleavable ADCs from having a bystander effect.[27] A bystander effect refers to the ability of the payload to spread through the cell membrane into the intercellular space and kill adjacent cells, which enables cancer cells without target antigens to be eliminated.[80] Therefore, non-cleavable linkers are mainly used to treat haematological (blood, leukaemia, lymphatic) cancers or tumours with high

antigen expression. Generally, more than 99% of tumour cells need to be killed to demonstrate effective therapeutic effects of non-cleavable ADCs.[9] Furthermore, the residual linkage fragment is a drastic modification of payload, which always reduces the cytotoxicity of the cytotoxin in most non-cleavable ADCs. Thus, the applicable scope of non-cleavable ADCs is much smaller than that of cleavable ADCs.[27]

1.4.2 Cleavable linkers

Cleavable linkers exploit different conditions of the target sites to release cytotoxic payloads.[27] Thus, the notable distinction between the cytoplasmic environment and the lysosomal environment becomes the key to the operation of cleavable linkers. Cleavage can be further subdivided into chemical cleavage and enzymatic cleavage. Chemical cleavage applies different chemical conditions, such as pH dependent and oxidation-reduction processes, while enzymatic cleavage uses various proteases to catalyse linker degradation.

Chemically cleavable linkers can be divided into three types: acid-cleavable, reducible disulfides, and those cleavable by exogenous stimuli.[75] Acid-cleavable linkers exploit pH differences in endosomes, lysosomes, and the bloodstream to selectively cleave in the tumour microenvironment.[81] **3** and **6** are typical examples of acid-cleavable ADCs. They use *N*-acyl hydrazone linkers to conjugate humanized IgG4 mAbs with the calicheamicin.[29,62] The payload of **3** is released at pH 4.5, corresponding to the acidic environment of lysosomal vesicles.[82] **6** releases its payload at the pH drops from 6 to 4 during trafficking from the cytoplasm to lysosomes.[83]

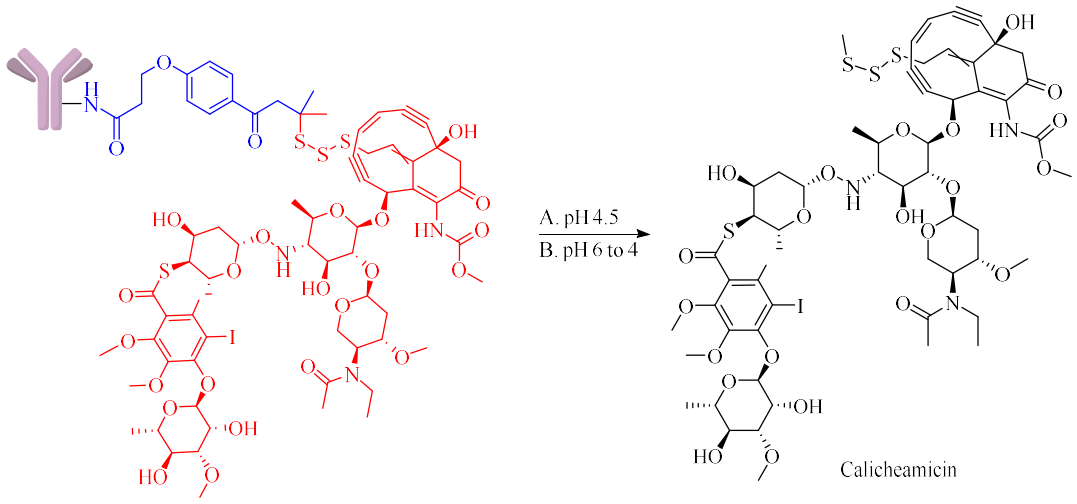

Figure 11. The hydrolysis of **3** (A) and **6** (B).

Sacituzumab govitecan-hziy (**13**) utilizes an acid-sensitive linker and is approved for the treatment of unresectable locally advanced or metastatic triple-negative breast cancer (mTNBC).[84] A para-aminobenzyloxycarbonyl (CL2A) linker is used to conjugate the humanized mAb hRS7 IgG1κ with the cytotoxic agent SN-38, a topoisomerase inhibitor. **13** can induce apoptosis through two mechanisms: (1) a targeted mechanism: after hRS7 IgG1κ binds to Trop-2-positive cells, the payload is released within the lysosomes within the cells; (2) a bystander mechanism: the linker is cleaved in the acidic tumour microenvironment, releasing SN-38 to act on neighbouring Trop-2-negative cells.[85]

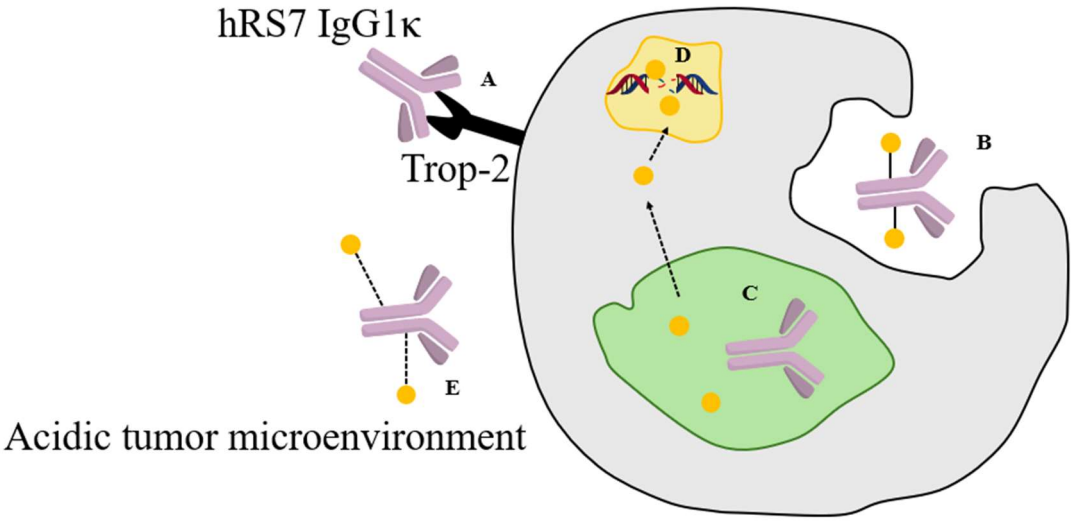

Figure 12. Mechanism of action of sacituzumab govitecan-hziy (**13**). (A) The hRS7 IgG1κ antibody binds to Trop-2-positive cells. (B) The ADC-antibody complex is internalized. (C) The acid-sensitive linker is hydrolysed in the lysosome. (D) The released payload SN-38 induces DNA strand breaks. (E) In the acidic tumour microenvironment, the acid-sensitive linker is hydrolysed, releasing SN-38, which subsequently acts on neighbouring Trop-2-negative cells.

Reducible disulfide linkers are one of the most common types of chemically cleavable linkers in ADC development and have been successfully applied in ADCs such as indatuximab ravtansine (**14**, BT062) and **8** (SGN-CD33A).[48,86] Unlike acid-sensitive linkers, disulfide linkers are relatively stable at physiological pH but are susceptible to nucleophilic attack by endogenous thiols.[87] In plasma, thiols are mainly derived from human serum albumin (HSA).[88] The only residue in HSA containing a free thiol, Cys34, is in a groove with limited solvent exposure, so the reducing capacity of plasma for disulfides is very low. In contrast, thiols in the cytosol mainly come from high concentrations of glutathione (GSH), resulting in a large redox potential difference between the cytosol and plasma.[89] Therefore, disulfide linkers can be selectively hydrolysed within cells.[90] In addition, compared with healthy tissues, tumour-associated oxidative stress usually leads to elevated GSH levels, providing additional selectivity for cancer cells.[91] However, in certain healthy cells (such as hepatocytes), the concentration of GSH is relatively high, which may lead to off-target release of the

payloads from disulfide-linked ADCs.[92]

Indatuximab ravtansine (**14**, BT062) is an example that utilizes a disulfide linker, and it was approved by FDA for the treatment of multiple myeloma.[92] It employs the SPDB (*N*-succinimidyl 4-(2-pyridyldithio)butyrate) linker to conjugate the mAb nBT062 with the microtubule-targeting cytotoxin DM4. **14** specifically recognizes CD138-expressing cells. Once the ADC-CD138 complex is internalized, the SPDB linker is cleaved in the lysosome to release DM4. Then, DM4 binds to microtubules, which causes cell cycle arrest and induces apoptosis.[93]

In addition to the abovementioned endogenous stimuli — such as acidic pH and elevated glutathione (GSH) levels — for selective drug release. Exogenous stimuli, including light, ionizing radiation, and ultrasound, have also been employed to trigger payload release.[94] Exogenous stimuli offer exceptional spatiotemporal precision, as they can be applied by clinicians at a specific time and location, enabling highly controllable drug activation while minimizing systemic side effects.[95] In a paper published in 2017, Nani proposed the use of near-infrared light for in vivo activation of duocarmycin-antibody conjugates. They prepared CyEt-Pan-Duo carrying a derivative of duocarmycin and found that CyEt-Pan-Duo released small-molecule payloads upon irradiation with 780 nm light.[96]

1.4.3 Enzyme cleavable linkers

There are various enzymes involved in human physiological activities in lysosomes.[97] After an ADC is internalized by target cells, it will be transported to lysosomes, which enables enzyme-cleavable linkers to be effectively hydrolysed. Because the hydrolysis of enzyme-cleavable linkers usually requires the participation of specific enzymes, they have better stability in the blood circulation than other cleavable linkers.[98] In recent years, the research on enzyme-cleavable linkers has mainly focused on cathepsin B and

glycosidases.[75] To date, there are 15 ADC drugs have been launched, 9 of them use cathepsin B-based linkers.[46]

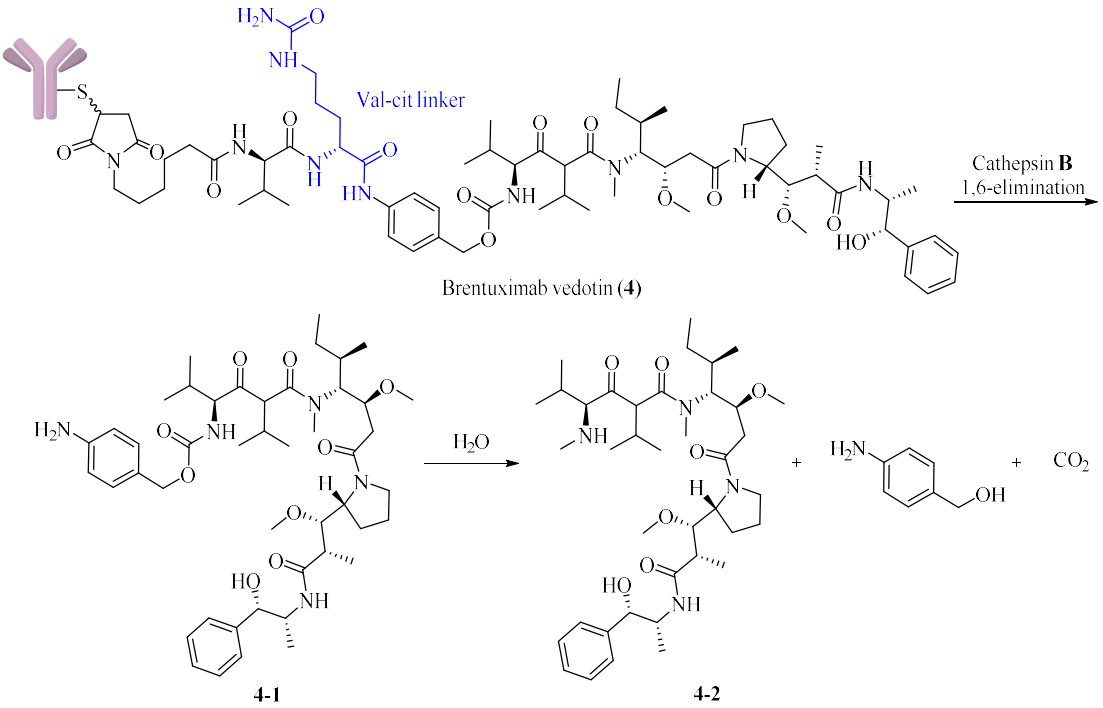

Scheme 1. Hydrolysis of brentuximab vedotin (**4**).

1.4.3.1 Peptidase cleavable linkers

Cathepsin B (EC 3.4.22.1) is a lysosome-localized cysteine protease that belongs to the papain enzyme family.[99] It primarily functions in the cleavage of proteins delivered to lysosomes either from the extracellular environment through endocytosis or phagocytosis, or from intracellular compartments via autophagic pathways. The resulting oligopeptides and amino acids can cross the lysosomal membrane and are subsequently recycled for cellular use. In the context of ADC linker design, cathepsin B plays a key role in triggering the cleavage of dipeptide-based linkers, such as valine-alanine or valine-citrulline.[100] This proteolytic event is mediated by a catalytic cysteine residue (C29) located on the enzyme's left domain, which acts in concert with a histidine residue (H199) on the opposing right domain.

Before the introduction of dipeptide linkers, ADCs carrying **2** mainly employed

hydrazone linkers, which relied on the pH difference between lysosomes and cytosol to trigger payload release.[101] However, linkers that can be cleaved by cathepsin B exhibit superior systemic stability.[102] Therefore, cathepsin B-cleavable linkers gradually replaced acid-labile hydrazone linkers. Initially, Gly-Phe-Leu-Gly and Ala-Leu-Ala-Leu tetrapeptides were investigated as recognition sequences for DOX-mAb conjugates.[100] However, their drugs have extremely slow release kinetics and lipophilicity, which may contribute to ADC precipitation or aggregation. As a result, they were not suitable as the linkers of DOX-mAb conjugates.

In 1998, Dubowchik and Firestone found that the molecular volumes of drugs such as DOX were large, making it difficult for conjugates to access the active sites of cathepsin B.[100] They designed and synthesized several substrates containing self-immolative p-aminobenzylcarbonyl (PABC) spacer, which can be spontaneously released after the enzymatic cleavage and deacylation. This process can achieve a traceless release of the free drug. In *in vitro* experiments, Z-Phe-Lys-PABC-DOX was verified to have the fastest drug-release rate. Moreover, the substrates containing D-Phe and D-Ala were not degraded in fresh human plasma at 37 °C over 6-7 h, demonstrating that these linkers of substrates were stable in blood circulation.

In 2003, Doronina and co-workers employed hydrazone and dipeptide linkers to conjugate cytotoxic payloads to mAbs.[103] The reduction-based conjugation strategy they developed demonstrated broad applicability, effectively preserving antibody binding affinity while being compatible with multiple humanized IgG antibodies. Using this approach, ADCs with uniform DARs and consistent conjugation sites were obtained at yields approaching 80%. Furthermore, there is no ADC aggregation in size-exclusion high-performance liquid chromatography (HPLC), and flow cytometry confirmed that the antigen-binding properties of the antibodies were retained after conjugation.

By monitoring the rate of drug release in human and mouse plasma, Doronina

concluded that the plasma stability of valine-citrulline linkers is far greater than that of hydrazone linkers.[103] Furthermore, in *in vitro* cytotoxicity studies, conjugates containing valine-citrulline exhibited high immunological specificity under both cBR96 Ag^+ and cAC10 Ag^- exposure conditions. Overall, based on a comprehensive evaluation of *in vitro* cytotoxicity, immunological specificity, and plasma stability, the valine-citrulline linker is more suitable than the hydrazone linker for the auristatin-based conjugate.

In 2006, Jeffrey and co-workers reported that, in addition to valine-citrulline, valine-alanine is another dipeptide sequence that can be efficiently cleaved by cathepsin B.[105] LC-MS analysis of the digestion products confirmed that both of valine-citrulline and valine-alanine linkers were efficiently cleaved under lysosomal conditions. The half-life of former is 72 min and that of later if 142 min. Spectroscopic analysis revealed that, compared with valine-citrulline, valine-alanine decreases the overall hydrophobicity of the conjugates. Consequently, ADCs containing valine-citrulline were more prone to precipitation and aggregation, making it difficult to achieve a high DAR (>4 drugs per antibody). In contrast, the valine-alanine linker enables ADCs to have a higher DAR of 7.4 while maintaining ADC aggregation at an acceptable level (<10%).

In 2007, Caulitan and colleagues found that, in addition to cathepsin B, other cathepsins are also capable of participating in the hydrolysis of valine-citrulline linkers.[104] Within individual cells, the functional redundancy and substrate specificities of cysteine cathepsins may allow other cathepsins to compensate for the absence of cathepsin B. Caulitan analysed the activity of multiple cysteine cathepsins toward valine-citrulline linkers by measuring the cleavage products generated in the exposure to purified cathepsins (B, K, L, and S) and human liver lysosomal extract. The results from mass spectrometry demonstrated that there was pronounced functional redundancy among different cysteine cathepsins during the cleavage of valine-citrulline linkers.

In 2016, Cazzamalli and co-workers investigated the serum stability of four dipeptide linkers.[106] The serum stability of dipeptide linkers is a decisive factor for the *in vivo* efficacy of small-molecule-drug conjugates. The results showed that valine-alanine and valine-citrulline linkers exhibited the highest serum stability, with half-lives of 23 h and 11.2 h, respectively. In contrast, valine-lysine and valine-arginine linkers were considerably more prone to degradation, displaying much shorter half-lives of 8.2 h and 1.8 h, respectively. Overall, higher serum stability of the linker correlated with improved antitumour efficacy *in vivo*. Furthermore, in an SKRC-52 renal carcinoma xenograft model, conjugates incorporating valine-alanine-MMAE and valine-citrulline-MMAE significantly inhibited tumour growth and were markedly more effective than those based on valine-lysine and valine-arginine linkers. In summary, valine-alanine and valine-citrulline linkers maintain high integrity *in vivo*, ensuring that drug release occurs predominantly at the tumour site rather than in the systemic circulation.

Although dipeptide cleavable linkers have long dominated the traditional ADC field, they still suffer from two persistent bottlenecks. First, their plasma stability is insufficient: dipeptides are readily hydrolysed by Ces1C enzymes in mouse plasma, leading to premature payload release in vivo, which affects toxicity assessment and clinical predictability.[107] Second, dipeptide linkers are inherently hydrophobic, making ADCs more prone aggregation. This limits the achievement of high drug-to-antibody ratios (DARs) and reduces the stability of ADCs during preparation and storage.[108,109]

1.4.3.2 β-Glucuronide cleavable linkers

In efforts to extend peptide-based linker strategies for improving ADC stability, a class of β-glucuronide–based linkers have been developed. The β-glucuronide bonds in these linkers can be hydrolysed by β-glucuronidases, enabling efficient release of the active drug.[110] β-Glucuronidases belong to the glycosidase family, and human β-glucuronidase is a member of glycosidase family 2. β-Glucuronidases are capable of

catalysing the hydrolysis of β-D-glucuronic acid residues from the non-reducing ends of mucopolysaccharides, such as heparan sulfate.[111] β-Glucuronidase is primarily localized in the lysosome and is overexpressed in certain tumour types, however, its extracellular activity is relatively low, providing potential advantages for the high serum-stability of ADCs and selective intracellular drug-release.[112] Furthermore, the high hydrophilicity of β-glucuronic acid may reduce the aggregation tendency of ADCs, particularly for conjugates carrying highly hydrophobic drugs, such as DNA minor-groove binders. Moreover, this property is important for improving the PK of ADCs.[113]

In 2006, the β-glucuronide-cleavable linker was first applied to ADC technology.[113] Jeffery and colleagues conjugated MMAE, MMAF, and doxorubicin propyloxazoline (DPO) with β-glucuronide linkers. An antibody attachment site was incorporated by functionalizing the aniline nitrogen with a maleimide-containing side chain. The susceptibility of β-glucuronide-cleavable linker to enzyme cleavage was determined by incubating the cysteine-quenched derivatives of these conjugates with E. coli β-glucuronidases. The results of HPLC assay showed the facile drug release, which verified the enzyme specificity of the β-glucuronide-cleavable linker. Under the catalysed by β-glucuronidase, the drug-linker would be hydrolysed at the glycosidic bond and undergo 1,6-elimination to release carbon dioxide and drug. The 1,6-elimination could be detected via LC-MS assay, and there were no detectable phenolic intermediates of β-glucuronide linker-drugs. Hence, the 1,6-elimination was very rapid. In controlled experiments, all cysteine-conjugates exhibited excellent stability in the absence of β-glucuronidase. Therefore, the β-glucuronide-cleavable linker was further confirmed to be the substrate for a β-glucuronidase, and the drug release would be smooth once the enzymatic hydrolysis was triggered.

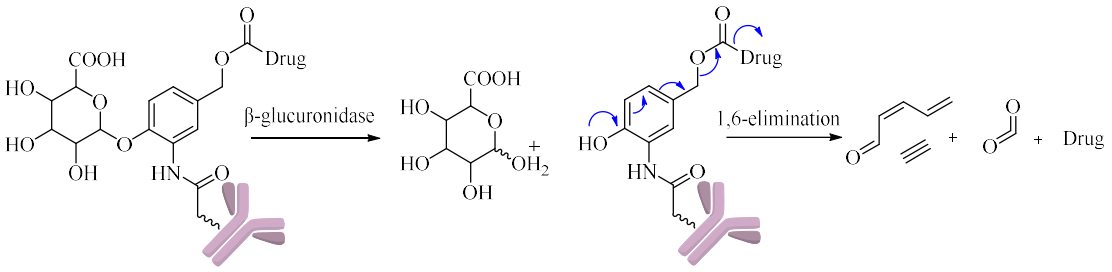

Figure 13. Hydrolysis of the β-glucuronide cleavable linker.

To explore the plasma stability of the glucuronide linker, the reduced conjugates was cultivated in rat plasma. The data from LC-MS indicated that the half-life of β-glucuronidase-MMAF (81 days) is markedly greater than that of valine-citrulline-MMAF (6.25 days). Therefore, the β-glucuronidase linker is much more stable in plasma than valine-citrulline linkers. Subsequently, Jeffery conjugated mAb cAC10 and c1F6 with various drugs via β-glucuronidase linker, and cAC10-β-glucuronidase-MMAF exhibited the highest DAR of 7.6. *In vitro* assays demonstrated that cAC10-MMAE-β-glucuronidase and c1F6-MMAE-β-glucuronidase could effectively deliver cytotoxin to target cells, and they had immunological specificity. *In vivo* study indicated cAC10-MMAE-β-glucuronidase displayed significant antitumour activity in subcutaneous Karpas 299 lymphoma xenografts, achieving complete tumour regression at doses ≥ 0.5 mg/kg and being tolerable at 100 mg/kg. Overall, the β-glucuronide linker is a robust strategy for generating highly potent and selective ADCs.

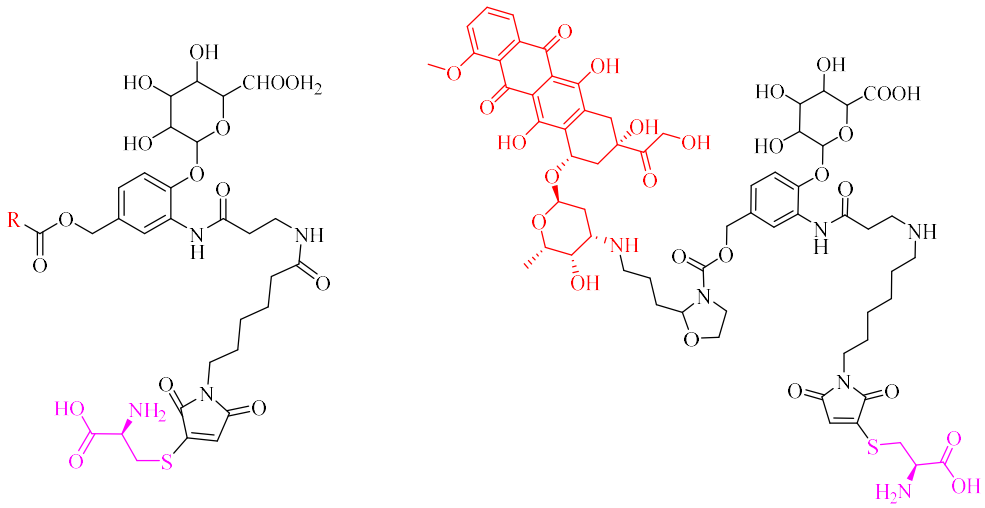

17 18

Figure 14. The chemical structure of cysteine-linker-MMAE/MMAF (**17**) and cysteine-linker-DPO (**18**).

In 2009, Burke and co-workers systematically compared the application of valine-citrulline cleavable linkers and β-glucuronide cleavable linkers in camptothecin (CPT)-based ADCs.[114] There were two main challenges in the design of CPT-containing ADCs: (1) the lack of suitable functional groups on the camptothecin (**19**) scaffold for conjugation; (2) the high hydrophobicity of the camptothecin (**19**), which readily induces ADC aggregation.

The only readily accessible functional group in **19** is the tertiary hydroxyl group at the C20 position, which is typically coupled to aliphatic alcohols via ester or carbonate linkages to construct conjugates. However, the high esterase activity present in mouse plasma can lead to rapid in vivo cleavage of ester and carbonate functional groups, thereby compromising systemic stability. To overcome the limitation of available conjugation sites, several camptothecin analogues were selected as payloads, such as 7-butyl-10-amino-CPT (**20**) and 7-butyl-9-amino-10,11-methylenedioxy-CPT, both of which exhibit markedly higher cytotoxic potency than **19**. One advantage of **20** is that, compared with ester linkages, the corresponding carbonate linkage generally provides improved resistance to hydrolytic cleavage. More importantly, the introduction of an

amino group in these CPT derivatives enables the use of the valine-citrulline-PABA dipeptide linker system. This dipeptide linker is designed to ensure stability in systemic circulation while allowing rapid release of the lysosomal drug payload after the ADC enters target tumour cells.

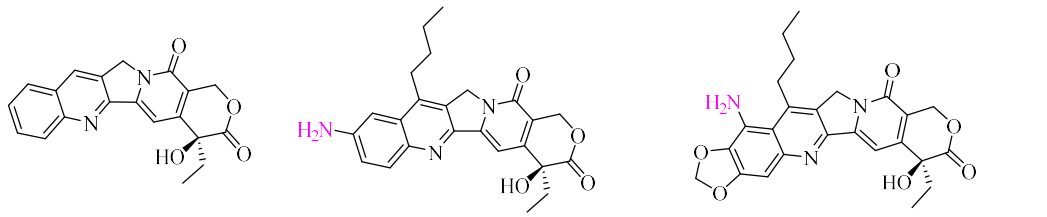

Figure 15. The chemical structure of camptothecin (**19**), 7-butyl-10-amino-CPT (**20**) and 7-butyl-9-amino-10,11-methylenedioxy-CPT (**21**).

The second challenge arises from the rigid and extended aromatic ring system of camptothecins, which confers limited aqueous solubility and readily leads to pronounced ADC aggregation. To address this issue, in addition to dipeptide linkers, CPT linker systems based on hydrophilic glucuronic acid were developed. These glucuronide linker systems markedly enhance the circulatory stability of ADCs and enable rapid and efficient drug release at the target site through the action of endogenous β-glucuronidase.

In *in vitro* biological evaluations, 7-butyl-9-amino-10,11-methylenedioxy-CPT (**21**) was identified as the most potent CPT analogue. After this payload was conjugated to antibodies via either dipeptide linkers or glucuronide linkers to generate ADCs, the resulting conjugates exhibited high cytotoxicity in Karpas 299 ($CD30^+$) anaplastic large cell lymphoma (ALCL) cells and H3396 (LeY^+) breast cancer cell lines, with IC_{50} values as low as 0.23-4.4 nM. Moreover, ADCs incorporating cAC10 or h1F6 were applied to Karpas 299, L540cy (Hodgkin lymphoma), and Caki-1 (renal cell carcinoma) cell lines, respectively. The results showed that these ADCs had remarkable immunological specificity. Furthermore, the in vivo study found that the valine-

citrulline-based ADCs showed minimal inhibition of tumour growth at a dose of 3 mg/kg, while the β-glucuronide-based ADCs significantly inhibited tumour growth. Hence, among CPT-based ADCs, ADCs containing β-glucuronide displayed superior efficacy compared with their valine-citrulline counterparts.

1.4.4 Sulfatase cleavable linker

To overcome ADC aggregation caused by dipeptide cleavable linkers, as well as the stereochemical complexity and enzymatic non-specificity associated with protease-cleavable linkers, researchers have gradually expended the scope of enzyme cleavable linkers to include the novel phosphatase- and sulfatase-based cleavable linkers. These linkers exhibit good stability in both human and rat blood circulation, thereby demonstrating promising potential for practical application.[98]

Sulfatases (EC 3.1.6) are a class of hydrolases that specifically cleave sulfate ester bonds in various metabolites.[115] Sulfatases have evolved from bacteria to mammals, and in humans, it is encoded by 17 different genes. Sulfatases play crucial roles in cellular activities and are closely involved in hormone regulation, cellular degradation, and signalling pathway modulation. In addition, sulfatases are overexpressed in certain cancer cells, providing higher selectivity for ADC targeting.[116] For example, compared with healthy tissues, the SULF2 gene is significantly overexpressed in skin cancer, colorectal cancer, testicular teratoma, and liver cancer. And, the expression of the SULF2 gene in colorectal cancer cells is also markedly higher than in benign colorectal adenoma cells.[117] Notably, sulfatase-based ADCs exhibit excellent stability in both mouse and human plasma while effectively releasing their payloads in lysosomes under sulfatase action, providing a solid foundation for their further development in anticancer therapy.[98]

Considering the challenges faced by cleavable linkers, Bargh's group published a paper in 2020 describing their progress in the development of novel aryl sulfate linkers.[98]

They designed two linkers using 7-amino-4-methylcoumarin (AMC) as a model payload.[98] Since AMC only exhibits fluorescence changes when released in the amino form, the fluorescence intensity after its release can be used to evaluate the stability of the designed ADC linker under simulated lysosomal environment and plasma conditions. The results showed that both linkers were recognized and hydrolysed by sulfatases, and the expected 1,6-elimination reaction occurred smoothly. Although both types of linkers can be cleaved by sulfatases under the same conditions, the enzymatic hydrolysis rate of the benzyl-type linker ($t_{1/2}$ = 24 min) is significantly faster than that of the amide-type linker ($t_{1/2}$ > 12 h). These results indicate that ADCs based on the benzyl-type linker are likely to release their payloads more efficiently in lysosomes, thereby potentially enhancing the cytotoxicity of the ADCs.

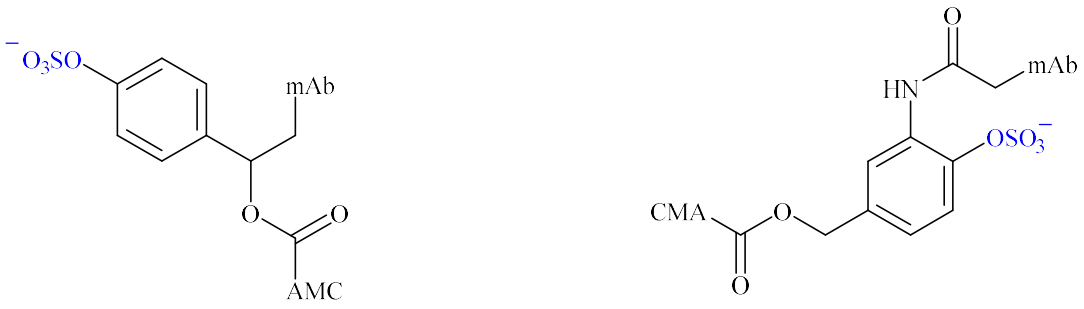

Figure 16. Design of linker-AMC model compounds by the Bargh's team. The linker-payloads were envisaged to be attached to mAb via an ortho-amide bond (A) or a benzyl-alkyl bond (B).

To investigate the enzymatic hydrolysis properties of these sulfatase linkers, David's team incubated two designed linkers in the presence of the known sulfatase inhibitor, phosphate.[98] Under these conditions, there was no fluorescence observed, confirming that payload-release depends on enzyme-catalysed hydrolysis. In further experiments, the benzyl-type linker was incubated under different pH conditions (pH 5, 7.4, and 9). The results showed that its optimal hydrolysis occurred at pH 5, and the cleavage rate decreased significantly as the pH increased. To assess its sensitivity to human lysosomal

sulfatases, the benzyl-type linker was incubated with recombinant human lysosomal arylsulfatase A (ARSA) and arylsulfatase B (ARSB), both of which resulted in fluorescence release, indicating that the benzyl-type linker can be efficiently cleaved by these human lysosomal sulfatases.

In plasma stability tests, the two linkers were incubated in mouse plasma.[98] Both of them exhibited excellent stability with almost no increase in fluorescence. In contrast, traditional dipeptide linkers were rapidly hydrolysed in mouse plasma, with a half-life of less than one hour. Further seven-day incubation experiments in both human and mouse plasma confirmed the exceptional stability of the sulfatase linkers, with only minimal hydrolysis observed. Moreover, the linkers remained stable even in the presence of intracellular nucleophiles, such as GSH.

For subsequent biological evaluation of ADCs, Bargh's team conjugated MMAE with trastuzumab via various linkers and assessed the cytotoxicity of these ADCs against HER2-positive (BT474) and HER2-negative (MCF7) cells.[98] They constructed a series of ADCs incorporating four distinct linkers: a sulfatase-cleavable linker containing a divinylpyrimidine (DVP) group; a sulfatase-cleavable linker bearing an electron-withdrawing nitro (NO_2) substituent on the aryl sulfate; a non-cleavable linker; and a valine-alanine cleavable linker.

In *in vitro* cytotoxicity assays, the cleavable ADCs exhibited higher toxicity against HER2-positive cells (IC_{50} = 92 pM), whereas the non-cleavable ADCs showed an IC_{50} of 609 pM, representing a six-fold increase in potency, which can be attributed to the "traceless release" of MMAE.[98] ADCs containing arylsulfate linkers showed comparable cytotoxicity to dipeptide ADCs, both being 5-10 times more potent than the non-cleavable ADCs. In contrast, an arylsulfate-based ADC containing an ortho-amide group was non-toxic to HER2-positive cells, indicating that this linker is unsuitable for ADCs, as the retained anionic sulfate group hinders auristatin binding to tubulin. All four ADCs were non-toxic to HER2-negative MCF7 cells at concentrations

up to 3 nM, confirming the stability of the linkers as well as the immunological specificity of mAbs. At the same time, trastuzumab alone was non-toxic to BT474 cells, highlighting the critical role of the MMAE in mediating the ADC's cytotoxicity. Additionally, the cleavage rates of different arylsulfate linkers appreciably impacted the cytotoxicity of various ADCs, indicating that payload-release rate is critical for the efficacy of ADCs. Therefore, selecting the appropriate aryl substituent is essential for enhancing the activity of sulfatase-cleavable ADCs.

1.5 Sulfatases

1.5.1 The sulfatase family

Sulfatases (EC 3.1.6) are a class of hydrolases that specifically catalyse the hydrolytic desulfonation of sulfate esters (CO-S) and sulfamates (CN-S).[115] Through genomic screening, researchers have identified 17 potential sulfatases in the human genome.[118] Except for the endosulfatases SULF1 and SULF2, which consist of approximately 870 amino acids, most human sulfatases range from 500 to 600 amino acids in length.[119]

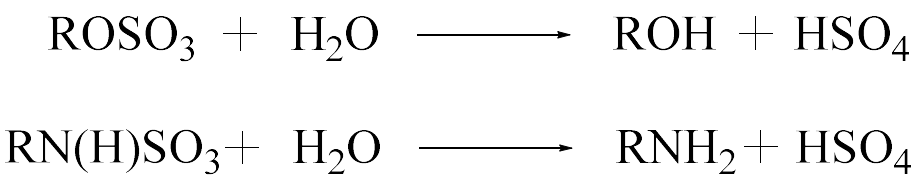

Figure 17. Hydrolysis reaction of sulfatases.

Sulfatases share a relatively high sequence similarity (20%-60%) and a common three-dimensional structure.[115] To date, the structures of five lysosomal sulfatases have been resolved. These crystal structures reveal a spherical fold with a mixed α/β topology, which can be divided into two domains.[120] The larger *N*-terminal domain is highly conserved, housing the critical formylglycine (FGly) residue that underpins the conserved mechanism of sulfatase hydrolysis.[121] In contrast, the C-terminal domain exhibits considerable variability.[122] Since the active site is located at the interface of

these two domains, differences in the C-terminal domain may play an important role in determining substrate specificity among sulfatases.

In humans, sulfatases exhibit strict specificity toward their natural substrates.[123] Each enzyme catalyses a precise desulfation step, which explains the non-redundant nature of sulfatases. Sulfatases hydrolyse sulfate esters of a variety of substrates, including glycosaminoglycans (heparin, heparan sulfate, dermatan/chondroitin sulfate, and keratan sulfate), sulfolipids (e.g., cerebroside-3-sulfate), and sulfated hormones (e.g., dehydroepiandrosterone-3-sulfate), thereby facilitating the degradation of macromolecules and cellular components or the activation of hormones.[124,125] The subcellular localization of different sulfatases varies, spanning the entire secretory pathway.[118,126]

All sulfatases are processed through the secretory pathway and undergo extensive glycosylation in the endoplasmic reticulum (ER) and Golgi apparatus during transport to their final subcellular compartments.[126] Based on subcellular localization and pH preference, they can be classified into non-lysosomal and lysosomal sulfatases.[127] The non-lysosomal group includes arylsulfatases C, D, and F, which are localized to the ER; arylsulfatase E, which is localized to the Golgi apparatus; and cell-surface sulfatases SULF1 and SULF2, all of which are active at neutral pH.[128,129]

FGly (2-amino-3-oxopropionic acid, α-formylglycine) residue, derived from a conserved cysteine (Cys) residue, is an essential prerequisite for sulfatase activity.[121] FGly modification occurs during the transport of newly synthesized sulfatase polypeptides into the ER and is catalysed by the FGly-generating enzyme (FGE) residing in the ER.[130] In the 1970s and 1980s, the correct coding sequence of sulfatase was introduced into the cells of patients with multiple sulfatase deficiency (MSD). It was discovered that all sulfatases lost their enzymatic activity when this residue was absent.[131]

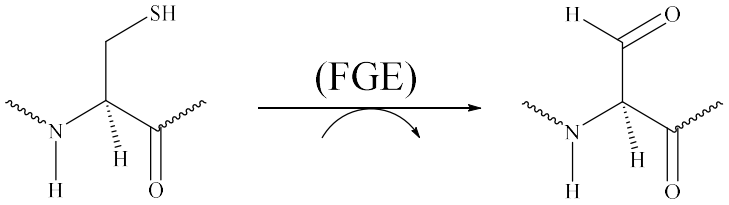

Figure 18. Formylglycine-generating enzyme (FGE) catalyses the post-translational oxidation of a conserved cysteine residue within the sulfatase active-site motif to formylglycine.

FGE is a 374-amino-acid protein with a unique fold that specifically recognizes a relatively simple linear sequence within cysteine-containing sulfatase precursors, which includes at minimum a CxPxR (x = variable amino acid) core motif.[132] In 2005, Roeser and colleagues used the crystal structure of FGE to elucidate the mechanism by which FGE catalyses FGly formation.[133] In this mechanism, two reduced cysteine residues in the active site coordinate the Cu(I) cofactor and simultaneously interact with the target sulfatase cysteine, forming a three-coordinate Cu(I) complex. Molecular oxygen (O_2) then binds to the copper centre, and a hydrogen atom is abstracted from the substrate cysteine. This process generates a thiol-aldehyde intermediate, which is rapidly hydrolysed to produce the final FGly-modified sulfatase, with hydrogen sulfide (H_2S) released as a by-product.

1.5.2 The hydrolytic mechanism

The currently resolved sulfatase structures show that the active site residues are almost completely homologous, supporting a common catalytic mechanism.[134] Based on the atomic-resolution (1.3 Å) X-ray crystal structure of *Pseudomonas aeruginosa arylsulfatase* (PARS), the transesterification/elimination mechanism is considered the most plausible model for sulfate ester hydrolysis.[135] During catalysis, FGly exists as an aldehyde hydrate (FGH), with its two geminal hydroxyl groups serving as the key catalytic residues in the active site.[136] First, one of the hydroxy groups acts as a nucleophile, performing an SN2 attack on the sulfur atom of the sulfate, hydrolysing the conjugated alcohol and transiently forming an FGly-sulfate intermediate.[137] The second hydroxyl group then facilitates elimination of the sulfate group, regenerating

the aldehyde. Finally, rehydration of the aldehyde restores FGH, completing the catalytic cycle. In addition to FGly, divalent metal ions (such as Ca^{2+} and Mg^{2+}) are also essential for catalysis, providing critical support for the stability of the active site and the formation of the sulfate ester intermediate.[138] These metal ions coordinate with the substrate's sulfur atom to generate an electrophilic sulfur centre, thereby facilitating nucleophilic attack by water.[137] This interaction also helps establish a metal coordination site that engages the second hydroxyl group of FGly.

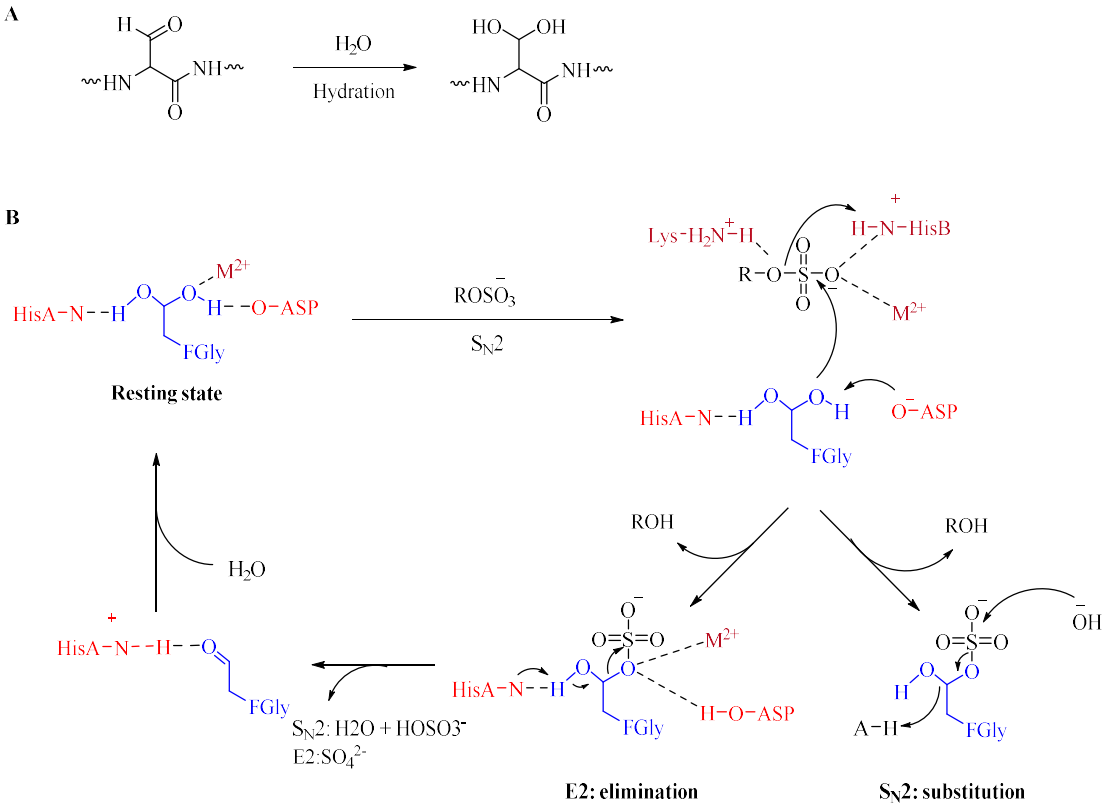

Scheme 2. (A) fGly is rapidly hydrated to a geminal diol, fGly-diol, and this form predominates in the sulfatase resting state. (B) Following the binding of sulfate ester substrate, fGly-diol is activated for nucleophilic attack at sulfur by aspartate. sulfoenzyme is formed, and desulfation may proceed by one of two pathways, hydrolysis by sulfur (SN2) or, more probable, elimination from the remaining fGly-diol hydroxyl (E2), catalysed by a histidine base.

Unlike the highly conserved active site residues, the C-terminal amino acid sequences of different sulfatases vary significantly, which is closely related to their substrate specificity.[115] Sulfatase substrates are highly diverse, ranging from small cytosolic

steroids, such as estrogen sulfate, to complex cell-surface carbohydrates, such as glycosaminoglycans. Taking the three major human sulfatases as examples, the primary physiological substrate of ARSA is sulfatide, specifically sphingolipids with galactose-3S (Gal-3S) head groups and ascorbic acid 2S.[139] ARSB is well known for its ability to specifically hydrolyse the 4-sulfate position of N-acetylgalactosamine (GalNAc) residues in dermatan sulfate (DS) and chondroitin sulfate (CS).[140] ARSC, more precisely referred to as steroid sulfatase (STS), hydrolyses steroid sulfate compounds.[141] Although ARSA, ARSB, and ARSC each target distinct natural substrates, they all exhibit "promiscuous" activity toward arylsulfate substrates, demonstrating general arylsulfatase activity and hydrolyzing synthetic sulfated compounds containing a phenolic ring, such as p-nitrocatechol sulfate or 4-methylumbelliferyl sulfate (4-MU sulfate).[142]

1.5.3 The function and related diseases

Sulfatases are a class of key enzymes that regulate the sulfation patterns of various physiological molecules, thereby influencing their biological functions. Their substrate conversion is closely linked to multiple critical cellular processes, including hormone regulation, cellular turnover, and the modulation of signaling pathways. Consequently, dysregulation of sulfatases is associated with the development of various pathological conditions, such as hormone-dependent cancers, lysosomal storage diseases, developmental disorders, and bacterial infections.[115]

Arylsulfatase A (ARSA)

ARSA is a 62 kDa polypeptide carrying three N-linked oligosaccharides.[143] Its key residue, FGly, is located within the metal-binding pocket and coordinates an octahedrally arranged Mg^{2+} ion.[139] ARSA is localized in lysosomes and primarily acts on the glycolipid cerebroside-3-sulfate. Cerebroside-3-sulfate, commonly referred to as sulfatide, is a critical sphingolipid in myelin, accounting for approximately 4% of total myelin lipids. Consequently, a deficiency of ARSA leads to sulfatide accumulation

within lysosomes, particularly in the central nervous system (CNS), ultimately causing demyelination and severe leukodystrophy, known as metachromatic leukodystrophy (MLD).[144] The cofactor saposin B plays a crucial role in facilitating the interaction between ARSA and its hydrophobic substrate, cerebroside-3-sulfate, ensuring proper binding.[145] A lack of saposin B prevents proper contact between ARSA and its substrate, thereby leading to MLD.

Arylsulfatase B (ARSB)

ARSB is a lysosomal sulfatase, and it catalyses the degradation of glycosaminoglycans under acidic conditions.[146] Its primary substrates are dermatan sulfate and chondroitin sulfate, and it specifically hydrolyses the sulfate ester at the C4 position of N-acetylgalactosamine residues, exhibiting high selectivity toward 4-O-sulfated GalNAc units.[147] Because dermatan sulfate and chondroitin sulfate are abundant components of connective tissue glycoproteins, deficiency of ARSB leads to abnormal accumulation of these GAGs in lysosomes, resulting in mucopolysaccharidosis type VI (MPS VI, Maroteaux–Lamy syndrome), which is characterized by clinical features such as short stature and joint deformities.[148]

The crystal structure of ARSB was determined by Bond and co-workers in 1996.[149] The enzyme comprises an N-terminal domain with a typical α/β topology, while a ribbon-like segment extending from the C-terminus spans the molecule and is linked to the N-terminal domain by a disulfide bond located near strand e of the main β-sheet, thereby stabilizing the overall conformation. Compared with other arylsulfatases, ARSB exhibits relatively low activity toward small-molecule aryl sulfate substrates, with its physiological function primarily directed toward macromolecular GAG substrates. Its active site is located within a surface-exposed cleft and is centred on the post-translationally modified Cys91 (formylglycine, FGly). The substrate-binding pocket is enriched in positively charged residues and coordinates a Ca^{2+} ion, and these structural features collectively confer high specificity toward 4-O-sulfated GalNAc-containing GAG substrates.

Steroid sulfatase (Arylsulfatase C)

Steroid sulfatase (STS, EC 3.1.6.2) is primarily localized to the microsomal fraction and is present in both the smooth and rough endoplasmic reticulum.[141] Its transmembrane region positions the catalytic core close to the membrane surface, enabling enzymatic activity within the membrane environment. STS mainly hydrolyses 3-hydroxysteroid sulfates, such as cholesterol sulfate and estrogen sulfate, participating in hormone metabolism and endocrine synthesis.[150] Its activity toward small-molecule aryl sulfate substrates remains unclear, but physiologically it primarily targets natural steroid substrates. STS deficiency leads to X-linked ichthyosis (XLI), characterized by skin scaling, with an estimated male incidence of approximately 1 in 6,000 to 1 in 2,000 and no significant differences observed among ethnic groups.[151] Moreover, STS defects are also implicated in hormone-dependent breast cancer, as the majority of estrogens in the breast of postmenopausal women are derived from intracrine synthesis mediated by P450arom, ES, and 17HSD1.[152]

In 2003, Hernandez-Guzman and colleagues resolved the three-dimensional structure of STS.[153] The tertiary structure consists of a polar, globular domain containing the catalytic core and a transmembrane α-helical domain. The catalytic core is located within subdomain 1 (SD1), which adopts an α/β sandwich fold and contains the key catalytic residues. Subdomain 2 (SD2), together with specific insertions, deletions, and substitutions in the transmembrane region, confers membrane-binding properties, positioning the catalytic core near the membrane surface to facilitate recognition of hydrophobic steroid substrates. Furthermore, the polar domain of STS is highly homologous in morphology and folding to human ARSA and ARSB, providing a stable structural framework for substrate binding and catalysis.

Heparan N-sulfatase (N-sulfoglucosamine sulfohydrolase)

N-sulfoglucosamine sulfohydrolase (SGSH) is a lysosomal enzyme that catalyses the desulfation of glycosaminoglycans (GAGs) within the lysosome.[154] Its primary substrates are the terminal N-sulfoglucosamine residues of GAGs, from which it

removes sulfate groups at the S-N bond at the non-reducing ends. Typical substrates include heparan sulfate and heparin, contributing to GAG degradation. Deficiency of SGSH leads to mucopolysaccharidosis type IIIA (MPS IIIA), an inherited disorder characterized by abnormal facial features, skeletal deformities, hepatosplenomegaly, and varying degrees of neurodegeneration.[155]

SGSH can adopt two crystal forms under different pH conditions: the S form at pH 7.5 and the L form at pH 5.1.[156] Its active site is highly conserved around FGly70, forming a deep conical cleft with a divalent Ca^{2+} ion coordinated by the catalytic nucleophile and four side chains at the bottom. Positively charged residues surrounding the cleft attract the highly negatively charged sulfate groups of substrates and guide them into the binding pocket. Compared with O-sulfatase homologs, SGSH exhibits structural differences around the active site, including the short tunnel leading to the site and surrounding surface clefts, enabling specific recognition of N-sulfated substrates. The overall spatial arrangement and shape of the active pocket provide a structural basis for its high specificity toward highly sulfated heparan-type GAGs.

Iduronate 2-sulfatase (IDS)

IDS is a lysosomal enzyme that primarily acts on dermatan sulfate and heparan sulfate.[157] It catalyses the hydrolysis of the C2 sulfate ester bond of 2-O-sulfo-α-L-iduronic acid residues at the non-reducing ends of glycosaminoglycans (GAGs), thereby participating in GAG degradation. These substrates play critical roles in cell adhesion, growth, proliferation, and repair; consequently, IDS deficiency leads to Hunter syndrome (Mucopolysaccharidosis type II, MPS II), characterized by pathological accumulation of GAGs in tissues and organs, progressively impairing cellular function and multiple organ systems.[158]

IDS exists as a monomer with a compact globular α/β sandwich fold, comprising an N-terminal SD1 and a C-terminal SD2 domain.[159] SD1 contains the catalytic core and is tightly associated with SD2 through extensive hydrophobic interactions, forming the enzymatically active “intermediate”. The polypeptide chain contains six cysteines, four

of which form disulfide bonds: one links a short β-strand near the substrate recognition site, and another stabilizes an extended solvent-exposed loop. One free cysteine is located at the tip of an 18-residue loop connecting the main β-sheet β1 strand to N-terminal α-helix 1. Another cysteine, C84, is post-translationally modified to form formylglycine (FGly), serving as the key catalytic residue in the active site. FGly84 coordinates a Ca^{2+} ion, enabling IDS to specifically recognize substrates and conferring high selectivity for naturally occurring, highly sulfated GAGs.

1.6 Sulfate synthesis

1.6.1 Direct methods (converting phenols to sulfates)

Sulfate monoesters (RSO_3H) are widely distributed in nature and in the human body, where they play important roles in numerous physiological processes, including hormonal regulation, detoxification metabolism, molecular recognition and cellular signal transduction, as well as mechanisms of viral entry into host cells.[160] As understanding of the biochemical functions of sulfate monoesters has continued to deepen, the synthesis of sulfated molecules has attracted increasing research interest. Historically, much of the interest in sulfate ester synthesis has originated from the field of carbohydrate chemistry, and the development of most reaction methodologies has been carried out within this context.[161]

The most commonly used reagents for the synthesis of sulfate monoesters are sulfur trioxide-amine or -amide complexes.[160,162] In order to develop a general, reliable, and controllable strategy for the synthesis of multisulfated peptides — and thereby overcome the long-standing bottleneck that "tyrosine sulfation is difficult to prepare and difficult to study" — Young and Kiessling reported in 2002 a method for achieving tyrosine sulfation during solid-phase peptide synthesis (SPPS).[163] In this approach, Azm (azidomethyl)-protected tyrosine was introduced during SPPS. After completion of peptide chain assembly, selective deprotection of the tyrosine side chain was carried

out on solid-phase peptides, followed by sulfation using DMF·SO_3 as the sulfating reagent. This strategy enabled efficient sulfation of tyrosine residues while avoiding intermediate isolation steps and issues associated with acid-sensitive conditions. In this system, the amino group was protected with Fmoc, whereas the phenolic hydroxyl group was protected with Azm.

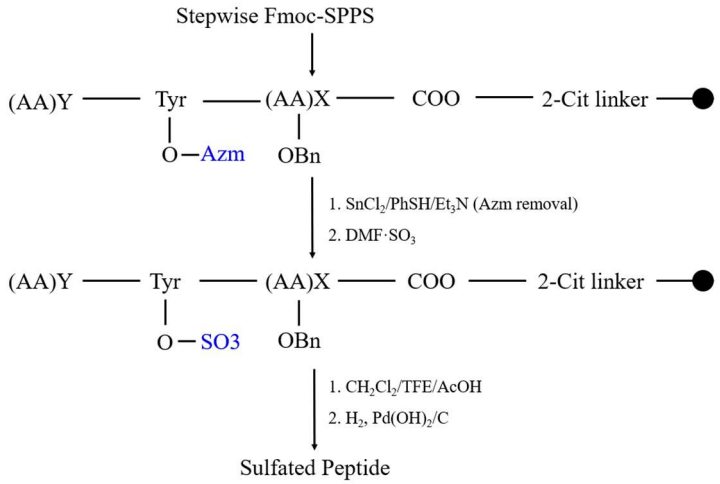

Scheme 3. Overview of sulfated peptide synthesis.

In 2019, Montero Bastidas' group employed an SO_3·pyridine complex to sulfate phenolic derivatives in studies on iridium-catalysed para-selective borylation of aromatic C-H bonds.[162] Specifically, phenols were first sulfated using SO_3·pyridine to generate the corresponding aryl hydrogen sulfates (essentially Ar-O-SO_3^- anions). Subsequent anion exchange with tetraalkylammonium salts afforded the desired tetraalkylammonium aryl sulfates, which were then used as substrates for C-H borylation. From a mechanistic perspective, this process involves nucleophilic attack of the phenolic hydroxyl group on SO_3 slowly released from the SO_3·pyridine complex to form an Ar-O-SO_3^- anion, which subsequently pairs with an NR_4^+ cation to give the corresponding tetraalkylammonium salt.

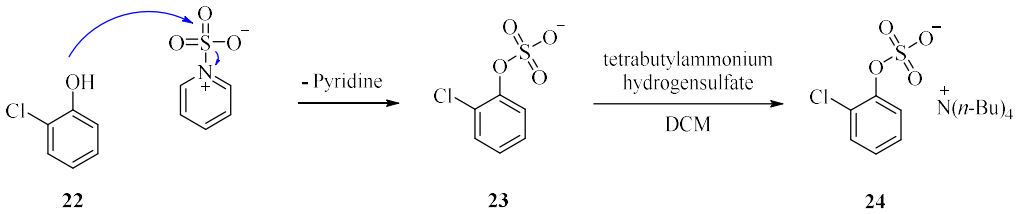

22 23 24

Scheme 4. Synthesis of tetrabutylammonium 2-chlorophenyl sulfate (**24**).

Overall, SO_3-amine, SO_3-amide, and DMF·SO_3 complexes serve as safe and weighable sources of SO_3, delivering "SO_3 equivalents" into reaction systems while avoiding the direct use of liquid SO_3 or fuming sulfuric acid, both of which are highly reactive sulfating media.[160] Direct sulfation using liquid SO_3 or fuming sulfuric acid is typically associated with significant safety hazards and issues of controllability.[164] Liquid SO_3 is extremely electrophilic and highly corrosive, and readily undergoes violent exothermic reactions with trace amounts of water or substrates bearing reactive functional groups.[165] Consequently, liquid SO_3 renders reactions difficult to control and poses serious risks to experimental operators. In addition, its stringent storage and handling requirements limit its practicality in routine laboratory settings.[166] In contrast, SO_3-amine, SO_3-amide, and DMF· SO_3 complexes can stably deliver SO_3 while reducing its instantaneous free concentration, thereby allowing sulfation reactions to proceed under milder and more controllable conditions, with improved selectivity and operational safety. Therefore, these reagents have been widely adopted in modern sulfation chemistry. Nevertheless, in multifunctional substrates, such sulfur trioxide-amine or -amide complexes often exhibit limited regioselectivity, readily leading to multisite sulfation and complex product mixtures, which complicate purification and reduce the yield of the desired sulfate monoesters.[167,168] Moreover, sulfated products are typically highly water-soluble, making purification challenging and restricting subsequent chemical transformations and applications.[169]

To achieve para-selective borylation of aromatic C-H bonds and overcome the difficulty of precisely controlling regioselectivity in traditional methods, the Phipps's team

reported in 2019 a para-selective borylation strategy based on steric shielding effects induced by bulky counterions.[170] In this study, chlorosulfonic acid (**25**) was selected as the sulfating reagent to prepare the sulfated substrates required for the borylation reaction. The reaction begins with nucleophilic attack of the phenolic hydroxyl group on the sulfur centre of **25**, forming a sulfate monoester intermediate with concomitant release of chloride anion. This step is carried out at 0 °C with the addition of excess triethylamine, which serves to trap the generated HCl as $Et_3NH^+Cl^-$, thereby driving the reaction toward product formation. The combined effect of low temperature and triethylamine effectively suppresses side reactions such as multisite sulfation and aromatic ring sulfonation, ensuring mild and controllable reaction conditions. Subsequent treatment with sodium hydroxide deprotonates the sulfate monoester under basic conditions to give the corresponding sodium salt, R-X-SO_3^- Na^+. The desired product dissolves in the aqueous phase as the sodium salt, while neutral impurities are partitioned into the organic phase and removed by extraction. Finally, ion exchange with tetrabutylammonium hydrogensulfate converts the sodium salt into the corresponding tetrabutylammonium salt.

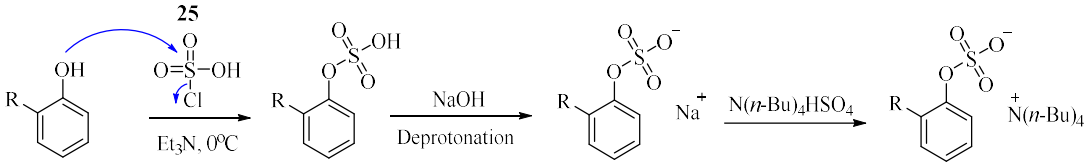

Scheme 5. Preparation of sulphated substrates using Chlorosulfonic acid (**25**).

Chlorosulfonic acid **25** was selected as the sulfating reagent primarily because of its extremely high reactivity and excellent sulfation efficiency.[171] **25** is essentially an activated form of SO_3; its sulfur centre exhibits pronounced electrophilicity and can be rapidly attacked by nucleophiles such as phenolic hydroxyl groups, enabling efficient formation of sulfate monoesters under relatively mild conditions.[172] Compared with SO_3–amine or SO_3–amide complexes, **25** follows a more direct reaction pathway and provides higher sulfation efficiency, particularly for aromatic phenol substrates.

Furthermore, the use of **25** enables controllable sulfation under low-temperature conditions. In the presence of triethylamine at low temperature, its high reactivity is effectively moderated, allowing sulfation to proceed at a fast yet controlled rate, thereby achieving site-specific O-sulfation within a short time while significantly suppressing side reactions.[173] In addition, the sulfation reaction mediated by **25** produces simple byproducts and allows facile control over reaction direction. The byproduct HCl generated during sulfation is rapidly captured by triethylamine to form $Et_3NH^+Cl^-$, which not only drives the reaction equilibrium toward sulfate monoester formation but also prevents excessive acidification of the reaction medium, thereby effectively reducing side reactions such as aromatic sulfonation and multisite sulfation.

1.6.2 Indirect methods (via protecting group approaches)

Although the sulfation methods described above are relatively well established, they still have limited applicability to highly complex molecular systems, such as various sulfated oligosaccharides. In addition, direct sulfation typically affords anionic sulfate salts, and the resulting sulfate esters and their salts are often difficult to manipulate in subsequent chemical transformations and challenging to characterize.[160] Consequently, in practical synthetic routes, sulfation is usually deferred to the final stage of synthesis.[174] The introduction of sulfate protecting groups that remain stable under standard synthetic conditions yet can be selectively removed at an appropriate stage would greatly expand the available strategies for the synthesis of sulfated compounds and is expected to play an important role in the preparation of carbohydrates and other natural products.[175]

In the development of protected sulfates, researchers have introduced sulfate groups at an early stage of synthesis in the form of protected sulfate diesters, thereby largely avoiding or alleviating the low yields and operational difficulties associated with traditional sulfating reagents.[176] This strategy also circumvents the need for selective

hydroxyl deprotection and sulfation at the end of the synthetic sequence.[177] Because protected sulfate diesters exhibit superior chemical stability and are more amenable to purification than highly polar and acid-sensitive sulfate monoesters, this approach can significantly enhance overall synthetic efficiency and total yields.

In 1981, Penney and Perlin encountered a critical challenge during the synthesis of complex sulfated oligosaccharides, such as heparin and chondroitin, namely the difficulty of preserving the integrity of sulfate groups ($-OSO_3^-$) under multistep synthetic conditions.[178] Sulfate groups have high reactivity toward various nucleophiles and are prone to desulfation reactions, showing poor stability under acidic, basic, reductive, or oxidative conditions.[179,180] As a result, they are incompatible with conventional protecting group manipulations and cannot withstand many of the reaction conditions commonly employed in carbohydrate chemistry. Consequently, how to effectively "protect" sulfate groups throughout multistep carbohydrate synthesis became the central issue of this study.

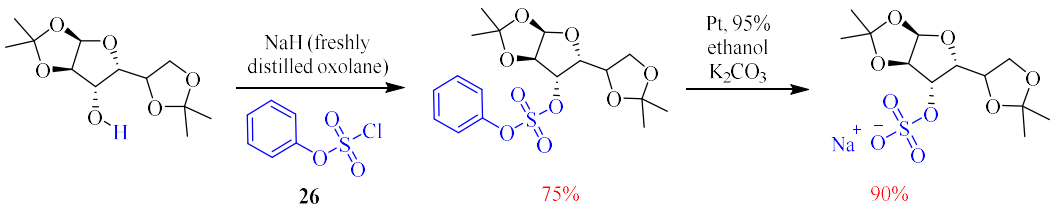

Scheme 6. The introduction of an SO_3 group via phenyl chlorosulfate (**26**).

To address this problem, Penney and Perlin developed a stable and synthetically practical sulfate protecting group based on an aryl moiety, phenyl group, which introduced aryl protecting group into sulfation chemistry for the first time.[178] By "masking" the sulfate group as a stable aryl sulfate ester (Ar-OSO_2-O-Sugar), they were able to preserve the sulfate functionality throughout multistep synthesis and remove the protecting group at the final stage. The key innovation of this approach lies in the use of **26** as the sulfating reagent. They found that direct use of **25** or SO_3·pyridine often

led to degradation of carbohydrate substrates, whereas **26** allowed the sulfate group to be introduced under mild conditions in the form of a phenyl-protected sulfate.

To validate the suitability of the phenyl group as a sulfate protecting group, Penney and Perlin systematically examined its stability under acidic, basic, and fluoride-ion-containing conditions, and further evaluated its tolerance toward acetylation and other common carbohydrate protecting group manipulations, such as acetal formation, silyl ether formation, and acetylation. The results demonstrated that the phenyl group exhibits high stability under a wide range of conditions commonly used in carbohydrate chemistry, which is the key factor enabling its effective application as a sulfate protecting group.

In addition, they discovered that phenyl-protected sulfates could undergo selective deprotection under mild hydrogenation conditions. In the presence of PtO_2, H_2, and K_2CO_3, the aryl group is cleaved by hydrogenation to give cyclohexanol, while the sulfate group ($-OSO_3^-$) remains intact. Because the aryl moiety undergoes selective cleavage under hydrogenation conditions without impacting the sulfate ester framework, this deprotection process is highly selective and effectively avoids undesired desulfation. Even if small amounts of desulfated byproducts are formed, they can be readily removed by anion-exchange resins. Overall, this method represents an efficient and elegant strategy for selective deprotection and provides an important and reliable tool for the multistep synthesis of sulfated carbohydrates.

In their 1996 study, Xie and Widlanski reported the first use of an isobutyl group as a protecting group for sulfate esters.[181] In an effort to identify a sulfate ester protecting group that had high stability under acidic or solvating conditions and could be efficiently removed by soft nucleophiles such as iodide, Xie and Widlanski evaluated four protecting groups — isopropyl, neopentyl, ethyl, and isobutyl — among which isobutyl exhibited the most favourable overall performance.

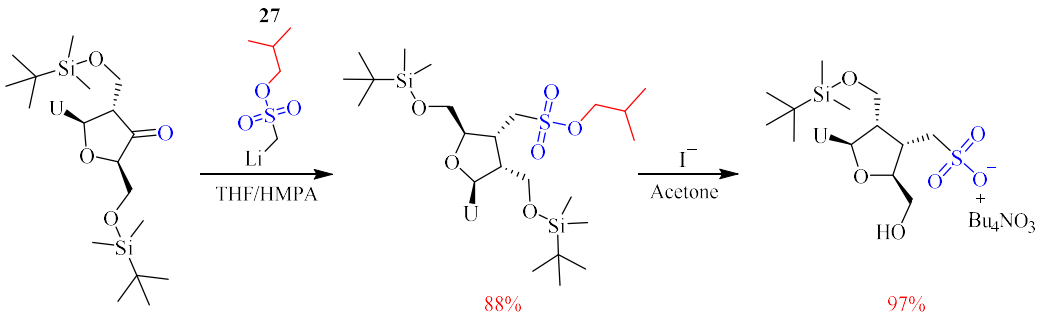

Scheme 7. Introduction of SO_3 group via isobutyl sulfonate (**27**).

First, isopropyl showed stability under a range of reaction conditions and was removable by tetrabutylammonium iodide or ammonia. However, it displayed significant limitations in multistep nucleotide synthesis. Moreover, isopropyl was acid-sensitive and readily degraded under glycosylation and hydrogenation conditions. Additionally, it was also unstable during column chromatography and difficult to be removed even in the presence of strong iodide nucleophiles. Consequently, isopropyl is unsuitable as a sulfate ester protecting group in complex synthesis. Second, ethyl group exhibited insufficient stability and was readily attacked by nucleophiles, rendering them inappropriate for multistep synthesis. Third, neopentyl group showed exceptional stability but required overly harsh conditions for deprotection, which limited their practical utility. In contrast, the isobutyl group achieved a favourable balance between stability and deprotectability. It tolerated a broad range of reaction conditions while allowing efficient deprotection under Bu_4NI conditions, making it the optimal choice. As a sulfate ester protecting group, isobutyl avoids the facile cleavage observed with isopropyl groups due to secondary carbocation formation and overcomes the excessive stability of neopentyl groups that hinders deprotection.

In 1997, Proud and co-workers investigated the feasibility of using 2,2,2-Trichloroethyl (TCE) and 2,2,2-Trifluoroethyl (TFE) as sulfate diester protecting groups.[182] First, their study examined the applicability of TCE as a sulfate protecting group. Although TCE is commonly employed for the protection of phosphates and carboxylic acids, it afforded only very low yields in carbohydrate sulfation, likely due to its substantial

steric hindrance and incompatible deprotection conditions. Flitseh's team subsequently turned their attention to the potential of TFE as a protecting group. They found that TFE-protected sulfates could be generated directly and efficiently from sulfate monoesters using 2,2,2-trifluorodiazoethane (CF_3CHN_2), whereas the application of 1,1,1-trifluoroethyl chlorosulfate were unsuccessful owing to excessive side reactions.

Flitseh's team further evaluated the stability of TFE-protected sulfates under reaction conditions commonly used in carbohydrate chemistry. The results showed that TFE-protected sulfates exhibit high stability under strongly acidic organic conditions (such as TFA/EtOH), basic conditions (such as NaOMe/MeOH and Zemplén deacetylation), hydrogenation conditions, in the presence of fluoride ions, and under refluxing methanol. These findings demonstrated that TFE was an excellent protecting group for sulfate functionalities. In addition, Proud's team developed a highly selective deprotection protocol: under refluxing KO*tBu*/*tBu*OH conditions, *tBu*O^- nucleophilically attacked S, displacing $CF_3CH_2O^-$, which subsequently underwent β-elimination to release isobutene, thereby efficiently generating $-OSO_3^-$ in yields of 82-96%.

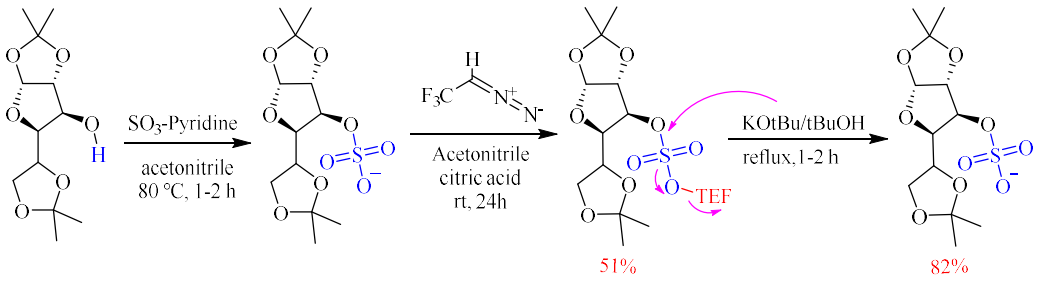

Scheme 8. Protection of SO_3 group via TFE group.

Overall, TFE was shown to be a highly effective sulfate protecting group. It was exceptionally stable under conditions commonly employed in carbohydrate chemistry, and could be selectively removed under defined conditions and exhibited good compatibility with other protecting groups. Moreover, TFE-protected sulfates could be directly derived from sulfate monoesters, avoiding cumbersome synthetic steps.

Nevertheless, the use of TFE as a sulfate protecting group had certain limitations. First, introduction of the TFE group required trifluorodiazoethane, a highly toxic reagent with potential explosive hazards that must be freshly prepared. Second, deprotection of the TFE group required relatively harsh conditions, namely refluxing in potassium tert-butoxide (KOtBu) and tert-butanol (*tBu*OH). Furthermore, when disaccharides were used as substrates, the deprotection yields of TFE-protected sulfates were often very low.

In 2004, the Taylor's team first proposed and validated TCE as a protecting group for aryl sulfate monoesters.[183] Compared with alkyl sulfates, aryl sulfate monoesters impose more stringent requirements on protecting groups. First, aryl sulfate monoesters are extremely unstable under acidic conditions and therefore are incompatible with acid-labile protecting groups. Second, because benzylic sulfate diesters are highly unstable, benzyl groups cannot be used to protect aryl sulfate monoesters. Third, protecting groups that require strongly basic conditions for removal (such as TFE and TCE groups) are likewise unsuitable, as aryl sulfate monoesters readily decompose under strong base.

The TCE protecting group had previously been investigated by Flitseh's team, but in their studies, it was abandoned due to excessive steric hindrance and deprotection conditions that were incompatible with sulfated carbohydrates. Moreover, TCE deprotection always relied on Zn/HOAc conditions, which are incompatible with many aryl sulfate monoesters, contributing to the long-standing neglect of TCE in this field. However, Paquet's team demonstrated that TCE can also be removed under mild hydrogenolysis conditions (10% Pd/C, H_2, aqueous ethanol). On the basis of these findings, Flitseh's team re-evaluated the potential of TCE and explored its feasibility as a protecting group for aryl sulfate monoesters.

For the preparation of the TCE reagent, Taylor's team reacted sulfuryl chloride (**29**) with 2,2,2-trichloroethanol (**30**) in the presence of pyridine to generate 2,2,2-

trichloroethyl chlorosulfate (**28**). This transformation proceeded via a typical nucleophilic substitution mechanism: **30** acted as a nucleophile and attacked the hexavalent sulfur centre, releasing HCl, which was scavenged by pyridine to prevent side reactions. The reaction thus afforded a stable **28**.

In the subsequent step, where the sulfate group was introduced into the substrate using **28**, Et_3N and DMAP acted cooperatively with **28** in THF. Mechanistically, DMAP first served as a nucleophilic catalyst and attacked the sulfur centre to form an activated DMAP-SO_3-TCE intermediate. The aryl phenol then attacked the sulfur atom, displacing DMAP and affording the desired aryl sulfate diester Ar-O-SO_2-O-TCE. In this process, Et_3N also scavenged chloride anions, preventing the accumulation of HCl that could otherwise lead to undesired desulfation. The role of DMAP was to promote the formation of the sulfopyridinium intermediate and thereby enhance the electrophilicity of the sulfur centre.

For TCE deprotection, Taylor's team employed two complementary methods. The first utilized Pd/C in combination with ammonium formate (NH_4HCO_2). Here, NH_4HCO_2 served both as a hydrogen source and as a buffer to prevent cleavage of the S-OAr bond, making this method suitable for most substrates. The second employed Zn with NH_4HCO_2, which was even milder and could avoid undesired side reactions such as dehalogenation of aryl halides or reduction of carbonyl groups. By exploiting the selectivity differences between these two deprotection systems, efficient TCE removal was achieved while accommodating substrate sensitivity.

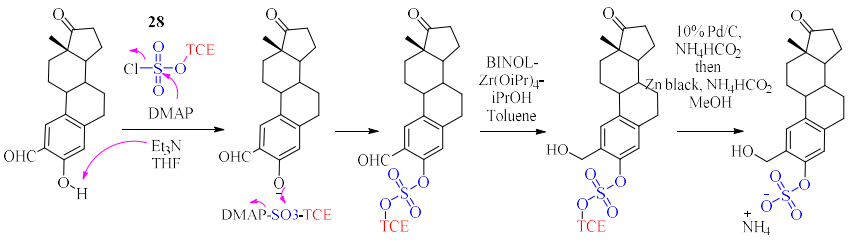

Scheme 9. Introduction of SO_3 group via 2,2,2-trichloroethyl chlorosulfate (**28**).

In 2006, Simpson and Widlanski proposed a general synthetic strategy for sulfate monoesters.[160] They employed tuneable alkyl chlorosulfates as sulphating reagents, and modulated the stability and deprotectability of sulfate monoesters by selecting three different alkyl protecting groups, neopentyl, isobutyl, and THP-CH_2. In this scheme, the reactivity of the protecting group was treated as an adjustable parameter.

Their studies showed that differences in reactivity among the alkyl protecting groups arise primarily from variations in S_N2 accessibility and electronic effects. The exceptional stability of the neopentyl group originates from its tertiary α-carbon, which severely hinders S_N2 attack. Consequently, I^- cannot attack from the carbon terminus and instead attacks the sulfur centre, generating phenoxide byproducts. This behaviour explains why neopentyl groups are mainly suitable for aromatic alcohol substrates. In contrast, the primary carbon of the isobutyl group allows I^- to attack from the carbon terminus. However, in aromatic alcohol systems, I^- preferentially attacks the sulfur centre, leading to desulfation side reactions, and therefore a softer, more carbon-directed nucleophile such as SCN^- is required. Moreover, the β-ether motif in THP-CH_2 substrates reduces S_N2 reactivity through electronic effects, causing the activity of THP-CH_2 to lie between that of neopentyl and isobutyl groups.

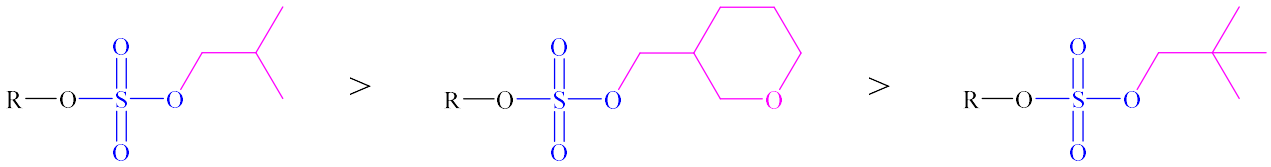

Figure 19. Order of reactivity for sulfate monoester protecting groups.

Overall, the central contribution of this work lies in establishing a tuneable framework for sulfate monoester synthesis, enabling flexible selection of protecting groups according to substrate type, downstream transformations, and stability requirements. The method also offers mechanistically clear and predictable deprotection conditions: N_3^- for neopentyl groups, I^- for aliphatic isobutyl groups, and SCN^- for aromatic isobutyl groups.

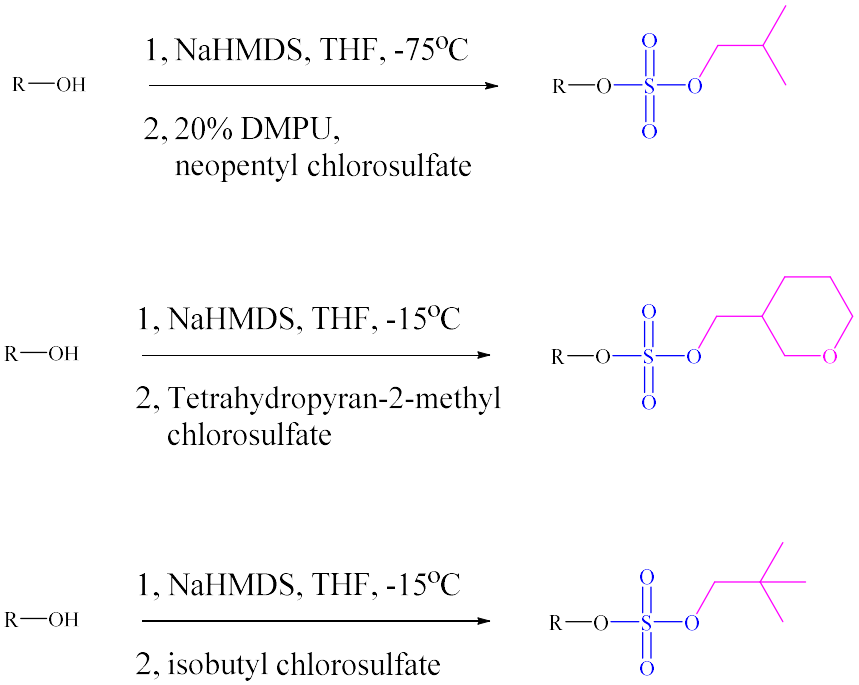

Scheme 10. Synthesis of protected sulfate monoesters via three protecting groups respectively.

In 2006, the Ingram group found that when **28** was used to introduce a sulfate group into diisopropylidene-D-galactose, the reaction predominantly produced glycosyl chloride byproducts rather than the desired sulfate ester.[176] Even when following the protocol reported by Taylor's team — adding AgCN, Et_3N, and DMAP during sulfation to suppress desulfation — the yield of the desired product remained only around 50%. Moreover, when the same conditions were applied to the sulfation of other monosaccharide substrates, the desired sulfate diesters were scarcely formed. This was attributed to the release of nucleophilic species such as Cl^- from **28** during the reaction, which severely impeded the sulfation process. Therefore, the goal of Ingram and co-workers was to develop efficient sulfating reagents that do not generate nucleophilic byproducts and to apply them to complex monosaccharide substrates.

Building on the sulfonyl imidazolium system proposed by O'Connell and Rapoport, Ingram and co-workers replaced Cl^- with the non-nucleophilic counteranion OTf^- and introduced imidazole as the leaving group, thereby developing a class of highly

activated sulfuryl imidazolium salts. These reagents were strongly electrophilic, enabling sulfation to proceed without the formation of nucleophilic byproducts and significantly enhancing the reactivity of the sulfur centre, which allowed for mild and highly selective sulfation of carbohydrates. Compared with traditional sulfuryl chloride systems, this approach did not release Cl^-, effectively avoiding glycosyl chloride side reactions, while also offering good stability and operational convenience. Additionally, *N*-Methylimidazole (NMI) was found to be essential in this sulfation system, and common bases such as triethylamine, pyridine, or lutidine could not replace its role. This indicated that NMI functioned not merely as an acid scavenger but also participated as a nucleophilic catalyst, possibly through the formation of more reactive intermediates or by facilitating proton transfer. In addition, Ingram and co-workers employed TCE to protect the sulfate group, maintaining its integrity during sulfation. In deprotection studies, Zn-NH_4HCO_2 was identified as the optimal system for removing the TCE protecting group. Since this method was mild, highly selective, did not induce desulfation, and afforded near-quantitative deprotection yields (94-99%).

The first sulfuryl imidazolium salt developed, 1-methylimidazolium sulfuryl 2,2,2-trichloroethyl sulfate (**31**), did not meet the expectations of Ingram's team. In 2009, the group published a subsequent study describing their efforts to optimize sulfuryl imidazolium salts.[184] By varying the substituents at the 2- and 3-positions of the imidazolium ring, they constructed a series of sulfuryl imidazolium salts (SIS) to explore sulfation pathways with improved solubility, enhanced stability, and reduced side reactions. 1,2-Dimethylimidazolium was identified as the optimal structure, since the methyl group at the 2-position provided moderate steric protection, while the methyl group at the 1-position improves leaving-group ability. Moreover, the compact structure did not hinder nucleophilic attack. In contrast, ethyl or isopropyl substituents at the 2-position reduce reactivity due to steric hindrance, whereas the absence of substitution leads to insufficient stability. Meanwhile, dichloromethane (DCM) was shown to be the best solvent, significantly improving the solubility of the 1,2-dimethylimidazolium

salts. Furthermore, 1,2-dimethylimidazole (1,2-dMeIm) proved to be the most effective base, while other bases such as 1-Me-2-EtIm or 1-Me-2-iPrIm resulted in decreased yields.

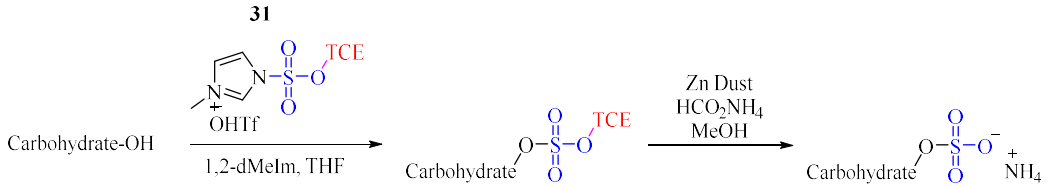

Scheme 11. Introduction of SO_3 group via sulfuryl imidazolium salt.

In summary, the synthesis of sulfate monoesters has evolved from direct sulfation toward indirect strategies based on tuneable protecting groups, enabling the stable introduction and selective deprotection of sulfate functionalities in multistep synthetic sequences. These approaches not only address long-standing challenges associated with selectivity and purification in traditional sulfation reactions, but also provide reliable tools for the efficient synthesis of complex carbohydrates, aryl compounds, and sulfated peptides, thereby laying a solid foundation for the application of sulfated molecules in biochemistry and medicinal chemistry.

1.7 This work

Aryl sulfates are significant in chemical biology and medicinal chemistry, particularly in the design of enzyme-cleavable linkers and prodrug systems. However, owing to the high polarity and intrinsic chemical reactivity of the sulfate group, the stable incorporation of sulfates into molecules during multistep organic synthesis has long remained a major challenge. In this study, a novel sulfating reagent, a sulfuryl imidazolium salt, was employed to enable the mild and controllable introduction of TCE-protected sulfate esters onto aryl substrates. This strategy proceeds via an activated sulfuryl imidazolium intermediate, achieving a favourable balance between reactivity and selectivity, and thereby avoiding product decomposition and non-

selective substitution commonly associated with conventional sulfation conditions.

By introducing the TCE group as a protecting group for sulfate monoesters, the chemical reactivity of sulfates was effectively attenuated during sulfation, while the stability of products was significantly enhanced during subsequent transformation and purification. Moreover, the TCE protecting group can be removed under relatively mild conditions to regenerate the free aryl sulfate, thereby minimizing undesired desulfation and substantially improving the overall yields.

In this work, a 2,2,2-trichloroethyl-protected sulfuryl imidazolium salt was applied to the sulfation of a series of aryl substrates, expanding the synthetic toolbox for the introduction of sulfate groups onto aromatic systems. By NMR, HPLC, MS, and UV-Vis absorption spectroscopy, the feasibility and reproducibility of this sulfating reagent across different aryl substrates were systematically evaluated. Furthermore, this study also aims to establish a robust and reliable foundation for the further development and application of aryl sulfate motifs in ADC linker design.

2. Result and Discussion

2.1 Evaluation of Synthetic Outcomes

2.1.1 Preparation of Chlorosulfate **28** and Imidazolium **33**

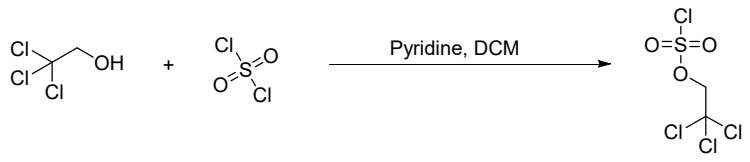

30 **29** **28**

Scheme 12. The synthesis of 2,2,2-trichloroethyl chlorosulfate (**28**).

Following the method of Liu and co-workers, 2,2,2-trichloroethyl chlorosulfate (**28**) was prepared from 2,2,2-trichloroethanol (**30**) and sulfuryl chloride (**29**).[185] The crude product 2,2,2-trichloroethyl chlorosulfate (**28**) was concentrated *in vacuo* without any further purification. Preparation of this material was carried out by other members of the lab group and made available for my work.

Imidazolyl sulfate **32** was prepared from 2-methyl imidazole and **28** following the method of Ingram and co-workers (Scheme 13).[176] Purification by column chromatography produced **32** in 96% yield and sufficient purity for the subsequent synthesis of imidazolium salt **33.** The purity and structure of compound **32** were confirmed by ^{1}H NMR spectroscopy.

Two weakly coupled doublets are observed at 7.49 ppm and 7.11 ppm, each integrating for one proton. These signals are assigned to the two protons on the imidazole ring. The small coupling between them is consistent with long-range coupling within the heteroaromatic system and with the electronic influence of the *N*-sulfonyl substituent, which modifies the electron density of the ring and slightly differentiates the two

aromatic environments.

A singlet appears at 4.81 ppm and integrates for two protons. This resonance corresponds to the methylene group of the TCE moiety. As this methylene group has no vicinal protons available for coupling, it appears as a singlet. Its relatively downfield position reflects the strong electron-withdrawing effect of both the -SO_3 group and the -CCl_3 substituent. And a singlet at 2.84 ppm integrating for three protons is assigned to the terminal methyl group of the imidazole ring.

Imidazolium salt **33** was then prepared by methylation of **32** with methyl triflate. During the synthesis of imidazolium salt **33**, the reaction was conducted under a nitrogen atmosphere using anhydrous diethyl ether. The reaction was maintained at 0 °C throughout, since an increase in temperature markedly enhanced the solubility of imidazolium salt **33** in diethyl ether. This prevented the use of product precipitation to drive the reaction forward and hindered efficient isolation of imidazolium salt **33**, ultimately leading to diminished yields. After the initial filtration, the combined mother liquor was stored at -20 °C to induce further precipitation of imidazolium salt **33**. The precipitated solid was then collected by a second filtration bringing the total yield to 88%.

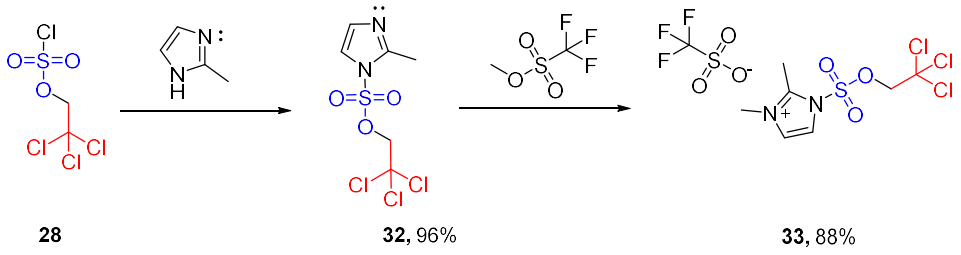

Scheme 14. The synthesis of 2,3-dimethyl-1-((2,2,2-trichloroethoxy)sulfonyl)-1H-imidazol-3-ium (**33**).[184]

The structure of imidazolium salt **33** was confirmed by ^{1}H NMR spectroscopy. Two doublets are observed at 8.20 and 7.94 ppm, each integrating for one proton. These signals are assigned to the two protons on the imidazolium ring, and in contrast to the

equivalent signals for **32** the downfield chemical shifts reflect the strong deshielding effect arising from the positively charged imidazolium ring.

As with **32** a singlet integrating for 2 protons and another integrating for 3 protons are found in the aliphatic region, albeit in both cases shifted downfield (5.52 ppm and 2.83 ppm respectively) by the influence of the imidazolium ring. In addition, a third singlet integrating for 3 protons arises from the newly installed *N*-methyl substituent at 3.86 ppm.

2.1.2 Synthesis and Characterisation of Aryl Sulfates Prepared with **33**

Subsequently, imidazolium **33** was employed for the sulfation of a range of aryl substrates in this study. This sulfation reaction proceeds via a classical nucleophilic substitution at the sulfur centre. During the reaction, the phenol acts as a nucleophile and attacks the sulfur centre of the sulfating reagent. Subsequently, 1,2-dimethylimidazole leaves and the S-O bond is formed, ultimately affording the desired aryl sulfate diester. The resulting TCE-protected sulfate diesters exhibit excellent stability under both acidic and mildly basic conditions, thereby providing favourable properties for subsequent transformations and purification steps.

Figure 20. Yields of sulfate diester formation via imidazolium **33**.

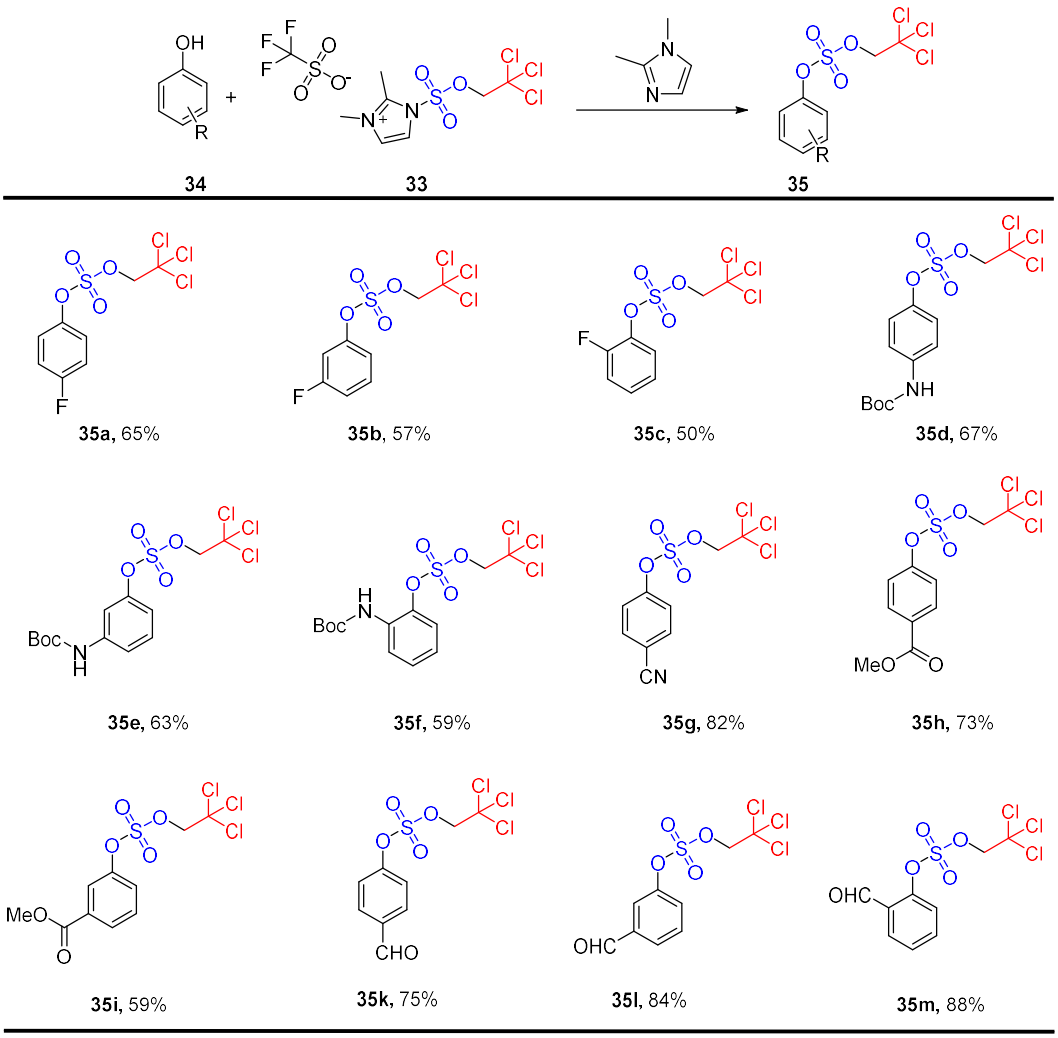

2.1.2.1 Synthesis of Fluorine-substituted Sulfate **35a-35c**

After establishing the synthetic methodology, fluorophenols were chosen as the initial substrates to explore the preparation of the corresponding aryl sulfate diesters. As a first attempt, compound **35a** was synthesized from 4-fluorophenol under the conditions reported by Taylor's team in 2009.[184]

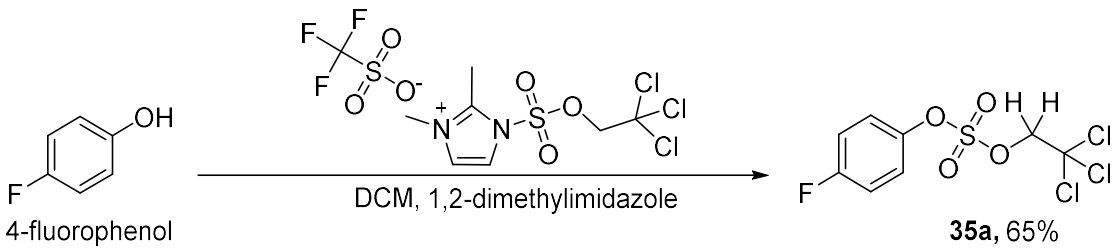

Scheme 15. The synthesis of **35a**.

4-Fluorophenol was combined with imidazolium salt **33** and 1,2-dimethylimidazole in an ice bath, then the mixture was allowed to warm to room temperature. After 1 hour, the reaction progress was monitored by TLC. The TLC analysis revealed that only a small amount of product had formed. In accordance with the reported literature procedure, the reaction was therefore allowed to proceed at room temperature for an additional 23 hours under continuous stirring.[184]

After 23 hours, TLC analysis showed progression, although starting material remained. This observation was consistent the literature report.[184] The reaction was therefore quenched and subjected to standard work-up procedures. TLC analysis of the organic extracts revealed four distinct spots, corresponding to the starting material, the desired product, and two unidentified minor impurities. The combined organic layers were concentrated under reduced pressure to afford a crude oil, which was subsequently purified by flash column chromatography using the unusual DCM/hexane (1:1) as the eluent. This afforded the target compound in 65% isolated yield. Notably, this relatively non-polar solvent system proved essential for effective separation. Increasing the polarity of the eluent led to significant co-elution of the product with impurities, whereas the DCM/hexane (1:1) mixture provided sufficient resolution of these very non-polar components.

The structure of compound **35a** was confirmed by ^{1}H and ^{13}C NMR spectroscopy. The ^{1}H NMR spectrum shows two multiplets at 7.38-7.31 ppm and 7.17-7.10 ppm, together accounting for four protons, which is consistent with a *para*-disubstituted benzene ring.

Due to the influence of the adjacent aromatic H's *ortho*-coupling and the *meta*-coupling with F, these two peak regions do not present the regular doublets pattern but appear in the form of multiplets. In addition, a singlet at 4.83 ppm is attributed to the methylene (-CH_2) group linking a -CCl_3 substituent. The relatively downfield chemical shift is consistent with the strong electron-withdrawing effect of the -CCl_3 group. The absence of observable splitting for this methylene signal suggests that it is not significantly coupled to adjacent protons.

This ^{13}C NMR spectrum further confirms the presence of compound **35a**, as evidenced by characteristic carbon-fluorine coupling patterns. In the ^{13}C NMR spectrum, two closely spaced signals are observed at 162.2 ppm and 160.6 ppm. These peaks arise from the carbon directly bonded to fluorine. The large one-bond coupling constant (^1J(C-F) = 241.6 Hz) is characteristic of a direct C-F bond in an aromatic system and is consistent with literature values for aryl fluorides.[186] A doublet is observed at 145.9 ppm, also resulting from carbon-fluorine coupling. This signal is assigned to the ipso quaternary carbon influenced by the strong inductive and resonance effects of the fluorine substituent.

Two additional doublets appear at 123.0 ppm and 117.0 ppm, each corresponding to two carbons, which are assigned to CH-2/6 and CH-3/5, respectively. These correspond to the four aromatic CH carbons of the *para*-disubstituted benzene ring. The observed splitting reflects long-range C-F coupling within the aromatic system. The coupling constant of these doublets are 9.1 and 24.2 Hz, respectively. These values are consistent with the long-range C-F coupling within the aromatic system, typically arising from two- or three-bond interactions.

A singlet at 80.5 ppm is assigned to the methylene carbon of the TCE group. Analysis of the HSQC spectrum shows that this ^{13}C NMR signal correlates with the proton resonance observed at 4.83 ppm in the ^1H NMR spectrum. The cross-peak in the HSQC spectrum provides clear evidence for the assignment of this carbon resonance to the -

O-CH_2- group, consistent with its expected chemical shift and structural environment.[184] Additionally, a singlet at 92.4 ppm corresponds to the quaternary carbon of the -CCl_3 group. The absence of splitting for these aliphatic carbons is consistent with their lack of direct coupling to fluorine.

Following the same procedure, compounds **35b** and **35c** were synthesized and purified, affording isolated yields of 57% and 50%, respectively. The structure of **35b** and **35c** were confirmed by ^{1}H NMR and ^{13}C NMR spectroscopy.

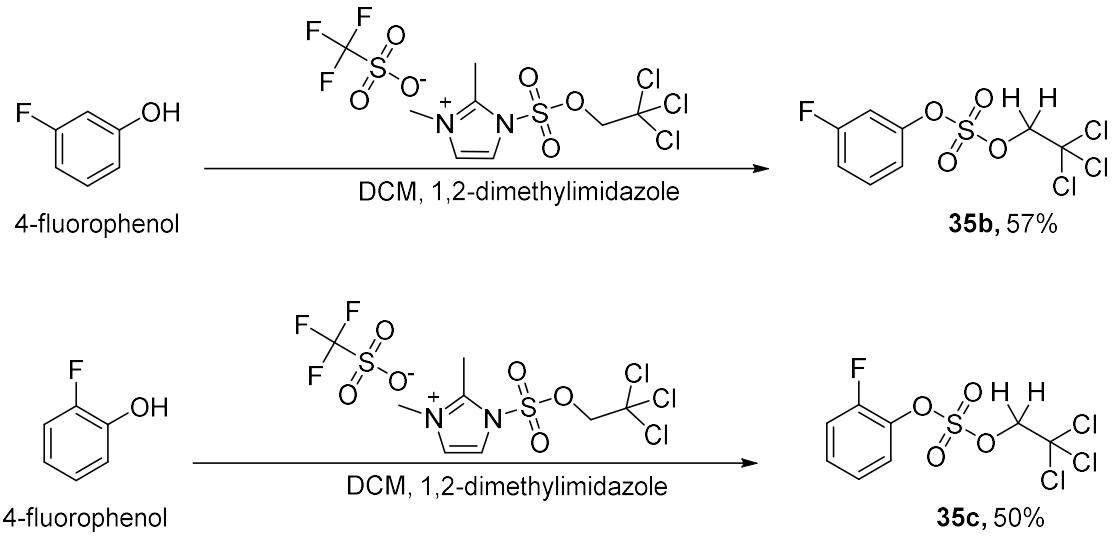

Scheme 16. The synthesis of **35b** and **35c**.

The ^{1}H NMR spectrum of **35b** displays four distinct aromatic resonances between 7.5 and 7.0 ppm, each integrating to one proton, consistent with a *meta*-substituted fluorophenyl system. The signals appear as a triplet of doublets at 7.42 ppm, a doublet of doublet of triplets at 7.18 ppm, a triplet of doublets at 7.10 ppm, and a doublet of doublet of triplets at 7.08 ppm. These splitting patterns arises from the effects of aromatic ^{1}H-^{1}H coupling. A singlet at 4.86 ppm integrating to two protons is characteristic of the methylene group of the TCE protecting group and serves as a clear diagnostic signal for the TCE group.

The ^{13}C NMR spectrum of **35b** provides further structural confirmation. Two closely spaced resonances at 163.8 and 162.1 ppm are assigned to the ipso carbon directly

bonded to fluorine. The coupling constant of 250.6 Hz, which is fully consistent with the magnitude expected for one-bond C-F coupling (^{1}J(C-F)). A signal at 150.6 ppm appears as a doublet arising from ^{3}J(C-F) coupling and is attributed to the carbon bearing -SO_4. The coupling constant of this doublet is 10.6 Hz. This value is consistent with long-range C-F coupling, such as ^{3}J(C-F) or ^{4}J(C-F), rather than one-bond coupling.

There are four signals observed in the aromatic region at 131.1, 117.0,115.3, 109.6 ppm, each corresponding to an aromatic CH carbon of the phenyl ring, and assigned to the meta position of the F-substituted carbon, the ortho position of the SO_4-substituted carbon, the positions ortho to both the F- and SO_4-substituted carbons, and the ortho position of the F-substituted carbon, respectively.. They appear as a doublet due to coupling with fluorine, reflecting the extended influence of the C-F bond across the ring. The coupling constants of these doublets are 9.1, 3.0, 21.1, and 25.7 Hz, respectively, which are consistent with two-bond, three-bond and four-bond C-F coupling interactions. In the aliphatic region, a singlet at 92.4 ppm is assigned to the -CCl_3 of the TCE group, while a singlet at 80.7 ppm corresponds to the methylene carbon of TCE attached to oxygen. Their patterns are not influenced by C-F coupling.

A similar pattern can also be observed in both the ^{1}H NMR and ^{13}C NMR spectra of compound **35c**. The ^{1}H NMR spectrum displays two sets of signals, corresponding to the four aromatic protons and the two protons of the TCE protecting group. In the aromatic region, one doublet of doublet of doublets, one doublet of doublet of doublet of doublets, and one multiplet are observed at 7.49, 7.35, and 7.28-7.19 ppm, respectively. The first two signals each integrate to one proton, while the final multiplet integrates to two protons. The downfield displacement of the proton located closest to the sulfate-bearing carbon reflects the pronounced deshielding effect exerted by the -OSO_3- group. The pronounced inductive effect of the sulfate group decreases the electron density of nearby aromatic protons, leading to deshielding and a corresponding shift to lower field. Consistent with **35a** and **35b** the characteristic singlet at 4.92 ppm

corresponds to the methylene group of the protecting group.

In the ^{13}C NMR spectrum of **35c**, two closely spaced resonances are observed at 154.8 ppm and 153.2 ppm. These arise from one-bond C-F coupling at the ipso carbon directly bonded to fluorine. The coupling constant is 252.2 Hz, which is characteristic of a large one-bond C-F coupling (^1J(C-F)). A doublet is observed at 137.4 ppm and is assigned to the aromatic carbon bonded to oxygen. This signal is split by long-range coupling with the fluorine atom (^2J(C-F)), with the coupling constant of 12.1 Hz. In addition, the strong electron-withdrawing effect of the -SO_3 group causes deshielding of this carbon, shifting it downfield relative to the other aromatic carbons.

In the aromatic region, four additional carbon signals are observed, three of them appearing as doublets due to long-range C-F coupling. These four resonances are located at 129.4 ppm, 125.3 ppm, 124.1 ppm, and 117.6 ppm. The coupling constants of these three doublets are 6.0 Hz, 4.5 Hz, and 18.1 Hz, respectively. These four resonances are assigned to the aromatic carbons *ortho*, *meta*, and *para* to the fluorine-bearing carbon, as well as the carbon *ortho* to the sulfate-bearing carbon.

Consistent with **35a** and **35b**, there is one singlet and one doublet observed in the aliphatic region. The resonances at 92.4 and 80.7 are assigned to the -CCl_3 carbon and the -CH_2 carbon of TCE. Their presence confirms the successful introduction of the TCE protecting group.

The structures of these compounds were further confirmed by ESI-HRMS analysis. The O-CH_2 bond appears to be relatively labile and prone to fragmentation during ionization, leading to cleavage of the TCE moiety prior to detection of the intact molecular ion. Consequently, instead of a clear $[M-H]^-$ signal, the spectra are dominated by fragment ions resulting from the loss of the TCE group. In the spectrum of the F-substituted sulfate diesters **35a**-**35c**, for which no distinct molecular ion peak corresponding to the intact TCE-protected species could be detected. This observation is consistent with the

susceptibility of the TCE-protected sulfate linkage to fragmentation under mass spectrometric conditions.

In the HRMS spectrum of **35a**, a single prominent ion at *m/z* 190.9811 was detected. This value closely matches the calculated mass for the molecule losing the TCE group, $[M\text{-}TCE]^-$. Notably, no ion corresponding to the TCE-protected precursor was observed, which are consistent with the formation of the deprotected sulfate species under the ionisation conditions. Similar to the peak pattern observed for 35a, the most intense peaks for **35b** and **35c** appear at m/z 190.9811 and 190.9812, respectively. This is consistent with the expected m/z value for $[M\text{-}TCE]^-$ of **35b** and **35c**.

In principle, the TCE-protected sulfate diesters contain three chlorine atoms. Therefore, their HRMS spectra would be expected to display a characteristic chlorine isotope cluster, comprising a series of peaks separated by 2 mass units (M, M+2, M+4, M+6), arising from the natural isotopic distribution of ^{35}Cl and ^{37}Cl. However, in the HRMS spectrum of the **35a**, no such isotope cluster was observed. For the *meta*-substituted derivative **35b**, only a single ion at *m/z* 325.1837 was detected, while the *ortho*-substituted analogue **35c** similarly exhibited only one peak at *m/z* 325.1839. In these cases, the absence of the expected multi-peak chlorine isotopic pattern suggests that the detected ions do not correspond to the intact trichloroethyl-protected species. Instead, the data indicate that fragmentation or deprotection of the TCE moiety likely occurred under the ionisation conditions, resulting in species that no longer contain the three chlorine atoms. Additionally, no detectable signal was observed in the HRMS under positive ion mode.

2.1.2.2 Synthesis of Boc-protected Amino-substituted Sulfate **35d**-**35f**

Direct sulfation of unprotected aminophenols may lead to competitive reactions at both the nitrogen and oxygen terminals.[184] This lack of chemo-selectivity could significantly complicate the reaction system, making purification more difficult and ultimately

reducing the yield of the desired *O*-sulfated product. Commercially produced *N*-Boc 3-aminophenol (**34e**) was available in our laboratory. Supplementing this, prior to the sulfation reaction, the 2- and 4-aminophenol were subjected to Boc protection. 2-Aminophenol and 4-aminophenol were reacted with di-tert-butyl dicarbonate (Boc_2O) to afford the corresponding *N*-Boc-protected phenols, **34d** and **34f**, respectively.

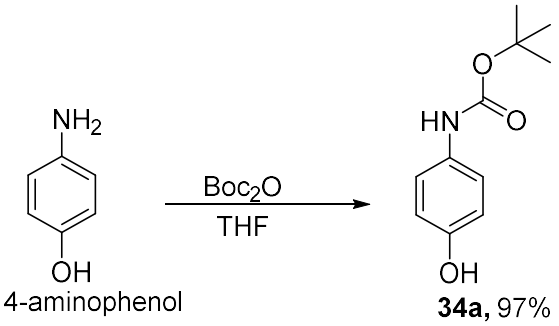

Scheme 17. The Boc protection of 4-aminophenol.[187]

The synthesis of **34a** began with the combination of Boc_2O and 4-aminophenol in an ice bath. Following the literature procedure, the mixture was maintained at 0 °C for 12 hours, allowing the protection step to proceed steadily under these cold conditions.[187] After this period, TLC analysis indicated that the starting material had been completely consumed, and only the desired product was detected. The remaining THF was removed under reduced pressure, leaving behind a brown solid as the crude product.

Following the reported protocol, the crude material was first dissolved in DCM in preparation for extraction.[187] However, this step revealed an unexpected challenge, as the crude product showed very poor solubility in DCM, which made the extraction process inefficient and more difficult to handle. Recognizing this limitation, a second attempt was made using ethyl acetate instead. This adjustment proved effective allowing workup by liquid-liquid extraction to proceed smoothly. Ultimately, the product **34a** was obtained in an excellent 97% yield.

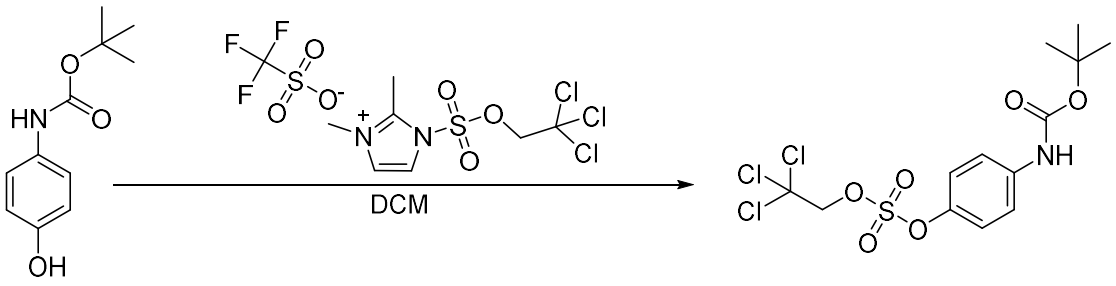

34a **35d**, 67%

Scheme 18. The synthesis of **35d**.

Subsequently, compound **34a** was subjected to the sulfation reaction, which followed the same procedure used for synthesis of **35a**. After 24 hours, TLC analysis showed the formation of product, while the unreacted starting material was still present. Then, the mixture was concentrated under reduced pressure, and a crude oil was obtained. In the first attempt to purify the crude oil by column chromatography, significant difficulties were encountered. Owing to the amide functionality of the target compound, pronounced tailing was observed on the TLC plate, which made it difficult to clearly assess the separation of the product. In addition, the compound proved to be unstable on silica gel. The slightly acidic nature of the silica surface led to gradual decomposition of the product during column chromatography, preventing successful isolation of the desired compound.

To address these issues, a second purification strategy was employed. Instead of flash column chromatography, preparative TLC using DCM/hexane/Et_3N (1:1:0.5, v/v) was used to minimize the compound's exposure to silica under prolonged acidic conditions. This approach significantly improved the outcome. The target compound was successfully isolated in 67% yield, demonstrating that preparative TLC was a more suitable purification method for this amide-containing substrate.

The structure of **35d** was well supported by the ^1H NMR spectrum. In the aromatic region, one doublet and one triplet of doublets are observed at 7.43 and 7.28 ppm, each

integrating for two protons and displaying coupling constants of 8.9 Hz and 9.1, 5.6 Hz. This pattern is consistent with a *para*-disubstituted benzene ring. A broad singlet at 6.54 ppm corresponds to the Boc-protected NH proton, appearing in the expected region for a carbamate N-H.[187] A sharp singlet at 4.80 ppm integrates to two protons and is assigned to the methylene group of the TCE moiety. The downfield position of this signal reflects the strong electron-withdrawing effect of the adjacent the $-CCl_3$ group. Finally, a prominent singlet at 1.52 ppm integrates to nine protons and corresponds to the *tert-butyl* protons.[187]

The structure of **35d** was further confirmed by the Attached Proton Test (APT) experiment, which contained thirteen signals. Four aromatic methine carbons and three methyl carbons are observed in the positive phase, while five quaternary carbons and one methylene carbon appear in the negative phase. According to the HSQC spectrum, which shows one-bond correlations between ^{1}H and directly attached ^{13}C nuclei, these resonances can be correlated with their corresponding protons and are consistent with the proposed structure of **35d**. In the downfield region, three carbon signals are observed at 152.6, 145.2, and 138.2 ppm, corresponding to the carbons connected with the carbonyl group, the amide moiety, and the $-SO_4$ group, respectively. Because all these carbons are attached to strongly electron-withdrawing substituents, they experience significant deshielding, resulting in their resonances appearing at lower field. In the aromatic region, two carbon signals appear at 121.9 and 119.7 ppm, which are assigned to the two carbons closer to the SO_4-substituted carbon and the two carbons adjacent to the F-substituted carbon, respectively. In the aliphatic region, a singlet at 92.5 ppm and another singlet at 80.3 ppm are assigned to the $-CCl_3$ and $-CH_2$ carbons of the TCE group, respectively. The presence of these characteristic signals provides clear evidence for the incorporation of the protecting group. In addition, a singlet at 28.4 ppm is observed, which is characteristic of the *tert*-butyl carbon atoms of the Boc group.

Using the same procedure described above, 2-aminophenol was reacted with *di-tert-butyl* dicarbonate (Boc_2O) to afford the Boc-protected compound **34b** in 95% yield. Subsequently, the *tert-butyl* (3-hydroxyphenyl)carbamate available in the laboratory and compound **34b** were each employed as substrates for the sulfation reaction with reagent **33**. After purification by preparative TLC, the corresponding products **35e** and **35f** were obtained in 63% and 59% yields, respectively.

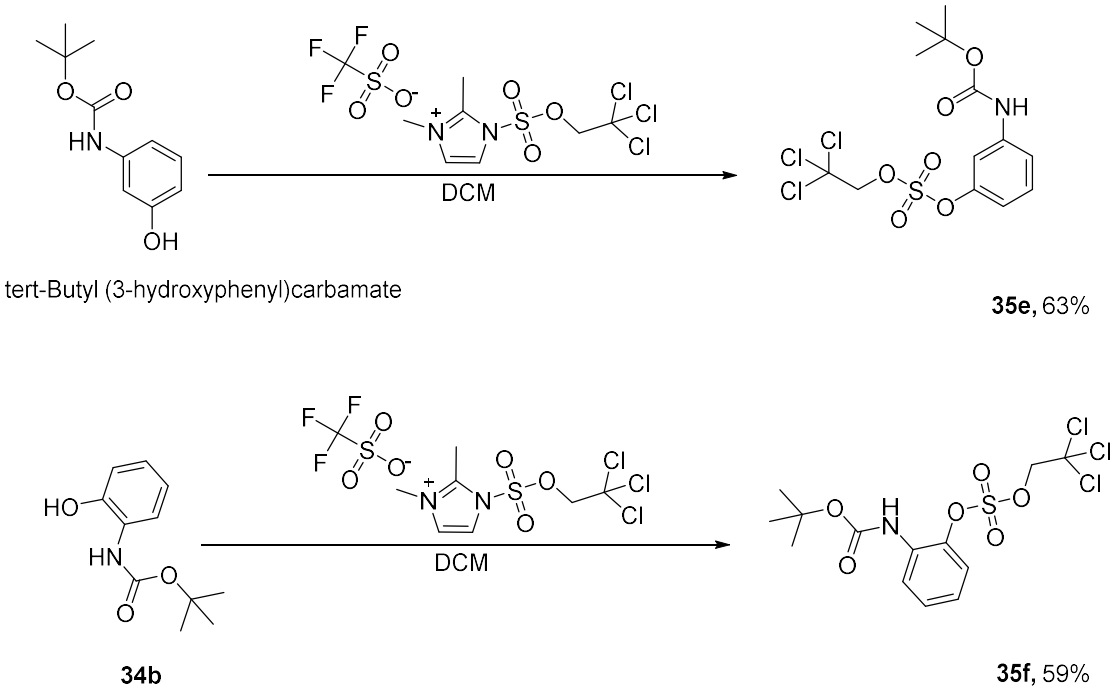

Scheme 19. The synthesis of **35e** and **35f**.

The structures of **35e** and **35f** were confirmed by ^{1}H NMR and ^{13}C NMR spectroscopy. In the ^{1}H NMR spectrum of **35e,** a singlet at 1.49 ppm integrating to nine protons corresponds to the *tert-butyl* group of the Boc protecting group. A singlet at 4.81 ppm integrating to two protons is the characteristic signal of TCE group. Four aromatic CH protons are observed at 7.60, 7.28, 7.17, and 6.98 ppm, they are singlet, triplet, doublet, and doublets of doublet respectively. Their patterns are caused by ^{1}H-^{1}H coupling. A downfield broad signal at 6.87 ppm is attributed to the carbamate NH proton.

According to HSQC, the ^{13}C NMR and APT spectrum of **35e** are consistent with the ^{1}H

NMR spectrum of **35e**. The signal at 152.5 ppm, together with the signals at 80.5 ppm and 28.3 ppm, are assigned to the carbons of the Boc protecting group. Due to the nature of the carbonyl carbon and the quaternary carbon of the *tert-butyl* group, both of them appear in the negative phase in the APT spectrum. Together, these signals constitute the characteristic resonances of the Boc group.

The signals at 150.5 ppm and 140.4 ppm are assigned to the aromatic carbons bonded to the sulfate group and the amide moiety, respectively. These carbons appear in the negative phase in the APT spectrum, since they are quaternary carbons. The four aromatic CH carbon resonances at 130.3, 117.5, 115.1, and 111.4 ppm, which are assigned to the meta position relative to the SO_4-substituted carbon, the ortho position relative to the SO_4-substituted carbon, the ortho position relative to the *N*-Boc-substituted carbon, and the position ortho to both the SO_4- and *N*-Boc-substituted carbons, respectively. In contrast, these four signals appear in the positive phase in the APT spectrum. The two singlets at 92.5 ppm and 81.3 ppm are assigned to the -CCl_3 and methylene carbons of the TCE group, respectively. The former is a quaternary carbon, and the latter is a methylene carbon, so both appears in the negative phase in the APT spectrum. Together, these signals provide clear evidence for the presence of the TCE moiety. Finally, the signals at 80.5 and 28.3 ppm are assigned to the quaternary carbon and the methyl carbons of the *tert-butyl* group, respectively.

The ^{1}H NMR spectrum of **35f** displays an expected aromatic pattern, consistent with a 1,2-disubstituted benzene ring. Four distinct aromatic resonances are observed between at 8.17, 7.40, 7.31, and 7.07 ppm, each integrating for one proton. These signals appear as a doublet, doublet of doublets, doublet of doublet of doublet of doublets, and doublet of doublet of doublets, respectively. They correspond to the proton *ortho* to the amide-substituted carbon, the proton *ortho* to the -SO_4-substituted group, the proton *meta* to the amide-substituted carbon, and the proton *para* to the amide-substituted carbon, respectively. The resonances corresponding to the TCE and Boc protecting groups

remain unchanged relative to **35d** and **35e**, appearing as singlets at 4.80 ppm (2H) and 1.53 ppm (9H), respectively.

The ^{13}C spectrum of **35f** exhibits the expected number of carbon resonances, consistent with the ^{1}H NMR spectrum. The diagnostic signals corresponding to the carbonyl carbon (152.4 ppm), the TCE methylene carbon (80.9 ppm), and the *tert-butyl* carbon (28.4 ppm) are observed at positions comparable to those in **35d** and **35e**. Four signals of aromatic carbons appear at 128.7, 123.5, 121.5, and 121.4 ppm, which correspond to the carbon *meta* to the amide-substituted carbon, the carbon *para* to the amide-substituted carbon, the carbon *ortho* to the -SO_4-substituted carbon, and the carbon *ortho* to the amide-substituted carbon, respectively.

The structures of the *N*-Boc-substituted sulfates were further supported by ESI-HRMS analysis. The HRMS spectrum shows peaks at *m/z* 417.9704, 417.9700, and 417.9786, which can be assigned to the $[M-O]^-$ fragment ion. These observed values are in good agreement with the calculated *m/z* value of 417.9683, supporting the proposed molecular composition of the compound.

The distinct fragmentation behaviour can be attributed to the influence of the Boc carbamate on the gas-phase ionisation and fragmentation pathways under ESI conditions. The Boc-NH- moiety is a strongly electron-withdrawing carbamate functionality due to the presence of the carbonyl group, while the nitrogen atom can also participate in conjugation with the aromatic ring. When introduced into the ESI source, the sulfate diester is overall neutral and does not readily form a stable deprotonated molecular ion. However, the polar Boc carbonyl group facilitates charge localisation within the aromatic-NHBoc framework. In the para- and ortho-substituted derivatives, this charge distribution appears to favour cleavage of the Ar-O bond, resulting in loss of the entire 2,2,2-trichloroethyl sulfate moiety and formation of the $[M-SO_4TCE]^-$ fragment as the predominant ion. The detection of $[M-H]^-$ for the meta isomer suggests that subtle differences in electronic distribution associated with the

substitution position can influence the stability of the intact deprotonated species relative to in-source fragmentation.

The *N*-Boc meta- and para-substituted sulfate diesters were successfully analysed by ESI+ HRMS. In the spectrum of **35e**, two well-defined isotope clusters were first observed at *m/z* 441.9704 / 443.9675 / 445.9644 and *m/z* 457.9445 / 459.9417 / 461.9387. The former set is fully consistent with the sodium adduct $[M+Na]^+$ (calculated for $[M+Na]^+$ = 441.9656). The approximately 2 Da spacing within the isotope cluster matches the expected chlorine isotopic distribution arising from the presence of three chlorine atoms (M, M+2, M+4, M+6). The latter set corresponds to the potassium adduct $[M+K]^+$ (calcd for $[M+K]^+$ = 457.9395), which likewise exhibits the characteristic chlorine isotope pattern. Under positive ionisation conditions, **35e** preferentially forms Na^+ and K^+ adducts rather than a strong protonated molecular ion $[M+H]^+$, a behaviour commonly observed for sulfate-containing and highly polar functional groups.

Two additional intense isotope clusters were observed at *m/z* 363.9254 / 365.9226 / 367.9193 and *m/z* 319.9356 / 321.9327 / 323.9294. The first set is assigned to $[M+H - C_4H_8]^+$, corresponding to the loss of isobutene (56 Da) from the Boc group (calculated for $[M+H - C_4H_8]^+$ = 363.9211). As the fragment still contains chlorine atoms, the expected isotopic pattern remains evident. The second set is attributed to $[M+H - C_4H_8 - CO_2]^+$, resulting from subsequent loss of CO_2 (44 Da) (calculated for $[M+H - C_4H_8 - CO_2]^+$ = 319.9312). This two-step fragmentation sequence, involving an initial loss of 56 Da followed by a subsequent loss of 44 Da, represents the characteristic in-source cleavage pathway of Boc-protected compounds under ESI conditions.

The ESI+ HRMS spectrum of **35f** is highly similar to that of **35e**. Two well-defined isotope clusters are observed at *m/z* 441.9704 / 443.9675 / 445.9644 and *m/z* 457.9445 / 459.9417 / 461.9387, which are assigned to $[M+Na]^+$ and $[M+K]^+$, respectively. In addition, two intense isotope clusters appear in the central region of the spectrum at

m/z 363.9254 / 365.9226 / 367.9193 and *m/z* 319.9356 / 321.9327 / 323.9294. These peaks correspond to the characteristic in-source fragmentation of the Boc group. The former arises from the loss of isobutene, while the latter results from the subsequent loss of CO_2.

2.1.2.3 Synthesis of cyano-substituted sulfate **35g**

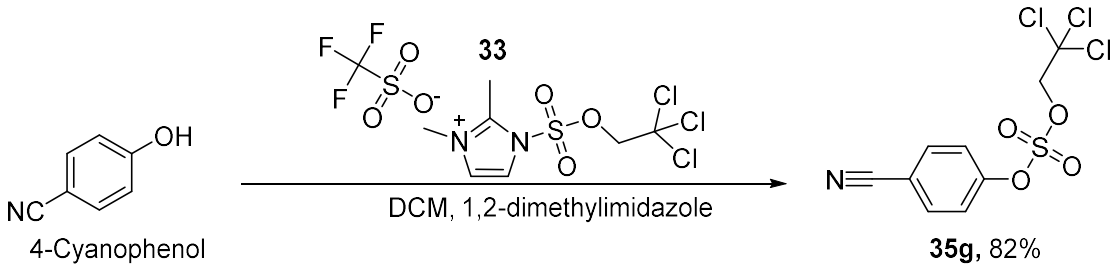

Scheme 20. The synthesis of **35g**.

Following the standard procedure, 4-cyanophenol was combined with **33** and dimethyl imidazole. Because **35g** does not contain the amide functional group, it remains amenable during purification on a silica gel column. Thus, the obtained mixture was purified by flash column chromatography using DCM/hexane (1:1) as the eluent to obtain the product in 82% yield.

The structure of sulfate **35g** was confirmed by ^{1}H NMR spectroscopy. As expected, the ^{1}H NMR spectrum displayed a *para*-disubstituted aromatic system. Two doublets were observed in the aromatic region at 7.77 and 7.50 ppm, each integrating to 2H. The coupling constants of them are 8.9 and 8.9 Hz, respectively. The more downfield signal corresponds to the two protons attached to the carbon atoms adjacent to the cyano group. Because the cyano group is strongly electron-withdrawing, it decreases the local electron density and causes these protons to become deshielded. A singlet at 4.87 ppm integrating to 2H corresponds to the methylene group of the TCE moiety. The downfield position of this methylene signal is consistent with deshielding effects from both the adjacent oxygen atom and the electron-withdrawing -CCl_3 group.

The structure of **35g** was further supported by ^{13}C NMR and APT spectroscopy. Nine aromatic resonances were observed, consistent with a *para*-disubstituted benzene ring. The signal at 152.8 ppm is assigned to the carbon bonded to the sulfate group, reflecting deshielding by the strongly electron-withdrawing sulfate functionality. In the APT spectrum, this quaternary carbon appears in the negative phase. The resonances at 134.5 and 122.2 ppm correspond to the aromatic CH carbons, while the signal at 117.4 ppm is attributed to the ipso carbon bearing the cyano substituent. The former two signals appear in the positive phase in the APT spectrum, whereas the latter one signal appears in the negative phase. The nitrile carbon appears at 112.3 ppm as a weak quaternary resonance, which appears in the negative phase in the APT spectrum. In the aliphatic region, signals at 92.2 and 80.8 ppm are assigned to the -CCl_3 and methylene carbons of the TCE group, respectively.[183]

In the HRMS spectrum of the para-cyano-substituted sulfate diester **35g**, a prominent deprotonated molecular ion was observed at *m/z* 327.9014, corresponding to $[M-H]^-$, which is in good agreement with the calculated value of 327.9005. Adjacent isotope peaks were also detected at m/z 329.8986 and 331.8955. The approximately 2 Da spacing and the relative intensity distribution of these peaks are consistent with the characteristic chlorine isotopic pattern arising from the presence of three chlorine atoms in the molecule (M, M+2, M+4, M+6).

2.1.2.4 Synthesis of Methyl Ester-substituted Sulfates **35h**-**35j**

Since methyl 4-hydroxybenzoate (**34c-1**) was not available in our laboratory, it was first synthesized from 4-hydroxybenzoic acid to serve as the substrate for the subsequent sulfation reaction.

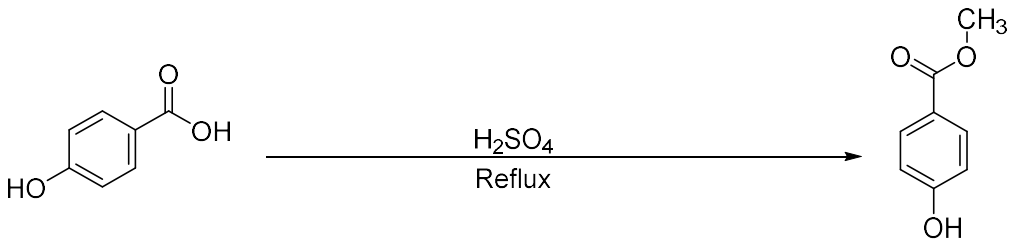

34c-1 **34c**, 95%

Scheme 21. The synthesis of **34c**.[188]

34c-1 was dissolved in methanol, and sulfuric acid was added. The reaction mixture was heated to 80 °C under reflux and stirred for 4 hours according to the reported procedure.[188] After 4 hours, TLC monitoring indicated that the reaction had not reached full conversion, as both starting material and product were still visible. This observation is consistent with the literature.[188] The residual acid was removed during aqueous workup producing the desired product in 95% yield which could be used without further purification.

The structure of **34c** was confirmed by ^{1}H NMR spectroscopy. The aromatic region displays one multiplet and one doublet at 7.96 and 6.86 ppm, each integrating for two protons (J = 8.8 Hz and 8.7 Hz). The more downfield signal is assigned to H-3/5, which are *ortho* to the electron-withdrawing ester carbonyl group, resulting in greater deshielding. In contrast, the signal at upfield corresponds to H-2/6, positioned *ortho* to the phenolic hydroxyl group, which donates electron density via resonance and therefore shifts these protons upfield.

A singlet at 3.89 ppm integrating for three protons is attributed to the methyl ester group. The absence of coupling confirms that these protons are not adjacent to any proton-bearing carbon. A broad singlet at 5.66 ppm corresponds to the phenolic hydroxyl proton, whose broadness is consistent with hydrogen bonding and rapid exchange processes in $CDCl_3$.

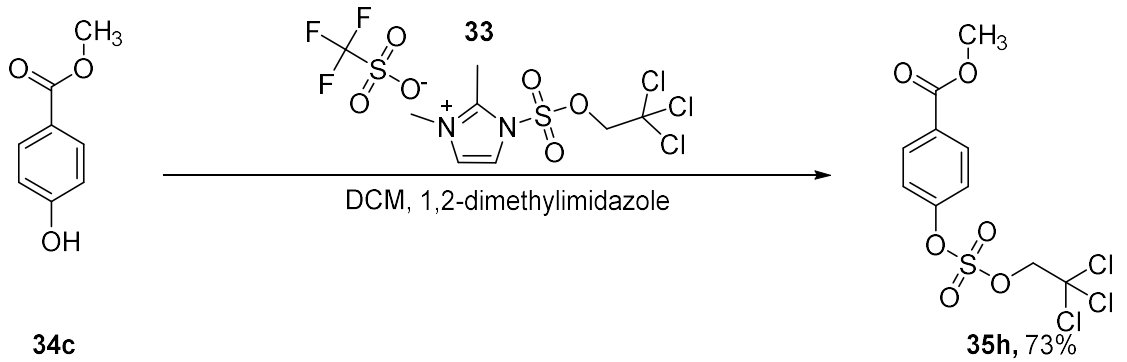

Scheme 22. The synthesis of **35h**.

Following the standard procedure, **34c** was combined with **33** and 1,2-dimethylimidazole. After reaction, the mixture was concentrated *in vacuo* to obtain a crude oil. Purification with flash column chromatography produced the desired product in 73% yield. It is worth noting that **35h** is amenable to column chromatography. Since it does not contain an amide functional group, **35h** is relatively stable on a silica gel column.

The structure of **35h** was confirmed by ^{1}H NMR spectroscopy. Two aromatic doublets are observed at approximately 8.11 ppm and 7.67 ppm, corresponding to the four symmetrical protons of a *para*-disubstituted benzene ring. The more downfield signal is attributed to the protons close to the electron-withdrawing ester group. A singlet at 5.42 ppm is assigned to the methylene group of the TCE moiety. The absence of splitting is consistent with the lack of vicinal protons on the adjacent -CCl_3 carbon. A singlet at 3.88 ppm corresponds to the methyl ester group (-$COOCH_3$). The integration ratio (2:2:2:3) matches the expected proton count, and no significant extraneous peaks are observed, supporting the successful formation and good purity of the target compound.

The structure of **35h** was further supported by ^{13}C NMR and APT spectroscopy. A resonance at 165.1 ppm is assigned to the ester carbonyl carbon (C=O). The aromatic carbon bonded to the sulfate group appears at 152.6 ppm, significantly deshielded due

to the strongly electron-withdrawing sulfonyl substituent, while the carbon attached to the ester group is observed at 129.4 ppm. Two signals at 131.6 and 121.9 ppm correspond to the aromatic CH carbons of the *para*-disubstituted benzene ring, consistent with the symmetry observed in the ^{1}H NMR spectrum. The TCE moiety is characterized by a signal at 92.8 ppm and a resonance at 80.3 ppm, which can be assigned to the -CCl_3 carbon and the methylene group, respectively. The methyl ester carbon appears at 52.5 ppm.

In the APT spectrum, the signals at 165.1, 152.6, 129.4, 92.8, and 80.3 ppm appear in the negative phase, indicating that they correspond to either quaternary carbons or methylene carbons. This is fully consistent with the assignments made from the ^{13}C NMR spectrum.

Methyl 3-hydroxybenzoate and methyl 2-hydroxybenzoate available in the laboratory, were subjected to the same synthetic procedure. Compound **35i** was successfully

obtained in an isolated yield of 59%, whereas the synthesis of **35j** was unsuccessful.

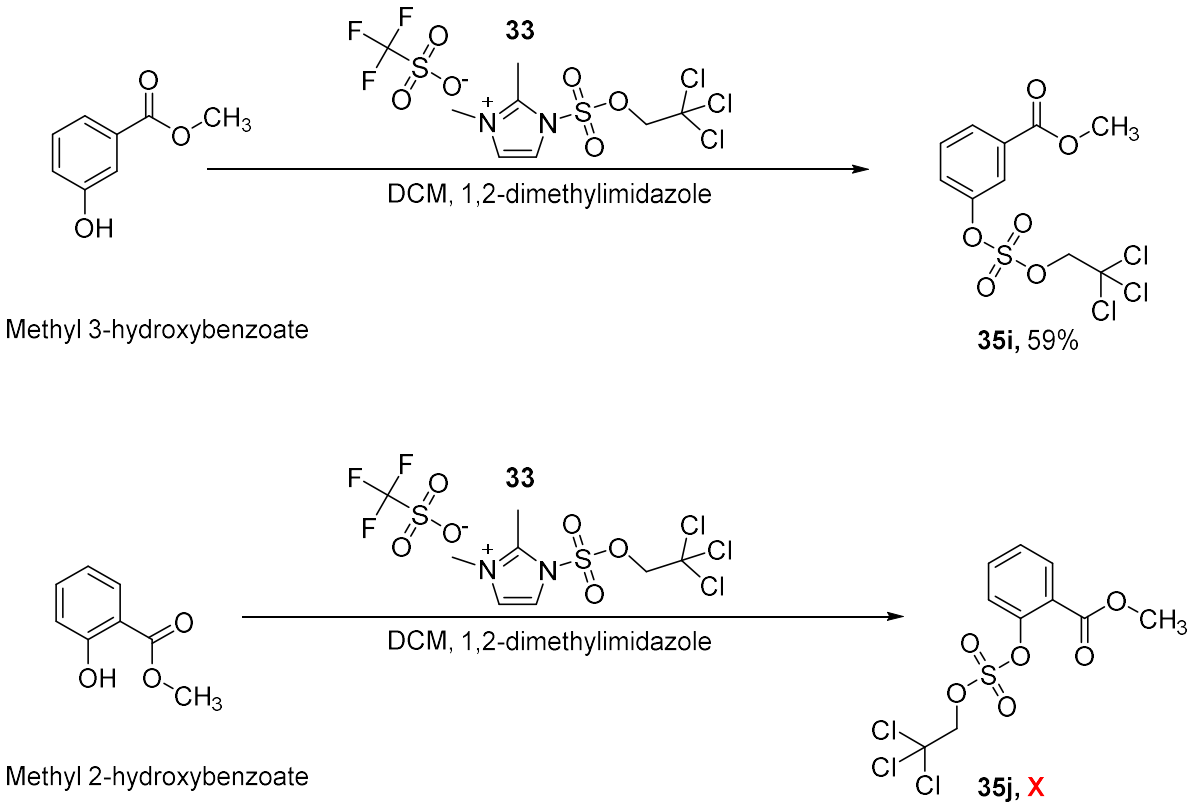

Scheme 23. The synthesis of **35i** and **35j**.

The structure of **35i** was confirmed by ^{1}H NMR, ^{13}C NMR and APT spectroscopy. In the ^{1}H NMR spectrum of **35i**, there are three sets of signals. In the aromatic region, a triplet of triplets appears at 8.04 ppm and a doublet of triplets at 7.57 ppm, and a triplet at 7.53 ppm. They are assigned to the aromatic protons of the *meta*-disubstituted benzene ring. A singlet at 4.86 ppm integrated to 2H is assigned to the methylene group of the TCE unit, significantly deshielded due to the strong electron-withdrawing effects of both the adjacent oxygen and the -CCl_3 group. The singlet at 3.94 ppm integrated to 3H, corresponding to the methyl ester group.

The ^{13}C NMR spectrum of **35i** shows several key characteristic resonances. The signal at 165.5 ppm is assigned to the carbonyl carbon, while the resonance at 52.7 ppm corresponds to the terminal methyl carbon of the methyl ester group (-CO_2CH_3).

Two singlets appear at 80.6 ppm and 92.4 ppm, which are attributed to the methylene carbon and the trichloromethyl carbon of the TCE moiety, respectively. In the aromatic region, six distinct resonances are observed. Two quaternary carbons appear at 150.1 ppm and 132.7 ppm. These signals are significantly deshielded due to the electron-withdrawing substituents -SO_4 and -C=O attached to them, leading to pronounced downfield shifts. The remaining four signals, corresponding to aromatic CH carbons, are observed at 130.4, 129.1, 125.8, 122.5 ppm, and they can be assigned to the aromatic carbons ortho to the -$COOCH_3$ substituent, meta to the -$COOCH_3$ substituent, the carbon ortho to both the -$COOCH_3$ and -SO_4 groups, and the carbon ortho to the -SO_4 group, respectively.

In the APT spectrum, the signals at 165.5, 150.1, 132.7, 92.4, and 80.6 ppm appear in the negative phase, indicating that they correspond to either quaternary carbons or methylene carbons. This is in full agreement with the assignments derived from the ^{1}H and ^{13}C NMR spectra, further confirming the correctness of the structure of **35i**.

Further structural confirmation was obtained by ESI-HRMS analysis. We begin with the para-substituted compound **35h**. In the ESI- HRMS spectrum of **35h**, no stable $[M-H]^-$ signal was observed. However, a peak was detected at *m/z* 230.9961, which can be assigned to the $[M-TCE]^-$ fragment ion. This value is in excellent agreement with the calculated mass of 230.9961. We attribute this phenomenon to the fact that the TCE moiety serves as an excellent leaving fragment under negative-ion conditions. Upon deprotonation, even if the $[M-H]^-$ ion is initially formed, the resulting anion strongly favours rearrangement and subsequent cleavage of the adjacent C-O or S-O bond within the sulfate or sulfonate linkage, leading to the loss of the TCE-related fragment. This process generates a more stable anionic species, corresponding to the observed $[M-TCE]^-$ ion. The peak corresponding to $[M-TCE]^-$ was likewise observed in the HRMS spectrum of the meta-substituted compound **35i**. Similar to its para-substituted analogue, no detectable $[M-H]^-$ signal was found in the

HRMS spectrum of **35i**.

Additionally, there is no usable signals were observed in the positive-ion mode HRMS of **35h** and **35i**. This may be attributed to the low tendency of these compounds to undergo protonation, as they do not contain strongly basic sites capable of readily accepting a proton to form the $[M+H]^+$ ion.

2.2.1.5 Synthesis of Aldehyde-Substituted Sulfate Diesters **35k-35m**

In our investigation of the synthesis of aldehyde-substituted sulfate diesters, 4-hydroxybenzaldehyde was employed as the starting material to synthesize the *para*-CHO-substituted sulfate diester. The phenolic hydroxyl group served as the reactive site for sulfation, enabling the introduction of the sulfate moiety.

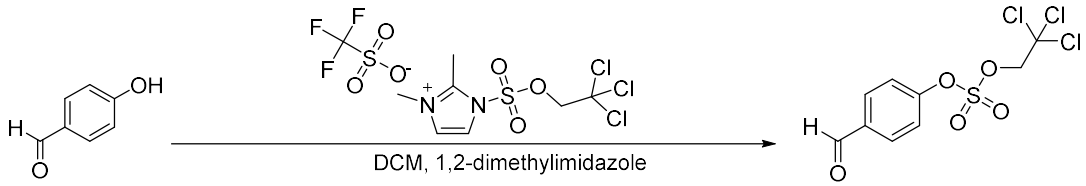

4-hydroxybenzaldehyde

35k, 75%

Scheme 24. The synthesis of **35k**.

Following the standard procedure, 4-hydroxybenzaldehyde was combined with imidazolium salt **33** and 1,2-dimethylimidazole in an ice bath. After reaction, the reaction mixture was concentrated under reduced pressure to obtain the crude oil. The crude product was purified by flash column chromatography using DCM/hexane (1:1) as the eluent, yielding the target compound in 75% isolated yield.

The structure of the **35k** was confirmed by ^{1}H NMR spectroscopy. A singlet at 10.03 ppm is attributed to the aldehydic proton, appearing significantly downfield due to the strong electron-withdrawing effect of the carbonyl group. In the aromatic region, two doublets appear at 7.99 and 7.54 ppm, each integrating for two protons, consistent with

a *para*-disubstituted benzene ring. The more downfield signal at 7.99 ppm corresponds to the aromatic protons located to the carbon close to the aldehyde group. The aldehyde group is electron-withdrawing, which reduce electron density of the adjacent and opposite aromatic protons. A singlet at 4.87 ppm integrating for two protons is a characteristic peak of the methylene group of the TCE unit. The downfield position of this methylene resonance is consistent with the strong inductive electron-withdrawing effects of both the adjacent oxygen atom and the -CCl_3 group.

The structure of the **35k** was further confirmed by ^{13}C NMR and APT spectroscopy. The resonance at 190.4 ppm corresponds to the aldehyde carbonyl carbon. The aromatic region shows four signals consistent with a para-disubstituted benzene ring, including two quaternary carbons at 154.1 ppm for the carbon bearing the sulfate ester and 135.6 ppm for the carbon bearing the formyl substituent, together with two signals of aromatic CH carbons at 131.8 and 121.8 ppm. They are assigned to two sets of carbon atoms located adjacent the -CHO and -SO_4 groups, respectively. The TCE protecting group is supported by signals at 92.3 ppm for the -CCl_3 carbon and 80.8 ppm for the -CH_2 carbon.

In the APT spectrum, the signals at 190.4, 154.1, 135.6, 92.3, and 80.8 ppm appear in the negative phase. The resonances at 190.4, 154.1, 135.6 and 92.3 ppm are assigned to quaternary carbons, while the signal at 80.8 ppm corresponds to a methylene carbon. These assignments are consistent with the ^{1}H and ^{13}C NMR data, further confirming the structural correctness of **35k**.

3-Hydroxybenzaldehyde and 2-hydroxybenzaldehyde available in the laboratory were subjected to the same synthetic protocol to afford the corresponding sulfate diesters, **35l** and **35m**. Under identical reaction and purification conditions, the desired products were obtained in isolated yields of 84% and 88%, respectively.

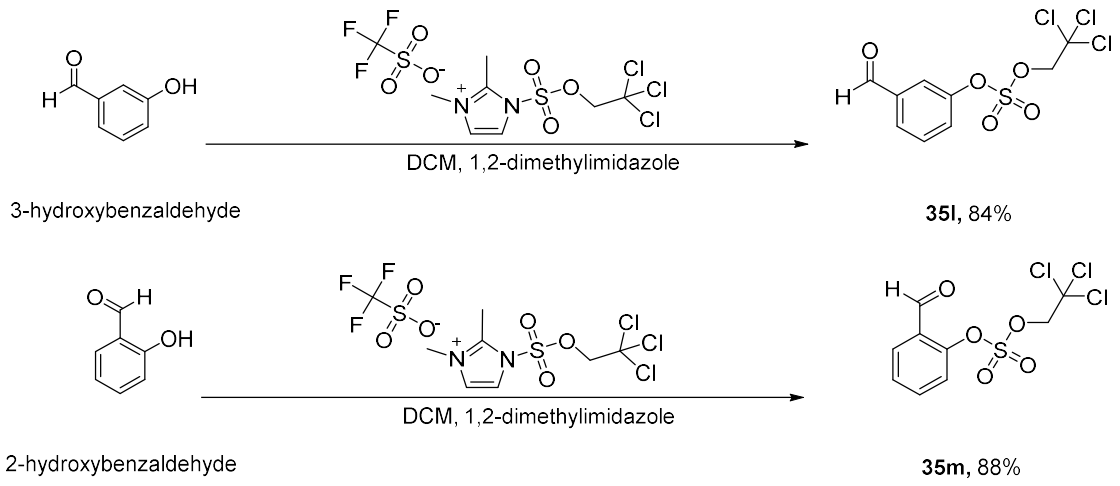

Scheme 25. The synthesis of **35l** and **35m**.

Like the ^{1}H NMR spectrum of **35k**, the spectra of **35l** and **35m** also display four distinct sets of signals. The most downfield resonance is assigned to the aldehydic proton, which is significantly deshielded due to the strong electron-withdrawing effect of the carbonyl group (-C=O). The signals in the aromatic region correspond to the four protons on the benzene ring. Owing to the different substitution patterns, slight variations in chemical shift are observed among these aromatic protons. A singlet appearing in the region of 5.0-4.5 ppm is attributed to the methylene group of the TCE moiety. This resonance serves as a characteristic signal for the presence of the TCE protecting group.

The ^{13}C NMR and APT spectra of **35k**, **35l**, and **35m** also exhibit a high degree of consistency. In the downfield region, three signals are sequentially assigned to the carbonyl carbon (-C=O), the aromatic carbon bonded to the sulfate group, and the aromatic carbon attached to the aldehyde substituent. These three carbons are all quaternary in nature and appear in the opposite phase in the APT spectrum. The remaining signals in the aromatic region correspond to the benzene ring carbons bearing protons. Depending on the substitution pattern on the ring, slight variations in chemical shift and in the number of resonances are observed. The signals at approximately 92 ppm and 80 ppm are assigned to the -CCl_3 carbon and the

methylene carbon of the TCE group, respectively. These two resonances serve as characteristic signals confirming the presence of the TCE protecting group.

The HRMS spectrum of the meta-formyl-substituted sulfate diester **35l** was subsequently examined. In the ESI+ spectrum of **35l**, a characteristic isotope cluster was observed at *m/z* 332.9189, 334.9159, 336.9128, and 338.3454. These peaks are separated by 2 Da and display the typical intensity distribution expected for a molecule containing three chlorine atoms (M, M+2, M+4, and M+6). This isotopic pattern is fully consistent with the presence of the TCE protecting group and supports the assigned molecular structure.

In addition to the molecular ion cluster, a fragment ion at *m/z* 296.9418 (accompanied by its corresponding M+2 isotopic peak at 298.9392) was detected. The 2 Da spacing indicates that chlorine atoms are still present in this fragment. This signal is tentatively assigned to $[M+H-Cl\cdot]^+$, arising from the loss of one chlorine atom during ionisation. Such fragmentation suggests partial cleavage of a C-Cl bond within the TCE moiety under the applied MS conditions.

Unfortunately, no usable signals for compounds **35k** and **35m** were detected in either positive- or negative-ion HRMS. This observation suggests that the ionisation behaviour of this class of compounds is highly sensitive to the substitution pattern. We speculate that in **35l**, the formyl and sulfate diester groups are neither strongly conjugated, as in **35k**, nor in close spatial proximity, as in **35m**. As a result, the overall electronic distribution may be more favourable for the formation of a relatively stable gas-phase cation. For **35m**, steric effects arising from the proximity of the substituents may reduce the efficiency of ion formation during the electrospray process. For **35k**, the para-arrangement may further decrease the overall electron density of the aromatic ring, making protonation or the formation of stable cationic adducts less favourable.

2.1.3 Preparation of Amino-substituted Sulfate Diesters **35n-35p**

Amino-substituted sulfate diesters **35n-p** were accessible from the Boc protected analogues **35d-f**. The Boc-deprotection process occurs under the acidic conditions. According to the report by Taylor and co-workers in 2004, aryl TCE sulfates exhibit excellent stability under the strongly acidic conditions commonly employed in Boc-based solid-phase peptide synthesis. Supporting this, in our study, no undesired cleavage of the TCE group was observed during the Boc deprotection process.[183]

In the process of the deprotection of Boc unit, the carbonyl oxygen of the carbamate is first protonated, which facilitates cleavage of the *tert-butyl* group. The *tert-butyl* fragment departs as isobutene, generating a transient carbamic acid intermediate. This intermediate subsequently undergoes decarboxylation, releasing CO_2 and forming the amine-sulfate diester.

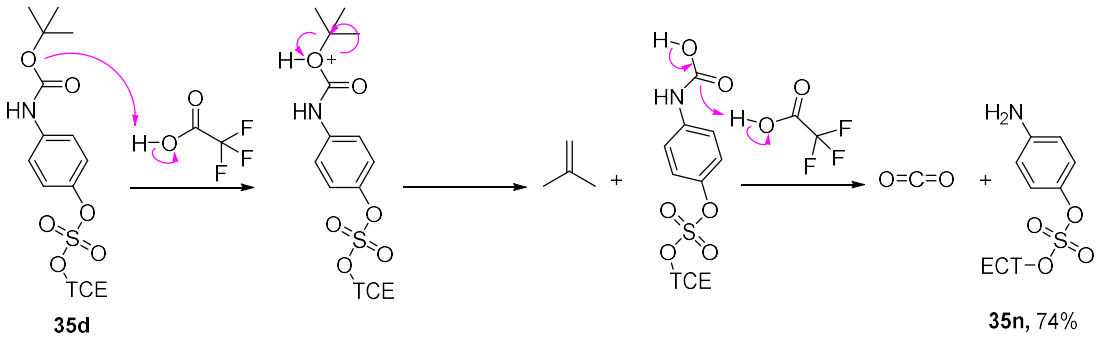

Scheme 26. The deprotection of the pre-synthesized Boc-protected sulfate **35d**.

We first employed compound **35d** as the starting material to access the *para*-substituted sulfate diester **35n**. Following Boc-deprotection examples from the literature, **35d** was combined with trifluoracetic acid (TFA) in an ice bath, and this reaction was stirred at 0 °C with monitoring for completion by TLC.[187] After 5 hours of reaction, TLC analysis indicated partial formation of the desired product, while a

noticeable amount of starting material remained. The reaction mixture was then gradually allowed to warm to room temperature and stirred for an additional 18 hours. Subsequent TLC analysis confirmed that only the product was present in the reaction mixture, indicating full consumption of the starting material. To remove residual TFA, a saturated solution of potassium carbonate was added dropwise to the reaction mixture until gas evolution ceased, indicating neutralization of the remaining acid. After extraction with DCM, the collected mixture was then concentrated under reduced pressure to remove the solvent, affording the desired product as a pure solid. The compound was obtained in an isolated yield of 74%.

The formation of **35n** was identified and confirmed by ^{1}H NMR spectroscopy. In the aromatic region, two doublets are observed at 7.11 ppm and 6.58 ppm, each integrating to two protons. This pattern is consistent with the *para*-substitution pattern of the benzene ring. The downfield set corresponds to the aromatic protons close to the strongly electron-withdrawing sulfate group, which decreases electron density of these protons and leads to deshielding. In contrast, the upfield set corresponds to the protons close to the amino group. The amino substituent donates electron density to these nearby protons, partially increasing the shielding effects. A broad singlet at 5.36 ppm integrating to two protons is assigned to the amino group, whose position and shape are influenced by hydrogen bonding and exchange effects. A singlet at 5.24 ppm integrating to two protons is attributed to the methylene group of the TCE unit. The chemical shift of the methylene proton is affected by the adjacent oxygen and -CCl_3 group.

The sulfate diesters bearing meta- and ortho-amino substitution were prepared using the same synthetic procedure and purification method described above. Compounds **35e** and **35f** were used as the starting materials for the meta- and ortho-substituted substrates, respectively. The reactions giving isolated yields of 85% for the meta-substituted product **35o** and 87% for the ortho-substituted product **35p**.

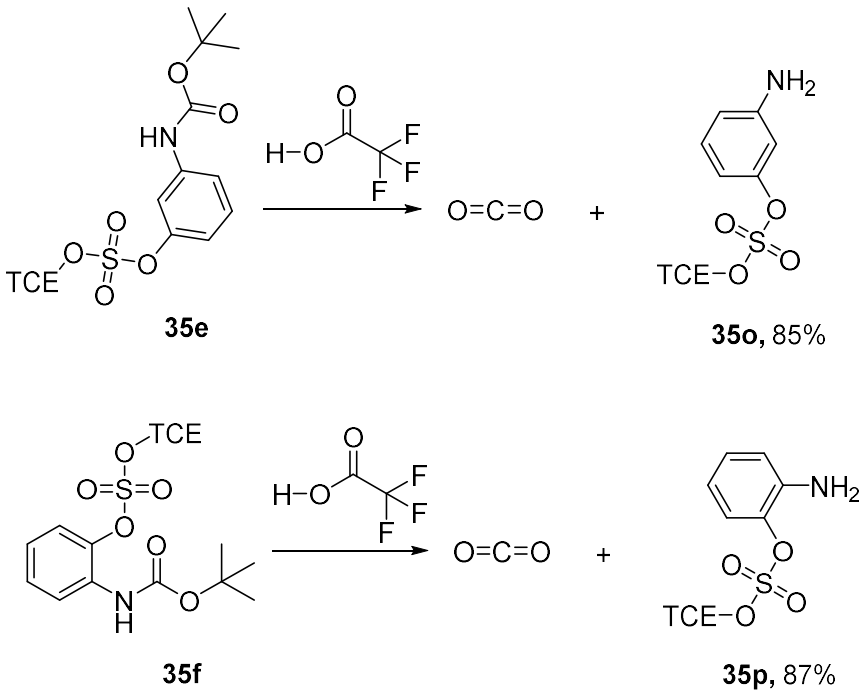

Scheme 27. The synthesis of **35o** and **35p**.

The structure of **35o** and **35p** were confirmed by ^{1}H NMR spectroscopy. Because the structures of **35n**, **35o**, and **35p** are highly similar, their ^{1}H NMR spectra also show a high degree of consistency. In the aromatic region, the total integration corresponds to four protons. However, the splitting patterns and relative integrations vary depending on the substitution pattern of the benzene ring. For example, in **35o**, which contains a *meta*-substituted aromatic system, the aromatic proton integration ratio appears as 1:1:2. In contrast, for **35p**, which features an ortho-substituted benzene ring, the aromatic protons give four distinct signals with an integration ratio of 1:1:1:1. In the region between 4 and 6 ppm, two singlets are observed, which are assigned to the -CH_2 group and the methylene group of the TCE moiety, respectively.

2.1.4 Preparation of Aryl Sulfate Diester **35q-35s** Bearing an Ethyl Carbamate Substituent

With the amino-substituted sulfate diesters in hand, we saw a convert single-step route

to the corresponding ethyl carbamate-substituted sulfate diesters. This reaction corresponds to the formation of a carbamate via acylation of an aniline derivative with ethyl chloroformate, in the presence of pyridine as base.

First, the lone pair on the nitrogen atom of the aromatic amine acts as a nucleophile and attacks the electrophilic carbonyl carbon of ethyl chloroformate. The carbonyl carbon is highly electrophilic since the strong electron-withdrawing effect of the carbonyl oxygen and the presence of a good leaving group, Cl^-. After this step, the nitrogen is now bonded to the carbonyl carbon, and the carbonyl oxygen temporarily carries a negative charge. Then, the intermediate collapses by re-forming the C=O bond, leading to the elimination of Cl^- as a leaving group and the formation of the protonated carbamate intermediate. Next, pyridine acts as a base and removes the proton from the positively charged nitrogen, and pyridinium chloride is generated as a by-product. In this stage, the positive nitrogen is restored to the neutral carbamate nitrogen.

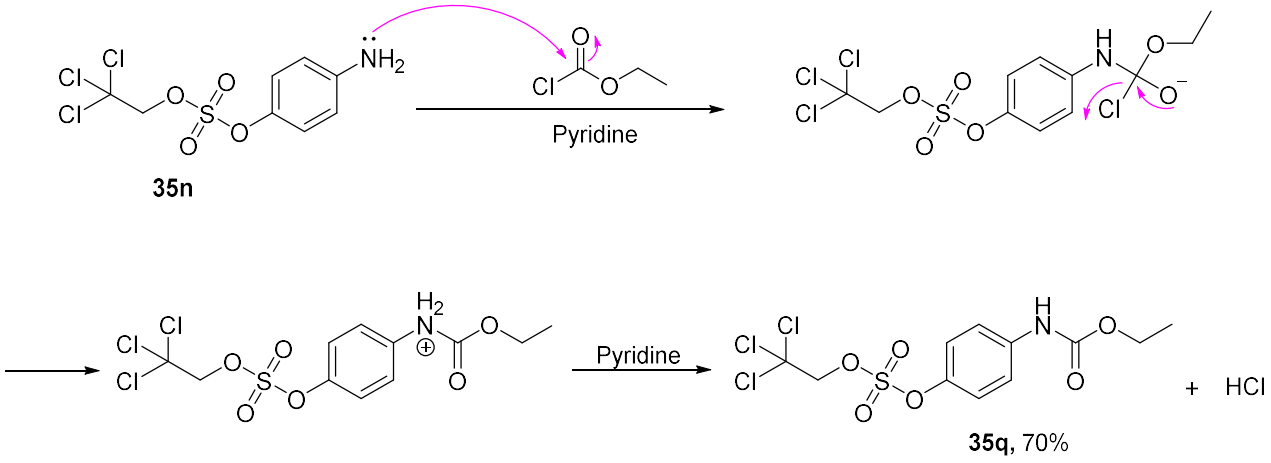

Scheme 28. The synthesis of **35q**.

Aniline **35n** was combined with ethyl chloroformate in pyridine at 0 °C.[189] The mixture was stirred at 0 °C for 2h and then warmed to ambient temperature. After initiating the reaction, its progress was monitored by TLC at 1-hour intervals. Five hours after the reaction began, TLC analysis indicated that the starting material had been fully

consumed. The reaction mixture was subsequently concentrated under reduced pressure to afford a crude oil. This residue was purified by preparative TCL chromatography to give the desired product **35q** in 70% isolated yield.

The structure of **35q** was confirmed by ^{1}H NMR spectroscopy. The aromatic region displays two doublets integrating to two protons each, consistent with a *para*-disubstituted benzene ring. One appears in the downfield region at 7.46 ppm, while the second is observed at slightly higher field, reflecting the electronic influence of the sulfate group. Another appears at 7.30 ppm, which is close to the ethyl carbamate group. A broad singlet at 6.66 ppm integrating to one proton is assigned to the carbamate NH. A distinct singlet at 4.81 ppm integrating to two protons corresponds to the methylene group of the TCE unit, serving as a diagnostic signal for successful sulfate installation. The methylene of ethyl carbamate moiety is evidenced by a quartet at 4.24 ppm integrating to two protons and a triplet at 1.32 ppm integrating to three protons for the terminal methyl group. The overall integration and splitting patterns are fully consistent with the desired structure.

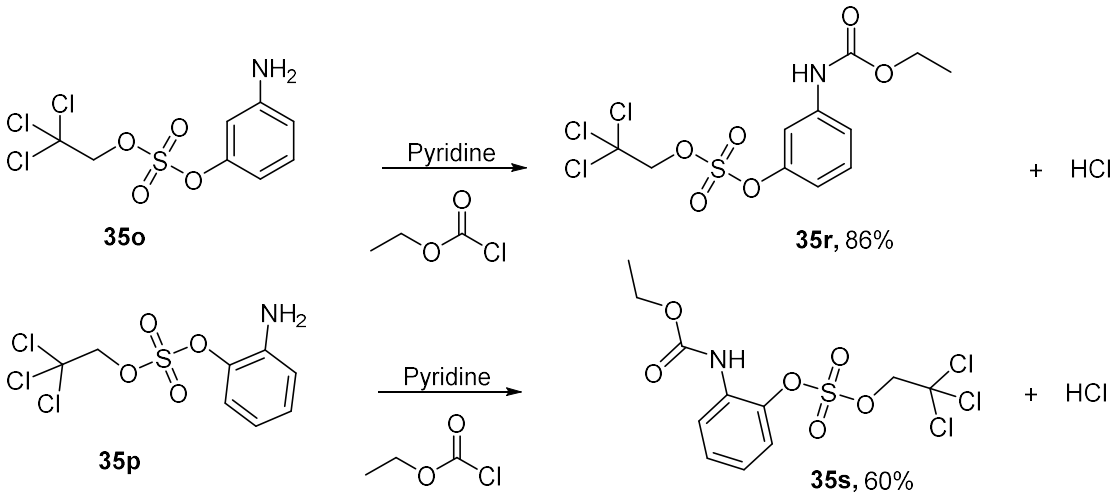

Scheme 29. The synthesis of **35r** and **35s.**

Compounds **35r** and **35s** were prepared using the same synthetic protocol. Their structures were confirmed by ^{1}H NMR spectroscopy. Owing to their structural

similarity, the spectra of **35r** and **35s** closely resemble that of **35q**. For example, a singlet at approximately 4.8 ppm is observed and is assigned to the methylene group of the TCE moiety. In addition, a quartet at around 4.2 ppm corresponds to the -CH_2 group of the ethyl substituent, while a triplet at approximately 1.3 ppm is attributed to the terminal methyl group. The remaining resonances are in the aromatic region, with a total integration of four protons, corresponding to the aromatic CH units. Depending on the substitution pattern of the benzene ring, variations in both the splitting pattern and chemical shifts are observed in this region. The observed chemical shifts reflect the combined influence of the strongly electron-withdrawing sulfate ester and the weakly electron-withdrawing ethyl carbamate group.

After the preparation of **35r** and **35s** using above method, the products were obtained in the yield of 85% and 60%. It was found that the yield of **35s** obtained was unsatisfactory. To address this limitation and improve the overall efficiency of the synthesis, an alternative strategy was therefore investigated. In the revised approach, **34d** was first synthesized from 2-aminophenol. **34d** was then subjected to a sulfation reaction using imidazolium salt **33**. Through this modified route, the desired product **35s-1** was successfully obtained in the yield of 72%.

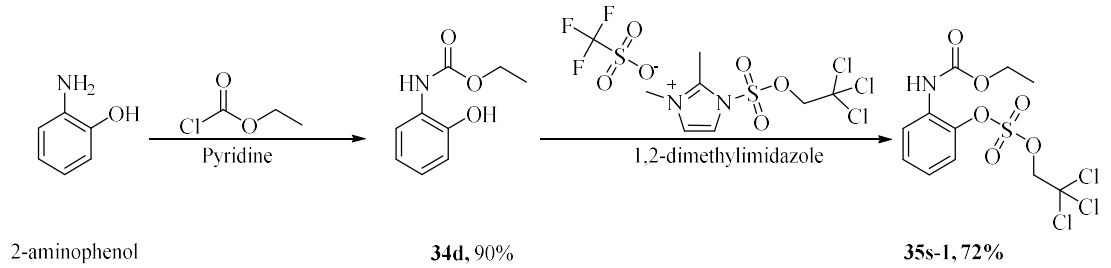

Scheme 30. The synthesis of **34d** and **35s-1**.

2-Aminophenol was first prepared in water, followed by the addition of sodium bicarbonate to generate a mildly basic aqueous solution. Dichloromethane was then added to create a biphasic system, allowing the organic reagent to interact efficiently with the substrate at the interface. Ethyl chloroformate was added dropwise to the

vigorously stirred biphasic mixture. The reaction was conducted according to the literature procedure and allowed to stir for 2 hours at room temperature.[190] After 2 hours, TLC analysis indicated complete consumption of the starting material, with the appearance of one major product spot along with a minor impurity. The crude product was purified by flash column chromatography (EtOAC/hexane = 1:1), affording the desired product **34d** in 90% yield.

The structure of **34d** was confirmed by ^{1}H NMR spectroscopy. In the aliphatic region, a quartet at 4.25 ppm integrating for two protons corresponds to the methylene group of the ethyl ester moiety attached to oxygen. This signal couples with a quartet at 1.33 ppm integrating for three protons, which is assigned to the terminal methyl group of the ethyl fragment. The coupling pattern and integration ratio of 2:3 confirm the presence of the -OCH_2CH_3 unit. In the aromatic region, two multiplets are observed at 7.11-7.00 ppm and 6.99-6.81 ppm, integrating to 1H and 3H, respectively. Both signals correspond to aromatic CH protons, which consistent with a 1,2-disubstituted benzene ring. A downfield broad singlet at 7.75 ppm integrating for one proton of the hydroxyl group, which appears broadened and weak due to solvent exchange. The singlet at 7.27 integrating for one proton is attributed to the carbamate NH proton, which appears broadened due to hydrogen bonding and exchange effects.

Following standard procedure, **34d** was combined with imidazolium **33** and 1,2-dimethylimidazole in an ice bath. After reaction, the reaction mixture was concentrated under reduced pressure to give a crude oil. Purification of the crude material by preparative TLC chromatography, employing DCM/hexane/Et_3N (1:1:1, v/v) as the eluent, afforded the desired compound **35s-1** in 72% isolated yield. The structure of **35s-1** obtained using the improved method was likewise confirmed by ^{1}H NMR spectroscopy, and the spectral data were fully consistent with those of compound **35s**.

In addition to NMR analysis, the structures were further confirmed by ESI-HRMS. In the ESI+ HRMS spectrum of para-substituted compound **35q**, the most intense peak

appears at *m/z* 391.9570 and can be assigned to the molecular ion $[M+H]^+$, which agrees well with the calculated value of 391.9527. In the vicinity of the molecular ion, a cluster of peaks arising from chlorine isotopes is observed at *m/z* 392.9590, 394.9567, and 395.9513. The characteristic 2 Da spacing and the relative intensity distribution of this cluster are fully consistent with the presence of three chlorine atoms in the molecule, providing strong evidence supporting the obtained structure.

Two additional representative adduct peaks are observed at *m/z* 413.9376 and 429.9121, corresponding to $[M+Na]^+$ and $[M+K]^+$, respectively. These values are in good agreement with the calculated masses of 413.9343 and 429.9082. The pair of peaks at *m/z* 363.9252 and 365.9222 also displays the characteristic 2 Da chlorine isotope pattern, indicating that chlorine atoms are retained in this fragment. The mass difference between the molecular ion and 363.9252 is approximately 28.03 Da, which is very close to the mass of C_2H_4. This suggests that $[M+H]^+$ undergoes a mild in-source fragmentation, likely involving elimination from the ethoxycarbonyl ($-COOCH_2CH_3$) moiety with loss of C_2H_4, to generate $[M+H-C_2H_4]^+$. This assignment is consistent with the calculated value of 363.9211 for $[M+H-C_2H_4]^+$.

The meta- and ortho-substituted analogues of **35q**, **35r** and **35s**, exhibit similar characteristic features in their HRMS spectra. In the ESI− HRMS spectrum of **35r**, a strong peak is observed at *m/z* 389.9391, which can be assigned to the deprotonated molecular ion $[M-H]^-$, in good agreement with the calculated value of 389.9378. In the vicinity of the molecular ion, a cluster of peaks arising from chlorine isotopes is detected at *m/z* 391.9361 (M+2) and 393.9331 (M+4). These peaks display an approximately 2 Da spacing relative to the main ion, and their relative intensity distribution is consistent with the expected isotopic pattern for a molecule containing three chlorine atoms. Therefore, this isotope cluster provides strong evidence for the presence of the TCE moiety within the molecule and further supports the proposed structure.

In the ESI$^+$ HRMS spectrum of **35s**, the most intense peak appears at *m/z* 391.9574 and is assigned to the protonated molecular ion $[M+H]^+$, in good agreement with the calculated value of 391.9527. Adjacent to the molecular ion, an isotope cluster arising from chlorine is observed at *m/z* 393.9546 (M+2) and 395.9515 (M+4). The characteristic 2 Da spacing and the relative intensity distribution of this cluster are fully consistent with the presence of the TCE moiety in the molecule, providing strong evidence in support of the proposed structure. Furthermore, typical alkali metal adduct ions are observed at higher *m/z* values: 413.9389, 415.9360, 429.9125, and 431.9098, corresponding to $[M+Na]^+$, $[M+Na+2]^+$, $[M+K]^+$, and $[M+K+2]^+$, respectively. The presence of these adduct ions and their associated isotope peaks further demonstrates that the compound readily forms a stable protonated molecular ion under positive-ion conditions and can also efficiently generate alkali metal adducts.

In this study, a total of twelve TCE-protected sulfate diesters were prepared in yields ranging from 55% to 88%. During the synthesis of these sulfate diesters, the main difficulties were encountered in the preparation of nitrogen-containing compounds. In the Boc deprotection step, when the reaction was first carried out using 100 mg of starting material, deprotection was complete within 5 h and no further purification was required. However, when the reaction was scaled up in a second attempt using 500 mg of starting material with an equivalent proportion of TFA, the reaction did not reach completion even after 10 h. As a result, purification was attempted by column chromatography and preparative TLC. During purification, the product underwent decomposition, leading to a substantial decrease in yield. Purification also became challenging because impurities consistently co-eluted with the product. In future work, alternative purification methods, such as anion-exchange chromatography, could be explored. In the NMR analysis of these sulfate diesters, a singlet integrating to 2H at around 4.8 ppm was readily observed. This signal is characteristic of the TCE group and therefore can be used as a diagnostic reference peak to assess whether the synthesis of TCE-containing compounds has proceeded successfully.

2.1.5 Synthesis and Characterization of Deprotected Aryl Sulfates **36**

In the final step of the sulfation reaction, the TCE-protected aryl sulfate esters underwent selective reductive deprotection under Zn/NH_4HCO_2 conditions. This process proceeded via the reductive activation of the TCE moiety, which triggers the cleavage of the *O*-CH_2CCl_3 bond and releases the free arylsulfate ammonium salt (Ar-$OSO_3^{-}\cdot NH_4^{+}$). Because this deprotection was carried out under mild conditions and did not involve strong acids or bases, it effectively avoided the degradation of the sulfate esters. Moreover, this approach exhibited good functional group compatibility toward a variety of substituents on the aromatic ring, thereby facilitating the efficient isolation of the target products and enabling subsequent manipulations.

During the TCE deprotection process, Zn acts as a mild single-electron reducing agent. At the initial stage of the reaction, metallic zinc was oxidized to Zn^{2+}, releasing electrons into the system. One of these electrons was transferred to the TCE side chain, generating a radical anion intermediate of the 2,2,2-trichloroethyl group. Subsequently, because the C-Cl bond was relatively weak, this intermediate underwent C-Cl bond cleavage, releasing Cl^- and forming a dichloroethyl radical. In this radical intermediate, electron delocalization along the σ bonds promoted a β-fragmentation process, which facilitated the cleavage of the O-CH_2 bond. As a result, the TCE protecting group was removed, liberating the free arylsulfate anion (RO-SO_3^-).[183]

Figure 21. Yields of sulfate diester deprotection.

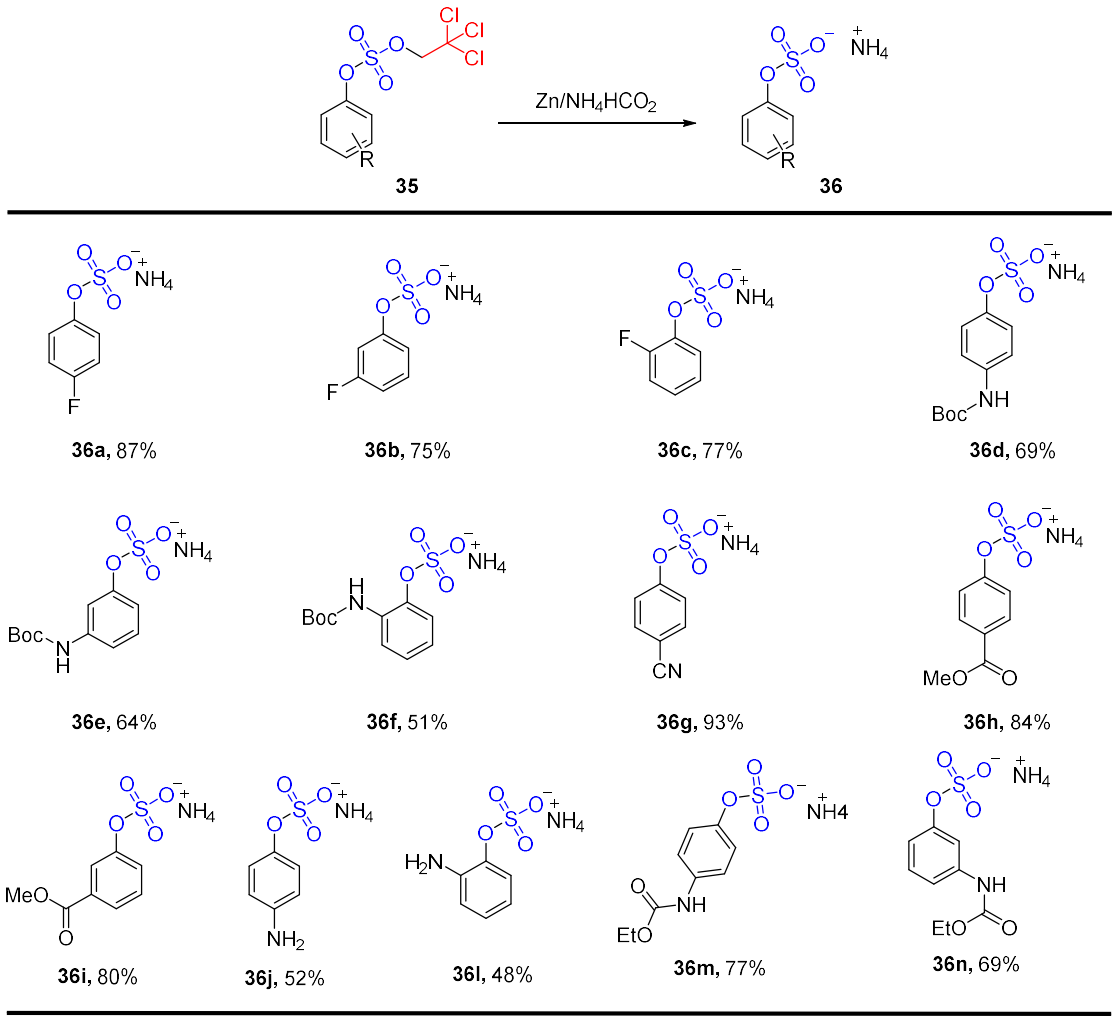

Based on the 2003 study reported by Taylor's group on TCE deprotection, we explored the deprotection of the TCE group starting from fluorinated sulfate diester **35a**.[183] Compound **35a** was treated with ammonium formate in the presence of zinc powder. The reaction mixture was stirred at room temperature until the ammonium formate was fully consumed as evidenced by a visible lack of residual formate crystals. After 1 hour, TLC analysis showed complete consumption of the starting material **35a**, with only a single spot corresponding to the desired product **36a**. The reaction mixture was subsequently concentrated under reduced pressure at room temperature (≤ 20 °C), since the synthesized sulfate salts underwent decomposition during the high-temperature and reduced-pressure rotary evaporation process.

In the initial purification attempt, flash column chromatography was performed using column chromatography, and a MeOH/DCM (1:4) solvent system was employed as the eluent. However, the product was only isolated in trace amounts, and its concentration in each fraction was insufficient to produce a clearly visible spot on the TLC plate, making collection difficult.

To address this issue, we used a pasteur pipette as the column to reduce the column length and diameter, making it more suitable for the small-scale quantities of our products. In this case, the product was successfully isolated. However, the calculated yield exceeded 100%. Subsequent analysis of ^{1}H NMR spectrum revealed that the isolated material contained residual inorganic ammonium salts, which contributed to the inflated mass.

To obtain a purer product, lyophilization was carried out as ammonium formate is known to sublime under these conditions.[183] The solid obtained after chromatography was dissolved in water, frozen in liquid nitrogen and subjected to freeze-drying for 24 hours. After lyophilization, the yield of **36a** was recalculated to be 87%. The ^{1}H NMR spectrum showed that the signals corresponding to ammonium formate were significantly reduced, confirming improved purity of the product. Comparison of **36a** obtained after column chromatography with that obtained after lyophilization shows that, in the ^{1}H NMR spectrum, the integration of the signal corresponding to inorganic ammonium decreased from 1.41 to 1.04. Although more extensive lyophilization could have been performed, the material was considered sufficiently pure for our purposes at this stage, and therefore no further treatment was undertaken.

The structure of **36a** was confirmed by ^{1}H NMR and ^{13}C spectroscopy. The ^{1}H NMR spectrum displays two multiplets at 7.01-6.93 ppm and 6.76-6.70 ppm, integrating to a total of four protons, consistent with a *para*-disubstituted benzene ring. These two signals appear as complex multiplets rather than the expected doublets of doublets, as the protons are subject to both H-H and H-F coupling interactions. Compared with **35a**,

the ^{1}H NMR spectrum of the deprotected compound **36a** shows the disappearance of the characteristic methylene singlet at 4.83 ppm, which was previously assigned to the -CH_2 group of the TCE protecting moiety. The absence of this signal clearly indicates successful removal of the TCE group.

Furthermore, the aromatic CH resonances that appeared at 7.38-7.31 and 7.17-7.10 ppm in **35a** were approximately shifted to a higher field by 0.4 ppm in **36a**. This change in chemical shift indicates that the electronic environment of the aromatic ring has changed after deprotection. Specifically, the removal of the TCE group will reduce the overall electron attraction effect transferred through the sulfate substituent, thereby weakening its deshielding effect on the benzene ring. Therefore, the aromatic protons have been slightly enhanced by a shielding effect, resulting in the observed change in the chemical shifts.

The ^{13}C APT spectrum of **36a** shows signals exclusively in the aromatic region, confirming removal of the protecting group. Compared with the APT spectrum of **35a**, the most significant changes in the APT spectrum of the deprotected compound **36a** occur in the 50-100 ppm region. In this region, the two characteristic resonances corresponding to the TCE protecting group have completely disappeared. Specifically, the signal at 92.4 ppm, previously assigned to the -CCl_3 carbon, and the signal at 80.5 ppm, attributed to the methylene (-CH_2) carbon of the TCE group, are no longer observed in **36a**. The absence of these two diagnostic peaks provides clear spectroscopic evidence for successful removal of the TCE protecting group. In addition, the chemical shift of the carbon attached to the -SO_4 group moved downfield by 3.9 ppm, and the coupling constant also changed from 3.9 Hz in **35a** to 2.0 Hz.

Using the same synthetic procedure as that used for the F-para-substituted sulfate **36a**, the meta- and para-substituted sulfates **36b** and **36c** were obtained in the yield of 75% and 77%, respectively. Owing to their closely related structures, both the ^{1}H NMR and APT spectra display similar overall features, particularly with respect to the

disappearance of the TCE-related resonances after deprotection. In the ^{1}H NMR of **36b**, the signals at 7.33-7.26, 7.02, 6.97, and 6.87 ppm are all assigned to protons on the aromatic CH groups. In the ^{1}H NMR of **36c**, the signals at 7.48, 7.17, and 7.08 ppm are all assigned to aromatic CH protons. In each case, the characteristic methylene (-CH_2) and -CCl_3 signals of the TCE group are absent in the deprotected products, confirming successful removal of the protecting group.

In addition, consistent changes are observed in the aromatic region after TCE removal. In both the ^{1}H NMR and APT spectra, the aromatic signals shift upfield compared with those of the protected sulfate diesters. In the ^{1}H NMR of **36b**, the aromatic signals are shifted upfield by approximately 0.1 ppm compared with those of its precursor **35b**. A similar upfield shift of about 0.1 ppm is also observed for the aromatic signals in **36c** relative to **35c**. As a result, the aromatic protons and carbons experience a relatively increased shielding environment, leading to the observed chemical shift changes.

The structures of **36a-36c** were further confirmed by ESI-HRMS analysis. For **36a**, the base peak appears at *m/z* 190.9821, corresponding to $[M]^-$, which is consistent with the calculated value of 190.9813. Adjacent to the main peak, two isotope peaks are observed at *m/z* 191.9848 and 192.9790, which can be assigned to the $[M+1]^-$ ion arising from ^{13}C and the $[M+2]^-$ ion resulting from ^{34}S, respectively. The presence of these isotope peaks further strengthens the reliability of the assignment. In addition, a fragment ion at *m/z* 111.0247 is observed and can be attributed to the $[M-SO_3]^-$ species.

A comparable pattern was observed for the regio-isomers **36b** and **36c** in their ESI-HRMS spectra. For **36b**, a cluster of peaks was detected at *m/z* 190.9822, 191.9849, and 192.9790. The ion at *m/z* 190.9822 represents the base peak corresponding to $[M]^-$, while the signals at *m/z* 191.9849 and 192.9790 are attributed to the ^{13}C-derived $[M+1]^-$ and the ^{34}S-associated $[M+2]^-$ isotopic species, respectively. Similarly, the spectrum of **36c** displayed a nearly identical isotopic distribution, with peaks at *m/z*

190.9822, 191.9848, and 192.9789. Again, $[M]^-$ was observed as the most intense signal, and the accompanying $[M+1]^-$ and $[M+2]^-$ peaks can be assigned to contributions from ^{13}C and ^{34}S, respectively.

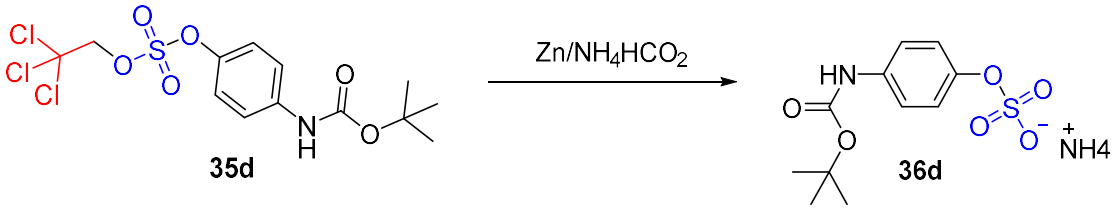

Scheme 31. The synthesis of **36d**.

Subsequently, compounds **35d-35f**, bearing an *N*-Boc substituent, were subjected to TCE deprotection under conditions identical to those previously applied to the F-substituted sulfate diesters. The overall deprotection procedure proceeded smoothly; however, significant difficulties were encountered during the purification stage. In contrast to the F-substituted analogues, the nitrogen-containing compounds proved unstable on silica gel. Owing to the mildly acidic nature of silica, partial decomposition of the products was observed during column chromatography. In addition, pronounced tailing occurred during TLC monitoring, which complicated the visualization of product elution and made clean separation difficult.

To address these issues, the purification conditions were modified. A small amount of triethylamine was added to the eluent to neutralize the acidic sites on silica gel, and the solvent system was adjusted to DCM/MeOH/Et_3N (20:1:1). Furthermore, preparative TLC plates were employed instead of conventional silica gel column chromatography to minimize exposure to acidic conditions. Under these improved conditions, decomposition was effectively suppressed, and the desired products were successfully eluted and isolated.

The structures of deprotected **36d-36f** were confirmed by both ^1H and ^{13}C NMR spectroscopy. In the ^1H NMR of **36d**, a signal at 9.17 ppm is attributed to the inorganic

ammonium ion. Two signals at 7.30 and 7.05-6.99 ppm correspond to aromatic CH protons, while a singlet at 1.46 ppm is assigned to the methyl groups of the Boc protecting group. In the ^{1}H NMR of **36e**, the signals at 7.22, 7.09, 7.06 and 6.76 ppm correspond to aromatic CH protons, while the singlet at 1.42 ppm is assigned to the methyl groups of the Boc protecting group. In the ^{1}H NMR of **36f**, the singlet at 8.09 ppm is attributed to the inorganic ammonium ion. The signals at 7.80, 7.12, 7.08, and 6.97 ppm correspond to aromatic CH protons, while the singlet at 1.46 ppm is assigned to the methyl groups of the Boc protecting group.

Compared with their TCE-protected precursors **35d-35f**, the most prominent change in the ^{1}H NMR spectra of **36d-36f** are the disappearance of the characteristic methylene singlet at approximately 4.8 ppm, which corresponds to the -CH_2 group of the TCE protecting group. The absence of this diagnostic resonance provides clear evidence for successful deprotection. By comparing **36d-f** with their precursors **35d-f**, we found that the aromatic signals all shifted upfield after the deprotection reaction. In **36d**, the shifts are 0.14 and 0.23 ppm. In **36e**, the shifts are 0.38, 0.09, 0.11, and 0.22 ppm. In 36f, the shifts are 0.37, 0.28, 0.23, and 0.10 ppm.

A similar trend is observed in the ^{13}C NMR spectra. In the ^{13}C NMR spectrum of **36d**, the signals at 153.0 and 148.4 ppm are assigned to the carbon attached to -C=O and the carbon bonded to the -SO_4 group, respectively. The signal at 135.0 ppm is attributed to the NH unit. The signals at 121.0 and 118.8 ppm correspond to the two aromatic CH carbons. The signal at 78.8 ppm is assigned to the quaternary carbon of the Boc group, while the signal at 28.2 ppm corresponds to the methyl carbons of the Boc group. In the ^{13}C NMR spectrum of **36e**, the signals at 154.1, 153.1, and 140.4 ppm are assigned to -C=O, -C-SO_4, and -C-NH, respectively. The signals at 129.0, 114.9, 113.5, and 111.4 ppm correspond to four aromatic CH carbons. The signal at 79.3 ppm is assigned to the quaternary carbon of the Boc group, while the signal at 28.5 ppm is attributed to the methyl carbons of the Boc group. In the ^{13}C NMR spectrum of **36f**, the signals at 152.4,

142.4, and 132.0 ppm are assigned to -C=O, -C-NH, and -C-SO_4, respectively. The signals at 124.7, 123.8, and 123.0 ppm correspond to the aromatic CH carbons. The signals at 79.7 and 28.2 ppm are assigned to the quaternary carbon and the methyl carbons of the Boc group, respectively.

The signals at around 92 ppm and 80 ppm, previously assigned to the -CCl_3 and -CH_2 carbons of the TCE group, respectively, are no longer present in the spectra of **36d-36f**. The disappearance of these characteristic carbon resonances further confirms the complete removal of the TCE protecting group. In addition, the chemical shift of the carbon attached to the -SO_4 group shifts downfield in **36d** and **36e**, by 3.2 ppm and 2.6 ppm, respectively. In contrast, in **36f** this carbon shows an upfield shift of 7.1 ppm.

The structures of the *N*-Boc-substituted sulfates were further supported by ESI-HRMS analysis. The HRMS analysis of para-substituted sulfate **36d** was analysed as the beginning. In the ESI- HRMS spectrum of **36d**, a prominent ion at *m/z* 288.0604 was observed and assigned to the deprotonated molecular ion $[M]^-$, in good agreement with the calculated value of 288.0538. Two adjacent minor peaks at *m/z* 289.0632 and 290.0585 correspond to the M+1 and M+2 isotopic peaks of $[M]^-$, arising predominantly from contributions of ^{13}C and ^{34}S, respectively. The presence of this characteristic isotopic cluster around *m/z* 288 further supports the molecular composition and provides strong confirmation of the structure of **36d**.

Similar features were observed in the ESI- HRMS spectra of the meta- and ortho-substituted isomers, **36e** and **36f**. In the spectrum of **36e**, a characteristic isotopic cluster was detected at *m/z* 288.0548, 289.0576, and 290.0529. Likewise, the HRMS spectrum of **36f** displayed a corresponding set of peaks at *m/z* 288.0548, 289.0574, and 290.0529. Based on the analysis discussed above for **36d**, these peak clusters can be assigned to the molecular ion and its associated M+1 and M+2 isotopic peaks. The presence of these consistent isotopic patterns therefore provides strong evidence supporting the structures of both **36e** and **36f**.

We also obtained the ESI+ HRMS spectrum of **36d**. In this spectrum, a peak at *m/z* 307.0985 was observed and assigned to the ammonium adduct $[M+NH_4]^+$ (calculated for $C_{11}H_{18}N2O_6S$, *m/z* 307.0958). This assignment is entirely reasonable, as the synthesized compound **36d** was isolated as the ammonium salt, making formation of the ammonium adduct under positive-ion conditions highly favourable. In addition, a signal at *m/z* 312.0534 was detected and attributed to the sodium adduct $[M+Na]^+$ (calculated for $C_{11}H_{14}NNaO_6S^+$, m/z 312.0512). The formation of sodium adducts is common in ESI+ mass spectrometry due to trace sodium ions present in solvents, glassware, or the sample matrix.

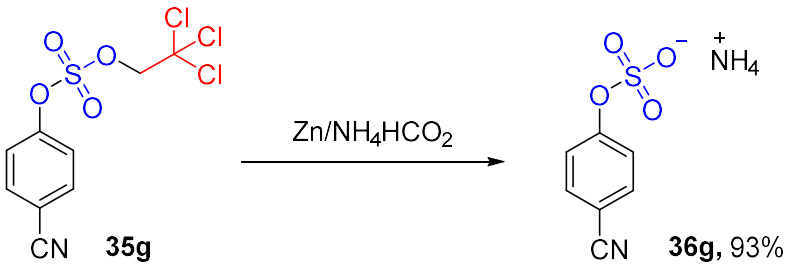

Scheme 32. The synthesis of **36g**.

The next stage involved removal of the TCE protecting group from **35g**, the para-cyano-substituted sulfate diester. Both the deprotection reaction and the purification procedure were carried out under conditions identical to those described above for the F-substituted sulfates. In contrast to the amino- and carbamate-containing analogues, the cyano-substituted compound exhibited excellent stability on silica gel. As a result, the product **36g** was isolated in a high yield of 93% after chromatographic purification.

The structure of **36g** was confirmed by ^{1}H NMR and APT NMR spectroscopy. In the ^{1}H NMR spectrum of **36g**, the singlet at 8.35 ppm is attributed to the inorganic ammonium ion, while the signals at 7.78-7.72 and 7.37-7.31 ppm are assigned to aromatic CH protons. Compared with the TCE-protected precursor **35g**, the most notable change in the ^{1}H NMR spectrum of **36g** is the disappearance of the singlet at 4.87 ppm, which is assigned to the methylene group of the TCE protecting group. The

absence of this characteristic resonance clearly indicates successful removal of TCE.

In the ^{13}C spectrum of **36g**, the signal at 157.7 and 119.3 ppm are assigned to -SO_4 and -CN, while the signals at 134.0 and 120.6 ppm correspond to aromatic CH carbons. The signal at 105.0 ppm corresponds to the carbon of -CN group. Consistent with the ^{1}H NMR spectrum of **36g**, the APT spectrum shows the same key difference between **35g** and **36g**: the signals at approximately 92 ppm and 80 ppm, corresponding to the -CCl_3 and -CH_2 carbons of the TCE group, are no longer present. The disappearance of these diagnostic carbon resonances further confirms complete deprotection.

In the ESI- HRMS spectrum of the para-cyano substituted compound **36g**, the base peak appears at *m/z* 197.9858, which is in excellent agreement with the calculated value for $[M–H]^-$ (*m/z* 197.9860). Adjacent to the main peak, characteristic isotope peaks are observed at *m/z* 198.9883 (M+1) and 199.9829 (M+2), arising from the natural abundance of ^{13}C and ^{34}S, respectively. This isotope pattern further confirms the presence of the sulfate group in the molecule and is fully consistent with the proposed structure. In addition, a fragment ion is detected at *m/z* 118.0286, which can be assigned to $[C_7H_4NO]^-$. This fragment corresponds to the species formed after loss of -SO_3 from **36g**, leaving the cyano-phenoxide moiety.

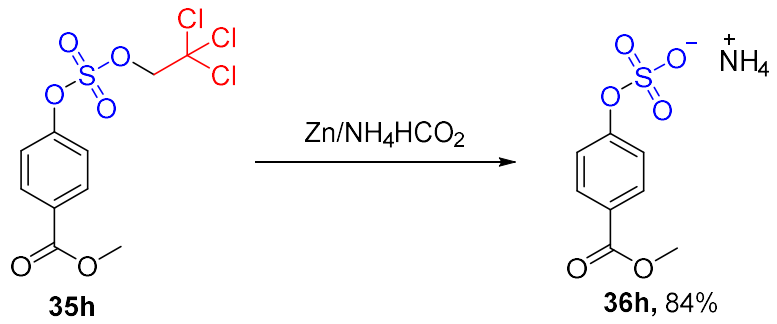

35h **36h**, 84%

Scheme 33. The synthesis of **36h**.

Like the cyano-substituted derivative, removal of the TCE protecting group from the methyl ester-substituted sulfate diesters was carried out under the same conditions

established for the F-substituted compounds. Both the reaction and purification procedures were identical. The para- and meta-substituted methyl ester derivatives, **36h** and **36i**, exhibited good stability on silica gel and were successfully eluted without noticeable decomposition. The desired products were obtained in 84% and 80% yields, respectively.

In contrast, attempts to prepare the ortho-methyl ester-substituted sulfate resulted in difficulties during purification. Although the deprotection reaction itself proceeded smoothly, consistent with its homologues, significant decomposition occurred during chromatographic purification. Even after modifying the eluent by adding a small amount of triethylamine and employing preparative TLC instead of conventional column chromatography, a pure product could not be obtained.

The structures of **36h** and **36i** were confirmed by ^{1}H NMR and APT spectroscopy. In the ^{1}H NMR spectrum of **36h**, the signals at 7.92-7.86 and 7.31-7.24 ppm were assigned to aromatic CH protons, whereas the singlet at 3.82 ppm corresponded to the terminal methyl group. In the ^{1}H NMR spectrum of **36i**, the signal at 8.36 ppm was assigned to the inorganic ammonium salt. The signals at 7.83-7.80, 7.65, 7.42, and 7.37 ppm were attributed to aromatic CH protons, while the signal at 3.85 ppm corresponds to the terminal methyl group. Compared with their TCE-protected precursors **35h** and **35i**, the most notable change in the ^{1}H NMR spectra is the disappearance of the characteristic methylene signal of the TCE group, previously observed at 5.42 ppm (for **35h**) and 4.86 ppm (for **35i**).

In the ^{13}C NMR spectrum of **36h**, the signals at 166.5, 158.3, and 124.2 ppm correspond to the carbonyl carbon, the carbon bonded to the -SO_4 group, and the carbon attached to the carbonyl group, respectively. The signals at 131.0 and 120.0 ppm were assigned to aromatic CH carbons, while the signal at 52.4 ppm corresponds to the terminal methyl carbon. In the ^{13}C NMR spectrum of **36i**, the signals at 166.5, 154.2, and 130.9 ppm were assigned to the carbonyl carbon, the carbon attached to the -SO_4 group, and

the carbon connected to the carbonyl group, respectively. The signals at 129.8, 125.9, 124.3, and 121.4 ppm correspond to aromatic CH carbons, while the signal at 52.7 ppm was attributed to the terminal methyl carbon.

In the APT spectra, the aromatic and carbonyl regions remain largely unchanged, indicating that the core structures are preserved. However, the characteristic resonances corresponding to the TCE group, the signals at approximately 92 ppm ($-CCl_3$) and 80 ppm ($-CH_2$), are no longer present. The disappearance of these diagnostic peaks provides clear evidence for successful removal of the TCE protecting group in **36h** and **36i**.

Further structural confirmation was obtained by ESI-HRMS analysis. First, the spectrum of the meta-substituted methyl ester derivative **36i** is discussed. In the ESI-HRMS spectrum of **36i**, the base peak appears at *m/z* 230.9969 and is assigned to the molecular ion $[M]^-$ of the target compound, which is in excellent agreement with the calculated value of 230.9961. Adjacent to the base peak, the expected isotopic signals are observed at *m/z* 231.9998 and 232.9946, arising from ^{13}C (M+1) and ^{34}S (M+2), respectively. This isotopic pattern is fully consistent with the presence of one sulfur atom and a carbon framework in the molecule.

Next, the ESI- HRMS spectrum of the para-substituted analogue **36h** was analysed. In this spectrum, the base peak is observed at *m/z* 230.9960, which matches well with the calculated value for $[M]^-$. The neighbouring isotopic peaks at *m/z* 231.9990 and 232.9938 correspond to ^{13}C (M+1) and ^{34}S (M+2), respectively, again confirming the presence of a single sulfur atom in the structure. A fragment ion is observed at *m/z* 151.0385. This peak is consistent with the $[M-SO_3]^-$ species, indicating in-source fragmentation of the sulfate ester with loss of $-SO_3$, thereby generating the desulfated phenoxide anion. From a calculated standpoint, subtraction of the exact mass of $-SO_3$ (79.9568) from 230.9960 gives approximately 151.0392, which is in very close agreement with the observed value of 151.0385. This suggests that a certain degree of

in-source fragmentation occurs under ESI- conditions. Nevertheless, the base peak remains $[M]^-$, indicating that the spectrum is overall clean and well defined.

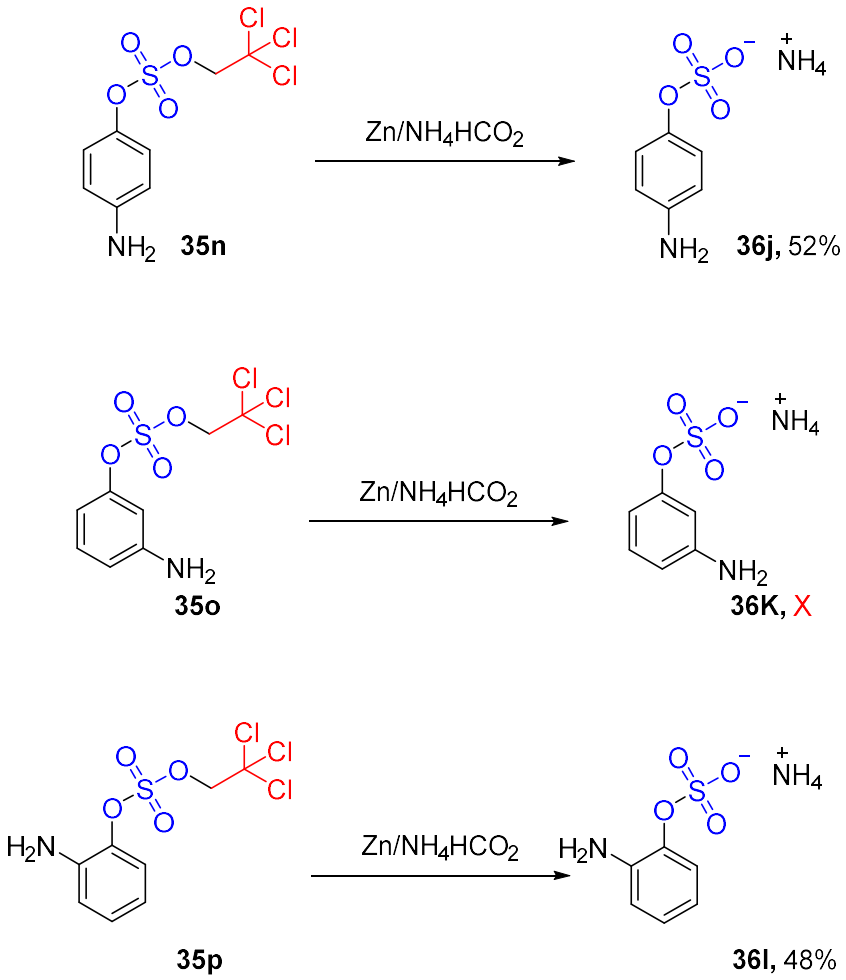

Scheme 34. The synthesis of **36j**.

The amino-substituted sulfate diesters **35n-35p** were subjected to TCE deprotection to afford the corresponding amino-substituted sulfates **36j-36l**. The deprotection reactions were carried out under conditions identical to those employed for the F-substituted analogues. However, during purification, preparative TLC chromatography was employed instead of conventional silica gel column chromatography, as our previous studies indicated that nitrogen-containing compounds are unstable on silica gel. Under these modified conditions, the desired products, **36j** and **36l**, were isolated in moderate yields of 52%, 48%, respectively. However, the synthesis of compound **36k** was

unsuccessful.

The structures of **36j** and **36l** were confirmed by ^{1}H NMR and APT spectroscopy. In the ^{1}H NMR spectra, compared with their TCE-protected precursors, the characteristic methylene signals of the TCE group, previously observed at 5.24 and 5.26 ppm, were no longer present. In addition, the aromatic region in **36j** shifts upfield by approximately 0.2 ppm compared with its precursor, while in **36l** an upfield shift of about 0.3 ppm is observed.

In the APT spectra of **36j** and **36l**, the aromatic carbons were clearly observed in the 110-130 ppm region. Due to differences in substitution patterns, distinct signal distributions were evident. For **36j**, which bears a para-amino substituent, the four aromatic CH carbons are symmetrically arranged and therefore give rise to only two signals, appearing at 121.8 and 113.7 ppm. In contrast, **36l**, the ortho-substituted derivative, exhibits four non-equivalent aromatic CH carbons, resonating at 124.6, 123.0, 116.4, and 115.7 ppm.

Although APT spectra of the corresponding sulfate diesters were not available for direct comparison, it is well established that the -CCl_3 and -CH_2 carbons of the TCE group consistently appear at approximately 92 ppm and 80 ppm, respectively. The absence of signals in this region in the APT spectra of **36j** and **36l** strongly supports the successful removal of the TCE protecting group.

Further structural confirmation of **35j** and **35l** was obtained by ESI-HRMS analysis. First, the mass spectrum of the para-aminophenyl sulfate **36j** was analysed. In the ESI- HRMS spectrum, a peak at *m/z* 188.0060 can be assigned to the deprotonated molecular ion $[M]^-$, which is in good agreement with the calculated value of 188.0016. A neighbouring peak at *m/z* 189.0084 is observed, differing from $[M]^-$ by +1.0024 Da, consistent with the characteristic ^{13}C isotopic peak (M+1). In this spectrum, the $[M]^-$ ion is not the base peak, as numerous additional signals are

present. These are presumed to arise from residual cleaning agents. Such species typically exhibit very strong responses in negative ion mode and may cause ion suppression, making the $[M]^-$ signal appear less prominent. Subsequently, the mass spectrum of the ortho-aminophenyl sulfate **36l** was examined. In the ESI- HRMS spectrum of **36l**, the base peak appears at *m/z* 188.0027 and can be assigned to $[M]^-$, in excellent agreement with the calculated mass. An adjacent peak at *m/z* 189.0051 corresponded to the ^{13}C isotopic peak of the molecular ion.

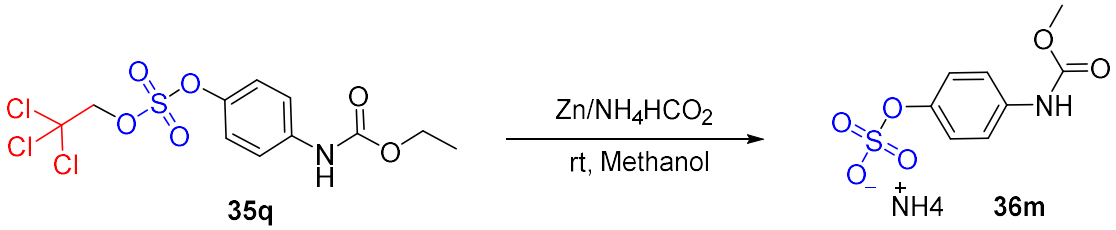

Scheme 35. The synthesis of **36m**.

Next, we attempted removal of the TCE protecting group from the ethyl carbamate-substituted sulfate diesters **35q-35s**. The deprotection reactions were carried out under conditions identical to those used for the F-substituted analogues. However, purification was performed by preparative TLC rather than silica gel column chromatography, as noted with compounds **36d-36f**. Under these conditions, the para- and meta-substituted sulfates **36m** and **36n** were successfully obtained, whereas attempts to prepare the ortho-substituted sulfate were unsuccessful.

For 36m, only ^1H NMR data were obtained, as the instability of this compound allowed a pure sample to be isolated only once. However, **36n** was characterized by both ^1H NMR and ^{13}C spectroscopy. Compared with their corresponding para- and meta-substituted sulfate diesters (**35r** and **35s**), the most significant change in the ^1H NMR spectra of **36m** and **36n** is the disappearance of the characteristic TCE methylene signal at around 4.8 ppm, confirming successful removal of the protecting group.

In the final stage of this study, we attempted the removal of the TCE protecting group

from the aldehyde-substituted sulfate diester. We anticipated that the aldehyde might be subject to reduction under these conditions as seen in, but nonetheless proceeded out of interest.[191] Initially, the deprotection reaction and purification were carried out under the same conditions used for the F-substituted analogues. TLC monitoring indicated that the reaction itself proceeded efficiently, with clear consumption of the starting material and formation of a new product spot. However, the desired product could not be successfully isolated by column chromatography, as significant decomposition occurred during purification.

To overcome this issue, the purification conditions were modified by adding a small amount of triethylamine to the eluent to neutralize the acidic sites on silica gel, and preparative TLC was employed instead of conventional column chromatography. Unfortunately, despite these adjustments, the second attempt also failed to afford any isolable product. These results suggest that the aldehyde-substituted sulfate is highly unstable under the purification conditions employed, likely due to its increased sensitivity in mildly acidic environments.

2.2 Investigation of analytical techniques to support enzymatic hydrolysis monitoring

In this study, a combination of analytical techniques was employed to characterize the synthesized products. High-performance liquid chromatography (HPLC) was applied to evaluate compound purity, stability, and the differences between sulfate esters and their corresponding phenols. Ultraviolet–visible (UV-Vis) absorption spectroscopy was utilized to investigate how changes in substituents and functional groups influence the electronic structure of the molecules.

In previous studies, UV-Vis spectroscopy has been used to monitor the conversion between phenolic compounds and their corresponding sulfate esters.[192] However, in our study, the UV-Vis absorption spectra of the sulfated products and their corresponding phenols showed only minimal differences, with significant overlap across a broad wavelength range. This observation indicates that UV-Vis spectroscopy is not a suitable method for reliably identifying sulfation reactions or enzymatic hydrolysis in our system.

Nevertheless, UV–Vis spectroscopy provided supportive data for the sulfated products. Although it was not feasible to monitor the sulfation process in real time, the absorption profiles depend on the nature of the electronic transitions and are strongly influenced by conjugation, electronic effects, and molecular conformation. Therefore, this technique enabled a systematic evaluation of how different substituents affect the absorption behaviour of the compounds.

2.2.1 Characteristics of Ultraviolet–Visible Absorption Spectroscopy

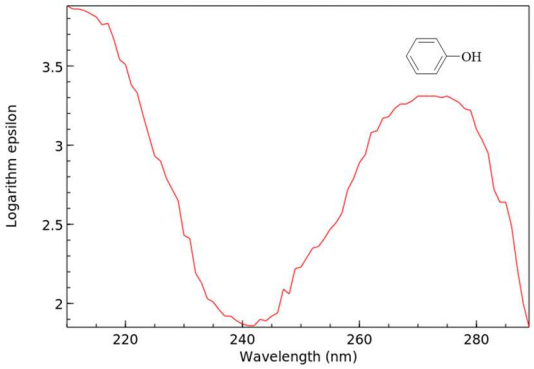

Figure 22. The UV-Vis spectrum of phenol.[193]

Phenol exhibits UV-Vis absorption dominated by an aromatic π→π* electronic transitions, with its λ_{max} typically appearing in the range of approximately 260-280 nm.[194,195] The resonance electron-donating effect of the hydroxyl group increases the π-electron density of the aromatic ring, leading to a slight bathochromic shift accompanied by enhanced absorption intensity. In polar solvents, hydrogen-bonding interactions may modulate the spectral profile to some extent. However, the overall absorption characteristics remain primarily governed by π→π* transitions.

The UV-Vis spectra of phenol derivatives are primarily influenced by the electronic effects of substituents on the aromatic ring.[196] In this study, -F, -NH_2, -NHCOO-*tBu*, -NHCOOEt, -CN, -$COOCH_3$, and -CHO were investigated as substituents on the phenyl ring. The -NH_2 group is a strong electron-donating substituent, as its lone pair can participate in effective resonance donation to the aromatic ring, thereby significantly increasing the π-electron density. Consequently, the presence of -NH_2 typically results in a pronounced bathochromic shift of the π→π absorption maximum. In contrast, in the -NHCOO-*tBu* substituent, the nitrogen lone pair is partially delocalised into the adjacent carbonyl group. This conjugation markedly reduces its electron-donating ability toward the aromatic ring compared with -NH_2.

Accordingly, a bathochromic shift is still observed in the UV-Vis spectrum, but to a lesser extent than that induced by -NH_2.

Fluorine substituents display a combination of a strong inductive electron-withdrawing effect and a weak resonance electron-donating effect, these two effects compete. Consequently, their overall perturbation of the aromatic π-electron system is relatively small, typically leading to only minor shifts in absorption wavelength or modest changes in absorption intensity. The -CN group is a strong electron-withdrawing substituent with a pronounced resonance-withdrawing effect, which effectively reduces the π-electron density of the aromatic ring. Its introduction generally causes a significant hypsochromic shift of the π→π* absorption band. The -$COOCH_3$ group is a moderately strong electron-withdrawing substituent, exerting both −M and −I effects through the carbonyl moiety. Its presence typically results in a slight hypsochromic shift of the λ_{max}.

Overall, electron-donating substituents enhance aromatic π-conjugation and induce a bathochromic shift of the λ_{max}, whereas electron-withdrawing substituents attenuate the aromatic π-electron system, leading to a hypsochromic shift the λ_{max}. In addition, substituents containing carbonyl groups may introduce additional n→π* transition features in the UV-Vis spectra.

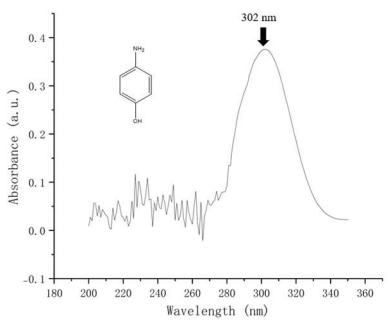

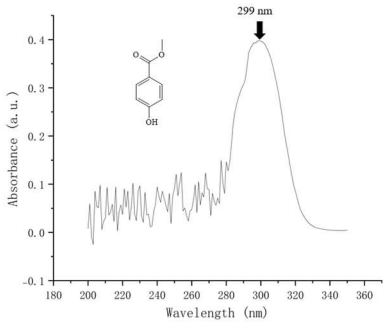

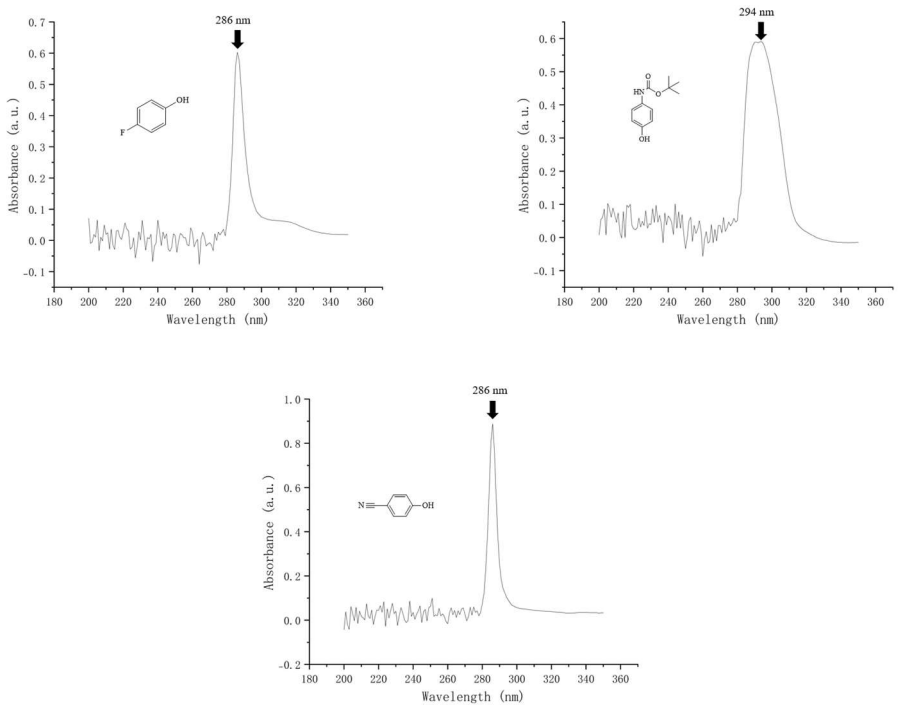

Figure 23. The UV-Vis results of 4-aminophenol, 4-fluorophenol, 4-N-Boc aminophenol, 4-cyanophenol, and 4-$COOCH_3$ phenol.

Phenolic compounds typically exhibit a distinct absorption band in the range of 280–300 nm. Compared with their corresponding phenols, aryl sulfates generally display a slight bathochromic shift in the maximum absorption wavelength (λ_{max}). This shift arises because the strongly electron-withdrawing sulfate group alters the electronic distribution of the aromatic ring and modifies its π–π conjugation system.

In polar solvents, solvation effects and hydrogen-bonding interactions further influence the n→π* transitions, leading to broader absorption bands for aryl sulfates. As a result, significant overlap is often observed between the UV–Vis absorption spectra of aryl sulfates and their parent phenols. Therefore, UV–Vis spectroscopy is suitable for confirming the complete conversion of phenols to sulfates, but it is not sufficiently sensitive to detect partial or incomplete conversion.

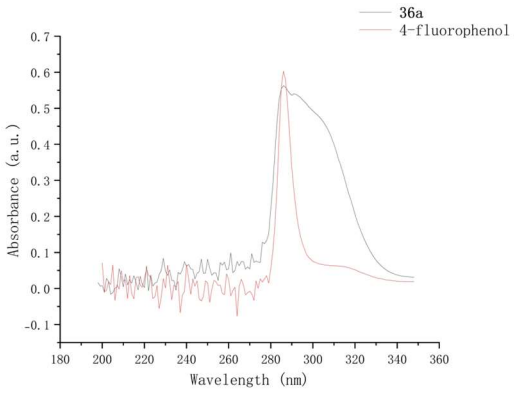
36a
4-fluorophenol
Absorbance (a.u.)
Wavelength (nm)

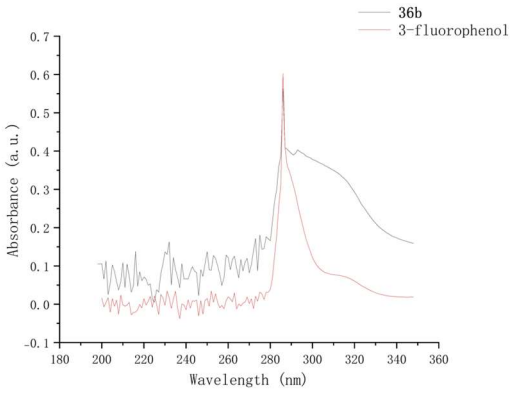
36b
3-fluorophenol
Absorbance (a.u.)
Wavelength (nm)

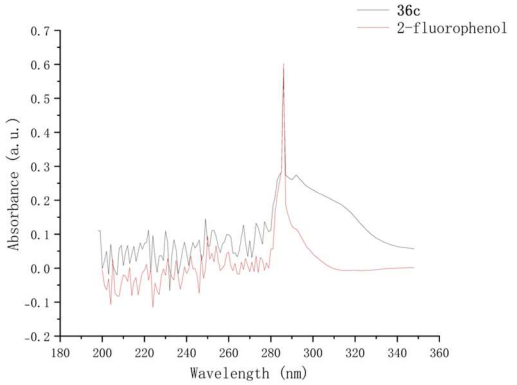
36c
2-fluorophenol
Absorbance (a.u.)
Wavelength (nm)

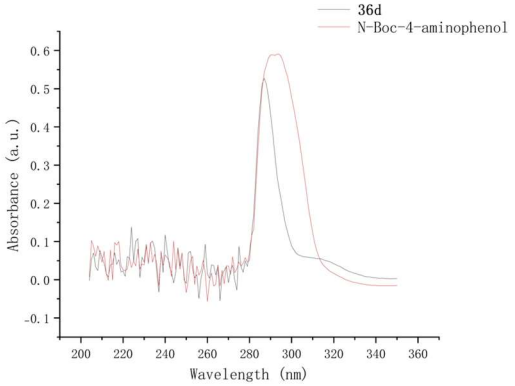
36d
N-Boc-4-aminophenol
Absorbance (a.u.)
Wavelength (nm)

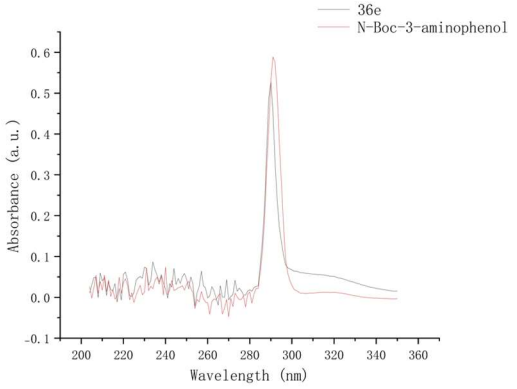
36e
N-Boc-3-aminophenol
Absorbance (a.u.)
Wavelength (nm)

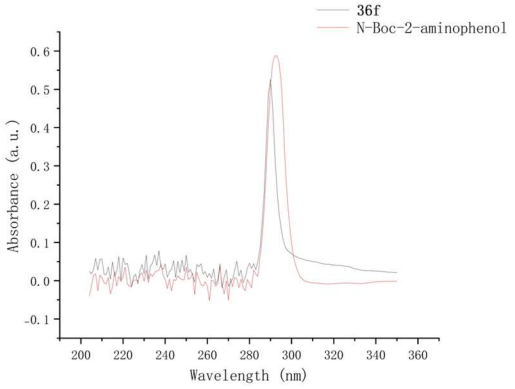
36f
N-Boc-2-aminophenol
Absorbance (a.u.)
Wavelength (nm)

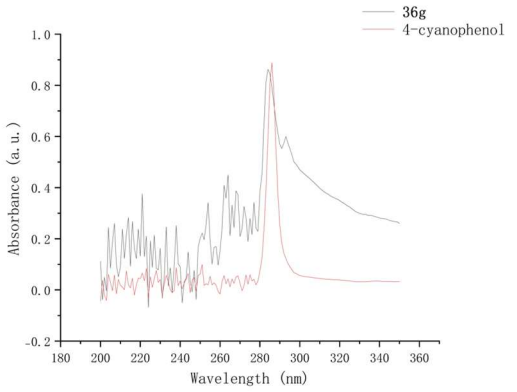
36g
4-cyanophenol
Absorbance (a.u.)
Wavelength (nm)

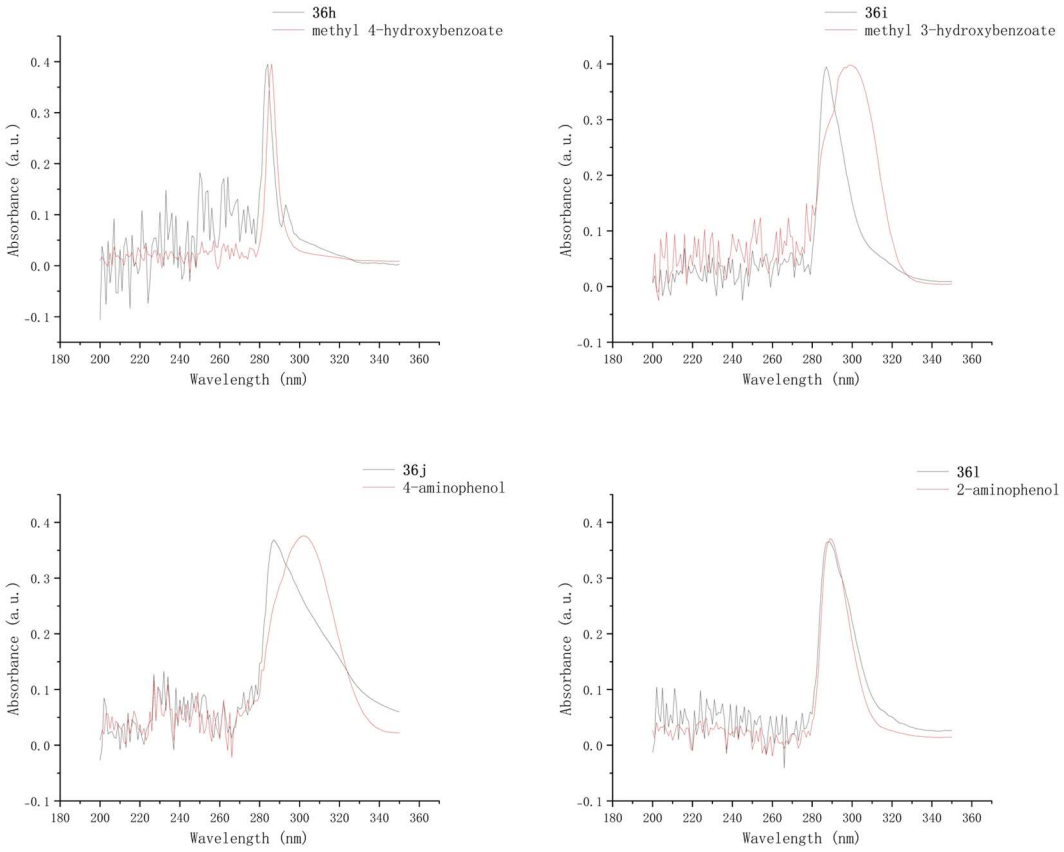

Figure 24. The UV-Vis results of sulfates and their responding phenols.

2.2.2 Analysis of High-Performance Liquid Chromatography (HPLC)

As a high-resolution separation technique, HPLC enables effective characterization of aryl sulfate esters and their corresponding phenols. In this study, HPLC was employed to verify the purity of the target compounds, to distinguish starting materials, products, and by-products, and to confirm the ability to separate the peaks.

The HPLC results show that, all aryl sulfate esters exhibit markedly shorter retention times under reversed-phase conditions, versus the corresponding phenols which have prolonged retention times. This pronounced difference can be primarily attributed to the introduction of the sulfate moiety, which substantially increases the molecular polarity and thereby weakens hydrophobic interactions with the C_{18} stationary phase.

Regardless of whether the substituent was an electron-withdrawing group, exemplified by -CN, or an electron-donating group, exemplified by -NH_2, the corresponding compounds exhibited very similar elution behaviour. The sulfate clearly produced the dominant effect as polarity of the other substituents didn't have a significant effect on elution time. Notably, the Boc-amino group even increases the overall hydrophobicity of the molecule, the dominant role of sulfate moiety in HPLC is still obvious. In all cases, this difference was sufficient to afford robust baseline separation across the entire set of systems studied.

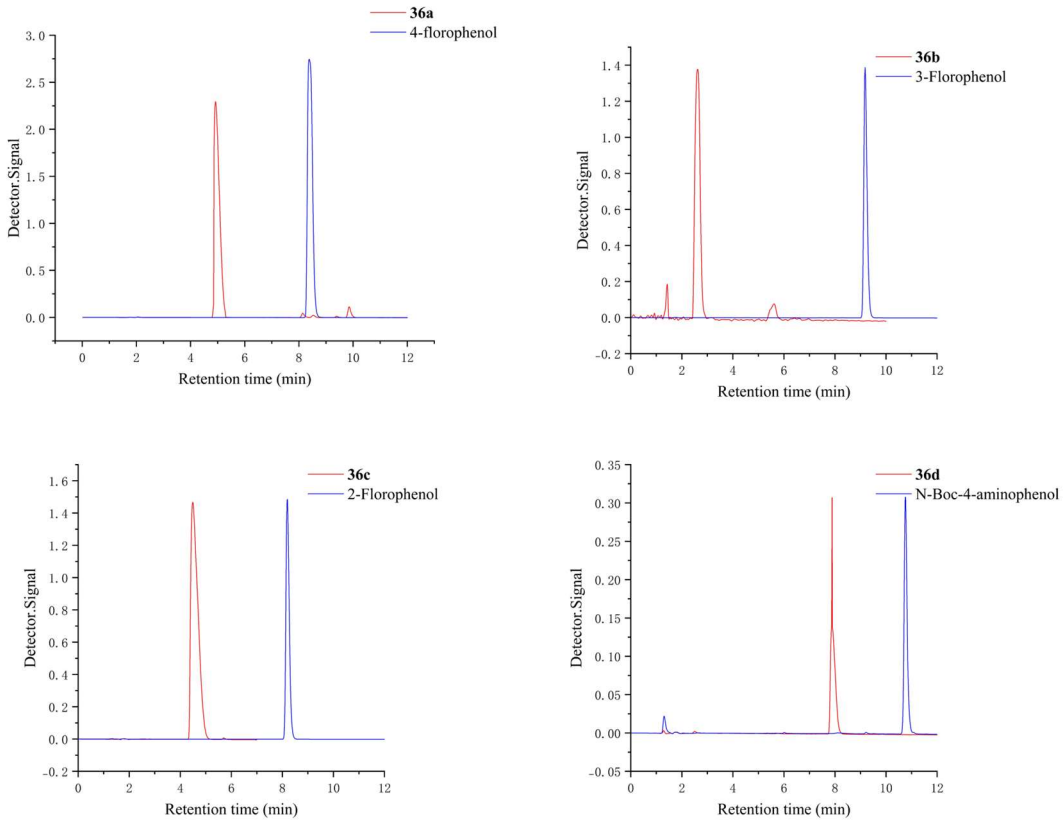

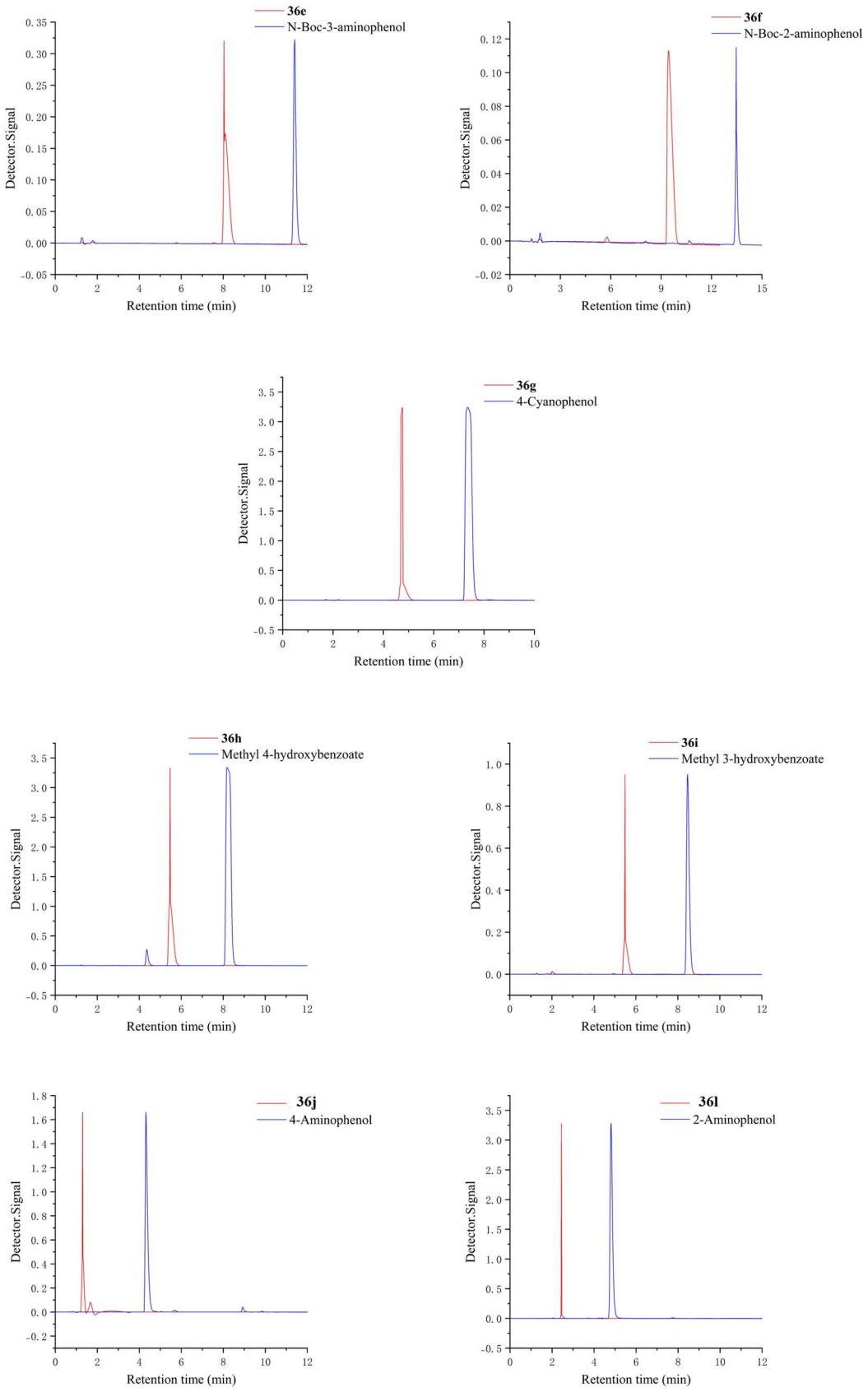

Figure 25. The HPLC results of sulfate and their corresponding phenols.

In the HPLC analysis of this series of products and their corresponding phenols, nearly all samples exhibited highly consistent and clean chromatographic behaviour across different detection wavelengths. The UV–Vis measurements indicated that the λ_{max} of these sulfate derivatives are all located around 290 nm. Based on this observation, and to streamline the analytical procedure, a single detection wavelength of 290 nm was selected for all subsequent HPLC analyses. At 290 nm, most chromatograms were dominated by a single peak, with variations observed only in peak intensity rather than peak number or retention time. This is expected, as each compound shows its strongest detector response at its characteristic absorption wavelength, while the response at other wavelengths is comparatively weaker.

In contrast, sulfate **36a** displayed a markedly different chromatographic profile. Multiple additional peaks were observed at all detection wavelengths, clearly distinguishing **36a** from the other samples. Because pure NMR spectra were obtained after the preparation of **36a**, confirming its integrity at that stage, we suspect that **36a** may undergo partial decomposition either in aqueous solution or under the HPLC conditions.

Overall, these HPLC results demonstrate that the established method is both general and robust across a diverse range of aryl sulfate systems. The method was successfully applied to TCE-protected sulfate diesters as well as the corresponding deprotected sulfate salts, encompassing electron-withdrawing substituents (-F, -CN, -$COOCH_3$) and electron-donating substituents (-NH_2) in ortho-, meta-, and para-substitution patterns. Despite the significant electronic differences among these substituents, clear chromatographic separation between aryl sulfates and their corresponding phenols was consistently achieved.

In all cases examined, the aryl sulfates eluted earlier than their parent phenols under the selected reversed-phase conditions, reflecting the increased polarity imparted by the sulfate group. This retention behaviour was reproducible across different substitution

patterns, indicating that the method is not highly sensitive to positional effects on the aromatic ring. Furthermore, no co-elution between sulfate species and phenolic starting materials was observed, confirming that the method provides sufficient resolution for reliable qualitative and quantitative assessment.

Regarding the phenol standards, minor additional peaks were observed in some of the chromatograms. In all HPLC experiments, freshly prepared phenol samples were used for analysis. This indicates that the small extra peaks most likely arise from trace impurities present in the commercial phenol materials, rather than being generated during the HPLC procedure itself.

Taken together, these results confirm that the established HPLC protocol provides a reliable and reproducible analytical platform for distinguishing aryl sulfates from phenols. It is therefore well suited for monitoring sulfate-to-phenol conversion in subsequent studies, including both chemically induced deprotection reactions and enzyme-catalysed sulfate hydrolysis experiments.

2.3 Future Work

This study establishes a reliable and general synthetic and analytical framework for a series of substituted aryl sulfates, which were systematically characterized by NMR, HPLC, mass spectrometry, and UV-Vis spectroscopy. In introducing the sulfate group into aromatic systems, a TCE-protected imidazolium salt was employed as the sulfating reagent. This approach is operationally straightforward and mechanistically well defined. However, the overall isolated yields were moderate. Even after 24 hours of reaction, TLC analysis frequently indicated the presence of substantial amounts of unreacted starting material. We hypothesize that this limitation is primarily associated with trace water contamination during the reaction. The sulfation process is highly moisture-sensitive, which motivated the use of dry dichloromethane as the reaction solvent. Nevertheless, incomplete system sealing or residual moisture in reagents may

still introduce water into the reaction mixture, thereby retarding conversion. In future studies, particularly when extending this methodology to a broader range of phenolic substrates, improving reaction system integrity and moisture exclusion will be essential.

In addition, product loss during column and preparative TLC chromatography was observed following the sulfation step, which further reduced overall yields. To minimize material loss during purification, alternative strategies should be explored, such as the use of ion-exchange chromatography or recrystallization-based methods, which may offer improved recovery and selectivity for these highly polar aryl sulfates.

Further optimization is also required for the deprotection step, as most reactions in this study afforded unsatisfactory yields. This issue is likely related to the ionic nature of the sulfate salts formed after deprotection. Charged sulfate products are inherently challenging to purify, and conventional silica gel chromatography did not provide consistently satisfactory results in this work. Future efforts should therefore focus on alternative purification techniques, particularly those capable of efficiently removing residual metals and inorganic salts.

Based on the work reported by Bargh's team[27], it is known that introduction of a -NO_2 group renders the sulfate moiety more susceptible to cleavage by sulfatases. As -NO_2 is a strongly electron-withdrawing substituent, this observation suggests that the electronic effects of substituents on the aromatic ring may play an important role in governing the enzymatic hydrolysis of aryl sulfates. However, because the -NO_2 group is incompatible with the Zn-mediated deprotection conditions, this direction was not investigated in the present study. In future studies, a broader library of aryl sulfates bearing diverse substituents can be synthesized and evaluated as sulfatase substrates. With a robust synthesis and analysis established differences in structural tolerances across the arylsulfatase family could be established allowing more specific targeting of sulfatase cleavable linkers to cell compartments and reducing off-target linker cleavage.

In previous reports, UV-Vis spectroscopy has often been used to distinguish sulfates from their corresponding phenols.[197–199] However, the data obtained in this work indicate that UV-Vis is not well suited for this purpose, as the absorption maxima of aryl sulfates and their parent phenols are often very close and difficult to resolve reliably. We therefore recommend the use of the HPLC method established in this study to differentiate aryl sulfates from their corresponding phenols and to monitor their enzymatic hydrolysis. Application of this robust and selective analytical approach will enable systematic investigation of substituent effects on sulfatase-catalysed cleavage, ultimately providing valuable data to support the rational development of sulfatase-cleavable linkers.

In addition, the aryl sulfate motifs explored in this study, as well as those to be synthesized in future work, can be further modified and optimized to form conjugates with a range of small-molecule drugs for biomedical research applications. In such systems, the drug release efficiency can be quantitatively evaluated and used as a key criterion to assess the suitability of these sulfates as linker candidates. This approach will provide a practical and functionally relevant basis for determining whether the developed sulfate structures are viable for incorporation into linker design and drug delivery studies.

Finally, future investigations could examine conjugation efficiency, linker stability, and drug-antibody ratio (DAR), followed by preliminary biological evaluation. Comparison with established peptide-based cleavable linkers would further contextualise the advantages and limitations of aryl sulfate-based linker design within the broader ADC linker landscape.

3. Experimental

3.1 General Experimental

All glassware was oven dried at 110 °C for several hours and cooled under ambient temperature and pressure. Unless otherwise noted, materials were obtained from commercial suppliers and used without further purification. Solvents designated as dry were dispensed from a PureSolv solvent purifier having passed over alumina drying columns under an inert atmosphere. Flash chromatography columns were packed with 245 mesh silica gel and plates were packed with 265 mesh silica gel. All NMR spectra were acquired using a JEOL ECZR 600 MHz spectrometer equipped with a Royal HFX probe. NMR data was processed using Delta 6.0.0 software. Indicative MS was carried out using a Bruker micrOTOF instrument, using ESI and a TOF analyser (positive- and negative- ion mode), until instrument failure in early 2025. MS spectrometric analysis was outsourced to the University of Auckland, where samples were run on a SCIEX TripleTOF 6600. HPLC separation was performed using a Phenomonex Luna 5 μM C18(2) 100 Å column (100 mm × 4.6 mm), with a Phenomonex SecurityGuard guard column. HPLC analysis was carried out using a sample prepared by dissolving 10 mg of analyte in a mixture of 8 mL deionized water and 2 mL of 45 mM ammonium formate buffer solution. The injection volume was 20 μL. The mobile phase consisted of solvent A: 45 mM ammonium formate buffer solution and solvent B: 80% acetonitrile in water. Elution was performed under isocratic conditions using an A:B ratio of 8:2. The flow rate was set at 1.0 mL/min, and the total run time was 26 min. Detection was carried out over the wavelength range of 210-400 nm. UV-visible absorption spectra were recorded on an Agilent Cary 100 UV-Vis spectrophotometer using quartz cuvettes (1 cm path length) over a wavelength range of 200-400 nm. Samples of phenolic compounds were prepared in deionised water and measured using deionised water as the solvent blank, while sulfate salts were prepared in ethanol and measured using

ethanol as the solvent blank.

3.2 Synthetic Compounds

3.2.1 General Procedure for sulfation reactions

General Procedure **A**:

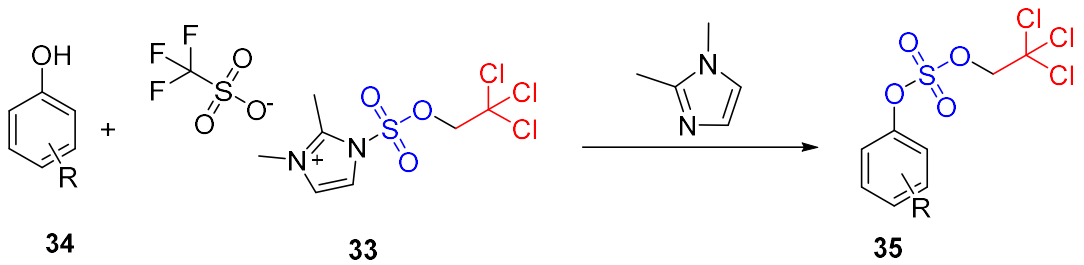

To phenol **34** (1 eq.) in DCM (10 mL) was added imidazolium salt **33** (1.05 eq.) at 0 °C. Then, 1,2-dimethylimidazole (2.05 eq.) was added dropwise to the mixture over a period of 15 minutes at 0°C. The reaction mixture was warmed to room temperature and stirred for 24 hours. After 24 hours, the reaction was quenched by addition of deionized water (5 mL). The aqueous phase was extracted with DCM (3 × 2 mL). The organic phase was collected and dried over Na_2SO_4, then filtered and concentrated *in vacuo*. The crude material was purified by flash chromatography or preparative TLC on silica gel eluting with DCM/Hexane (1:1, v/v) to afford the product.

General Procedure **B**:

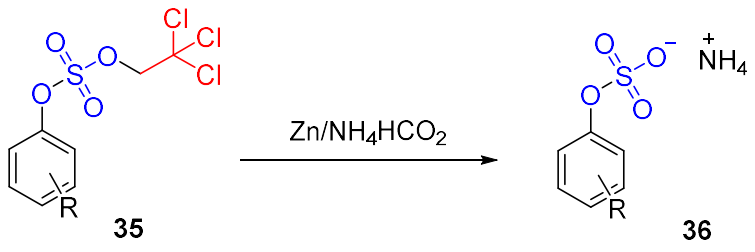

To the protected sulfate **35** (1 eq.) in MeOH (5 mL) was added ammonium formate (8 eq.) and zinc dust (4 eq.) at room temperature. The reaction mixture was stirred until all ammonium formate had dissolved, which took approximately 1 hour. The mixture was filtered through Celite. The filtrate was collected and concentrated *in vacuo* to give a crude solid. The crude material was dissolved in a minimal CH_2Cl_2/MeOH/Et_3N (20:1:0.5, v/v) and purified by flash chromatography or preparative TLC to afford the product as a white solid, which was lyophilized at -60 °C for 24 h to afford the final product.

3.2.2 Synthetic compounds

2,2,2-Trichloroethyl 2-methyl-1*H*-imidazole-1-sulfonate (**32**)

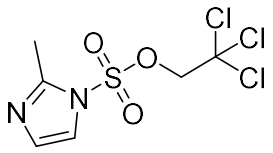

To a solution of 2-methylimidazole (4.06 g, 49.5mmol) in dry THF (20 mL) at 0 ℃ was added dropwise a solution of chlorosulfate **28** in THF (30 mL). The reaction was stirred at 0 ℃ for 1 h, warmed to rt, and stirred for an additional 1 h. The reaction mixture was filtered, the residue was washed with THF (3 × 5 mL), and the filtrate was concentrated under vacuum. The crude material was purified by flash chromatography (EtOAc : hexanes = 1:2) to give **32** as a white solid (3.87 g, 96%): ^{1}H NMR (600 MHz, $CDCl_3$) δ 7.49 (d, *J* = 1.2 Hz, 1H, H-5), 7.11 (d, *J*= 1.9 HZ, 1H, H-4), 4.81 (s, 2H, CH_2), 2.84 (s, 3H, 2-CCH_3). The observed chemical shifts and coupling patterns are consistent with literature reports.[184]

2,3-Dimethyl-1-((2,2,2-trichloroethoxy)sulfonyl)-1*H*-imidazol-3-ium (**33**)

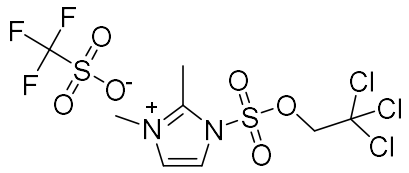

To a solution of **32** (3.5 g, 11.9 mmol) in dry Et_2O (55 mL) at 0 ℃ was added dropwise methyl triflate (1.35 mL, 11.9 mmol). The reaction solution was stirred for 3 h at 0 ℃ during which time a white precipitate formed. The mixture was filtered, the filter cake was washed with cold ether, and the mother liquor was cooled to - 20 ℃ for 0.5 h and filtered again. This second precipitate was washed with cold ether and then combined with the first precipitate, which afforded **33** as a white solid (4.80 g, 88%): ^{1}H NMR (600 MHz, DMSO-d_6) δ 8.20 (d, J = 2.5 Hz, 1H, H-5), 7.94 (d, J = 2.4 Hz, 1H, H-4), 5.52 (s, 2H, CH_2), 3.82 (s, 3H, 3-NCH_3), 2.83 (s, 3H, 2-CCH_3). The observed chemical shifts and coupling patterns are consistent with literature reports.[184]

tert-Butyl (4-hydroxyphenyl)carbamate (**34a**)

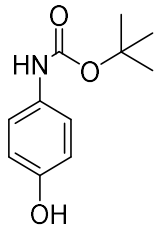

To 4-aminophenol (0.50 g, 4.6 mmol) in dry THF (20 mL) was added Boc_2O (1.10 g, 5.0 mmol) at 0 ℃. The reaction was stirred at 0 ℃ for 12 h until the starting material was consumed. The reaction was concentrated under reduced pressure. The residue was dissolved in DCM (20 mL) and extracted with water (3 × 5 mL). The organic layer was dried over anhydrous sodium sulfate, filtered, and concentrated under reduced pressure. Finally, the product **34a** was obtained as a brown solid (0.93 g, 4.44 mmol, 97%), which was used in the next step without further purification: ^{1}H NMR (600 MHz, $CDCl_3$) δ 9.02 (s, 1H, OH), 7.20 (d, J = 8.0 Hz, 2H, H-3, H-5), 6.64 (d, J= 8.9 Hz, 2H, H-2, H-6), 1.44 (s, 9H, $C(CH_3)_3$,). The observed chemical shifts and coupling patterns are

consistent with literature reports.[187]

tert-Butyl (2-hydroxyphenyl)carbamate (**34b**)

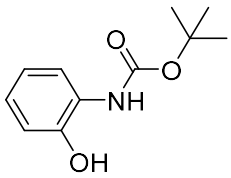

To 2-aminophenol (0.50 g, 4.6 mmol) in dry THF (20 mL) was added Boc_2O (1.10 g, 5.0 mmol) at 0 °C. The reaction was stirred at 0 °C for 12 h until the starting material was completed. The reaction was concentrated under reduced pressure. The residue was dissolved in DCM (20 mL) and extracted with water (3 × 5 mL). The organic layer was dried over anhydrous sodium sulfate, filtered, and concentrated under reduced pressure. Finally, the product **34b** was obtained as a brown solid (0.91 g, 4.35 mmol, 95%), which was used in the next step without further purification: ^{1}H NMR (600 MHz, $CDCl_3$) δ 8.16 (s, 1H, OH), 7.11 (d, J = 7.9 Hz, 1H, 1-NH), 7.03 (ddd, *J* = 8.0, 7.3, 1.6 Hz, 1H, H-6), 6.96 (dd, *J* = 8.1, 1.5 Hz, 1H, H-4), 6.85 (d, *J*= 7.8, 1.5 Hz, 1H, H-3), 6.71 (s, 1H, H-5), 1.52 (d, *J* = 1.9 Hz, 9H, $(CH_3)_3$). The observed chemical shifts and coupling patterns are consistent with literature reports.[200]

Methyl 4-hydroxybenzoate (**34c**)

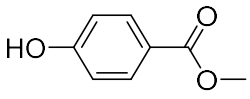

To 4-hydroxybenzoic acid (1.00 g, 7.2 mmol) in MeOH (13 mL) was added H_2SO_4 (0.19 mL, 3.62 mmol) at 80 ºC. The reaction was stirred for 4 hours under reflux. The reaction was concentrated *in vacuo* to get a crude oil. The crude material was diluted in water and extracted with EtOAc (3 × 5 mL). The organic phase was washed with brine and was dried over Na_2SO_4. The resulting liquid was concentrated under reduced

pressure to afford **34c** as a white solid (1.05 g, 6.88 mmol, 95%): ^{1}H NMR (600 MHz, $CDCl_3$) δ 7.96 (m, *J* = 8.8 Hz, 2H, H-3, H-5), 6.86 (d, *J* = 8.7 Hz, 2H, H-2, H-6), 5.66 (b.s, 1H, OH), 3.89 (s, 3H, OCH_3). The observed chemical shifts and coupling patterns are consistent with literature reports.[201]

Ethyl (2-hydroxyphenyl)carbamate (**34d**)

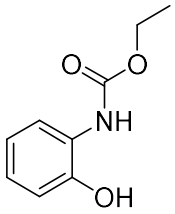

To a solution of 2-aminophenol (0.98 g, 9.0 mmol) in water (10 mL) was added sodium bicarbonate (1.26 g, 15.0 mmol) and DCM (30 mL) to generate a biphasic mixture. The reaction was vigorously stirred at room temperature, and ethyl chloroformate (1.03 g, 9.5 mmol) was added dropwise. After complete addition, stirring was continued at room temperature for 2 h. The reaction was concentrated under reduced pressure, the crude residue was suspended in acetone (5 mL), filtered, and the organic residues were dried over Na_2SO_4. Purification by flash column chromatography on silica gel using EtOAc/hexanes (1:1) as the eluent afforded the desired product as a white solid (1.46 g, 8.06 mmol, 90%): ^{1}H NMR (600 MHz, $CDCl_3$) δ 7.75 (b.s, 1H, OH), 7.27 (b.s, 1H, 1-NH), 7.11-7.00 (m, 1H, H-6), 6.99-6.81 (m, 3H, H-3, H-4, H-5), 4.25 (q, J = 7.2 Hz, 2H, O*CH*$_2$CH$_3$), 1.33 (q, J = 7.8 Hz, 3H, OCH$_2$*CH*$_3$). The observed chemical shifts and coupling patterns are consistent with literature reports.[190]

4-Fluorophenyl (2,2,2-trichloroethyl) sulfate (**35a**)

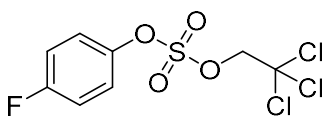

Following general procedure A, 4-fluorophenol (80 mg, 0.711 mmol) and **33** (342 mg,

0.747 mmol) were combined to give the crude product that was purified by flash chromatography on silica gel eluting with DCM/Hexane (0:1 to 1:1, v/v) to afford the product as a white solid (150 mg, 0.462 mmol, 65%): mp 78.9-80.2 ºC; ^{1}H NMR (600 MHz, $CDCl_3$) δ 7.38-7.31 (m, 2H, H-3, H-5), 7.17-7.10 (m, 2H, H-2, H-6), 4.83 (s, 2H, CH_2). ^{13}C NMR (151 MHz, $CDCl_3$) δ 161.4 (d, ^{1}JCF ≈ 241.6 Hz, 4-C), 145.9 (d, ^{4}JCF ≈ 3.0 Hz, 1-C), 123.0 (d, ^{3}JCF ≈ 9.1 Hz, 2-CH, 6-CH), 117.0 (d, ^{2}JCF ≈ 24.2 Hz, 3-CH, 5-CH), 92.4 (CCl_3), 80.5 (CH_2); HRMS calculated for $C_6H_4FO_4S$ [M-TCE]$^-$ *m/z* 190.9814, found 190.9811 (-1.57 ppm).

3-Fluorophenyl (2,2,2-trichloroethyl) sulfate (**35b**)

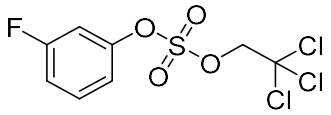

Following general procedure **A**, 3-fluorophenol (80 mg, 0.711 mmol) and **33** (342 mg, 0.747 mmol) were combined to give the crude product that was purified by flash chromatography on silica gel eluting with DCM/Hexane (0:1 to 1:1, v/v) to afford the product as a white solid (131mg, 0.405 mmol, 57%): mp 75.4-75.8 ºC; ^{1}H NMR (600 MHz, $CDCl_3$) δ 7.42 (td, *J* = 8.3, 6.3 Hz, 1H, 2-H), 7.18 (ddt, *J* = 8.4, 2.3, 0.8 Hz, 1H, 4-H), 7.10 (td, *J* = 6.0 Hz, 2.4 Hz, 1H, 5-H), 7.08 (ddt, *J* = 12.0 Hz, 2.49 Hz, 1.0 Hz, 1H, 6-H), 4.86 (s, 2H, CH_2); ^{13}C NMR (151 MHz, $CDCl_3$) δ 163.0 (d, ^{1}JCF ≈ 250.6 Hz, 3-C), 150.6 (d, ^{3}JCF ≈ 10.6 Hz, 1-C), 131.1 (d, ^{3}JCF ≈ 9.1 Hz, 5-CH), 117.0 (d, ^{4}JCF ≈ 3.0 Hz, 6-CH), 115.3 (d, ^{2}JCF ≈ 21.1 Hz, 2-CH), 109.6 (d, ^{2}JCF ≈ 25.7 Hz, 4-CH), 92.4 (CCl_3), 80.7 (CH_2); HRMS calculated for $C_6H_4FO_4S$ [M-TCE]$^-$ *m/z* 190.9814, found 190.9811 (-1.57 ppm).

2-Fluorophenyl (2,2,2-trichloroethyl) sulfate (**35c**)

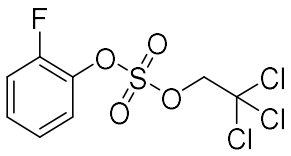

Following general procedure **A**, 2-fluorophenol (80 mg, 0.711 mmol) and **33** (342 mg, 0.747 mmol) were combined to give the crude product that was purified by flash chromatography on silica gel eluting with DCM/Hexane (0:1 to 1:1, v/v) to afford the product as a white solid (115 mg, 0.355 mmol, 50%): mp 76.8-77.1 ºC; ^{1}H NMR (600 MHz, $CDCl_3$) δ 7.49 (ddd, *J* = 8.2, 7.6, 1.6 Hz, 1H, H-6), 7.35 (dddd, *J* = 8.3, 7.5, 4.8, 1.7 Hz, 1H, H-4), 7.28-7.19 (m, 2H, H-4, H-3), 4.92 (s, 2H, CH_2). ^{13}C NMR (151 MHz, $CDCl_3$) δ 154.0 (d, ^{1}JCF ≈ 252.2 Hz, 2-C), 137.4 (d, ^{2}JCF ≈ 12.1 Hz, 1-C), 129.4 (d, ^{3}JCF ≈ 6.0 Hz, 4-CH), 125.3 (d, ^{4}JCF ≈ 4.5 Hz, 5-CH), 124.1 (s, 6-CH), 117.6 (d, ^{2}JCF ≈ 18.1 Hz, 3-CH), 92.4 (s, CCl_3), 80.7 (d, *J* = 1.5 Hz, CH_2); HRMS calculated for $C_6H_4FO_4S$ $[M\text{-}TCE]^-$ *m/z* 190.9814, found 190.9812 (-1.05 ppm).

4-((tert-butoxycarbonyl)amino)phenyl (2,2,2-trichloroethyl) sulfate (**35d**)

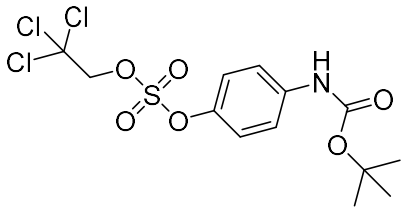

Following general procedure **A**, **34a** (149 mg, 0.710 mmol) and **33** (341 mg, 0.746 mmol) were combined to give the crude product that was purified by preparative TLC on silica gel eluting with DCM/hexane/Et_3N (1:1:1, v/v) to afford the product as a white solid (200 mg, 0.476 mmol, 67%): mp 107.9-108.1 ºC; ^{1}H NMR (600 MHz, $CDCl_3$) δ 7.43 (d, *J* = 8.9 Hz, 2H, H-3, H-5), 7.28 (dt, *J* = 9.1, 5.6 Hz, 2H, H-2, H-6), 6.54 (b.s, 1H, NH), 4.80 (s, 2H, CH_2), 1.52 (s, 9H, $C(CH_3)_3$); ^{13}C NMR (151 MHz, $CDCl_3$) δ 152.6 (C=O), 145.2 (1-C), 138.2 (4-C), 121.9 (CH-2/6), 119.7 (CH-3/5), 92.5 (CCl_3), 80.4 ($C(CH_3)_3$), 80.3 (CH_2), 28.4 ($C(CH_3)_3$). HRMS calculated for $C_{13}H_{15}Cl_3NO_6S$ [M-

O]$^-$ *m/z* 417.9683, found 417.9704 (5.2 ppm).

3-((tert-butoxycarbonyl)amino)phenyl (2,2,2-trichloroethyl) sulfate (**35e**)

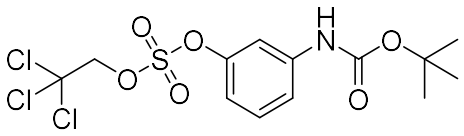

Following general procedure **A**, tert-butyl (3-hydroxyphenyl)carbamate (149 mg, 0.710 mmol) and **33** (341 mg, 0.746 mmol) were combined to give the crude product that was purified by preparative TLC on silica gel eluting with DCM/hexane/Et_3N (1:1:1, v/v) to afford the product as a white solid (188 mg, 0.447 mmol, 63%): mp 74.8-75.0 ºC; ^{1}H NMR (600 MHz, $CDCl_3$) δ 7.60 (s, 1H, H-2), 7.28 (t, *J* = 8.4 Hz, 1H, H-5), 7.17 (d, *J* = 8.2 Hz, 1H, H-6), 6.98 (dd, *J* = 8.3, 2.3, 1.0 Hz, 1H, H-4), 6.87 (s, 1H, NH), 4.81 (s, 2H, CH_2), 1.49 (s, 9H, $C(CH_3)_3$). ^{13}C NMR (151 MHz, $CDCl_3$) δ 152.5 (C=O), 150.5 (1-C), 140.4 (3-C), 130.3 (5-CH), 117.5 (6-CH), 115.1 (4-CH), 111.4 (2-CH), 92.5 (CCl_3), 81.3 (CH_2), 80.5 ($C(CH_3)_3$), 28.3 ($C(CH_3)_3$). HRMS calculated for $C_{13}H_{15}Cl_3NO_6S$ [M-O]$^-$ *m/z* 417.9683, found 417.9700 (4.1 ppm).

2-((tert-butoxycarbonyl)amino)phenyl (2,2,2-trichloroethyl) sulfate (**35f**)

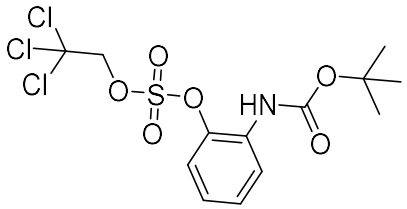

Following general procedure **A**, **34b** (149 mg, 0.710 mmol) and **33** (341 mg, 0.746 mmol) were combined to give the crude product that was purified by preparative TLC on silica gel eluting with DCM/hexane/Et_3N (1:1:1, v/v) to afford the product as a white solid (176 mg, 0.419 mmol, 59%): mp 94.0-94.2 ºC; ^{1}H NMR (600 MHz, $CDCl_3$) δ 8.17 (d, *J* = 8.3 Hz, 1H, H-3), 7.40 (dd, *J* = 8.3, 1.4 Hz, 1H, H-6), 7.31 (dddd, *J* = 8.1,

7.4, 1.4, 0.5 Hz, 1H, H-4), 7.07 (ddd, *J* = 8.1, 7.4, 1.6 Hz, 1H, H-5), 6.85 (s, 1H, NH), 4.80 (s, 2H, CH_2), 1.53 (s, 9H, $C(CH_3)_3$); ^{13}C NMR (151 MHz, $CDCl_3$) δ 152.4 (C=O), 139.1 (1-C), 131.1 (2-C), 128.7 (4-CH), 123.5 (5-CH), 121.5 (6-CH), 121.4 (3-CH), 92.3 (CCl_3), 81.7 ($C(CH_3)_3$), 80.9 (CH_2), 28.4 ($C(CH_3)_3$); HRMS calculated for $C_{13}H_{15}C_{l3}NO_6S$ $[M-O]^-$ *m/z* 417.9683, found 417.9786 (24.6 ppm).

4-Cyanophenyl (2,2,2-trichloroethyl) sulfate (**35g**)

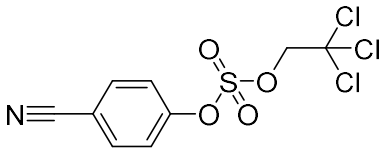

Following general procedure **A**, 4-hydroxybenzonitrile (100 mg, 0.839 mmol) and **33** (403 mg, 0.881 mmol) were combined to give the crude product that was purified by flash chromatography on silica gel eluting with DCM/Hexane (0:1 to 1:1, v/v) to afford the product as a white solid (228 mg, 0.688 mmol, 82%): mp 64.5-64.7 ºC; ^1H NMR (600 MHz, $CDCl_3$) δ 7.77 (d, *J* = 8.9 Hz, 2H, H-3, H-5), 7.50 (d, *J* = 8.9 Hz, 2H, H-2, H-6), 4.87 (s, 2H, CH_2); ^{13}C NMR (151 MHz, $CDCl_3$) δ 152.8 (1-C), 134.5 (3-CH, 5-CH), 122.2 (2-CH, 6-CH), 117.5 (4-C), 112.3 (CN), 92.2 (CCl_3), 80.8 (CH_2); HRMS calculated for $C_9H_5{}^{35}Cl_3NO_4S$ $[M-H]^-$ *m/z* 327.9005, found 327.9014 (2.7 ppm); $C_9H_5{}^{35}Cl_2{}^{37}ClNO_4S$ $[M-H]^-$ *m/z* 329.8975, found 329.8986 (3.3 ppm); $C_9H_5{}^{35}Cl^{37}Cl_2NO_4S$ $[M-H]^-$ *m/z* 331.8945, found 331.8955 (3.0 ppm).

Methyl 4-(((2,2,2-trichloroethoxy)sulfonyl)oxy)benzoate (**35h**)

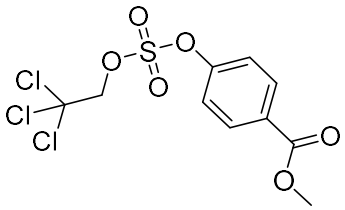

Following general procedure **A**, **34c** (100 mg, 0.658 mmol) and **33** (316 mg, 0.690

mmol) were combined to give the crude product that was purified by flash chromatography on silica gel eluting with DCM/Hexane (0:1 to 1:1, v/v) to afford the product as a white solid (168 mg, 0.480 mmol, 73%): mp 63.9-64.1 ºC; ^{1}H NMR (600 MHz, $CDCl_3$) δ 8.11 (d, *J* = 8.9 Hz, 2H, H-3, H-5), 7.67 (d, *J* = 8.9 Hz, 2H, H-2, H-6), 5.42 (s, 2H, CH_2), 3.88 (s, 3H, CH_3). ^{13}C NMR (151 MHz, $CDCl_3$) δ 165.1 (C=O), 152.6 (1-C), 131.6 (3-CH, 5-CH), 129.4 (4-C), 121.9 (2-CH, 6-CH), 92.8 (CCl_3), 80.3 (CH_2), 52.5 (CH_3); HRMS calculated for $C_8H_7O_6S$ [M-TCE]$^-$ *m/z* 230.9961, found 230.9961 (0 ppm).

Methyl 3-(((2,2,2-trichloroethoxy)sulfonyl)oxy)benzoate (**35i**)

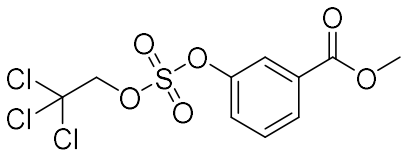

Following general procedure **A**, methyl 3-hydroxybenzoate (100 mg, 0.658 mmol) and **33** (316 mg, 0.690 mmol) were combined to give the crude product that was purified by flash chromatography on silica gel eluting with DCM/Hexane (0:1 to 1:1, v/v) to afford the product as a white solid (141 mg, 0.388 mmol, 59%): mp 48.8-49.1 ºC; ^{1}H NMR (600 MHz, $CDCl_3$) δ 8.04 (tt, *J* = 6.4 Hz, 1.3 Hz, 2H, H-4, H-6), 7.57 (dt, *J* = 6.0, 1.8 Hz, 1H, H-2), 7.53 (t, *J* = 7.4 Hz, H-5), 4.86 (s, 2H, CH_2), 3.94 (d, *J* = 0.7 Hz, 3H, CH_3); ^{13}C NMR (151 MHz, $CDCl_3$) δ 165.5 (C=O), 150.1 (1-C), 132.7 (3-C), 130.4 (4-CH), 129.1 (5-CH), 125.8 (2-CH), 122.5 (6-CH), 92.4 (CCl_3), 80.6 (CH_2), 52.7 (CH_3); HRMS calculated for $C_8H_7O_6S$ [M-TCE]$^-$ *m/z* 230.9961, found 230.9963 (0.9 ppm).

4-Formylphenyl (2,2,2-trichloroethyl) sulfate (**35k**)

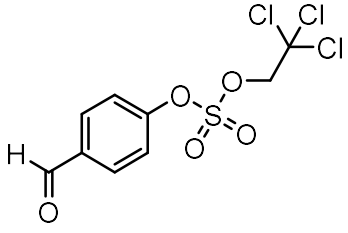

Following general procedure **A**, 4-hydroxybenzaldehyde (100 mg, 0.819 mmol) and **33** (394 mg, 0.860 mmol) were combined to give the crude product that was purified by flash chromatography on silica gel eluting with DCM/Hexane (0:1 to 1:1, v/v) to afford the product as a white solid (205 mg, 0.614 mmol, 75%): mp 67.8-68.0 ºC; ^{1}H NMR (600 MHz, $CDCl_3$) δ 10.03 (s, 1H, 4-CHO), 7.99 (d, *J* = 12.0 Hz, 2H, H-3, H-5), 7.54 (d, J= 8.6 Hz, 2H, H-2, H-6), 4.87 (s, 2H, CH_2). ^{13}C NMR (151 MHz, $CDCl_3$) δ 190.4 (4-CHO), 154.1 (1-C), 135.6 (4-C), 131.8 (3-CH, 5-CH), 121.8 (2-CH,6-CH), 92.3 (CCl_3), 80.8 (CH_2).

3-Formylphenyl (2,2,2-trichloroethyl) sulfate (**35l**)

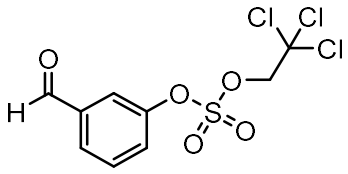

Following general procedure **A**, 3-hydroxybenzaldehyde (100 mg, 0.819 mmol) and **33** (394 mg, 0.860 mmol) were combined to give the crude product that was purified by flash chromatography on silica gel eluting with DCM/Hexane (0:1 to 1:1, v/v) to afford the product as a white solid (230 mg, 0.688 mmol, 84%): mp 46.6-47.0 ºC; ^{1}H NMR (600 MHz, $CDCl_3$) δ 10.03 (s, 1H, 3-CHO), 7.93-7.86 (m, 2H, H-4, H-6), 7.69-7.61 (m, 2H, H-2, H-5), 4.88 (s, 2H, CH_2); ^{13}C NMR (151 MHz, $CDCl_3$) δ 190.2 (C=O), 150.7 (1-C), 138.4 (3-C), 131.1 (5-CH), 129.3 (6-CH), 127.0 (4-CH), 121.6 (2-CH), 92.3 (CCl_3), 80.6 (CH_2); HRMS calculated for $C_9H_8Cl_3O_5S$ $[M+H]^+$ m/z 332.9157, found 332.9189 (9.6 ppm).

2-Formylphenyl (2,2,2-trichloroethyl) sulfate (**35m**)

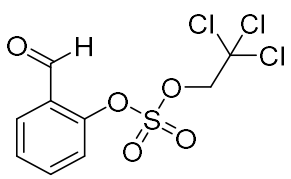

Following general procedure **A**, 2-hydroxybenzaldehyde (100 mg, 0.819 mmol) and **33** (394 mg, 0.860 mmol) were combined to give the crude product that was purified by flash chromatography on silica gel eluting with DCM/Hexane (0:1 to 1:1, v/v) to afford the product as a white solid (240 mg, 0.721 mmol, 88%): mp 65.3-65.5 ºC; ^{1}H NMR (600 MHz, $CDCl_3$) δ 10.33 (d, *J* = 0.6 Hz, 1H, 2-CHO), 7.98 (dd, *J* = 7.7, 1.8 Hz, 1H, H-6), 7.71 (ddd, *J* = 8.2, 7.4, 1.8 Hz, 1H, H-3), 7.57-7.47 (m, 2H, H-4, H-5), 4.93 (s, 2H, CH_2); ^{13}C NMR (151 MHz, $CDCl_3$) δ 187.4 (2-CHO), 150.9 (1-C), 135.9 (2-C), 130.7 (6-CH), 128.5 (3-CH), 128.5 (5-CH), 122.5 (4-CH), 92.3 (CCl_3), 80.9 (CH_2).

4-Aminophenyl (2,2,2-trichloroethyl) sulfate (**35n**)

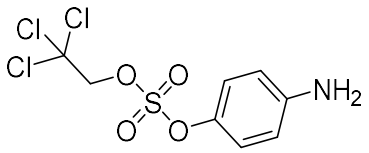

To a solution of **35d** (100 mg, 0.238 mmol) in DCM (10 mL) was added TFA (177 mg, 1.55 mmol) at 0 °C. The reaction was stirred at 0 °C for 5 h until the starting material was consumed. A saturated solution of $NaHCO_3$ was added slowly, keeping the reaction on ice, until effervescence ceased (the mixture was neutralized). The reaction was then extracted with DCM (3 × 5 mL), the combined organic extracts were dried over Na_2SO_4 and evaporated in vacuo to get the crude oil. The crude material was purified by preparative TLC on silica gel eluting with DCM/hexane/Et_3N (1:1:1, v/v) to afford the product as a white solid (56 mg, 0.176 mmol, 74%): mp 75.4-75.6 ºC; ^{1}H NMR (600 MHz, $CDCl_3$) δ 7.11 (d, *J* = 8.9 Hz, 2H, H-3, H-5), 6.58 (d, *J* =8.9 Hz, 2H, H-2, H-6), 5.37 (br.s, 2H, 4-NH_2), 5.24 (s, 2H, CH_2).

3-Aminophenyl (2,2,2-trichloroethyl) sulfate (**35o**)

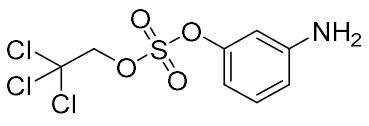

To a solution of **35e** (100 mg, 0.238 mmol) in DCM (10 mL) was added TFA (177 mg, 1.55 mmol) at 0 °C. The reaction was stirred at 0 °C for 5 h until the starting material was consumed. A saturated solution of $NaHCO_3$ was added slowly, keeping the reaction on ice, until effervescence ceased (the mixture was neutralized). The reaction was then extracted with DCM (3 × 5 mL), the combined organic extracts were dried over Na_2SO_4 and evaporated in vacuo to get the crude oil. The crude material was purified by preparative TLC on silica gel eluting with DCM/hexane/Et_3N (1:1:1, v/v) to afford the product as a white solid (65 mg, 0.202 mmol, 85%): mp 66.1-66.3 ºC; ^{1}H NMR (600 MHz, $CDCl_3$) δ 7.18 (t, *J* = 8.1 Hz, 1H, H-5), 6.71 (ddd, *J* = 8.2, 2.3, 0.9 Hz, 1H, H-6), 6.67-6.61 (m, 2H, H-2, H-4), 4.80 (s, 2H, CH_2).

2-Aminophenyl (2,2,2-trichloroethyl) sulfate (**35p**)

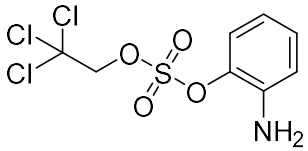

To a solution of **35f** (100 mg, 0.238 mmol) in DCM (10 mL) was added TFA (177 mg, 1.55 mmol) at 0 °C. The reaction was stirred at 0 °C for 5 h until the starting material was consumed. A saturated solution of $NaHCO_3$ was added slowly, keeping the reaction on ice, until effervescence ceased (the mixture was neutralized). The reaction was then extracted with DCM (3 × 5 mL), the combined organic extracts were dried over Na_2SO_4 and evaporated in vacuo to get the crude oil. The crude material was purified by preparative TLC on silica gel eluting with DCM/hexane/Et_3N (1:1:1, v/v) to afford the product as a white solid (66 mg, 0.207 mmol, 87%): ^{1}H NMR (600 MHz, $CDCl_3$) δ 7.30 (dd, *J* = 8.2, 1.4 Hz, 1H, H-3), 7.13 (ddd, *J* = 8.1, 7.3, 1.4 Hz, 1H, H-4), 6.83 (dd, *J* = 8.0, 1.5 Hz, 1H, H-2), 6.77 (ddd, *J* = 8.2, 7.4, 1.6 Hz, 1H, H-5), 4.83 (s, 2H, CH_2).

4-((Ethoxycarbonyl)amino)phenyl (2,2,2-trichloroethyl) sulfate (**35q**)

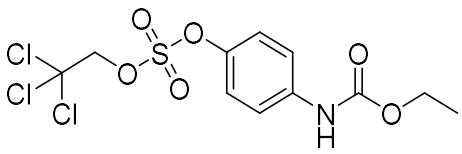

To a solution of **35n** (100 mg, 0.320 mmol) in pyridine (5 mL) was added ethyl chloroformate (170 mg, 0.160 mmol) at 0 °C. The mixture was stirred at 0 °C for 2h and then warmed to ambient temperature. The reaction was stirred at rt for 3 h until the starting material was consumed. The solution was washed with water (3 × 5 mL) and extracted with ethyl acetate (3 × 5 mL). The organic layer was dried over Na_2SO_4 and condensed under reduced pressure to afford the crude oil. The crude material was purified by preparative TLC on silica gel eluting with DCM/hexane/Et_3N (1:1:1, v/v) to afford the product as a white solid (91 mg, 0.224 mmol, 70%): mp 71.8-72.3 ºC; ^{1}H NMR (600 MHz, $CDCl_3$) δ 7.46 (d, *J* = 8.6 Hz, 2H, H-3, H-5), 7.30 (d, *J* = 9.1 Hz, 2H, H-2, H-6), 6.66 (s, 1H, 4-NH), 4.81 (s, 2H, CH_2CCl_3), 4.24 (q, *J* = 7.1 Hz, 2H, CH_2CH_3), 1.32 (t, *J* = 7.1 Hz, 3H, CH_2CH_3); HRMS calculated for $C_{11}H_{13}{}^{35}Cl_3O_6NS$ $[M+H]^+$ *m/z* 391.9527, found 391.9570 (11.0 ppm); $C_{11}H_{13}{}^{35}Cl_2{}^{37}Cl_1O_6NS$ $[M+H]^+$ *m/z* 393.9497, found 393.9542 (11.4 ppm); $C_{11}H_{13}{}^{35}Cl^{37}Cl_2O_6NS$ $[M+H]^+$ *m/z* 395.9467, found 395.9513 (11.6 ppm).

3-((Ethoxycarbonyl)amino)phenyl (2,2,2-trichloroethyl) sulfate (**35r**)

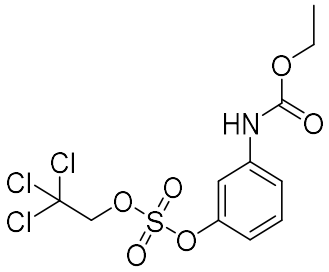

To a solution of **35o** (100 mg, 0.320 mmol) in 5 mL pyridine was added ethyl chloroformate (170 mg, 0.160 mmol) at 0 °C. The mixture was stirred at 0 °C for 2h and then warmed to ambient temperature. The reaction was stirred at rt for 3 h until the starting material was consumed. The solution was washed with water (3 × 5 mL) and

extracted with ethyl acetate (3 × 5 mL). The organic layer was dried over Na_2SO_4 and condensed under reduced pressure to afford the crude oil. The crude material was purified by preparative TLC on silica gel eluting with DCM/hexane/Et_3N (1:1:1, v/v) to afford the product as a white solid (111.8 mg, 0.275 mmol, 86%): mp 68.6-68.8 ºC ; ^{1}H NMR (600 MHz, $CDCl_3$) δ 7.61 (s, 1H, 3-NH), 7.35 (t, *J* = 8.2 Hz, 1H, H-2), 7.26 (d, *J* = 12 Hz, 2H, H-5, H-4), 7.06 (ddd, *J* = 8.3, 2.4, 0.9 Hz, 1H, H-6), 4.84 (s, 2H, CH_2CCl_3), 4.24 (q, *J* = 7.1 Hz, 2H, CH_2CH_3), 1.32 (t, *J* = 7.1 Hz, 3H, CH_2CH_3); HRMS calculated for $C_{11}H_{11}{}^{35}Cl_3O_6NS$ $[M-H]^-$ *m/z* 389.9371, found 389.9391 (5.1 ppm), $C_{11}H_{11}{}^{35}Cl_1{}^{37}ClO_6NS$ $[M-H]^-$ *m/z* 391.9341, found 391.9361 (5.1 ppm), $C_{11}H_{11}{}^{35}Cl_2{}^{37}ClO_6NS$ $[M-H]^-$ *m/z* 393.9311, found 393.9331 (5.1 ppm).

2-((Ethoxycarbonyl)amino)phenyl (2,2,2-trichloroethyl) sulfate (**35s**)

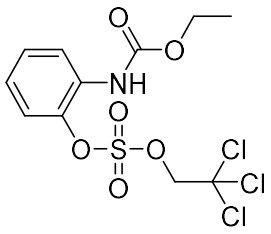

Method A: To a solution of **35o** (100 mg, 0.320 mmol) in 5 mL pyridine was added ethyl chloroformate (170 mg, 0.160 mmol) at 0 °C. The mixture was stirred at 0 °C for 2h and then warmed to ambient temperature. The reaction was stirred at rt for 3 h until the starting material was consumed. The solution was washed with water (3 × 5 mL) and extracted with ethyl acetate (3 × 5 mL). The organic layer was dried over Na_2SO_4 and condensed under reduced pressure to afford the crude oil. The crude material was purified by preparative TLC on silica gel eluting with DCM/hexane/Et_3N (1:1:1, v/v) to afford the product as a white solid (78 mg, 0.192 mmol, 60%).

Method B: Following general procedure **A**, **34d** (100 mg, 0.552 mmol) and **33** (265 mg, 0.580 mmol) were combined to give the crude product that was purified by preparative TLC on silica gel eluting with DCM/hexane/Et_3N (1:1:1, v/v) to afford the product as

a white solid (94 mg, 0.230 mmol, 72%).

Experimental data: mp 83.1-83.4 ºC; ^{1}H NMR (600 MHz, $CDCl_3$) δ 7.61 (s, 1H, 2-NH) 7.35 (t, *J* = 8.2 Hz, 1H, H-3), 7.25 (dd, *J* = 8.3, 2.1 Hz, 1H, H-5), 7.04 (ddd, *J* = 8.3, 2.4, 0.9 Hz, 1H, H-6), 6.70 (s, 1H, H-4), 4.84 (s, 2H, CH_2CCl_3), 4.24 (q, *J* = 7.1 Hz, 2H, CH_2CH_3), 1.32 (t, *J* = 7.1 Hz, 3H, CH_2CH_3). HRMS calculated for $C_{11}H_{13}{}^{35}Cl_3O_6NS$ $[M+H]^+$ *m/z* 391.9527, found 391.9574 (12.0 ppm); $C_{11}H_{13}{}^{35}Cl_2{}^{37}ClO_6NS$ $[M+H]^+$ *m/z* 393.9497, found 393.9546 (12.4 ppm); $C_{11}H_{13}{}^{35}Cl{}^{37}Cl_2O_6NS$ $[M+H]^+$ *m/z* 395.9467, found 395.9515 (12.1 ppm).

4-Fluorophenyl sulfate (**36a**)

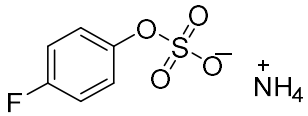

Following general procedure **B, 35a** (100 mg, 0.320 mmol) was combined with ammonium formate (162 mg, 2.556 mmol) and zinc dust (84 mg, 1.278 mmol) at room temperature. The crude material was purified by flash chromatography on silica gel eluting with CH_2Cl_2/MeOH/Et_3N (10:1:0.5, v/v) to afford the product as a white solid (52.2 mg, 0.278 mmol, 87%): ^{1}H NMR (600 MHz, DMSO-d_6) δ 7.01-6.93 (m, 2H, H-3, H-5), 6.76-6.70 (m, 2H, H-2, H-6); ^{13}C NMR (151 MHz, DMSO-d_6) δ 159.5 (d, ^{1}JCF ≈ 238.6 Hz, 4-C), 149.8 (d, ^{4}JCF = 2 Hz, 1-C), 122.4 (d, ^{3}JCF ≈ 9.1 Hz, H-2, H-6), 115.3 (d, ^{2}JCF ≈ 22.7 Hz, H-3, H-5); HRMS calculated for $C_6H_4FO_4S$ $[M]^-$ *m/z* 190.9813, found 190.9821 (4.2 ppm); HPLC (RT 4.81-5.33 min).

3-Fluorophenyl sulfate (**36b**)

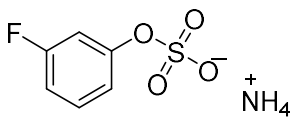

Following general procedure **B, 35b** (100 mg, 0.320 mmol) was combined with

ammonium formate (162 mg, 2.556 mmol) and zinc dust (84 mg, 1.278 mmol) at room temperature. The crude material was purified by flash chromatography on silica gel eluting with CH_2Cl_2/MeOH/Et_3N (10:1:0.5, v/v) to afford the product as a white solid (45.0 mg, 0.240 mmol, 75%): ^{1}H NMR (600 MHz, DMSO-*d*$_6$) δ 7.33-7.26 (m, 1H, H-5), 7.02 (dt, *J* = 11.1, 2.4 Hz, 1H, H-4), 6.97 (dd, *J* = 8.4, 2.0 Hz, 1H, H-2), 6.87 (td, *J* = 8.6, 2.5 Hz, 1H, H-6); ^{13}C NMR (151 MHz, DMSO-*d*$_6$) δ 162.1 (d, ^{1}*J*CF ≈ 243.1 Hz, 3-C), 154.8 (d, ^{3}*J*CF ≈ 10.6, 1-C), 129.8 (d, ^{3}*J*CF ≈ 10.6, 5-CH), 116.1 (d, ^{4}*J*CF ≈ 3.0 Hz, 4-CH), 109.4 (d, ^{2}*J*CF ≈ 21.1 Hz, 2-CH), 107.3 (d, ^{2}*J*CF ≈ 24.2 Hz, 6-CH); HRMS calculated for $C_6H_4FO_4S$ $[M]^-$ *m/z* 190.9813, found 190.9822 (4.7 ppm); HPLC (RT 9.15-9.35 min).

2-Fluorophenyl sulfate (**36c**)

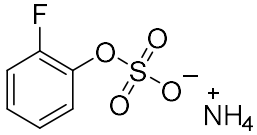

Following general procedure **B, 35c** (100 mg, 0.320 mmol) was combined with ammonium formate (162 mg, 2.556 mmol) and zinc dust (84 mg, 1.278 mmol) at room temperature. The crude material was purified by flash chromatography on silica gel eluting with CH_2Cl_2/MeOH/Et_3N (10:1:0.5, v/v) to afford the product as a white solid (46.2 mg, 0.246 mmol, 77%): ^{1}H NMR (600 MHz, DMSO-*d*$_6$) δ 7.48 (td, *J* = 8.1, 2.1 Hz, 1H, H-6), 7.17 (ddd, *J* = 11.0, 7.7, 2.0 Hz, 1H, H-3), 7.08 (dd, *J* = 7.8, 2.2 Hz, 2H, H-4, H-5); ^{13}C NMR (151 MHz, DMSO-*d*$_6$) δ 153.8 (d, ^{1}*J*CF ≈ 244.6 Hz, 2-C), 141.5 (d, ^{2}*J*CF ≈ 12.1 Hz, 1-C), 124.3 (d, ^{4}*J*CF ≈ 3.0 Hz, 5-CH), 124.2 (d, ^{3}*J*CF ≈ 7.1 Hz, 4-CH), 123.4 (6-CH), 116.2 (d, ^{2}*J*CF ≈ 18.1 Hz, 3-CH); HRMS calculated for $C_6H_4FO_4S$ $[M]^-$ *m/z* 190.9813, found 190.9822 (4.7 ppm); HPLC (RT 4.21-5.09 min).

4-((tert-Butoxycarbonyl)amino)phenyl sulfate (**36d**)

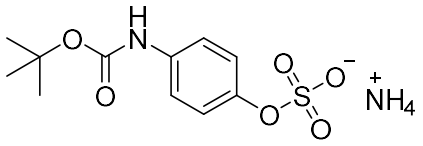

Following general procedure **B, 35d** (50 mg, 0.238 mmol) was combined with ammonium formate (120 mg, 1.904 mmol) and zinc dust (62 mg, 0.952 mmol) at room temperature. The crude material was purified by preparative TLC on silica gel eluting with CH_2Cl_2/MeOH/Et_3N (20:1:0.5, v/v) to afford the product as a white solid (47.3 mg, 0.164 mmol, 69%): ^{1}H NMR (600 MHz, DMSO-*d*$_6$) δ 7.30 (d, *J* = 8.4 Hz, 2H, H-3/5), 7.05-6.99 (m, 2H, H-2/6), 1.46 (s, C(CH_3)$_3$); ^{13}C NMR (151 MHz, DMSO-*d*$_6$) δ 153.0 (C=O), 148.4 (1-C), 135.0 (4-C), 121.0 (3-CH, 5-CH), 118.8 (2-CH, 6-CH), 78.8 (*C*(CH_3)$_3$), 28.2 (C(*CH*$_3$)$_3$); HRMS calculated for $C_{11}H_{14}NO_6S$ $[M]^-$ *m/z* 288.0538, found 288.0604 (22.9 ppm); HPLC (RT 7.88-8.21 min)

3-((tert-Butoxycarbonyl)amino)phenyl sulfate (**36e**)

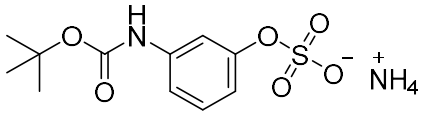

Following general procedure **B, 35e** (50 mg, 0.238 mmol) was combined with ammonium formate (120 mg, 1.904 mmol) and zinc dust (62 mg, 0.952 mmol) at room temperature. The crude material was purified by preparative TLC on silica gel eluting with CH_2Cl_2/MeOH/Et_3N (20:1:0.5, v/v) to afford the product as a white solid (43.9 mg, 0.153 mmol, 64%): ^{1}H NMR (600 MHz, DMSO-*d*$_6$) δ 7.22 (t, *J* = 2.2 Hz, 1H, H-2), 7.09 (d, *J* = 12.0 Hz, 1H, H-5), 7.06 (t, *J* = 6.0 Hz, 1H, H-6), 6.76 (ddd, *J* = 7.8, 2.3, 1.3 Hz, 1H, H-4), 1.42 (s, C(CH_3)$_3$); ^{13}C NMR (151 MHz, DMSO-*d*$_6$) δ 154.1 (C=O), 153.1 (1-C), 140.4 (3-C), 129.0 (4-CH), 114.9 (6-CH), 113.5 (5-CH), 111.4 (2-CH), 79.3 (*C*(CH_3)$_3$), 28.6 (C(*CH*$_3$)$_3$); HRMS calculated for $C_{11}H_{14}NO_6S$ $[M]^-$ *m/z* 288.0538, found 288.0548 (3.5 ppm); HPLC (RT 7.92-8.46).

2-((tert-Butoxycarbonyl)amino)phenyl sulfate (**36f**)

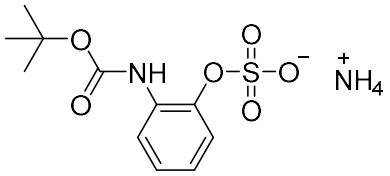

Following general procedure **B, 35f** (50 mg, 0.238 mmol) was combined with ammonium formate (120 mg, 1.904 mmol) and zinc dust (62 mg, 0.952 mmol) at room temperature. The crude material was purified by preparative TLC on silica gel eluting with CH_2Cl_2/MeOH/Et_3N (20:1:0.5, v/v) to afford the product as a white solid (35.0 mg, 0.121 mmol, 51%): ^{1}H NMR (600 MHz, DMSO-*d*$_6$) δ 7.80 (d, *J* = 8.1 Hz, 1H, H-3), 7.12 (dd, *J* = 7.8, 1.4 Hz, 1H, H-6), 7.08 (td, *J* = 7.1, 1.6 Hz, 1H, H-4), 6.97 (ddd, *J* = 8.0, 7.4, 1.6 Hz, 1H, H-5), 1.46 (s, C(CH_3)$_3$); ^{13}C NMR (151 MHz, DMSO-*d*$_6$) δ 152.4 (C=O), 142.4 (2-C), 132.0 (1-C), 124.7 (4-CH), 123.8 (6-CH), 123.0 (5-CH), 120.3 (3-CH), 79.7 (*C*(CH_3)$_3$), 28.2 (C(*CH*$_3$)$_3$); HRMS calculated for $C_{11}H_{14}NO_6S$ $[M]^-$ *m/z* 288.0538, found 288.0548 (3.5 ppm); HPLC (RT 9.17-9.63 min).

4-Cyanophenyl sulfate (**36g**)

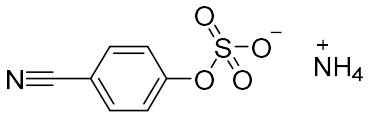

Following general procedure **B, 35f** (100 mg, 0.302 mmol) was combined with ammonium formate (152 mg, 2.417 mmol) and zinc dust (79 mg, 1.209 mmol) at room temperature. The crude material was purified by flash chromatography on silica gel eluting with CH_2Cl_2/MeOH/Et_3N (10:1:0.5, v/v) to afford the product as a white solid (55.7 mg, 0.281 mmol, 93%): ^{1}H NMR (600 MHz, DMSO-*d*$_6$) δ 7.78-7.72 (m, 2H, H-3, H-5), 7.37-7.31 (m, 2H, H-2, H-6); ^{13}C NMR (151 MHz, DMSO-*d*$_6$) δ 157.7 (1-C), 134.0 (3-CH, 5-CH), 120.6 (2-CH, 6-CH), 119.3 (4-C), 105.0 (CN); HRMS calculated for $C_7H_4NO_4S$ $[M]^-$ *m/z* 197.9860, found 197.9858 (-1.0 ppm); HPLC (RT 4.59-5.30 min).

Methyl 4-(((2,2,2-trichloroethoxy)sulfonyl)oxy)benzoate (**36h**)

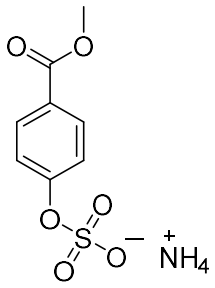

Following general procedure **B, 35h** (100 mg, 0.275 mmol) was combined with ammonium formate (139 mg, 2.200 mmol) and zinc dust (72 mg, 1.100 mmol) at room temperature. The crude material was purified by flash chromatography on silica gel eluting with CH_2Cl_2/MeOH/Et_3N (10:1:0.5, v/v) to afford the product as a white solid (53.42 mg, 0.231 mmol, 84%): ^{1}H NMR (600 MHz, DMSO-*d*$_6$) δ 7.92-7.86 (m, 2H, H-3, H-5), 7.31-7.24 (m, 2H, H-2, H-6), 3.82 (s, 3H, CH_3); ^{13}C NMR (151 MHz, DMSO-*d*$_6$) δ 166.5 (C=O), 158.3 (1-C), 131.0 (3-CH, 5-CH), 124.2 (4-C), 120.0 (2-CH, 6-CH), 52.4 (CH_3); HRMS calculated for $C_8H_7O_6S$ $[M]^-$ *m/z* 230.9961, found 230.9960 (-0.4 ppm); HPLC (RT 5.31-6.03 min).

3-(Methoxycarbonyl)phenyl sulfate (**36i**)

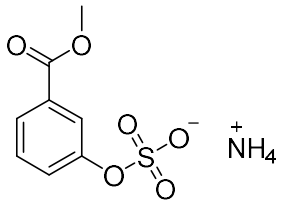

Following general procedure **B, 35i** (100 mg, 0.275 mmol) was combined with ammonium formate (139 mg, 2.200 mmol) and zinc dust (72 mg, 1.100 mmol) at room temperature. The crude material was purified by flash chromatography on silica gel eluting with CH_2Cl_2/MeOH/Et_3N (10:1:0.5, v/v) to afford the product as a white solid (50.9 mg, 0.220 mmol, 80%): ^{1}H NMR (600 MHz, DMSO-*d*$_6$) δ 7.83-7.80 (m, 1H, H-2), 7.65 (dt, *J* = 7.6, 1.4 Hz, 1H, H-6), 7.42 (t, *J* = 7.9 Hz, 1H, H-5), 7.37 (ddd, *J* = 8.2,

2.4, 1.2 Hz, 1H, H-4), 3.85 (s, 3H, CH_3); ^{13}C NMR (151 MHz, DMSO-d_6) δ 166.5 (C=O), 154.2 (1-C), 130.9 (3-C), 129.8 (5-CH), 125.9 (4-CH), 124.3 (6-CH), 121.4 (2-CH), 52.7 (CH_3); HRMS calculated for $C_8H_7O_6S$ $[M]^-$ *m/z* 230.9961, found 230.9969 (-0.4 ppm); HPLC (RT 5.37-5.94 min).

4-Aminophenyl sulfate (**36j**)

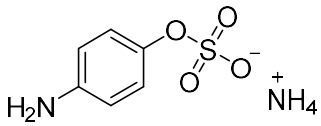

Following general procedure **B, 35n** (76 mg, 0.238 mmol) was combined with ammonium formate (120 mg, 1.904 mmol) and zinc dust (62 mg, 0.952 mmol) at room temperature. The crude material was purified by preparative TLC on silica gel eluting with CH_2Cl_2/MeOH/Et_3N (20:1:0.5, v/v) to afford the product as a white solid (39.5 mg, 0.124 mmol, 52%): ^1H NMR (600 MHz, DMSO-d_6) 6.80 (d, *J* = 8.7 Hz, 2H, H-2, H-6), 6.44 (d, *J* = 8.8 Hz, 2H, H-3, H-5); ^{13}C NMR (151 MHz, DMSO-d_6) δ 144.6 (1-C), 143.8 (4-C), 121.8 (2-CH, 6-CH), 113.7 (3-CH, 5-CH); HRMS calculated for $C_6H_6NO_4S$ $[M]^-$ *m/z* 188.0016, found 188.0060 (23.4 ppm).

2-Aminophenyl sulfate (**36l**)

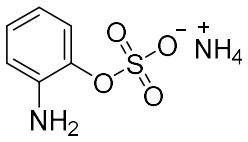

Following general procedure **B, 35p** (30 mg, 0.094 mmol) was combined with ammonium formate (47 mg, 0.752 mmol) and zinc dust (25 mg, 0.376 mmol) at room temperature. The crude material was purified by preparative TLC on silica gel eluting with CH_2Cl_2/MeOH/Et_3N (20:1:0.5, v/v) to afford the product as a white solid (9 mg, 0.045 mmol, 48%): ^1H NMR (600 MHz, DMSO-d_6) δ 6.94 (dd, *J* = 7.9, 1.5 Hz, 1H, H-

5), 6.75 (td, J = 7.6, 1.5 Hz, 1H, H-4), 6.61 (dd, J = 7.9, 1.6 Hz, 1H, H-2), 6.43 (td, J = 7.6, 1.6 Hz, 1H, H-3); ^{13}C NMR (151 MHz, DMSO-d_6) δ 141.5 (2-C), 140.3 (1-C), 124.6 (4-CH), 123.0 (3-CH), 116.4 (5-CH), 115.7 (6-CH); HRMS calculated for $C_6H_6NO_4S$ $[M]^-$ m/z 188.0016, found 188.0027 (5.9 ppm).

3-((Ethoxycarbonyl)amino)phenyl sulfate (**36m**)

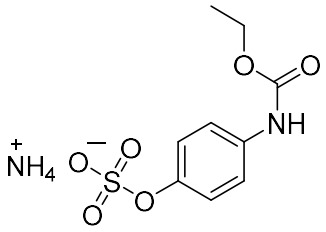

Following general procedure **B, 35q** (100 mg, 0.255 mmol) was combined with ammonium formate (128 mg, 2.036 mmol) and zinc dust (67 mg, 1.018 mmol) at room temperature. The crude material was purified by preparative TLC on silica gel eluting with CH_2Cl_2/MeOH/Et_3N (20:1:0.5, v/v) to afford the product as a white solid (51.05 mg, 0.196 mmol, 77%): ^{1}H NMR (600 MHz, DMSO-d_6) δ 7.31 (d, J = 12 Hz, 2H, H-2, H-6), 7.04 (d, J = 12 Hz, 2H, H-3, H-5), 4.09 (q, J = 7.2 Hz, 2H, CH_2), 1.22 (t, J = 4.2 Hz, 3H, CH_3); HPLC (RT 2.47-2.53 min).

2-((Ethoxycarbonyl)amino)phenyl sulfate (**36n**)

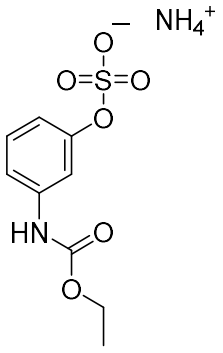

Following general procedure **B, 35r** (100 mg, 0.255 mmol) was combined with ammonium formate (128 mg, 2.036 mmol) and zinc dust (67 mg, 1.018 mmol) at room

temperature. The crude material was purified by preparative TLC on silica gel eluting with CH_2Cl_2/MeOH/Et_3N (20:1:0.5, v/v) to afford the product as a white solid (45.75 mg, 0.176 mmol,69%): ^{1}H NMR (600 MHz, DMSO-*d*$_6$) δ 7.28 (s, 1H, H-2), 7.14 (d, J = 6 Hz, 2H, H-4, H-6), 6.83-6.79 (m, 1H, H-5), 4.07 (q, J = 6.9 Hz, 2H, CH_2), 1.19 (t, J = 7.8 Hz, 3H, CH_3).

References:

(1) Zitvogel, L.; Apetoh, L.; Ghiringhelli, F.; Kroemer, G. Immunological Aspects of Cancer Chemotherapy. *Nat. Rev. Immunol.* **2008**, *8* (1), 59–73. https://doi.org/10.1038/nri2216.

(2) Benz, E. J. THE JEREMIAH METZGER LECTURE CAnCER In THE TWEnTY-FIRST CEnTURY: An InSIdE VIEW FRoM An oUTSIdER.

(3) Liu, B.; Zhou, H.; Tan, L.; Siu, K. T. H.; Guan, X.-Y. Exploring Treatment Options in Cancer: Tumor Treatment Strategies. *Signal Transduct. Target. Ther.* **2024**, *9* (1), 175. https://doi.org/10.1038/s41392-024-01856-7.

(4) Debela, D. T.; Muzazu, S. G.; Heraro, K. D.; Ndalama, M. T.; Mesele, B. W.; Haile, D. C.; Kitui, S. K.; Manyazewal, T. New Approaches and Procedures for Cancer Treatment: Current Perspectives.

(5) Formenti, S. C.; Demaria, S. Systemic Effects of Local Radiotherapy. *Lancet Oncol.* **2009**, *10* (7), 718–726. https://doi.org/10.1016/S1470-2045(09)70082-8.

(6) What Is Cancer Chemotherapy? *Chemotherapy Hahau*. https://www.cancer.org.nz/cancer/cancer-treatment/chemotherapy.

(7) Crawford, J.; Herndon, D.; Gmitter, K.; Weiss, J. The Impact of Myelosuppression on Quality of Life of Patients Treated with Chemotherapy. *Future Oncol.* **2024**, *20* (21), 1515–1530. https://doi.org/10.2217/fon-2023-0513.

(8) Batchelor, D. Hair and Cancer Chemotherapy: Consequences and Nursing Care - a Literature Study: *European Journal of Cancer Care*. *Eur. J. Cancer Care (Engl.)* **2001**, *10* (3), 147–163. https://doi.org/10.1046/j.1365-2354.2001.00272.x.

(9) Chari, R. V. J.; Miller, M. L.; Widdison, W. C. Antibody–Drug Conjugates: An Emerging Concept in Cancer Therapy. *Angew. Chem. Int. Ed.* **2014**, *53* (15), 3796–3827. https://doi.org/10.1002/anie.201307628.

(10) Hurvitz, S.; Kakkar. Role of Lapatinib Alone or in Combination in the Treatment of HER2-Positive Breast Cancer. *Breast Cancer Targets Ther.* **2012**, 35. https://doi.org/10.2147/BCTT.S29996.

(11) Tsang, R. Y.; Finn, R. S. HER2-Positive Breast Cancer: Trastuzumab, Lapatinib

and Emerging Therapies. *Drug Discov. Today Ther. Strateg.* **2012**, *9* (2–3), e55–e60. https://doi.org/10.1016/j.ddstr.2011.04.004.

(12) Genentech, Inc. *HERCEPTIN® (Trastuzumab) for Injection, for Intravenous Use: Full Prescribing Information*; Reference ID: 5399895; U.S. Food and Drug Administration (FDA): South San Francisco, CA, United States, 2024. https://www.fda.gov.

(13) U.S. Food and Drug Administration. *TYKERB (Lapatinib) Tablets: Full Prescribing Information*; Drug label / Prescribing Information; U.S. Food and Drug Administration (FDA), 2007. https://www.fda.gov/drugsatfda.

(14) Bang, Y.-J.; Van Cutsem, E.; Feyereislova, A.; Chung, H. C.; Shen, L.; Sawaki, A.; Lordick, F.; Ohtsu, A.; Omuro, Y.; Satoh, T.; Aprile, G.; Kulikov, E.; Hill, J.; Lehle, M.; Rüschoff, J.; Kang, Y.-K. Trastuzumab in Combination with Chemotherapy versus Chemotherapy Alone for Treatment of HER2-Positive Advanced Gastric or Gastro-Oesophageal Junction Cancer (ToGA): A Phase 3, Open-Label, Randomised Controlled Trial. *The Lancet* **2010**, *376* (9742), 687–697. https://doi.org/10.1016/S0140-6736(10)61121-X.

(15) Davis, F. D. *A Technology Acceptance Model for Empirically Testing New End-User Information Systems: Theory and Results*; Ph.D. Dissertation; Massachusetts Institute of Technology: Cambridge, MA, 2013. http://dspace.mit.edu/handle/1721.1/7582

(16) Pucci, C.; Martinelli, C.; Ciofani, G. Innovative Approaches for Cancer Treatment: Current Perspectives and New Challenges. *ecancermedicalscience* **2019**, *13*. https://doi.org/10.3332/ecancer.2019.961.

(17) Zhong, L.; Li, Y.; Xiong, L.; Wang, W.; Wu, M.; Yuan, T.; Yang, W.; Tian, C.; Miao, Z.; Wang, T.; Yang, S. Small Molecules in Targeted Cancer Therapy: Advances, Challenges, and Future Perspectives. *Signal Transduct. Target. Ther.* **2021**, *6* (1), 201. https://doi.org/10.1038/s41392-021-00572-w.

(18) Pettinato, M. C. Introduction to Antibody-Drug Conjugates. *Antibodies* **2021**, *10* (4), 42. https://doi.org/10.3390/antib10040042.

(19) Liu, J. K. H. The History of Monoclonal Antibody Development - Progress, Remaining Challenges and Future Innovations. *Ann. Med. Surg.* **2014**, *3* (4), 113–116. https://doi.org/10.1016/j.amsu.2014.09.001.

(20) Köhler, G.; Milstein, C. Continuous Cultures of Fused Cells Secreting Antibody of Predefined Specificity. *Nature* **1975**, *256* (5517), 495–497.

https://doi.org/10.1038/256495a0.

(21) Iqbal, N.; Iqbal, N. Human Epidermal Growth Factor Receptor 2 (HER2) in Cancers: Overexpression and Therapeutic Implications. *Mol. Biol. Int.* **2014**, *2014*, 1–9. https://doi.org/10.1155/2014/852748.

(22) Wang, Z.; Li, H.; Gou, L.; Li, W.; Wang, Y. Antibody–Drug Conjugates: Recent Advances in Payloads. *Acta Pharm. Sin. B* **2023**, *13* (10), 4025–4059. https://doi.org/10.1016/j.apsb.2023.06.015.

(23) Armstrong, G. B.; Graham, H.; Cheung, A.; Montaseri, H.; Burley, G. A.; Karagiannis, S. N.; Rattray, Z. Antibody-Drug Conjugates as Multimodal Therapies against Hard-to-Treat Cancers. *Adv. Drug Deliv. Rev.* **2025**, *224*, 115648. https://doi.org/10.1016/j.addr.2025.115648.

(24) Wang, D.; Yin, F.; Li, Z.; Zhang, Y.; Shi, C. Current Progress and Remaining Challenges of Peptide–Drug Conjugates (PDCs): Next Generation of Antibody-Drug Conjugates (ADCs)? *J. Nanobiotechnology* **2025**, *23* (1), 305. https://doi.org/10.1186/s12951-025-03277-2.

(25) Sheyi, R.; De La Torre, B. G.; Albericio, F. Linkers: An Assurance for Controlled Delivery of Antibody-Drug Conjugate. *Pharmaceutics* **2022**, *14* (2), 396. https://doi.org/10.3390/pharmaceutics14020396.

(26) Sasso, J. M.; Tenchov, R.; Bird, R.; Iyer, K. A.; Ralhan, K.; Rodriguez, Y.; Zhou, Q. A. The Evolving Landscape of Antibody–Drug Conjugates: In Depth Analysis of Recent Research Progress. *Bioconjug. Chem.* **2023**, *34* (11), 1951–2000. https://doi.org/10.1021/acs.bioconjchem.3c00374.

(27) Bargh, J. D.; Isidro-Llobet, A.; Parker, J. S.; Spring, D. R. Cleavable Linkers in Antibody–Drug Conjugates. *Chem. Soc. Rev.* **2019**, *48* (16), 4361–4374. https://doi.org/10.1039/C8CS00676H.

(28) Panowski, S.; Bhakta, S.; Raab, H.; Polakis, P.; Junutula, J. R. Site-Specific Antibody Drug Conjugates for Cancer Therapy. *mAbs* **2014**, *6* (1), 34–45. https://doi.org/10.4161/mabs.27022.

(29) U.S. Food and Drug Administration (FDA). *MYLOTARG™ (Gemtuzumab Ozogamicin) for Injection: Full Prescribing Information*; U.S. Food and Drug Administration: United States, 2017. https://www.fda.gov/ (accessed 2026-01-17).

(30) Bross, P. F.; Beitz, J.; Chen, G.; Chen, X. H.; Duffy, E.; Kieffer, L.; Roy, S.;

Sridhara, R.; Rahman, A.; Williams, G.; Pazdur, R. Approval Summary: Gemtuzumab Ozogamicin in Relapsed Acute Myeloid Leukemia.

(31) Tibau, A.; Cliff, E. R. S.; Romano, A.; Borrell, M.; Molto, C.; Kesselheim, A. S. Predictors of Withdrawal of Anticancer Drug Indications Granted Accelerated Approval: A Retrospective Cohort Study. *eClinicalMedicine* **2025**, *84*, 103088. https://doi.org/10.1016/j.eclinm.2025.103088.

(32) Bakhtiar, R. Antibody Drug Conjugates. *Biotechnol. Lett.* **2016**, *38* (10), 1655–1664. https://doi.org/10.1007/s10529-016-2160-x.

(33) Jiang, Q.; Patel, B.; Jin, X.; Di Grandi, D.; Bortell, E.; Czapkowski, B.; Lerch, T. F.; Meyer, D.; Patel, S.; Pegg, J.; Arbuckle, A.; Lagliva, J.; Sriskanda, V.; Letendre, L.; Li, H.; Thomas, E.; Nadkarni, D. Structural Characterization of the Aggregates of Gemtuzumab Ozogamicin. *ACS Omega* **2019**, *4* (4), 6468–6475. https://doi.org/10.1021/acsomega.8b03627.

(34) Wang, R.; Hu, B.; Pan, Z.; Mo, C.; Zhao, X.; Liu, G.; Hou, P.; Cui, Q.; Xu, Z.; Wang, W.; Yu, Z.; Zhao, L.; He, M.; Wang, Y.; Fu, C.; Wei, M.; Yu, L. Antibody–Drug Conjugates (ADCs): Current and Future Biopharmaceuticals. *J. Hematol. Oncol.J Hematol Oncol* **2025**, *18* (1), 51. https://doi.org/10.1186/s13045-025-01704-3.

(35) Hanf, K. J. M.; Arndt, J. W.; Chen, L. L.; Jarpe, M.; Boriack-Sjodin, P. A.; Li, Y.; Van Vlijmen, H. W. T.; Pepinsky, R. B.; Simon, K. J.; Lugovskoy, A. Antibody Humanization by Redesign of Complementarity-Determining Region Residues Proximate to the Acceptor Framework. *Methods* **2014**, *65* (1), 68–76. https://doi.org/10.1016/j.ymeth.2013.06.024.

(36) Shepard, H. M.; Phillips, G. L.; Thanos, C. D.; Feldmann, M. Developments in Therapy with Monoclonal Antibodies and Related Proteins. *Clin. Med.* **2017**, *17* (3), 220–232. https://doi.org/10.7861/clinmedicine.17-3-220.

(37) Hingorani, D. V.; Allevato, M. M.; Camargo, M. F.; Lesperance, J.; Quraishi, M. A.; Aguilera, J.; Franiak-Pietryga, I.; Scanderbeg, D. J.; Wang, Z.; Molinolo, A. A.; Alvarado, D.; Sharabi, A. B.; Bui, J. D.; Cohen, E. E. W.; Adams, S. R.; Gutkind, J. S.; Advani, S. J. Monomethyl Auristatin Antibody and Peptide Drug Conjugates for Trimodal Cancer Chemo-Radio-Immunotherapy. *Nat. Commun.* **2022**, *13* (1), 3869. https://doi.org/10.1038/s41467-022-31601-z.

(38) Lopus, M.; Oroudjev, E.; Wilson, L.; Wilhelm, S.; Widdison, W.; Chari, R.; Jordan, M. A. Maytansine and Cellular Metabolites of Antibody-Maytansinoid Conjugates Strongly Suppress Microtubule Dynamics by Binding to

Microtubules. *Mol. Cancer Ther.* **2010**, *9* (10), 2689–2699. https://doi.org/10.1158/1535-7163.MCT-10-0644.

(39) Fujii, T.; Reiling, C.; Quinn, C.; Kliman, M.; Mendelsohn, B. A.; Matsuda, Y. Physical Characteristics Comparison between Maytansinoid-Based and Auristatin-Based Antibody-Drug Conjugates. *Explor. Target. Anti-Tumor Ther.* **2021**. https://doi.org/10.37349/etat.2021.00064.

(40) Behrens, C. R.; Ha, E. H.; Chinn, L. L.; Bowers, S.; Probst, G.; Fitch-Bruhns, M.; Monteon, J.; Valdiosera, A.; Bermudez, A.; Liao-Chan, S.; Wong, T.; Melnick, J.; Theunissen, J.-W.; Flory, M. R.; Houser, D.; Venstrom, K.; Levashova, Z.; Sauer, P.; Migone, T.-S.; Van Der Horst, E. H.; Halcomb, R. L.; Jackson, D. Y. Antibody–Drug Conjugates (ADCs) Derived from Interchain Cysteine Cross-Linking Demonstrate Improved Homogeneity and Other Pharmacological Properties over Conventional Heterogeneous ADCs. *Mol. Pharm.* **2015**, *12* (11), 3986–3998. https://doi.org/10.1021/acs.molpharmaceut.5b00432.

(41) Katz, J.; Janik, J. E.; Younes, A. Brentuximab Vedotin (SGN-35). *Clin. Cancer Res.* **2011**, *17* (20), 6428–6436. https://doi.org/10.1158/1078-0432.CCR-11-0488.

(42) Lambert, J. M.; Chari, R. V. J. Ado-Trastuzumab Emtansine (T-DM1): An Antibody–Drug Conjugate (ADC) for HER2-Positive Breast Cancer. *J. Med. Chem.* **2014**, *57* (16), 6949–6964. https://doi.org/10.1021/jm500766w.

(43) Dahl, J.; Marx, K.; Jabbour, E. Inotuzumab Ozogamicin in the Treatment of Acute Lymphoblastic Leukemia. *Expert Rev. Hematol.* **2016**, *9* (4), 329–334. https://doi.org/10.1586/17474086.2016.1143771.

(44) Bosi, C.; Bartha, Á.; Galbardi, B.; Notini, G.; Naldini, M. M.; Licata, L.; Viale, G.; Mariani, M.; Pistilli, B.; Ali, H. R.; André, F.; Piras, M.; Callari, M.; Barreca, M.; Locatelli, A.; Viganò, L.; Criscitiello, C.; Pusztai, L.; Curigliano, G.; Győrffy, B.; Dugo, M.; Bianchini, G. Pan-Cancer Analysis of Antibody-Drug Conjugate Targets and Putative Predictors of Treatment Response. *Eur. J. Cancer* **2023**, *195*, 113379. https://doi.org/10.1016/j.ejca.2023.113379.

(45) Long, R.; Zuo, H.; Tang, G.; Zhang, C.; Yue, X.; Yang, J.; Luo, X.; Deng, Y.; Qiu, J.; Li, J.; Zuo, J. Antibody-Drug Conjugates in Cancer Therapy: Applications and Future Advances. *Front. Immunol.* **2025**, *16*, 1516419. https://doi.org/10.3389/fimmu.2025.1516419.

(46) Fu, Z.; Li, S.; Han, S.; Shi, C.; Zhang, Y. Antibody Drug Conjugate: The

"Biological Missile" for Targeted Cancer Therapy. *Signal Transduct. Target. Ther.* **2022**, *7* (1), 93. https://doi.org/10.1038/s41392-022-00947-7.

(47) Pegram, M. D.; Hamilton, E. P.; Tan, A. R.; Storniolo, A. M.; Balic, K.; Rosenbaum, A. I.; Liang, M.; He, P.; Marshall, S.; Scheuber, A.; Das, M.; Patel, M. R. First-in-Human, Phase 1 Dose-Escalation Study of Biparatopic Anti-HER2 Antibody–Drug Conjugate MEDI4276 in Patients with HER2-Positive Advanced Breast or Gastric Cancer. *Mol. Cancer Ther.* **2021**, *20* (8), 1442–1453. https://doi.org/10.1158/1535-7163.MCT-20-0014.

(48) Stein, E. M.; Walter, R. B.; Erba, H. P.; Fathi, A. T.; Advani, A. S.; Lancet, J. E.; Ravandi, F.; Kovacsovics, T.; DeAngelo, D. J.; Bixby, D.; Faderl, S.; Jillella, A. P.; Ho, P. A.; O'Meara, M. M.; Zhao, B.; Biddle-Snead, C.; Stein, A. S. A Phase 1 Trial of Vadastuximab Talirine as Monotherapy in Patients with CD33-Positive Acute Myeloid Leukemia. *Blood* **2018**, *131* (4), 387–396. https://doi.org/10.1182/blood-2017-06-789800.

(49) Kovtun, Y.; Noordhuis, P.; Whiteman, K. R.; Watkins, K.; Jones, G. E.; Harvey, L.; Lai, K. C.; Portwood, S.; Adams, S.; Sloss, C. M.; Schuurhuis, G. J.; Ossenkoppele, G.; Wang, E. S.; Pinkas, J. IMGN779, a Novel CD33-Targeting Antibody–Drug Conjugate with DNA-Alkylating Activity, Exhibits Potent Antitumor Activity in Models of AML. *Mol. Cancer Ther.* **2018**, *17* (6), 1271–1279. https://doi.org/10.1158/1535-7163.MCT-17-1077.

(50) Selby, PharmD, Bcop, C.; R. Yacko, PharmD, Bcps, L.; E. Glode, PharmD, Bcop, A. Gemtuzumab Ozogamicin: Back Again. *J. Adv. Pract. Oncol.* **2019**, *10* (1). https://doi.org/10.6004/jadpro.2019.10.1.6.

(51) Hamann, P. R.; Hinman, L. M.; Hollander, I.; Beyer, C. F.; Lindh, D.; Holcomb, R.; Hallett, W.; Tsou, H.-R.; Upeslacis, J.; Shochat, D.; Mountain, A.; Flowers, D. A.; Bernstein, I. Gemtuzumab Ozogamicin, A Potent and Selective Anti-CD33 Antibody−Calicheamicin Conjugate for Treatment of Acute Myeloid Leukemia. *Bioconjug. Chem.* **2002**, *13* (1), 47–58. https://doi.org/10.1021/bc010021y.

(52) Usui, N.; Takeshita, A.; Nakaseko, C.; Dobashi, N.; Fujita, H.; Kiyoi, H.; Kobayashi, Y.; Sakura, T.; Yahagi, Y.; Shigeno, K.; Ohwada, C.; Miyazaki, Y.; Ohtake, S.; Miyawaki, S.; Naoe, T.; Ohnishi, K.; for the Japan Adult Leukemia Study Group. Phase I Trial of Gemtuzumab Ozogamicin in Intensive Combination Chemotherapy for Relapsed or Refractory Adult Acute Myeloid Leukemia (AML): Japan Adult Leukemia Study Group (JALSG)-AML206 Study. *Cancer Sci.* **2011**, *102* (7), 1358–1365. https://doi.org/10.1111/j.1349-7006.2011.01957.x.

(53) Cortes, J. E.; De Lima, M.; Dombret, H.; Estey, E. H.; Giralt, S. A.; Montesinos, P.; Röllig, C.; Venditti, A.; Wang, E. S. Prevention, Recognition, and Management of Adverse Events Associated with Gemtuzumab Ozogamicin Use in Acute Myeloid Leukemia. *J. Hematol. Oncol.J Hematol Oncol* **2020**, *13* (1), 137. https://doi.org/10.1186/s13045-020-00975-2.

(54) Giles, F. J.; Kantarjian, H. M.; Kornblau, S. M.; Thomas, D. A.; Garcia-Manero, G.; Waddelow, T. A.; David, C. L.; Phan, A. T.; Colburn, D. E.; Rashid, A.; Estey, E. H. Mylotarg? (Gemtuzumab Ozogamicin) Therapy Is Associated with Hepatic Venoocclusive Disease in Patients Who Have Not Received Stem Cell Transplantation. *Cancer* **2001**, *92* (2), 406–413. https://doi.org/10.1002/1097-0142(20010715)92:2%253C406::AID-CNCR1336%253E3.0.CO;2-U.

(55) Petersdorf, S. H.; Kopecky, K. J.; Slovak, M.; Willman, C.; Nevill, T.; Brandwein, J.; Larson, R. A.; Erba, H. P.; Stiff, P. J.; Stuart, R. K.; Walter, R. B.; Tallman, M. S.; Stenke, L.; Appelbaum, F. R. A Phase 3 Study of Gemtuzumab Ozogamicin during Induction and Postconsolidation Therapy in Younger Patients with Acute Myeloid Leukemia. *Blood* **2013**, *121* (24), 4854–4860. https://doi.org/10.1182/blood-2013-01-466706.

(56) Jen, E. Y.; Ko, C.-W.; Lee, J. E.; Del Valle, P. L.; Aydanian, A.; Jewell, C.; Norsworthy, K. J.; Przepiorka, D.; Nie, L.; Liu, J.; Sheth, C. M.; Shapiro, M.; Farrell, A. T.; Pazdur, R. FDA Approval: Gemtuzumab Ozogamicin for the Treatment of Adults with Newly Diagnosed CD33-Positive Acute Myeloid Leukemia. *Clin. Cancer Res.* **2018**, *24* (14), 3242–3246. https://doi.org/10.1158/1078-0432.CCR-17-3179.

(57) Lambert, J.; Pautas, C.; Terré, C.; Raffoux, E.; Turlure, P.; Caillot, D.; Legrand, O.; Thomas, X.; Gardin, C.; Gogat-Marchant, K.; Rubin, S. D.; Benner, R. J.; Bousset, P.; Preudhomme, C.; Chevret, S.; Dombret, H.; Castaigne, S. Gemtuzumab Ozogamicin for *de Novo* Acute Myeloid Leukemia: Final Efficacy and Safety Updates from the Open-Label, Phase III ALFA-0701 Trial. *Haematologica* **2019**, *104* (1), 113–119. https://doi.org/10.3324/haematol.2018.188888.

(58) Ali, S.; Dunmore, H.-M.; Karres, D.; Hay, J. L.; Salmonsson, T.; Gisselbrecht, C.; Sarac, S. B.; Bjerrum, O. W.; Hovgaard, D.; Barbachano, Y.; Nagercoil, N.; Pignatti, F. The EMA Review of Mylotarg (Gemtuzumab Ozogamicin) for the Treatment of Acute Myeloid Leukemia. *The Oncologist* **2019**, *24* (5), e171–e179. https://doi.org/10.1634/theoncologist.2019-0025.

(59) Abdollahpour-Alitappeh, M.; Lotfinia, M.; Gharibi, T.; Mardaneh, J.;

Farhadihosseinabadi, B.; Larki, P.; Faghfourian, B.; Sepehr, K. S.; Abbaszadeh-Goudarzi, K.; Abbaszadeh-Goudarzi, G.; Johari, B.; Zali, M. R.; Bagheri, N. Antibody–Drug Conjugates (ADCs) for Cancer Therapy: Strategies, Challenges, and Successes. *J. Cell. Physiol.* **2019**, *234* (5), 5628–5642. https://doi.org/10.1002/jcp.27419.

(60) Ricart, A. D. Antibody-Drug Conjugates of Calicheamicin Derivative: Gemtuzumab Ozogamicin and Inotuzumab Ozogamicin. *Clin. Cancer Res.* **2011**, *17* (20), 6417–6427. https://doi.org/10.1158/1078-0432.CCR-11-0486.

(61) Kantarjian, H. M.; Boissel, N.; Papayannidis, C.; Luskin, M. R.; Stelljes, M.; Advani, A. S.; Jabbour, E. J.; Ribera, J.; Marks, D. I. Inotuzumab Ozogamicin in Adult Acute Lymphoblastic Leukemia: Development, Current Status, and Future Directions. *Cancer* **2024**, *130* (21), 3631–3646. https://doi.org/10.1002/cncr.35505.

(62) U.S. Food and Drug Administration (FDA). *BESPONSA (Inotuzumab Ozogamicin) Prescribing Information*; U.S. Food and Drug Administration: United States, 2024. https://www.fda.gov/drugsatfda.

(63) Lanza, F.; Maffini, E.; Rondoni, M.; Massari, E.; Faini, A. C.; Malavasi, F. CD22 Expression in B-Cell Acute Lymphoblastic Leukemia: Biological Significance and Implications for Inotuzumab Therapy in Adults. *Cancers* **2020**, *12* (2), 303. https://doi.org/10.3390/cancers12020303.

(64) Sievers, E. L. Efficacy and Safety of Gemtuzumab Ozogamicin in Patients with CD33-Positive Acute Myeloid Leukaemia in First Relapse. *Expert Opin. Biol. Ther.* **2001**, *1* (5), 893–901. https://doi.org/10.1517/14712598.1.5.893.

(65) Sehn, L. H.; Herrera, A. F.; Flowers, C. R.; Kamdar, M. K.; McMillan, A.; Hertzberg, M.; Assouline, S.; Kim, T. M.; Kim, W. S.; Ozcan, M.; Hirata, J.; Penuel, E.; Paulson, J. N.; Cheng, J.; Ku, G.; Matasar, M. J. Polatuzumab Vedotin in Relapsed or Refractory Diffuse Large B-Cell Lymphoma. *J. Clin. Oncol.* **2020**, *38* (2), 155–165. https://doi.org/10.1200/JCO.19.00172.

(66) Seattle Genetics, Inc. *ADCETRIS (Brentuximab Vedotin) Prescribing Information*; Reference ID: 3662552; Silver Spring, MD, 2014. https://www.accessdata.fda.gov/.

(67) U.S. Food and Drug Administration. *KADCYLA™ (Ado-Trastuzumab Emtansine) Prescribing Information*; Reference ID: 3265306; U.S. Food and Drug Administration (FDA): United States. https://www.fda.gov/drugsatfda (accessed 2026-01-17).

(68) U.S. Food and Drug Administration (FDA). *POLIVY™ (Polatuzumab Vedotin-Piiq) for Injection: Prescribing Information*; Silver Spring, MD, USA, 2019. https://www.fda.gov/drugsatfda (accessed 2026-01-17).

(69) Powles, T.; Rosenberg, J. E.; Sonpavde, G. P.; Loriot, Y.; Durán, I.; Lee, J.-L.; Matsubara, N.; Vulsteke, C.; Castellano, D.; Wu, C.; Campbell, M.; Matsangou, M.; Petrylak, D. P. Enfortumab Vedotin in Previously Treated Advanced Urothelial Carcinoma. *N. Engl. J. Med.* **2021**, *384* (12), 1125–1135. https://doi.org/10.1056/NEJMoa2035807.

(70) Modi, S.; Saura, C.; Yamashita, T.; Park, Y. H.; Kim, S.-B.; Tamura, K.; Andre, F.; Iwata, H.; Ito, Y.; Tsurutani, J.; Sohn, J.; Denduluri, N.; Perrin, C.; Aogi, K.; Tokunaga, E.; Im, S.-A.; Lee, K. S.; Hurvitz, S. A.; Cortes, J.; Lee, C.; Chen, S.; Zhang, L.; Shahidi, J.; Yver, A.; Krop, I. Trastuzumab Deruxtecan in Previously Treated HER2-Positive Breast Cancer. *N. Engl. J. Med.* **2020**, *382* (7), 610–621. https://doi.org/10.1056/NEJMoa1914510.

(71) Halford, Z.; Anderson, M. K.; Clark, M. D. Enfortumab Vedotin-Ejfv: A First-in-Class Anti–Nectin-4 Antibody-Drug Conjugate for the Management of Urothelial Carcinoma. *Ann. Pharmacother.* **2021**, *55* (6), 772–782. https://doi.org/10.1177/1060028020960402.

(72) U.S. Food and Drug Administration. *PADCEV™ (Enfortumab Vedotin-ejfv) for Injection: Full Prescribing Information*; U.S. Food and Drug Administration: Silver Spring, MD, USA, 2019. https://www.fda.gov/drugsatfda (accessed 2026-01-17).

(73) Cortés, J.; Kim, S.-B.; Chung, W.-P.; Im, S.-A.; Park, Y. H.; Hegg, R.; Kim, M. H.; Tseng, L.-M.; Petry, V.; Chung, C.-F.; Iwata, H.; Hamilton, E.; Curigliano, G.; Xu, B.; Huang, C.-S.; Kim, J. H.; Chiu, J. W. Y.; Pedrini, J. L.; Lee, C.; Liu, Y.; Cathcart, J.; Bako, E.; Verma, S.; Hurvitz, S. A. Trastuzumab Deruxtecan versus Trastuzumab Emtansine for Breast Cancer. *N. Engl. J. Med.* **2022**, *386* (12), 1143–1154. https://doi.org/10.1056/NEJMoa2115022.

(74) U.S. Food and Drug Administration (FDA). *ENHERTU® (Fam-Trastuzumab Deruxtecan-Nxki) for Injection: Prescribing Information*; United States, 2021. https://www.fda.gov/drugsatfda (accessed 2026-01-17).

(75) Su, Z.; Xiao, D.; Xie, F.; Liu, L.; Wang, Y.; Fan, S.; Zhou, X.; Li, S. Antibody–Drug Conjugates: Recent Advances in Linker Chemistry. *Acta Pharm. Sin. B* **2021**, *11* (12), 3889–3907. https://doi.org/10.1016/j.apsb.2021.03.042.

(76) Lewis Phillips, G. D.; Li, G.; Dugger, D. L.; Crocker, L. M.; Parsons, K. L.;

Mai, E.; Blättler, W. A.; Lambert, J. M.; Chari, R. V. J.; Lutz, R. J.; Wong, W. L. T.; Jacobson, F. S.; Koeppen, H.; Schwall, R. H.; Kenkare-Mitra, S. R.; Spencer, S. D.; Sliwkowski, M. X. Targeting HER2-Positive Breast Cancer with Trastuzumab-DM1, an Antibody–Cytotoxic Drug Conjugate. *Cancer Res.* **2008**, *68* (22), 9280–9290. https://doi.org/10.1158/0008-5472.CAN-08-1776.

(77) Jeon, E.-J.; Han, J.-H.; Seo, Y.; Koh, E. M.; Han, K.-H.; Hwang, K.; Jung, K. J. Implementation of Systematic Bioanalysis of Antibody–Drug Conjugates for Preclinical Pharmacokinetic Study of Ado-Trastuzumab Emtansine (T-DM1) in Rats. *Pharmaceutics* **2023**, *15* (3), 756. https://doi.org/10.3390/pharmaceutics15030756.

(78) Ponte, J. F.; Sun, X.; Yoder, N. C.; Fishkin, N.; Laleau, R.; Coccia, J.; Lanieri, L.; Bogalhas, M.; Wang, L.; Wilhelm, S.; Widdison, W.; Pinkas, J.; Keating, T. A.; Chari, R.; Erickson, H. K.; Lambert, J. M. Understanding How the Stability of the Thiol-Maleimide Linkage Impacts the Pharmacokinetics of Lysine-Linked Antibody–Maytansinoid Conjugates. *Bioconjug. Chem.* **2016**, *27* (7), 1588–1598. https://doi.org/10.1021/acs.bioconjchem.6b00117.

(79) Jain, N.; Smith, S. W.; Ghone, S.; Tomczuk, B. Current ADC Linker Chemistry. *Pharm. Res.* **2015**, *32* (11), 3526–3540. https://doi.org/10.1007/s11095-015-1657-7.

(80) Wang, R.; Zhou, T.; Liu, W.; Zuo, L. Molecular Mechanism of Bystander Effects and Related Abscopal/Cohort Effects in Cancer Therapy. *Oncotarget* **2018**, *9* (26), 18637–18647. https://doi.org/10.18632/oncotarget.24746.

(81) Lei, Y.; Zheng, M.; Chen, P.; Seng Ng, C.; Peng Loh, T.; Liu, H. Linker Design for the Antibody Drug Conjugates: A Comprehensive Review. *ChemMedChem* **2025**, *20* (15), e202500262. https://doi.org/10.1002/cmdc.202500262.

(82) Rafiq, S.; McKenna, S. L.; Muller, S.; Tschan, M. P.; Humbert, M. Lysosomes in Acute Myeloid Leukemia: Potential Therapeutic Targets? *Leukemia* **2021**, *35* (10), 2759–2770. https://doi.org/10.1038/s41375-021-01388-x.

(83) Uy, N.; Nadeau Nguyen, M.; Stahl, M.; Zeidan, A. Inotuzumab Ozogamicin in the Treatment of Relapsed/Refractory Acute B Cell Lymphoblastic Leukemia. *J. Blood Med.* **2018**, *Volume 9*, 67–74. https://doi.org/10.2147/JBM.S136575.

(84) Syed, Y. Y. Sacituzumab Govitecan: First Approval. *Drugs* **2020**, *80* (10), 1019–1025. https://doi.org/10.1007/s40265-020-01337-5.

(85) Seligson, J. M.; Patron, A. M.; Berger, M. J.; Harvey, R. D.; Seligson, N. D.

Sacituzumab Govitecan-Hziy: An Antibody-Drug Conjugate for the Treatment of Refractory, Metastatic, Triple-Negative Breast Cancer. *Ann. Pharmacother.* **2021**, *55* (7), 921–931. https://doi.org/10.1177/1060028020966548.

(86) Jagannath, S.; Heffner, L. T.; Ailawadhi, S.; Munshi, N. C.; Zimmerman, T. M.; Rosenblatt, J.; Lonial, S.; Chanan-Khan, A.; Ruehle, M.; Rharbaoui, F.; Haeder, T.; Wartenberg-Demand, A.; Anderson, K. C. Indatuximab Ravtansine (BT062) Monotherapy in Patients With Relapsed and/or Refractory Multiple Myeloma. *Clin. Lymphoma Myeloma Leuk.* **2019**, *19* (6), 372–380. https://doi.org/10.1016/j.clml.2019.02.006.

(87) Pillow, T. H.; Sadowsky, J. D.; Zhang, D.; Yu, S.-F.; Del Rosario, G.; Xu, K.; He, J.; Bhakta, S.; Ohri, R.; Kozak, K. R.; Ha, E.; Junutula, J. R.; Flygare, J. A. Decoupling Stability and Release in Disulfide Bonds with Antibody-Small Molecule Conjugates. *Chem. Sci.* **2017**, *8* (1), 366–370. https://doi.org/10.1039/C6SC01831A.

(88) Turell, L.; Radi, R.; Alvarez, B. The Thiol Pool in Human Plasma: The Central Contribution of Albumin to Redox Processes. *Free Radic. Biol. Med.* **2013**, *65*, 244–253. https://doi.org/10.1016/j.freeradbiomed.2013.05.050.

(89) Wu, G.; Lupton, J. R.; Turner, N. D.; Fang, Y.-Z.; Yang, S. Glutathione Metabolism and Its Implications for Health. *J. Nutr.* **2004**, *134* (3), 489–492. https://doi.org/10.1093/jn/134.3.489.

(90) Prange, C. J.; Hu, X.; Tang, L. Smart Chemistry for Traceless Release of Anticancer Therapeutics. *Biomaterials* **2023**, *303*, 122353. https://doi.org/10.1016/j.biomaterials.2023.122353.

(91) Traverso, N.; Ricciarelli, R.; Nitti, M.; Marengo, B.; Furfaro, A. L.; Pronzato, M. A.; Marinari, U. M.; Domenicotti, C. Role of Glutathione in Cancer Progression and Chemoresistance. *Oxid. Med. Cell. Longev.* **2013**, *2013*, 1–10. https://doi.org/10.1155/2013/972913.

(92) Forman, H. J.; Zhang, H.; Rinna, A. Glutathione: Overview of Its Protective Roles, Measurement, and Biosynthesis. *Mol. Aspects Med.* **2009**, *30* (1–2), 1–12. https://doi.org/10.1016/j.mam.2008.08.006.

(93) Schönfeld, K.; Zuber, C.; Pinkas, J.; Häder, T.; Bernöster, K.; Uherek, C. Indatuximab Ravtansine (BT062) Combination Treatment in Multiple Myeloma: Pre-Clinical Studies. *J. Hematol. Oncol.J Hematol Oncol* **2017**, *10* (1), 13. https://doi.org/10.1186/s13045-016-0380-0.

(94) Edupuganti, V. V. S. R.; Matikonda, S. S.; Lawer, A.; Fairhall, J. M.; Lewin, H. M.; Kueh, J. T. B.; Tyndall, J. D. A.; Gamble, A. B. Stimuli-Responsive Prodrug Linkers That Simultaneously Release Cargo and Neutralize In Situ Generated (Aza)Quinone Methides. *Chem. – Eur. J.* **2025**, *31* (31), e202501278. https://doi.org/10.1002/chem.202501278.

(95) Wang, L.; Li, J.; Zeng, X.; Lu, Q.; Wang, Y.; Anwar, Z.; Xue, L.; Fan, H.; Sun, H. Exogenous/Endogenous Stimuli-Responsive Antitumor Prodrugs Advance Precision Chemotherapy. *Bioorg. Med. Chem.* **2026**, *132*, 118485. https://doi.org/10.1016/j.bmc.2025.118485.

(96) Nani, R. R.; Gorka, A. P.; Nagaya, T.; Yamamoto, T.; Ivanic, J.; Kobayashi, H.; Schnermann, M. J. *In Vivo* Activation of Duocarmycin–Antibody Conjugates by Near-Infrared Light. *ACS Cent. Sci.* **2017**, *3* (4), 329–337. https://doi.org/10.1021/acscentsci.7b00026.

(97) Saftig, P. *Lysosomes*; Medical Intelligence Unit Ser; Springer: New York, NY, 2005.

(98) Bargh, J. D.; Walsh, S. J.; Isidro-Llobet, A.; Omarjee, S.; Carroll, J. S.; Spring, D. R. Sulfatase-Cleavable Linkers for Antibody-Drug Conjugates. *Chem. Sci.* **2020**, *11* (9), 2375–2380. https://doi.org/10.1039/C9SC06410A.

(99) Xie, Z.; Zhao, M.; Yan, C.; Kong, W.; Lan, F.; Narengaowa; Zhao, S.; Yang, Q.; Bai, Z.; Qing, H.; Ni, J. Cathepsin B in Programmed Cell Death Machinery: Mechanisms of Execution and Regulatory Pathways. *Cell Death Dis.* **2023**, *14* (4), 255. https://doi.org/10.1038/s41419-023-05786-0.

(100) Dubowchik, G. M.; FirestoneI, R. A. Cathepsin B-Sensitive Dipeptide Prodrugs. 1. A Model Study of Structural Requirements for Efficient Release of Doxorubicin.

(101) Trail, P. A.; Willner, D.; Lasch, S. J.; Henderson, A. J.; Hofstead, S.; Casazza, A. M.; Firestone, R. A.; Hellström, I.; Hellström, K. E. Cure of Xenografted Human Carcinomas by BR96-Doxorubicin Immunoconjugates. *Science* **1993**, *261* (5118), 212–215. https://doi.org/10.1126/science.8327892.

(102) Balamkundu, S.; Liu, C.-F. Lysosomal-Cleavable Peptide Linkers in Antibody–Drug Conjugates. *Biomedicines* **2023**, *11* (11), 3080. https://doi.org/10.3390/biomedicines11113080.

(103) Doronina, S. O.; Toki, B. E.; Torgov, M. Y.; Mendelsohn, B. A.; Cerveny, C. G.; Chace, D. F.; DeBlanc, R. L.; Gearing, R. P.; Bovee, T. D.; Siegall, C. B.;

Francisco, J. A.; Wahl, A. F.; Meyer, D. L.; Senter, P. D. Development of Potent Monoclonal Antibody Auristatin Conjugates for Cancer Therapy. *Nat. Biotechnol.* **2003**, *21* (7), 778–784. https://doi.org/10.1038/nbt832.

(104) Caculitan, N. G.; Dela Cruz Chuh, J.; Ma, Y.; Zhang, D.; Kozak, K. R.; Liu, Y.; Pillow, T. H.; Sadowsky, J.; Cheung, T. K.; Phung, Q.; Haley, B.; Lee, B.-C.; Akita, R. W.; Sliwkowski, M. X.; Polson, A. G. Cathepsin B Is Dispensable for Cellular Processing of Cathepsin B-Cleavable Antibody–Drug Conjugates. *Cancer Res.* **2017**, *77* (24), 7027–7037. https://doi.org/10.1158/0008-5472.CAN-17-2391.

(105) Jeffrey, S. C.; Nguyen, M. T.; Andreyka, J. B.; Meyer, D. L.; Doronina, S. O.; Senter, P. D. Dipeptide-Based Highly Potent Doxorubicin Antibody Conjugates. *Bioorg. Med. Chem. Lett.* **2006**, *16* (2), 358–362. https://doi.org/10.1016/j.bmcl.2005.09.081.

(106) Cazzamalli, S.; Dal Corso, A.; Neri, D. Linker Stability Influences the Anti-Tumor Activity of Acetazolamide-Drug Conjugates for the Therapy of Renal Cell Carcinoma. *J. Controlled Release* **2017**, *246*, 39–45. https://doi.org/10.1016/j.jconrel.2016.11.023.

(107) Gan, C.; Wang, J.; Wang, Y.; Martínez-Chávez, A.; Hillebrand, M.; De Vries, N.; Beukers, J.; Lebre, M. C.; Wagenaar, E.; Rosing, H.; Klarenbeek, S.; Bleijerveld, O. B.; Song, J.-Y.; Altelaar, M.; Beijnen, J. H.; Schinkel, A. H. Natural Deletion of Mouse Carboxylesterases Ces1c/d/e Impacts Drug Metabolism and Metabolic Syndrome Development. *Biomed. Pharmacother.* **2023**, *164*, 114956. https://doi.org/10.1016/j.biopha.2023.114956.

(108) Chen, X.; Zaro, J. L.; Shen, W.-C. Fusion Protein Linkers: Property, Design and Functionality. *Adv. Drug Deliv. Rev.* **2013**, *65* (10), 1357–1369. https://doi.org/10.1016/j.addr.2012.09.039.

(109) Fu, Q.; Kong, X.; Liu, Y.; Liu, M.; Huang, K.; Wang, P. G.; Wu, K. The Role of Hydrophilic Linkers in Next-Generation Antibody-Drug Conjugates. *J. Controlled Release* **2026**, *391*, 114612. https://doi.org/10.1016/j.jconrel.2026.114612.

(110) Davies, G.; Henrissat, B. Structures and Mechanisms of Glycosyl Hydrolases. *Structure* **1995**, *3* (9), 853–859. https://doi.org/10.1016/S0969-2126(01)00220-9.

(111) Dashnyam, P.; Mudududdla, R.; Hsieh, T.-J.; Lin, T.-C.; Lin, H.-Y.; Chen, P.-Y.; Hsu, C.-Y.; Lin, C.-H. β-Glucuronidases of Opportunistic Bacteria Are the

Major Contributors to Xenobiotic-Induced Toxicity in the Gut. *Sci. Rep.* **2018**, *8* (1), 16372. https://doi.org/10.1038/s41598-018-34678-z.

(112) Tranoy-Opalinski, I.; Legigan, T.; Barat, R.; Clarhaut, J.; Thomas, M.; Renoux, B.; Papot, S. β-Glucuronidase-Responsive Prodrugs for Selective Cancer Chemotherapy: An Update. *Eur. J. Med. Chem.* **2014**, *74*, 302–313. https://doi.org/10.1016/j.ejmech.2013.12.045.

(113) Jeffrey, S. C.; Andreyka, J. B.; Bernhardt, S. X.; Kissler, K. M.; Kline, T.; Lenox, J. S.; Moser, R. F.; Nguyen, M. T.; Okeley, N. M.; Stone, I. J.; Zhang, X.; Senter, P. D. Development and Properties of β-Glucuronide Linkers for Monoclonal Antibody−Drug Conjugates. *Bioconjug. Chem.* **2006**, *17* (3), 831–840. https://doi.org/10.1021/bc0600214.

(114) Burke, P. J.; Senter, P. D.; Meyer, D. W.; Miyamoto, J. B.; Anderson, M.; Toki, B. E.; Manikumar, G.; Wani, M. C.; Kroll, D. J.; Jeffrey, S. C. Design, Synthesis, and Biological Evaluation of Antibody−Drug Conjugates Comprised of Potent Camptothecin Analogues. *Bioconjug. Chem.* **2009**, *20* (6), 1242–1250. https://doi.org/10.1021/bc9001097.

(115) Hanson, S. R.; Best, M. D.; Wong, C. Sulfatases: Structure, Mechanism, Biological Activity, Inhibition, and Synthetic Utility. *Angew. Chem. Int. Ed.* **2004**, *43* (43), 5736–5763. https://doi.org/10.1002/anie.200300632.

(116) Dwivedi, S. K.; Bhise, A.; Subramani, R.; Yoo, J. Recent Progress of Enzyme Cleavable Linker in Antibody-Drug Conjugates: Sulfatase and Phosphatase. *J. Radiopharm. Mol. Probes* **2021**, *7* (1), 33–40. https://doi.org/10.22643/JRMP.2021.7.1.33.

(117) Hatabe, S.; Kimura, H.; Arao, T.; Kato, H.; Hayashi, H.; Nagai, T.; Matsumoto, K.; De Velasco, M.; Fujita, Y.; Yamanouchi, G.; Fukushima, M.; Yamada, Y.; Ito, A.; Okuno, K.; Nishio, K. Overexpression of Heparan Sulfate 6-O-Sulfotransferase-2 in Colorectal Cancer. *Mol. Clin. Oncol.* **2013**, *1* (5), 845–850. https://doi.org/10.3892/mco.2013.151.

(118) Sardiello, M.; Annunziata, I.; Roma, G.; Ballabio, A. Sulfatases and Sulfatase Modifying Factors: An Exclusive and Promiscuous Relationship. *Hum. Mol. Genet.* **2005**, *14* (21), 3203–3217. https://doi.org/10.1093/hmg/ddi351.

(119) Lübke, T.; Damme, M. Lysosomal Sulfatases: A Growing Family. *Biochem. J.* **2020**, *477* (20), 3963–3983. https://doi.org/10.1042/BCJ20200586.

(120) Ghosh, D. Human Sulfatases: A Structural Perspective to Catalysis. *Cell. Mol.*

Life Sci. **2007**, *64* (15), 2013–2022. https://doi.org/10.1007/s00018-007-7175-y.

(121) Dierks, T.; Schmidt, B.; Von Figura, K. Conversion of Cysteine to Formylglycine: A Protein Modification in the Endoplasmic Reticulum. *Proc. Natl. Acad. Sci.* **1997**, *94* (22), 11963–11968. https://doi.org/10.1073/pnas.94.22.11963.

(122) Hettle, A. G.; Vickers, C.; Robb, C. S.; Liu, F.; Withers, S. G.; Hehemann, J.-H.; Boraston, A. B. The Molecular Basis of Polysaccharide Sulfatase Activity and a Nomenclature for Catalytic Subsites in This Class of Enzyme. *Structure* **2018**, *26* (5), 747-758.e4. https://doi.org/10.1016/j.str.2018.03.012.

(123) Farooqui, AkhlaqA.; Horrocks, LloydA. On the Role of Sulfolipids in Mammalian Metabolism. *Mol. Cell. Biochem.* **1985**, *66* (1). https://doi.org/10.1007/BF00231827.

(124) Kertesz, M. A. Riding the Sulfur Cycle – Metabolism of Sulfonates and Sulfate Esters in Gram-Negative Bacteria. *FEMS Microbiol. Rev.* **2000**, *24* (2), 135–175. https://doi.org/10.1111/j.1574-6976.2000.tb00537.x.

(125) Dodgson, K. S. Sulfatases of Microbial Origin.

(126) Buono, M.; Cosma, M. P. Sulfatase Activities towards the Regulation of Cell Metabolism and Signaling in Mammals. *Cell. Mol. Life Sci.* **2010**, *67* (5), 769–780. https://doi.org/10.1007/s00018-009-0203-3.

(127) Trivedi, P. C.; Bartlett, J. J.; Pulinilkunnil, T. Lysosomal Biology and Function: Modern View of Cellular Debris Bin. *Cells* **2020**, *9* (5), 1131. https://doi.org/10.3390/cells9051131.

(128) Wiegmann, E. M.; Westendorf, E.; Kalus, I.; Pringle, T. H.; Lübke, T.; Dierks, T. Arylsulfatase K, a Novel Lysosomal Sulfatase. *J. Biol. Chem.* **2013**, *288* (42), 30019–30028. https://doi.org/10.1074/jbc.M113.499541.

(129) Dhoot, G. K.; Gustafsson, M. K.; Ai, X.; Sun, W.; Standiford, D. M.; Emerson, C. P. Regulation of Wnt Signaling and Embryo Patterning by an Extracellular Sulfatase. *Science* **2001**, *293* (5535), 1663–1666. https://doi.org/10.1126/science.293.5535.1663.

(130) Gande, S. L.; Mariappan, M.; Schmidt, B.; Pringle, T. H.; Von Figura, K.; Dierks, T. Paralog of the Formylglycine-generating Enzyme – Retention in the Endoplasmic Reticulum by Canonical and Noncanonical Signals. *FEBS J.* **2008**, *275* (6), 1118–1130. https://doi.org/10.1111/j.1742-4658.2008.06271.x.

(131) Schmidt, B.; Selmer, T.; Ingendoh, A.; Figurat, K. V. A Novel Amino Acid Modification in Sulfatases That Is Defective in Multiple Sulfatase Deficiency. *Cell* **1995**, *82* (2), 271–278. https://doi.org/10.1016/0092-8674(95)90314-3.

(132) Preusser-Kunze, A.; Mariappan, M.; Schmidt, B.; Gande, S. L.; Mutenda, K.; Wenzel, D.; Von Figura, K.; Dierks, T. Molecular Characterization of the Human Cα-Formylglycine-Generating Enzyme. *J. Biol. Chem.* **2005**, *280* (15), 14900–14910. https://doi.org/10.1074/jbc.M413383200.

(133) Roeser, D.; Preusser-Kunze, A.; Schmidt, B.; Gasow, K.; Wittmann, J. G.; Dierks, T.; Von Figura, K.; Rudolph, M. G. A General Binding Mechanism for All Human Sulfatases by the Formylglycine-Generating Enzyme. *Proc. Natl. Acad. Sci.* **2006**, *103* (1), 81–86. https://doi.org/10.1073/pnas.0507592102.

(134) Demydchuk, M.; Hill, C. H.; Zhou, A.; Bunkóczi, G.; Stein, P. E.; Marchesan, D.; Deane, J. E.; Read, R. J. Insights into Hunter Syndrome from the Structure of Iduronate-2-Sulfatase. *Nat. Commun.* **2017**, *8* (1), 15786. https://doi.org/10.1038/ncomms15786.

(135) Boltes, I.; Czapinska, H.; Kahnert, A.; Von Bülow, R.; Dierks, T.; Schmidt, B.; Von Figura, K.; Kertesz, M. A.; Usón, I. 1.3 Å Structure of Arylsulfatase from Pseudomonas Aeruginosa Establishes the Catalytic Mechanism of Sulfate Ester Cleavage in the Sulfatase Family. *Structure* **2001**, *9* (6), 483–491. https://doi.org/10.1016/S0969-2126(01)00609-8.

(136) Carlson, B. L.; Ballister, E. R.; Skordalakes, E.; King, D. S.; Breidenbach, M. A.; Gilmore, S. A.; Berger, J. M.; Bertozzi, C. R. Function and Structure of a Prokaryotic Formylglycine-Generating Enzyme. *J. Biol. Chem.* **2008**, *283* (29), 20117–20125. https://doi.org/10.1074/jbc.M800217200.

(137) Appel, M. J.; Bertozzi, C. R. Formylglycine, a Post-Translationally Generated Residue with Unique Catalytic Capabilities and Biotechnology Applications. *ACS Chem. Biol.* **2015**, *10* (1), 72–84. https://doi.org/10.1021/cb500897w.

(138) Tokheim, A. M.; Spannaus-Martin, D. J.; Martin, B. L. Evidence for the Cd2+ Activation of the Aryl Sulfatase from Helix Pomatia. *BioMetals* **2005**, *18* (5), 537–540. https://doi.org/10.1007/s10534-005-0836-0.

(139) Hermann, S.; Schestag, F.; Polten, A.; Kafert, S.; Penzien, J.; Zlotogora, J.; Baumann, N.; Gieselmann, V. Characterization of Four Arylsulfatase A Missense Mutations G86D, Y201C, D255H, and E312D Causing Metachromatic Leukodystrophy. *Am. J. Med. Genet.* **2000**, *91* (1), 68–73. https://doi.org/10.1002/(SICI)1096-8628(20000306)91:1%253C68::AID-

AJMG13%253E3.0.CO;2-G.

(140) Zhang, X.; Bhattacharyya, S.; Kusumo, H.; Goodlett, C. R.; Tobacman, J. K.; Guizzetti, M. Arylsulfatase B Modulates Neurite Outgrowth via Astrocyte Chondroitin-4-sulfate: Dysregulation by Ethanol. *Glia* **2014**, *62* (2), 259–271. https://doi.org/10.1002/glia.22604.

(141) Oyama, N.; Satoh, M.; Iwatsuki, K.; Kaneko, F. Novel Point Mutations in the Steroid Sulfatase Gene in Patients with X-Linked Ichthyosis: Transfection Analysis Using the Mutated Genes. *J. Invest. Dermatol.* **2000**, *114* (6), 1195–1199. https://doi.org/10.1046/j.1523-1747.2000.00004.x.

(142) Franco, B.; Meroni, G.; Parenti, G.; Levilliers, J.; Bernard, L.; Gebbia, M.; Cox, L.; Maroteaux, P.; Sheffield, L.; Rappold, G. A.; Andria, G.; Petit, C.; Ballabio, A. A Cluster of Sulfatase Genes on Xp22.3: Mutations in Chondrodysplasia Punctata (CDPX) and Implications for Warfarin Embryopathy. *Cell* **1995**, *81* (1), 15–25. https://doi.org/10.1016/0092-8674(95)90367-4.

(143) Morena, F.; Di Girolamo, I.; Emiliani, C.; Gritti, A.; Biffi, A.; Martino, S. A New Analytical Bench Assay for the Determination of Arylsulfatase A Activity Toward Galactosyl-3-Sulfate Ceramide: Implication for Metachromatic Leukodystrophy Diagnosis. *Anal. Chem.* **2014**, *86* (1), 473–481. https://doi.org/10.1021/ac4023555.

(144) Halsall, D. J.; Halligan, E. P.; Elsey, T. S.; Cox, T. M. Metachromatic Leucodystrophy: A Newly Identified Mutation in Arylsulphatase A, D281Y, Found as a Compound Heterozygote with I179L in an Adult Onset Case. *Hum. Mutat.* **1999**, *14* (5), 447–447. https://doi.org/10.1002/(SICI)1098-1004(199911)14:5%253C447::AID-HUMU12%253E3.0.CO;2-1.

(145) Ahn, V. E.; Faull, K. F.; Whitelegge, J. P.; Fluharty, A. L.; Privé, G. G. Crystal Structure of Saposin B Reveals a Dimeric Shell for Lipid Binding. *Proc. Natl. Acad. Sci.* **2003**, *100* (1), 38–43. https://doi.org/10.1073/pnas.0136947100.

(146) Bhattacharyya, S.; Tobacman, J. K. Arylsulfatase B Regulates Colonic Epithelial Cell Migration by Effects on MMP9 Expression and RhoA Activation. *Clin. Exp. Metastasis* **2009**, *26* (6), 535–545. https://doi.org/10.1007/s10585-009-9253-z.

(147) Peters, C.; Schmidt, B.; Rommerskirch, W.; Rupp, K.; Zühlsdorf, M.; Vingron, M.; Meyer, H. E.; Pohlmann, R.; Von Figura, K. Phylogenetic Conservation of Arylsulfatases. cDNA Cloning and Expression of Human Arylsulfatase B. *J.*

Biol. Chem. **1990**, *265* (6), 3374–3381. https://doi.org/10.1016/S0021-9258(19)39778-9.

(148) Villani, G. R. D.; Balzano, N.; Vitale, D.; Saviano, M.; Pavone, V.; Natale, P. D. Maroteaux^Lamy Syndrome: ¢ve Novel Mutations and Their Structural Localization.

(149) Bond, C. S.; Clements, P. R.; Ashby, S. J.; Collyer, C. A.; Harrop, S. J.; Hopwood, J. J.; Guss, J. M. Structure of a Human Lysosomal Sulfatase. *Structure* **1997**, *5* (2), 277–289. https://doi.org/10.1016/S0969-2126(97)00185-8.

(150) Matsumoto, J.; Ariyoshi, N.; Ishii, I.; Kitada, M. Functional Characterization of Seven Single-Nucleotide Polymorphisms of the Steroid Sulfatase Gene Found in a Japanese Population. *J. Hum. Genet.* **2013**, *58* (5), 267–272. https://doi.org/10.1038/jhg.2013.12.

(151) Basler, E.; Grompe, M.; Parenti, G. Identification of Point Mutations in the Steroid Sulfatase Gene of Three Patients with X-Linked Ichthyosis.

(152) Chanplakorn, N.; Chanplakorn, P.; Suzuki, T.; Ono, K.; Chan, M. S. M.; Miki, Y.; Saji, S.; Ueno, T.; Toi, M.; Sasano, H. Increased Estrogen Sulfatase (STS) and 17β-Hydroxysteroid Dehydrogenase Type 1(17β-HSD1) Following Neoadjuvant Aromatase Inhibitor Therapy in Breast Cancer Patients. *Breast Cancer Res. Treat.* **2010**, *120* (3), 639–648. https://doi.org/10.1007/s10549-010-0785-3.

(153) Hernandez-Guzman, F. G.; Higashiyama, T.; Pangborn, W.; Osawa, Y.; Ghosh, D. Structure of Human Estrone Sulfatase Suggests Functional Roles of Membrane Association. *J. Biol. Chem.* **2003**, *278* (25), 22989–22997. https://doi.org/10.1074/jbc.M211497200.

(154) Muschol, N.; Storch, S.; Ballhausen, D.; Beesley, C.; Westermann, J.-C.; Gal, A.; Ullrich, K.; Hopwood, J. J.; Winchester, B.; Braulke, T. Transport, Enzymatic Activity, and Stability of Mutant Sulfamidase (SGSH) Identified in Patients with Mucopolysaccharidosis Type III A. *Hum. Mutat.* **2004**, *23* (6), 559–566. https://doi.org/10.1002/humu.20037.

(155) Beesley, C. E.; Young, E. P.; Vellodi, A.; Winchester, B. G. Mutational Analysis of Sanfilippo Syndrome Type A (MPS IIIA): Identification of 13 Novel Mutations. *J. Med. Genet.* **2000**, *37* (9), 704–707. https://doi.org/10.1136/jmg.37.9.704.

(156) Sidhu, N. S.; Schreiber, K.; Pröpper, K.; Becker, S.; Usón, I.; Sheldrick, G. M.; Gärtner, J.; Krätzner, R.; Steinfeld, R. Structure of Sulfamidase Provides Insight into the Molecular Pathology of Mucopolysaccharidosis IIIA. *Acta Crystallogr. D Biol. Crystallogr.* **2014**, *70* (5), 1321–1335. https://doi.org/10.1107/S1399004714002739.

(157) Villani, G. R. D.; Daniele, A.; Balzano, N.; Natale, P. D. Expression of ¢ve Iduronate-2-Sulfatase Site-Directed Mutations.

(158) Hartog, C.; Fryer, A.; Upadhyaya, M. Mutation Analysis of Iduronate-2-Sulphatase Gene in 24 Patients with Hunter Syndrome: Characterisation of 6 Novel Mutations. *Hum. Mutat.* **1999**, *14* (1), 87–87. https://doi.org/10.1002/(SICI)1098-1004(1999)14:1%253C87::AID-HUMU14%253E3.0.CO;2-N.

(159) Demydchuk, M.; Hill, C. H.; Zhou, A.; Bunkóczi, G.; Stein, P. E.; Marchesan, D.; Deane, J. E.; Read, R. J. Insights into Hunter Syndrome from the Structure of Iduronate-2-Sulfatase. *Nat. Commun.* **2017**, *8* (1), 15786. https://doi.org/10.1038/ncomms15786.

(160) Simpson, L. S.; Widlanski, T. S. A Comprehensive Approach to the Synthesis of Sulfate Esters. *J. Am. Chem. Soc.* **2006**, *128* (5), 1605–1610. https://doi.org/10.1021/ja056086j.

(161) Kaiser, D.; Klose, I.; Oost, R.; Neuhaus, J.; Maulide, N. Bond-Forming and -Breaking Reactions at Sulfur(IV): Sulfoxides, Sulfonium Salts, Sulfur Ylides, and Sulfinate Salts. *Chem. Rev.* **2019**, *119* (14), 8701–8780. https://doi.org/10.1021/acs.chemrev.9b00111.

(162) Montero Bastidas, J. R.; Oleskey, T. J.; Miller, S. L.; Smith, M. R.; Maleczka, R. E. Para-Selective, Iridium-Catalyzed C–H Borylations of Sulfated Phenols, Benzyl Alcohols, and Anilines Directed by Ion-Pair Electrostatic Interactions. *J. Am. Chem. Soc.* **2019**, *141* (39), 15483–15487. https://doi.org/10.1021/jacs.9b08464.

(163) Young, T.; Kiessling, L. L. A Strategy for the Synthesis of Sulfated Peptides. *Angew. Chem. Int. Ed.* **2002**, *41* (18), 3449–3451. https://doi.org/10.1002/1521-3773(20020916)41:18%253C3449::AID-ANIE3449%253E3.0.CO;2-U.

(164) *ATSDR's Toxicological Profiles: Web Version*; CRC Press, 2002. https://doi.org/10.1201/9781420061888.

(165) John Riddick Hazards of Sulphuric Acid. *Loss Prevention Bulletin* **2014**, *236*,

3–9. https://www.icheme.org/media/2236/lpb236p03.pdf

(166) NJHEALTH. *Hazardous Substance Fact Sheet of Sulfuric Acid*; 2008. https://nj.gov/health/eoh/rtkweb/documents/fs/1761.pdf.

(167) Alshehri, J.; Jones, A. Approaches to the Sulfation of Small Molecules: Current Progress and Future Directions. April 8, 2024. https://doi.org/10.26434/chemrxiv-2024-26pv5.

(168) Alshehri, J. A.; Jones, A. M. Chemical Approaches to the Sulfation of Small Molecules: Current Progress and Future Directions. *Essays Biochem.* **2024**, *68* (4), 449–466. https://doi.org/10.1042/EBC20240001.

(169) Uali, A.; Kazymbetova, A.; Belgibayeva, A.; Nurpeissova, A.; Bakenov, Z.; Mukanova, A. Industrial Sulfur Separation and Purification: Paving the Way to Energy Applications. *Chem. Eng. J.* **2025**, *510*, 161574. https://doi.org/10.1016/j.cej.2025.161574.

(170) Mihai, M. T.; Williams, B. D.; Phipps, R. J. *Para* -Selective C–H Borylation of Common Arene Building Blocks Enabled by Ion-Pairing with a Bulky Countercation. *J. Am. Chem. Soc.* **2019**, *141* (39), 15477–15482. https://doi.org/10.1021/jacs.9b07267.

(171) Glace, M.; Armstrong, C.; Puryear, N.; Bailey, C.; Moazeni-Pourasil, R. S.; Scott, D.; Abdelwahed, S.; Roper, Thomas. D. An Automated Continuous Synthesis and Isolation for the Scalable Production of Aryl Sulfonyl Chlorides. *Molecules* **2023**, *28* (10), 4213. https://doi.org/10.3390/molecules28104213.

(172) Gordon, G. S.; Burwell, R. L. The Action of Sulfuric Acid, Ethanesulfonic Acid and Chlorosulfonic Acid on Aliphatic Hydrocarbons. *J. Am. Chem. Soc.* **1949**, *71* (7), 2355–2359. https://doi.org/10.1021/ja01175a029.

(173) Reitz, H. C.; Ferrel, R. E.; Olcott, H. S.; Fraenkel-Conrat, H. Action of Sulfating Agents on Proteins and Model Substances. II. Pyridine-Chlorosulfonic Acid. *J. Am. Chem. Soc.* **1946**, *68* (6), 1031–1035. https://doi.org/10.1021/ja01210a037.

(174) Liu, C.; Liu, X.; Deng, Y.; Niu, J. Chemical Strategies for Controlling Sulfation in Biomacromolecules. *ACS Chem. Biol.* **2026**, acschembio.5c00876. https://doi.org/10.1021/acschembio.5c00876.

(175) Gill, D. M.; Male, L.; Jones, A. M. Sulfation Made Simple: A Strategy for Synthesising Sulfated Molecules. *Chem. Commun.* **2019**, *55* (30), 4319–4322.

https://doi.org/10.1039/C9CC01057B.

(176) Ingram, L. J.; Taylor, S. D. Introduction of 2,2,2-Trichloroethyl-Protected Sulfates into Monosaccharides with a Sulfuryl Imidazolium Salt and Application to the Synthesis of Sulfated Carbohydrates. *Angew. Chem. Int. Ed.* **2006**, *45* (21), 3503–3506. https://doi.org/10.1002/anie.200600153.

(177) Yue, S.; Ding, G.; Zheng, Y.; Song, C.; Xu, P.; Yu, B.; Li, J. Dimethyl Sulfate and Diisopropyl Sulfate as Practical and Versatile O-Sulfation Reagents. *Nat. Commun.* **2024**, *15* (1), 1861. https://doi.org/10.1038/s41467-024-46214-x.

(178) Penney, L.; Perlin, S. A Method for the Sulfation of Sugars Employing a Stable Aryl Sulfate Intermediate.

(179) Aoki, E.; Sarrimanolis, J. N.; Lyon, S. A.; Elrod, M. J. Determining the Relative Reactivity of Sulfate, Bisulfate, and Organosulfates with Epoxides on Secondary Organic Aerosol. *ACS Earth Space Chem.* **2020**, *4* (10), 1793–1801. https://doi.org/10.1021/acsearthspacechem.0c00178.

(180) Byun, H.-S.; He, L.; Bittman, R. Cyclic Sulfites and Cyclic Sulfates in Organic Synthesis. *Tetrahedron* **2000**, *56* (37), 7051–7091. https://doi.org/10.1016/S0040-4020(00)00494-4.

(181) Xie, M.; Widlanski, T. S. A New Protecting Group for the Synthesis of Complex Sulfonates. **1996**, *36* (26), 4443–4446. https://doi.org/10.1016/0040-4039(96)00883-0.

(182) Proud, A. D.; Prodger, J. C.; Flitsch, S. L. Development of a Protecting Group for Sulfate Esters. *Tetrahedron Lett.* **1997**, *38* (41), 7243–7246. https://doi.org/10.1016/S0040-4039(97)01681-X.

(183) Liu, Y.; Lien, I.-F. F.; Ruttgaizer, S.; Dove, P.; Taylor, S. D. Synthesis and Protection of Aryl Sulfates Using the 2,2,2-Trichloroethyl Moiety. *Org. Lett.* **2004**, *6* (2), 209–212. https://doi.org/10.1021/ol036157o.

(184) Ingram, L. J.; Desoky, A.; Ali, A. M.; Taylor, S. D. *O* - and *N* -Sulfations of Carbohydrates Using Sulfuryl Imidazolium Salts. *J. Org. Chem.* **2009**, *74* (17), 6479–6485. https://doi.org/10.1021/jo9014112.

(185) Yu, M.; Zhang, T.; Jalani, H. B.; Dong, X.; Lu, H. Iridium-Catalyzed Aryl C−H Sulfonamidation and Amide Formation Using a Bifunctional Nitrogen Source.

(186) Van Loo, B.; Berry, R.; Boonyuen, U.; Mohamed, M. F.; Golicnik, M.; Hengge,

A. C.; Hollfelder, F. Transition-State Interactions in a Promiscuous Enzyme: Sulfate and Phosphate Monoester Hydrolysis by *Pseudomonas Aeruginosa* Arylsulfatase. *Biochemistry* **2019**, *58* (10), 1363–1378. https://doi.org/10.1021/acs.biochem.8b00996.

(187) Khanra, P.; Singh, A. K.; Roy, L.; Das, A. Supporting Information For.

(188) Raposo Moreira Dias, A.; Pina, A.; Dal Corso, A.; Arosio, D.; Belvisi, L.; Pignataro, L.; Caruso, M.; Gennari, C. Multivalency Increases the Binding Strength of RGD Peptidomimetic-Paclitaxel Conjugates to Integrin αVβ3. *Chem. – Eur. J.* **2017**, *23* (58), 14410–14415. https://doi.org/10.1002/chem.201703093.

(189) Zhang, Y.; Li, Y.; Yang, X.; Ding, Y.; Zhao, Z.; Liu, X.; Yang, Z.; Cui, Y. A Single-State Fluorescent with Bright White-Light Emission in the Solid Station and Aggregation-Induced Emission Enhancement Compound for Pd0 Detection. *Talanta* **2018**, *179*, 177–185. https://doi.org/10.1016/j.talanta.2017.11.002.

(190) Mahy, W.; Plucinski, P. K.; Frost, C. G. Copper-Catalyzed One-Pot Synthesis of *N* -Aryl Oxazolidinones from Amino Alcohol Carbamates. *Org. Lett.* **2014**, *16* (19), 5020–5023. https://doi.org/10.1021/ol502322c.

(191) Tsukiji, S.; Pattnaik, S. B.; Suga, H. Reduction of an Aldehyde by a NADH/Zn^{2+} -Dependent Redox Active Ribozyme. *J. Am. Chem. Soc.* **2004**, *126* (16), 5044–5045. https://doi.org/10.1021/ja0495213.

(192) Olmez-Hanci, T.; Arslan-Alaton, I. Comparison of Sulfate and Hydroxyl Radical Based Advanced Oxidation of Phenol. *Chem. Eng. J.* **2013**, *224*, 10–16. https://doi.org/10.1016/j.cej.2012.11.007.

(193) Martynoff, M. Note de Laboratoire: Spectres d'absorption de Quelques p-Quinones. *Bull. Soc. Chim. Fr.* **1949**, *16*, 258–261.

(194) *The Relationship Between UV-VIS Absorption and Structure of Organic Compounds*. https://www.shimadzu.com/an/service-support/technical-support/technical-information/uv-vis/uv-ap/apl/index.html (accessed 2026-02-01).

(195) Himmi, M. F. B. M.; Yih, B. S.; Yusoff, F.; Saleh, N. M. Extraction of Phenol from Water Using Dispersive Liquid-Liquid Microextraction Coupled with UV-VIS Spectroscopy. *J. Anal. Chem.* **2022**, *77* (1), 8–17. https://doi.org/10.1134/S1061934822010051.

(196) *14.8: Interpreting Ultraviolet Spectra- The Effect of Conjugation*. Chemistry LibreTexts. https://chem.libretexts.org/Bookshelves/Organic_Chemistry/Organic_Chemistry_(Morsch_et_al.)/14%3A_Conjugated_Compounds_and_Ultraviolet_Spectroscopy/14.08%3A_Interpreting_Ultraviolet_Spectra-_The_Effect_of_Conjugation (accessed 2026-02-01).

(197) Murtaza, G.; Khan, S. A.; Shabbir, A.; Mahmood, A.; Asad, H. H. B.; Farzana, K.; Malik, N. S.; Hussain, I. Development of a UV-Spectrophotometric Method for the Simultaneous Determination of Aspirin and Paracetamol in Tablets.

(198) Falcone, G.; Giuffrè, O.; Sammartano, S. Acid–Base and UV Properties of Some Aminophenol Ligands and Their Complexing Ability towards Zn2+ in Aqueous Solution. *J. Mol. Liq.* **2011**, *159* (2), 146–151. https://doi.org/10.1016/j.molliq.2011.01.003.

(199) Bertolacini, R. J.; Barney, J. E. Ultraviolet Spectrophotometric Determination of Sulfate, Chloride, and Fluoride with Chloranilic Acid. *Anal. Chem.* **1958**, *30* (2), 202–205. https://doi.org/10.1021/ac60134a012.

(200) Reuß, F.; Heretsch, P. Synthesis of Aspidodispermine via Pericyclic Framework Reconstruction.

(201) Song, Z.-Q.; Wang, D.-H. Palladium-Catalyzed Hydroxylation of Aryl Halides with Boric Acid.